Thermomechanical And Metallurgical Modelling Of Laser Hardening And Laser Cladding Processes

PhD Thesis

Alejandro Suárez Díaz

Departament of Industrial Engineering
Escuela Politécnica Superior
Universidade da Coruña

March 2011

Thermomechanical And Metallurgical Modelling Of Laser Hardening And Laser Cladding Processes

PhD Thesis
Alejandro Suárez Díaz

Directed by the Professors:
Armando J. Yáñez Casal
María J. Tobar Vidal

Departament of Industrial Engineering
Escuela Politécnica Superior
Universidade da Coruña

March 2011

ISBN

Dedicated to
my parents.

Acknowledgements

I want to express my special gratitude to my parents, who encouraged me to learn things and gave me the freedom I need since I was a child. They always supported me, both in the good and bad moments. Their qualities are an example to follow. Special thanks to the rest of my family and friends, for always been so supportive, teach me so many things and be responsible of some of the best moments of my life.

I want to thank all the colleagues from the Laboratory of Laser Industrial Applications of the Universidade Da Coruña, for their help, ideas and interesting things that I have learned with them. Specially to my director, Armando, who encouraged me to do postgraduate studies from the beginning and was always supportive and optimistic. Also to Jose, who introduced me to the field of laser materials processing and taught me lots of interesting things during this four years, and to Diego, my apprentice, who served as a meticulous editor for the thesis.

I also want to express my gratitude to my supervisor in Siemens AG at Mülheim an der Ruhr during my six months stay, and to the friendly people I met there. I want to acknowledge the excellent people working at the ESRF who helped me with the experimental procedure as well as the processing of the data. Also my gratitude to the funny professors of materials science at the University Rey Juan Carlos, in Madrid, where I was doing another six months stay. And finally, I want to acknowledge the funding given by the spainish Ministery of Science and Innovation as a FPI grant.

Summary

The development of high stresses and distortions is one of the main concerns in laser surface heat treatments. The objective of the present thesis is to contribute to the better understanding of the thermomechanical behavior during laser transformation hardening and laser metal deposition techniques, including as well the development of a flexible tool with customizable models for the numerical calculation of the thermomechanical variables, and the microstructural evolution through phase transformation models.

Such a tool will be useful for the prediction of the residual strains and stresses after the processes as well as the phase changes, helping with its optimization and understanding, thus reducing the number of test trials necessary to achieve the desired results. Something that has paramount importance when unique or expensive workpieces should be treated.

The model was validated using several experimental techniques to assess its predictions and fine tune some of its parameters.

Resumen

La generación de altas tensiones y deformaciones es una de las mayores preocupaciones en los tratamientos térmicos superficiales por láser. El objetivo de la presente tesis es el de contribuir al mejor entendimiento del comportamiento termomecánico durante el endurecimiento superficial por láser y las técnicas de deposición de metal por láser, incluyendo también la creación de una herramienta flexible con modelos adaptables para el cálculo numérico de las variables termomecánicas, así como la evolución microestructural mediante modelos de transformación de fase.

Tal herramienta será útil en la predicción de los esfuerzos y deformacíones residuales después del tratamiento, ayudando con su optimización y mejor entendimiento, y por tanto reduciendo el número de ensayos necesarios para alcanzar los resultados deseados. Algo de gran importancia cuando piezas únicas o de gran valor deben tratarse.

El modelo ha sido validado utilizando varias técnicas experimentales para comparar sus predicciones y ajustar algunos de sus parámetros.

Resumo

A xeración de altas tensións e deformacións é unha das maiores preocupacións dos tratamentos térmicos superficiais por láser. O obxectivo da presente tesis é o de contribuir ao mellor entendemento do comportamento termomecánico durante o endurecemento superficial por láser e as técnicas de deposición de metal por láser, incluindo tamén o desenvolvemento dunha ferramenta flexible con modelos adaptables para o cálculo numérico das variables termomecánicas, así como da evolución microestrutural mediante modelos de transformación de fase.

Tal ferramenta será de utilidade na predicción dos esforzos e deformacións residuais despois do tratamento, axudando coa sua optimización e mellorando o seu entendemento, e por tanto diminuindo o número de ensaios necesarios para obter os resultados desexados. Algo de meirande importancia cando pezas únicas ou de gran custo deben ser tratadas.

O modelo foi validado mediante o uso de varias técnicas experimentais para comparar o grao de axeitamento das súas prediccións e axustar algúns dos seus parámetros.

Contents

List of Figures

List of Tables

Part I

Introduction

The first part of the thesis consists of the presentation of the objectives and motivation of the present work, followed by some introductory chapters which aim is to establish the knowledge foundations for the laser material processing techniques that will be modeled in the next part of the thesis: laser transformation hardening and laser cladding. Some fundamental basics of light matter interaction of special relevance are included, as well as a comprehensive review of the numerical modelling of these techniques, widening its influence to encompass CFD simulations and laser welding processes.

Chapter 1

Introduction

In the beginning the Universe was created. This has made a lot of people very angry and been widely regarded as a bad move.

Douglas Adams (*The Hitch Hiker's Guide to the Galaxy*).

Abstract: The objectives and scope of the present thesis along with the motivations of the research in this particular field are exposed in this chapter. A brief description of the structure of the thesis is included at the end of it.

1.1 Motivation

The laser is one of the most relevant inventions of the 20th century, with thousands of applications in numerous fields. In material processing it serves as a focalized power source, outperforming conventional processes and allowing special applications, like rapid prototyping.

The development of high stresses and distortions is one of the main concerns in laser surface heat treatments, and it has special relevance in the laser cladding technique. Residual stresses are detrimental to the integrity of the workpiece. During the process the stresses can reach values high enough to produce cracks in the material. But even if cracks do not appear, the residual stresses can enhance the susceptibility to fatigue, stress-corrosion cracking and lower the failure criterion. Additionally it is of great importance to keep distortions to a minimum, because the development of large deformations could render the workpiece unusable.

Metallurgy has to be taken into account when the working material shows phase transformations, as in the case of carbon and low alloy steels. Stresses and strains change completely when the phase transformation occurs, leading to completely wrong values if metallurgy is neglected. However this increases the complexity of the models, because metallurgy is deeply interrelated with the thermal and mechanical fields generated during the treatments, making difficult the accurate simulation of these processes.

Empirical methods to measure residual stresses are usually complex, expensive or time consuming. In contrast computer simulations can supply a great amount of information, allowing

also the calculation of relevant variables during the ongoing process with great flexibility, helping to get an insightful understanding of the underlying thermomechanical aspects.

1.2 Objectives and Scope

The objective of the present thesis is to contribute to the better understanding of the thermomechanical behavior of laser transformation hardening and laser cladding techniques, including the development of a flexible tool with customizable models for the numerical calculation of the thermomechanical variables of these processes and the microstructure evolution through phase transformation models.

Such a tool will be useful for the estimation of the residual strains and stresses after the processes as well as the phase changes, helping with its optimization too, thus reducing the number of test trials necessary to achieve the desired results. Something that has paramount importance when unique or expensive workpieces have to be treated.

Research within this area has been focused on the modelling of welding, especially the fluid dynamics of the process, and also to the prediction of the microstructural evolution during laser transformation hardening. Less efforts have been made to model the laser cladding yet, or the mechanical aspects of laser transformation hardening.

The scope of the present work is to primarily establish methodologies for the numerical prediction of the relevant variables during laser transformation hardening and laser cladding techniques. Emphasis is made in the detailed prediction of the qualitative and quantitative response of small size structures. The computational efficiency and the overcoming of convergence problems are studied for the improvement of the numerical solution.

Experimental tests performed in the laboratory using methods for the measurement of temperatures, residual stresses and strains were used to validate the predictions of the model.

1.3 Structure of the Thesis

The contents of the thesis are presented in three parts composed as follows.

Part I consists of the presentation of the objectives and motivation of the present work, followed by some introductory chapters which aim is to establish the knowledge foundations for the laser material processing techniques that will be modeled in the next part of the thesis: laser transformation hardening and laser cladding, including a comprehensive review of the numerical modelling of both techniques, and some basics of light matter interaction of special relevance.

The aim of Part II is to present the finite element theory and the metallurgical phase transformation models used in the numerical simulations. After these introductory chapters, the numerical analysis of laser hardening and laser cladding is treated in detail, with special emphasis in the key aspects.

Part III deals with experimental methods for the characterization of temperatures, microstructures and residual stresses in metal plates. The scope of this part is to validate the predictions of the model.

Chapter 2

Light In Materials Processing

For the rest of my life I will reflect on what light is.

Albert Einstein (*in S. Perkowitz, Empire of Light*).

Abstract: This chapter gives a brief introduction to the evolution in the field of laser materials processing over the last decades. Afterwards the basic principles of the absorption of laser light are treated at the end of the chapter.

2.1 Laser Materials Processing

2.1.1 Introduction

The laser is becoming an important tool for many engineering applications. Laser material processing has proved to be able to achieve higher qualities than other conventional processes that are commonly used in the industry. The key for this success is an intense light beam which can be focused to achieve high power densities, making possible some of its most successful industrial applications: laser cutting and laser welding, and also originating more recent applications with great potential, like laser cladding and rapid prototyping. Lower power densities are sufficient for processes like laser hardening and laser forming, and the extremely high power densities achieved by pulsed lasers have made possible the micromachining of materials by direct ablation of its surface. In Fig. 2.1 are represented the different effects and window processes for several applications, depending on the laser irradiance and interaction time.

2.1.2 Development of the Laser

The first laser was created in 1960 by Theodore Maiman [26]. It consisted of a pink ruby cylinder 1 cm in diameter and 2 cm long, which had both ends polished flat and parallel, and coated with silver. One hole of 1 mm in diameter at one end allowed the light to scape. The ruby was mounted on the axis of a helical xenon flashlamp, contained in a polished aluminium cylinder. It was a pulsed laser that produced red light.

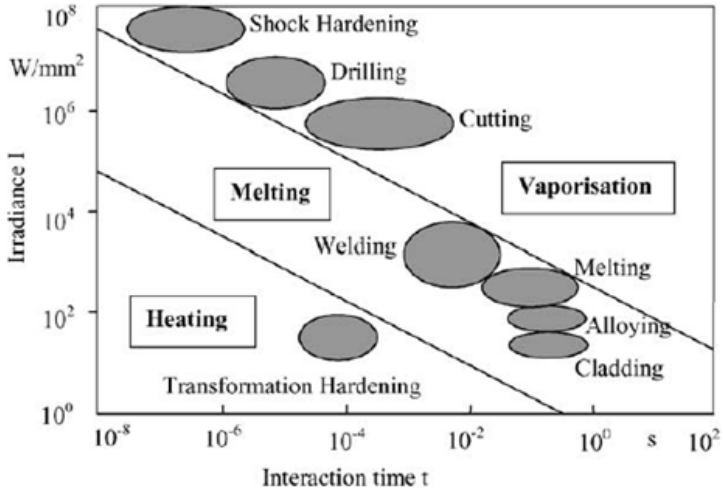

Figure 2.1: Effects and applications of lasers under various operating conditions *(from [1])*

It is remarkable that most of the laser types used today were invented in the decade of the 1960s. However most of them were not ready for the industrial use until next decades. By December 1960 Ali Javan and coworkers [27] created a gas laser: a continuous wave (CW) He-Ne. Kumar Patel developed in 1964 [28] another gas laser, a CW CO_2 laser. By September 1962 Gunther Fenner [29] created the first semiconductor laser, made from gallium arsenide (GaAs). The first neodymium yttrium aluminium garnet (Nd:YAG) laser was developed in 1964 by Geusic and coworkers [30], being a pulsed laser. Metal vapours were investigated leading to the creation of the copper vapour laser in 1965 by William Walter and coworkers [31]. Liquid lasers or dye lasers, which allow the production of tunable laser radiation, were first demonstrated on February 1966 by Peter Sorokin and John Lankard [32].

The first techniques to modulate the laser output were also demonstrated during that period. The principles of Q-switching, which allow pulses of nanoseconds (10^{-9} s), were presented in 1962 by McClung and Hellwarth [33]. Two years later, in 1964, the mode-locking was presented by Hargrove and coworkers [34], allowing pulses in the order of picoseconds (10^{-12} s) or femtoseconds (10^{-15} s).

2.1.3 History of Laser Materials Processing

The first laser industrial applications date from the the same decade in which lasers were created, the 1960s. It took little time to realize the potential applications of laser in the field of materials processing. Laser welds in conduction mode in 0.25 mm stainless steel foils were made around 1963 [35]. Wires and circuit boards were joined afterwards [36]. Diamond wire-drawing dies were drilled in 1965 [37]. All of these initial applications employed ruby lasers. Carbon dioxide lasers were first used to perform cutting in 1967 [38]. Heat treating was studied in the early 60s [39]. Surface melting and alloying were investigated in 1963 [40]. At the end of the decade laser shock hardening was demonstrated [41].

Other applications were developed in the next decades. Laser forming was studied in the early 1980s. The first patent of laser cladding was published in 1976 by the Avco Everett Research Laboratory [42], using the laser to melt a wire of a metallic alloy to create the coating. On 1977 the Caterpillar company patented a laser cladding process by melting a predeposited powder

[43]. The blown powder laser cladding process was patented on 1981 by Rolls-Royce [44], for producing hardfaced surfaces on aeroengine turbine blades. Rapid prototyping techniques were pioneered by C.R. Deckard who patented a method of selective laser sintering in 1987 [45].

Improvements in laser systems result in new generations of multikilowatt CW lasers, mainly CO_2, Nd:YAG and diode lasers. Computer numerically controlled axis and afterwards robotic arms helped with the industrial establishment of lasers. Research was spread also to other areas, like the monitoring of signals emitted during laser processing, allowing real time control of some process parameters in order to maintain constant certain process variables, like temperature, by means of closed-loop feedback control systems.

2.2 Absorption of Laser Light

The absorption of laser light in the surface of a material is governed by Fresnel absorption, which depends on the polarization and angle of incidence of the laser light [46]. In metals the absorptivity consists of the contribution of a series of terms [47] which can be dependent on the intrinsic properties of the metal or the external surface. The intrinsic term includes the effect of the normal (Drude) absorption, anomalous skin effect and interband transitions. The external term contains the effect of the surface roughness, oxides and impurities.

When the laser irradiates the surface of a metal the photons interact predominantly with the free electrons in the conduction band. A fraction of these photons are reflected, the rest are absorbed accelerating the electrons of the conduction band, transforming the kinetic energy into heat through successive collisions between electrons and lattice phonons [48], and transmitting the energy through the structure by normal diffusion processes before reaching an equilibrium state through relaxation process, which in metals is of the order of 10^{-13} s [49]. The resultant absorptivity is dependent on the wavelength of the light, increasing with the decreasing wavelength of the laser radiation.

The surface of the materials usually has a characteristic roughness, resulting in multiple reflections that involve multiple absorption events. Besides it is covered with oxides which can absorb the radiation, create multiple reflections or wave guide it [50, 51]. Therefore the absorption process is very difficult to simulate and the best way to establish the absorptivity of a material is by direct measurement. The absorptivity is the key parameter for modelling the laser absorption in the thermal simulation of laser surface treatments.

The absorption coefficient shows an increase with the temperature (Fig. 2.2a), however for wavelengths of 1 μm the change is usually small until the onset of the melting of the material. In that point the absorption coefficient increases abruptly. In case of the use of a coating to increase the absorptivity of the surface, the absorption coefficient usually diminishes with the temperature due to the vaporization of the coating product, dropping at the melting temperature of the alloy to the value without coating.

The wavelength of the laser light also has an important effect on the absorption coefficient. Shorter wavelengths like the emitted by Nd:YAG lasers (1064 nm) or diode lasers (810 nm) are less reflected by metals (Fig. 2.2b) than the CO_2 wavelength (10.6 μm). On the other hand, the CO_2 wavelength is optimum for the laser processing of organic materials.

Due to the electron gas within the metal, the photons are unable to penetrate inside the material

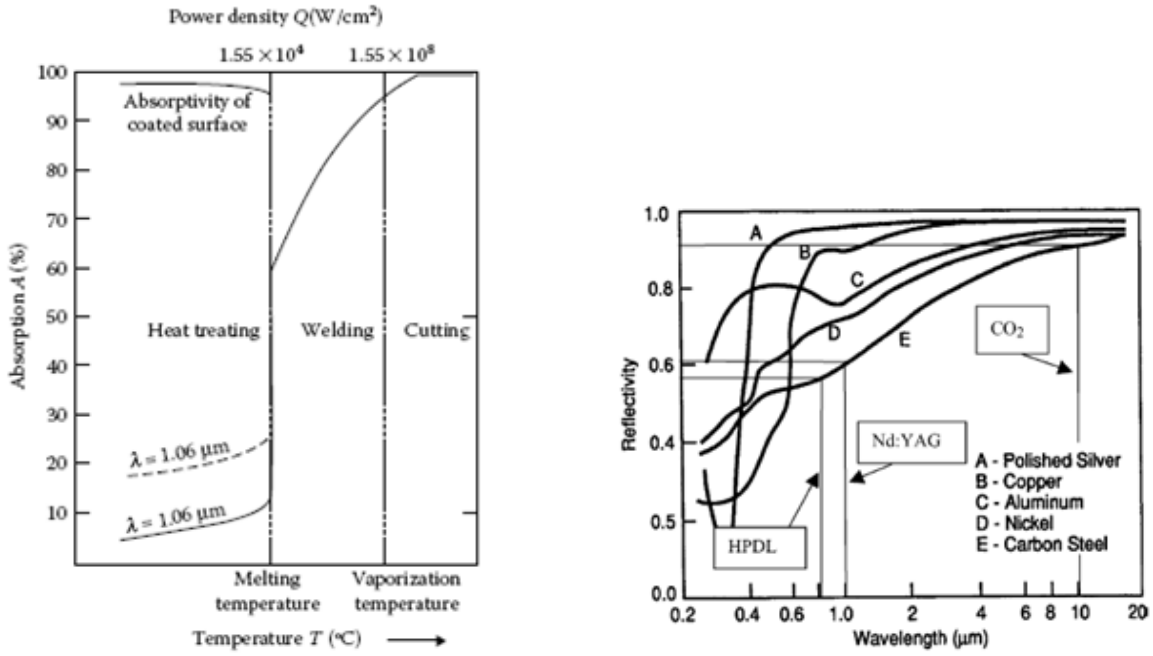

(a) (b)

Figure 2.2: (a) Effect of temperature on laser light absorptivity *(from [2])*. (b) Reflectivity as a function of wavelength for various materials *(from [3])*.

and the absorption takes place in a layer of the order of tens of nanometers. Therefore the laser can be considered as a plane source in most of the numerical models. However, in deep penetration (keyhole) welding, and blown powder laser cladding it is usually modelled as a volumetric source because, in the first case, the laser penetrates inside the material by creating a vapour cavity, and in the second case the laser interacts with the blown powder melting it.

The absorption of laser light by a keyhole cavity is a complex process in which the main mechanisms are [52] direct Fresnel absorption in the multiple reflections inside the keyhole, and the two step process of energy absorption by inverse Bremsstrahlung in the ionized vapour inside the cavity, followed by thermal conduction to the keyhole wall. In laser cladding with blown powder the light suffers multiple reflections in powder stream, heating and even melting the particles before arriving at the melt pool, and attenuating the laser power distribution that reaches the workpiece, making difficult a precise simulation of the whole process [53, 54].

Chapter 3

State Of The Art

If I have seen further than others, it is by standing upon the shoulders of giants.
Sir Isaac Newton.

Abstract: This chapter gives an overview of three techniques that share many similarities in their way to be modelled during a thermomechanical analysis: laser transformation hardening, laser welding and laser cladding, as well as a bibilographical review of the published material regarding the numerical modelling of these techniques. The time frame of the review spans to the year 2010.

3.1 Laser Transformation Hardening

3.1.1 Introduction to Laser Transformation Hardening

Laser Transformation Hardening (LTH) is an advanced heat treatment process used to obtain hard wear resistant surfaces without affecting the bulk material. Compared with conventional hardening methods as flame, induction and especially case hardening, LTH has several advantages: low thermal distortion, adaptability to the component geometry, good controllability of the laser power, easy automation, etc. [55]. For these reasons it is becoming the optimal technological solution for the surface treatment of small or complex components.

The process does not involve melting, the transformations occur in the solid state. The hardness of the martensite formed when steel is heat treated enhances the wear resistance of the surface. Examples of components that are hardened by LTH include wear tracks for power steering housing, camshafts, automobile valve guides and seats, gear teeth, diesel cylinder liner bores, surface hardening of cylinder head units in aluminum car engines, hard-facing of car distribution shafts and surface hardening of mill rollers [56].

In some cases costly post-hardening operations like honing, can be avoided with LTH [57]. Furthermore, the compressive stresses in the hardened zone due to the martensitic transformation enhance fatigue strength; De la Cruz et al. [58] measured an increase in the fatigue limit of smooth and notched B-Mn steel specimens of 18% and 56% respectively. D. Pantelis et al. [59]

Figure 3.1: LTH of a cylindrical workpiece at high rotational speeds *(from [4])*

studied laser treated samples of a structural steel CK60, showing higher corrosion resistance. Additionally, Lo et al. [60] improve the cavitation-erosion resistance of a martensitic stainless steel AISI 440C by means of LTH.

The basis of the technique is to induce a thermal cycle on the surface of the workpiece, reaching a maximum temperature high enough to transform the initial microstructure, usually composed of ferrite and pearlite, into austenite. The next part of the cycle is a fast cooling to transform the newly formed austenite into hard and resistant martensite. The main cooling mechanism is simply conduction heat transfer to the rest of the material of the workpiece, which acts as an efficient heat sink, in a process called "self-quenching". Only the surface of the workpiece is affected by the procedure whereas the core maintains its mechanical properties.

Hardness values up to 1000 HV and hardened depths of about 1.5 mm can be achieved using alloys with high hardenability. However, due to the limited spot size, when several passings are necessary to cover the surface of the workpiece, the heating effect from the last track produces a region of back-tempering in the previous one, hence reducing the hardness and constituting the major drawback of the technique. With cylindrical workpieces it is possible to distribute the energy homogeneously along an annular circumference on the surface of the treated workpiece using high rotational speeds [4], instead of the low speeds typical of LTH, generating a heating ring and overcoming the backtempering effect (Fig. 3.1). A uniformly distributed beam on non-rotating surfaces can also be achieved by rastering or scanning a finely focused beam to cover a wide area (Fig. 3.2). The process involves two vibrating mirrors to get the beam to move back and forth at a high frequency to create the required pattern [5].

With higher power densities the surface of the component will melt. This process called Laser Surface Melting (LSM) allows a greater hardened depth, and produces a fine and homogeneous microstructure in the melted zone containing fine precipitates. The dissolution of large carbides and precipitation of ultra-fine carbides leads to a better corrosion resistance in stainless steels and tool steels [61, 62, 63]. Also in magnesium alloys the grain refinement and precipitation of fine intermetallics improved significantly the corrosion resistance [64].

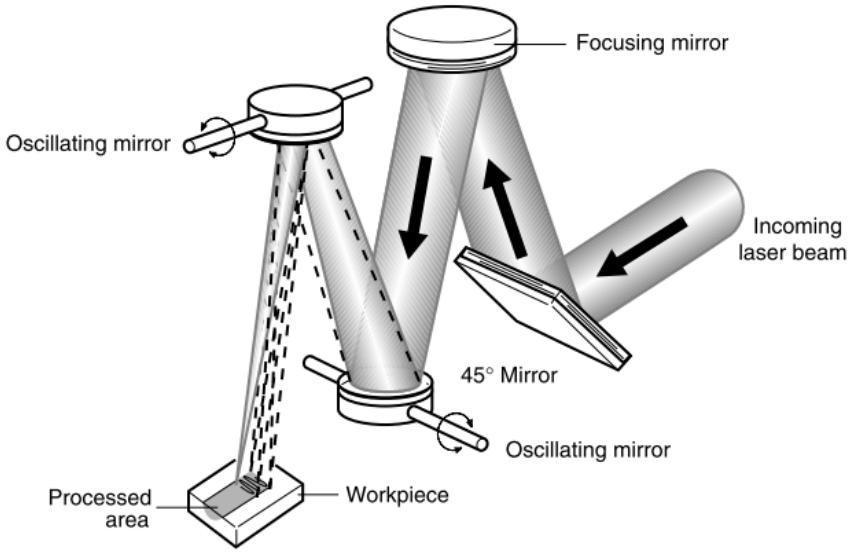

Figure 3.2: LTH with a rastering beam *(from [5])*

Numerous investigations were done in an attempt to improve the process by creating analytical and numerical models to predict the temperature evolution, hardness depth, phase evolution and 3D hardness profiles. Later on, stress generation was the subject of several studies.

3.1.2 Principles of Laser Transformation Hardening

The principles of LTH are similar to those of conventional hardening, though the heating and cooling cycles are much faster. Typically the austenitizing time is very short, between 0.01-1.0 s, whereas cooling rates can be as high as 10^7 K/s (compared with cooling rates of about 300 K/s for arc welding) [56].

The laser beam can be shaped into different patterns, obtaining different hardness profiles (Fig. 3.3). The temperature must be raised above the austenitizing temperature at the desired hardened depth, but without melting the surface of the workpiece. Usually the initial microstructure is composed of ferritic-pearlitic grains. During the austenitizing stage the carbon diffuses from the dissolved pearlite colonies homogenizing the carbon distribution if the temperature and time are sufficient. The cooling stage is very fast producing hard martensitic structures. However, homogeneous austenite is formed only on the surface, resulting in homogeneous martensitic structures with retained austenite. In zones situated beneath, the final microstructure is composed of inhomogeneous martensite, retained carbides, untransformed ferrite and retained austenite.

The temperatures of the phase transformation can be estimated with an equilibrium Fe-C diagram (Fig. 3.4), however the high heating rates typical of laser processes, which are in excess of 1000 K/s, shift the austenitizing temperatures above the equilibrium values. The high cooling rates also shift the martensite start temperatures below the equilibrium values.

Prior to the treatment is necessary the cleaning of the surface of the workpiece and if the finish presents high reflectivity, the employ of a coating in order to increase the absorption of the laser energy. Process gas is used and has two functions: shields the interaction zone preventing

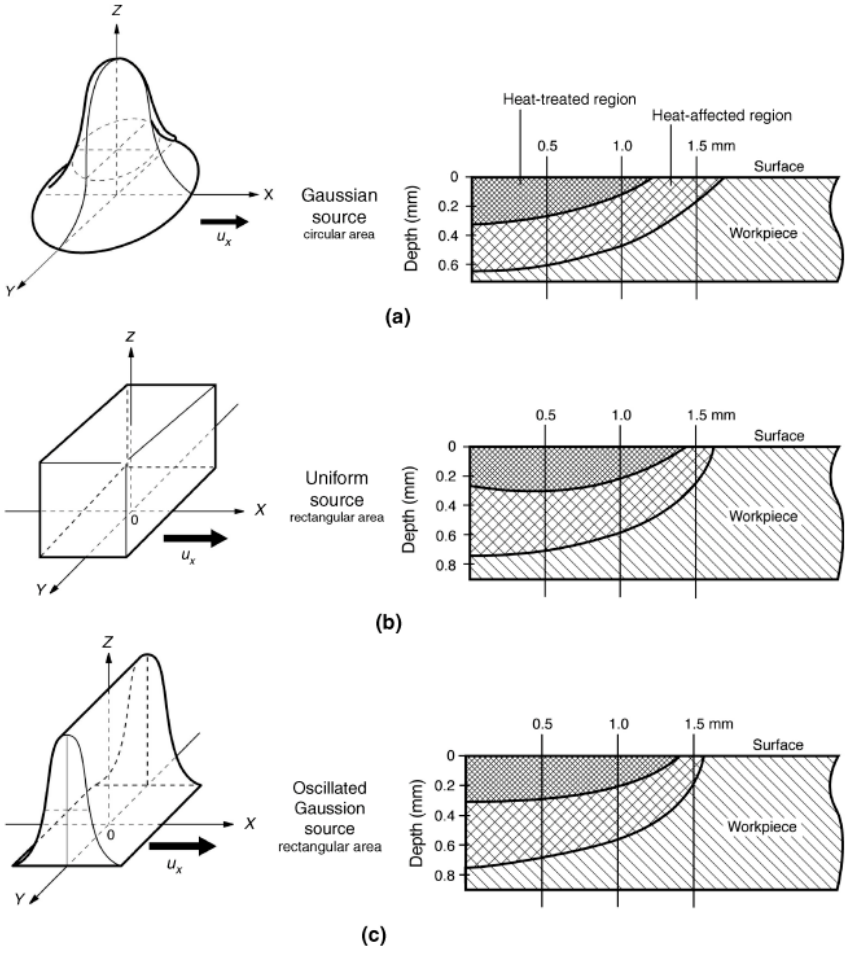

Figure 3.3: Commom beam shapes used in LTH and their corresponding hardened profiles. (a) Gaussian beam. (b) Rectangular beam. (c) Rectangular-Gaussian beam. *(from [6])*

oxidation, which apart from spoiling the finish of the surface, can increase the absorptivity which may result in melting. Also protects the optics from smokes and vapors during the process.

Usually the set of parameters for the treatment is fixed, but with complex geometries a control system for stabilizing the temperature of the surface is required, in order to adaptively vary the parameters to prevent melting. The temperature measured by a pyrometer or simply the signal of a photodiode can be measured and input to a control loop which adjusts the power of the laser beam.

3.1.3 Thermal Models

Several researchers proposed theoretical models with the aim of establishing a relationship between laser processing parameters and temperature, which is the main variable related with the phase transformations and hardness.

Carlslaw and Jaeger [65] used an analytical semi-infinite plate solution for a uniform heat source. Lax [66] pioneered the modelling of temperature distributions induced by laser irradiation in solids. He determined the temperature distribution produced by a stationary Gaussian laser

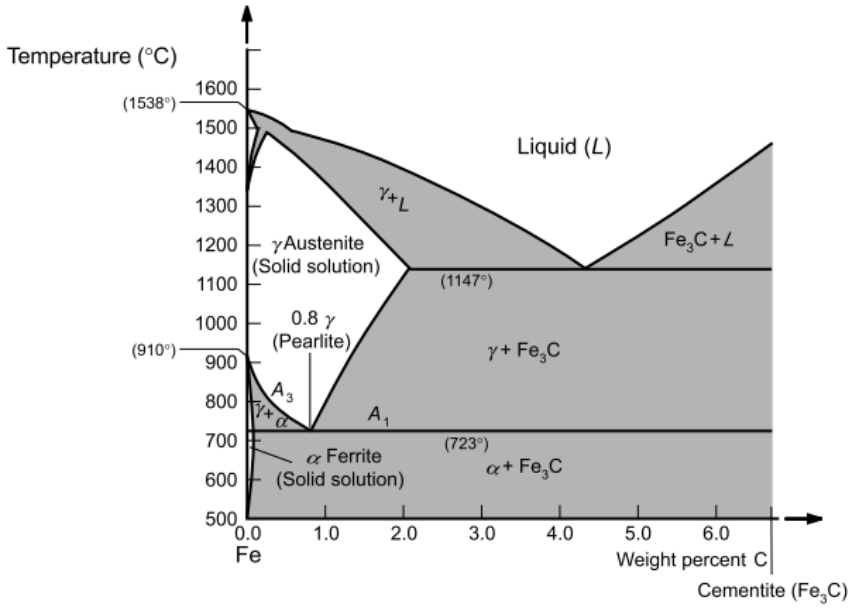

Figure 3.4: Iron-Carbon equilibrium phase diagram

beam, reducing the problem to a 1D steady-state. Based on this work Sandven [67], and later on Gregson [68], developed 1D transient models for the fast prediction of the temperature distribution in the vicinity of a moving laser spot. Chen and Lee [69] investigated transient temperature profiles during laser heating, particularly of semiconductor materials, using a circular laser beam with a Gaussian profile. They showed that when the input power is varied linearly with the scan velocity, the input energy density is maintained constant. Maier et al. [70] proposed a method for calculating temperature profiles based on the integration of a superposition of Green's functions. Later on, Zubair and Chaudhry [71] developed an analytical model for the computation of temperature and heat flux distributions in a semi-infinite solid when subjected to a spatially decaying, time dependent laser source. As in the analytical models only one value of thermal conductivity can be used, the problem of its variation with temperature was addressed by Isenberg and Malking [72] and Kou et al. [73].

For a detailed analysis 2D and 3D heat input models are required. 2D heat flow models with temperature dependent surface absorptivity were developed for cylindrical geometries by Kou et al. [73], Koai et al. [74] and for semi-infinite bodies by Festa et al. [75, 76] using a uniform strip moving heat source, applicable also to electron beam hardening. Cline and Anthony [77] and Sanders [78] developed the first 3D thermal models for semiinfinite plates under Gaussian laser beams. Sanders based on the solutions developed by Lax [66] to create a model for a moving circular disc with a Gaussian distribution. Kou et al. [79] also presented a 3D heat flow model using the finite difference method and compared the predictions with the experiments conducted on AISI 1018 steel with a 15 kW CO2 laser, using a square laser profile at different beam powers and scanning speeds. Wang et al. [80] simulated temperature fields in LTH using the commercial FEM software MSC.Marc, and analyze the effect of the energy density. Sowdari and Majumdar [81] using a 3D enthalpy based FEM model in the commercial FEM software ANSYS studied the temperature distribution of laser irradiated metals during heating and melting processes.

Application of laser heating to special geometries was undertaken by several authors. Komanduri

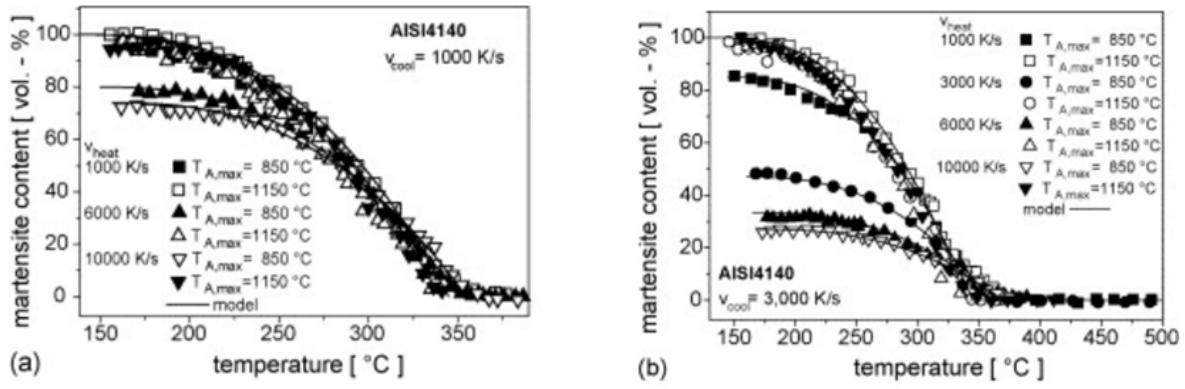

(a) (b)

Figure 3.5: Experimentally determined and calculated volume fraction of martensite for TA_{max}=850 and 1150°C and different heating rates at cooling rate of: (a) 1000 K/s and (b) 3000 K/s *(from [7])*

and Hou [82] developed a general analytical thermal model (transient as well as quasi-steady state) using a disk heat source with a pseudo-Gaussian heat intensity distribution, and applied it for the hardening of gears, taking into account the special geometrical boundary conditions. Yáñez et al. [83] developed a 3D transient thermal model based on the commercial FEM software ANSYS and applied it to a ring of AISI 420 martensitic stainless steel. They pointed out the necessity of decreasing the laser power during the following passes of the helical laser trajectory, in order to maintain the maximum temperature and obtain a homogenous treatment.

Pulsed laser heating was studied by Yilbas [84], who developed an analytical formulation for the unsteady analysis of this problem, showing that the conditions for thermal integration to occur require a minimum pulse rate of 100 KHz.

3.1.4 Phase Transformations and Hardness

Ashby and Easterling [22] and Li et al. [85] developed phase transformation models for steels in normalized condition and examined the effect of several process variables in the hardened depth. They used the thermal analysis to obtain the temperature profiles and apply the kinetic equations describing the microstructural changes. Later on, this model was extended by Shercliff and Ashby [86] using dimensional relationships between various process variables to create processing diagrams in order to determine the case depth for Gaussian and rectangular laser sources. Both models constitute the basis for numerous subsequent investigations from many researchers.

Davis et al. [87], based on the work of Ashby and Easterling, [22] developed a thermal/kinetic model for a rectangular workpiece including metallurgical phase transformations. Although they neglected the effect of the cooling rate on the phase transformations, considering the self-quenching mechanism fast enough to allow a complete conversion to martensite. Chen et al. [88] studied the austenite transformation and developed a mathematical model for laser austenization based on atom diffusion theory and thermal elastoplasticity theory. In their analysis the effects of temperature and heating rates are considered, as well as the formation of austenite by non-diffusion process at high heating rates.

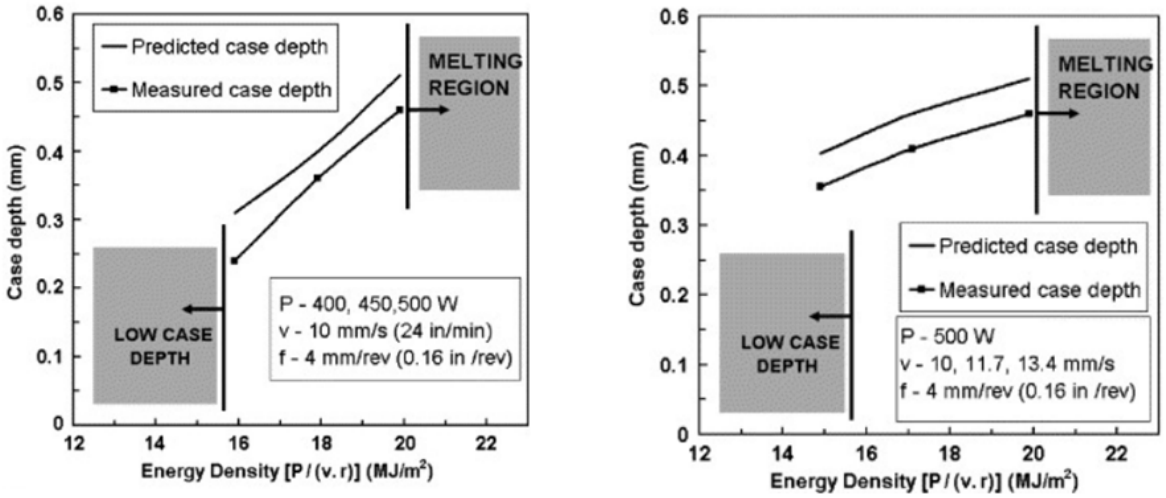

Figure 3.6: Comparison of predicted case depth from thermal-kinetic modelling with experimental measures, with respect to energy density variation under: (a) constant speed; (b) constant power *(from [8])*

Felde et al. [89] and Reti et al. [90] developed a 3D numerical model for the prediction of the hardened profile after rapid austenization and cooling. Haidemenopoulos [91] used a coupled thermodynamic/kinetic model with diffusion transformations to analyze the effect of heating and cooling rates as well as dwell time on the microstructure, performing the thermal calculations using the commercial FEM software ABAQUS. Miokovic et al. [7] also used ABAQUS to model the LTH of an AISI 4140 steel, implementing the phase transformations through user defined material subroutines, including the effect of inhomogeneous austenite formation. They studied the influence of heating and cooling rates on the phase transformations (Fig. 3.5) and hardness. Tobar et al. [92], continuing the work of Yáñez et al. [83], applied their 3D thermal model for the prediction of the temperature profile in LTH of a hot work tool steel AISI H13, and used a metallurgical phase transformation model for the subsequent prediction of hardened areas. Lusquiños et al. [93] also used ANSYS to predict the temperature cycles in laser hardening of a AISI 1045 steel, and estimated the hardened depth based on the peak temperature. Skvarenina and Shin [94] presented a numerical study for laser hardening of AISI 1536 steel with complex geometric features, as well as experimental results. Their model consists of a 3D FEM for the calculation of the temperature field coupled with a 2D kinetic model to predict the resultant hardness and phase distribution, in which the initial microstructure is modelled by digitizing a photomicrograph and assigning a phase to each point of the 2D grid. Patwa and Shin [8] also developed a 3D FEM thermal model based on the model presented by Rozzi et al. [95, 96] for laser assisted machining of cylindrical workpieces, and coupled it with diffusion and martensitic transformations utilizing data from CCT diagrams for hypoeutectoid steels. They applied the model to the LTH of AISI 5150 cylinders and presented their results as processing maps, which show how the case depth and hardness profiles depend on the input parameters (Fig. 3.6). Orazi et al. [97] presented a 3D finite difference model for the prediction of the austenization and subsequent hardening through martensitic transformation, for hypoeutectoid steels during fast heating cycles like in LTH. They model the fast austenization process by calculating the austenite time transformation parameter, using experimental data to calibrate their model.

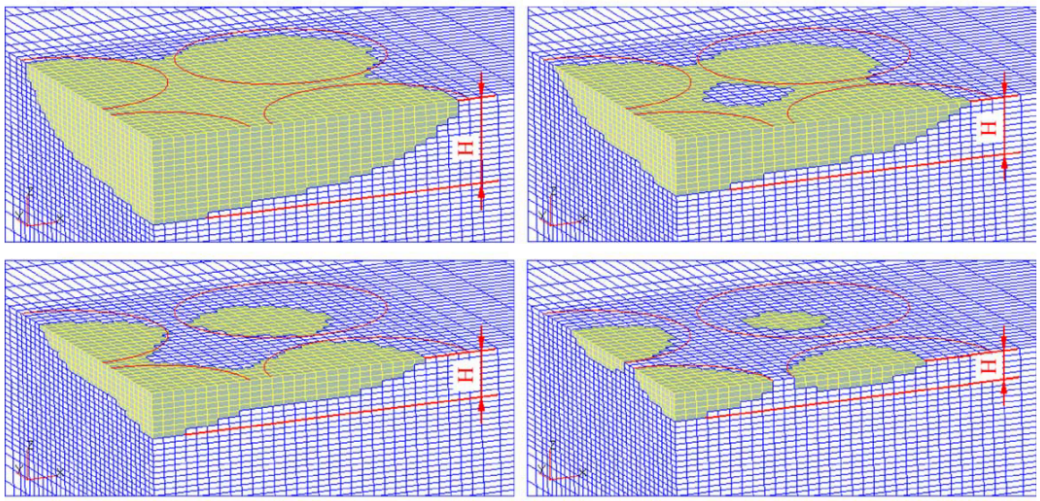

Figure 3.7: Commom shapes of hardened zone after LTH with pulsed beam *(from [9])*

Other effects and possibilities were also explored in laser hardening. The influence of the initial microstructure prior to the LTH was addressed by Shiue and Chen [98], who studied the microstructural evolution of a tempered AISI 430 steel at different temperatures, using a simple mathematical model based on the work of Ashby and Easterling [22]. The effects of using non-uniform beam energy distributions were studied by Galantucci and Tricario [99] in the laser hardening of carbon steels, using a transient numerical model based on the finite element method. Also Leung et al. [100] derived an exact solution for modelling the moving-interface heat transfer of LTH with a beam customized to a flat-top rectangular shape, taking into account the latent heat and using IT and CCT diagrams for phase evolution. Pulsed laser hardening was analyzed by Wu et al. [9] who presented a numerical investigation by means of a 3D FEM model which includes multiphase transformations. They studied the influence of temporal pulse shape on the maximum surface temperatures and connectivity of hardened zone (Fig. 3.7).

Laser surface melt hardening was investigated by Grum and Sturm [101] who developed a thermal analytical model based on the work of Ashby and Easterling [22] and Gregson [68], and applied it to gray and nodular irons, comparing the results with experimental measurements. Roy and Manna [102] study the localized melting around graphite nodules during LTH of austempered ductile iron. They applied the equations given by Ashby and Easterling [22] for the calculation of the temperature profile, and subsequently use a carbon diffusion equation, obtaining a hardness depth linearly proportional to the laser power.

3.1.5 Back-Tempering

Many studies have been carried out to model the LTH process and improve the understanding of the underlying physics. Coupled thermo-kinetic models for the carbon diffusion during austenization and the subsequent simulation of the martensitic transformation, allow the prediction of hardness profiles after the treatment. However the effect of back tempering in multitrack LTH is not included in these models.

Tempering can be considered as a phase transformation promoted by diffusion from an unstable state towards a quasi-equilibrium state. During the process, the carbon in the martensite, which is a supersaturated solid solution of carbon in α-Fe, diffuses precipitating in form of carbides

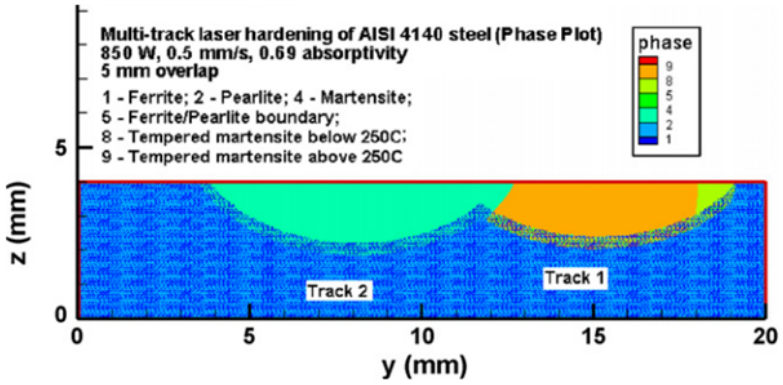

(a)

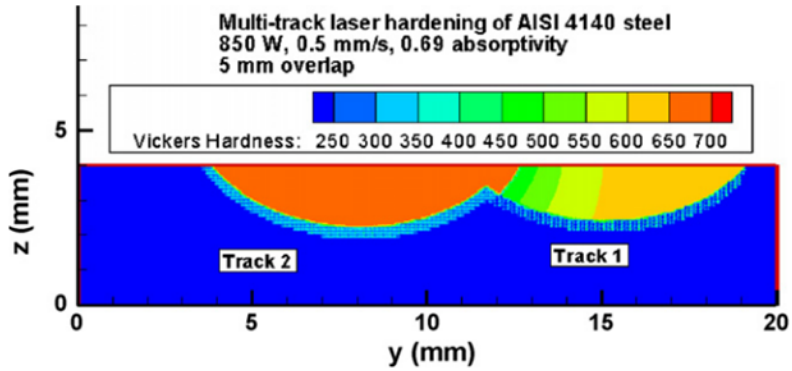

(b)

Figure 3.8: Cross section plots in laser hardened tracks including the effect of back-tempering: (a) phases; (b) hardness *(from [10])*

like the ε-carbide, cementite and alloy carbides, leading to a final microstructure composed of ferrite and fine globular carbides dispersed. Additionally, if retained austenite is present it is also transformed during the process.

Back-tempering is produced by the temperature increase in the previous tracks due to the heat deposited during the last track, causing non-uniform hardness profiles. Lakhar et al. [10] modified a tempering model developed by Zhang et al. [103] which describes tempering as a solid phase transformation governed by the Johnson-Mehl-Avrami diffusion kinetic law. They combined this model with existing models of thermal behaviour and phase change kinetics, developed earlier by its group, to predict phase transformations (Fig. 3.8a) and three-dimensional hardness profiles after multi-track LTH (Fig. 3.8b), validating the model with hardness measurements (Fig. 3.9).

G. Tani et al. [104] instead of modelling the microstructural evolution after quenching considered the softening effect of back-tempering on the hardness of the previous clad tracks by means of empirical equations for the softening of bainite and martensite in carbon steels, obtained from [105]. They also applied this model to the LTH of a cylindrical hollow part [106] with helical trajectories. This time the steel treated was an AISI 420 martensitic stainless steel, which is relatively insensitive to tempering unlike plain carbon steels, obtaining an even hardness profile.

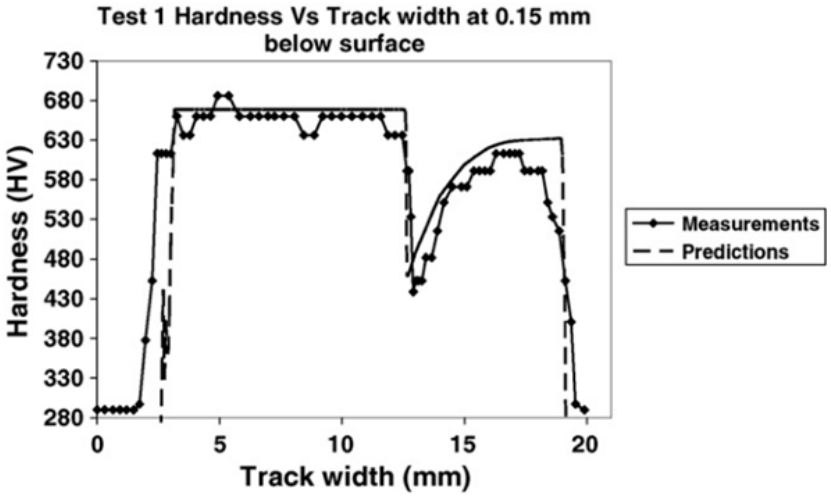

Figure 3.9: Predicted and measured hardness profile along the width of the sample for a two pass LTH process including the effect of back-tempering *(from [10])*

3.1.6 Mechanical Models

Thermal stresses are caused by the uneven thermal distribution on the workpiece. Phase transformations have an important effect on the stresses developed, so the stress field can be completely different between materials that present phase transformations and materials without them. The austenization process reduces the specific volume, therefore lowering the compression stresses arising during the heating, whereas the martensitic transformation increases the specific volume, creating compression stresses that counteract the tensile stresses developed during the cooling stage.

Li and Easterling [11] developed a simple analytical model for the calculation of the residual stresses. They analysed the magnitude of the stresses as a function of the carbon content of the steel and the laser input energy applied (Fig. 3.10). Bokota and Iskierta [107, 108] proposed a mathematical model for the thermal field calculation and phase transformations based on the diffusion-convection equation solved by a suitable superposition of Green's functions, originally proposed by Maier et al. [70]. The phase transformations were described using TTT diagrams. The stresses were calculated by means of a numerical model which includes isotropic hardening for the plastic flow. However the model allows the calculation of the longitudinal stresses only, which limits its use to slender elements. Grevey et al. [109] proposed a simple analytical method for the estimation of the residual stresses on low alloy and medium alloy steels. The authors based on the known expected residual stress profile and divided the depth in three zones. Zones I and II have compressive stresses and zone III have tensile stresses, proposing equations for the calculation of the transition between zones.

Yang and Na [110, 111] presented a 2D FEM model for the calculation of residual stresses after LTH of a medium-carbon steel, including the effect of the martensitic transformation on the stresses and several beam profiles. Fattorini et al. [112] developed a thermomechanical axis-symmetric FEM model for the LTH of flat faces of cylindrical samples. The samples were characterized by X-Ray diffraction measurements as well as microstructure and hardness. The results show an excellent correlation for some samples.

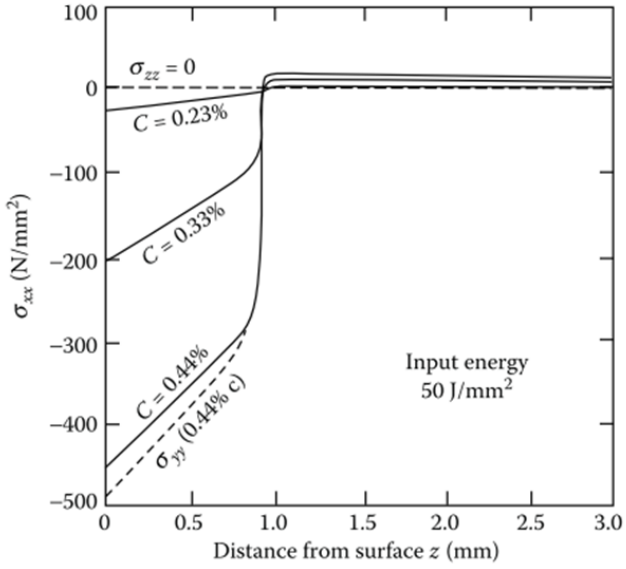

(a)

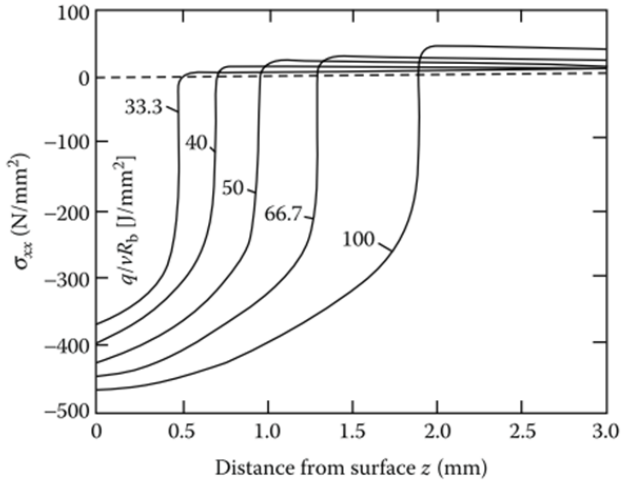

(b)

Figure 3.10: Predicted longitudinal residual stresses (in the laser moving direction) below surface as a function of depth below surface for: (a) different carbon contents; (b) different laser input energy for a 0.44% C steel *(from [11])*

Denis et al. [113] analyzed the residual stresses in the LTH of hypoeutectoid carbon steel plates with 0.42% carbon, by means of the commercial FEM software SYSWELD. They used the software's metallurgical model and analyzed the effect of different laser velocities, showing deeper residual stresses in the simulations with lower velocities as a result of the lower penetration of the treatment (Fig. 3.11a). However the magnitude of the stresses seemed to have a small variation with process parameters. They explained this phenomenon as a consequence of the limited cooling rate due to the heat conduction mechanism to the inside of the workpiece. In order to increase the residual stresses, higher cooling rates are required. They simulate traditional LTH plus a subsequent quenching media assuming a high heat transfer coefficient in the surface of the workpiece, obtaining residual stresses in the surface that nearly double the previous ones.

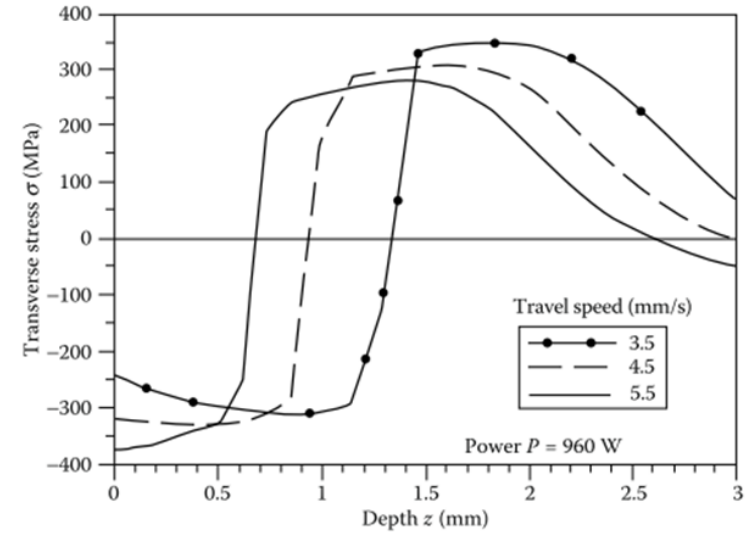

(a)

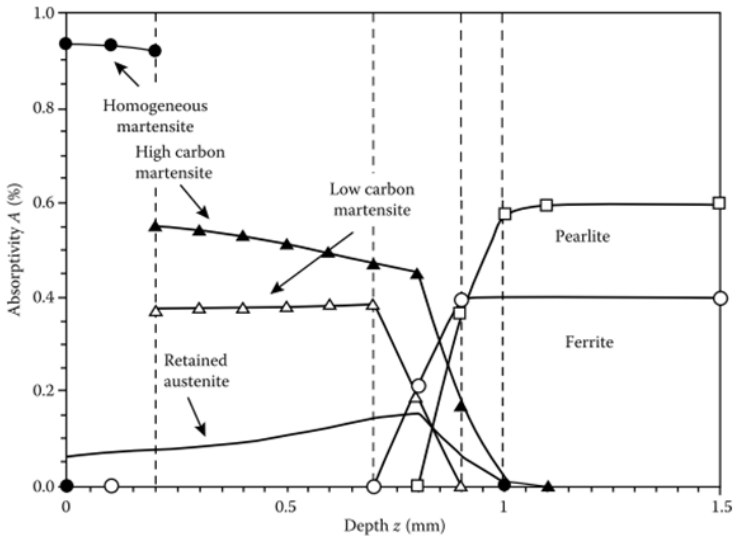

(b)

Figure 3.11: Predicted longitudinal residual stresses (in the laser moving direction) below surface as a function of depth below surface for: (a) different carbon contents; (b) different laser input energy for a 0.44% C steel *(from [11])*

Zhan et al. [114] also used SYSWELD for analyze the temperature fields, phase transformations, hardness and residual stress distributions in the melt-hardening of a roller. The stresses calculated in the melted zone are compressive showing its maximum value at the boundary of the melted zone, whereas the stresses in the HAZ are tensile, causing initiation of cracking in this zone in some experimental tests. Bailey et al. [12] developed a 3D transient thermal/kinetic finite volume model for the calculation of temperatures and phase transformations in the LTH of a AISI 4140 steel block. The thermal and phase histories were introduced in the FEM software ABAQUS for the calculation of the stress field. They implemented several user subroutines for including volumetric dilatation effects due to phase transformations and TRIP. They compared the effect of including phase transformations, showing that the stresses change from compressive

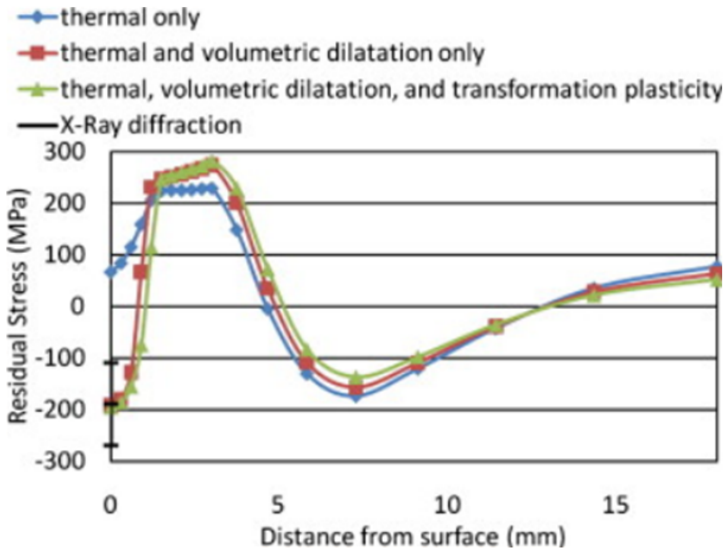

Figure 3.12: Predicted and measured hardness profile along the width of the sample for a two pass LTH process including the effect of back-tempering *(from [12])*

to tensile in the hardened zone if they are not considered, although the stress profile in the rest of the depth is the same. They also found that including TRIP has a minor effect on the stresses (Fig. 3.12).

3.2 Laser Welding

Laser welding is a high energy density welding process, capable of deep penetration and small heat affected zones. As a result, it has been increasingly used in several industrial sectors such as marine, automotive, aerospace... for the welding of special components, materials and geometries, with the aim of reducing distortions, increase quality or produce lightweight structures [115].

A great number of process parameters, along with the material properties of the alloy been welded, influence the characteristics and quality of the seams obtained. Numerous investigations were carried out aiming for improve the understanding of the underlying physics of the process and try to simulate the effect of some input parameters on the weld pool as well as the residual stresses and distortions arising.

In recent years hybrid laser/arc welding has received significant attention due to its attractive advantages such as large penetration depth, high welding speed, less deformation than conventional welding processes and good bridging ability for relatively large gaps [116]. Therefore numerical models have been developed to study laser welding process, taking into account some of the main considerations in laser keyhole welding (Fig. 3.13).

3.2.1 Numerical Modelling of Welding

During the last 30 years extensive modelling efforts have been undertaken to simulate conventional welding processes. The number of papers and publications related to welding could

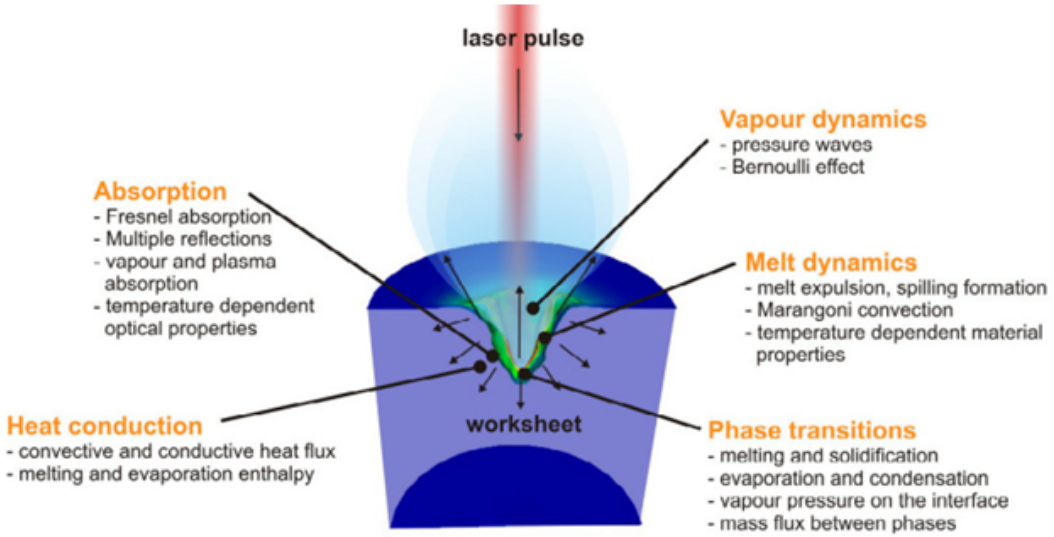

Figure 3.13: Overview of the main considerations in laser keyhole welding *(from [13])*

be estimated in excess of a thousand. Only some important features developed for conventional welding, and applicable to laser welding and even laser cladding, will be briefly discussed in this chapter. The rest of the review is focused exclusively on laser welding models.

Analytical equations based on the Rosenthal's solution [117, 48] may give sufficiently accurate calculations far from the welding point, but numerical simulations are needed for an accurate description of the process. The temperature field can be calculated prescribing a certain temperature at the boundary of the weld pool, and then removing this load and computing the resulting temperature field, as done by Goldak et al. [118]. Jones et al. [119, 120] defined the temperature of the weld pool as the liquidus temperature of the alloy. Roelens et al. [121, 122] and Lindgren et al. [123] prescribed the temperature in case of multipass welds. Other approach is the calculation of the temperature field using a heat flux as surface or volumetric thermal load. Goldak et al. [124] proposed the so-called double ellipsoid heat source, which is a more accurate representation of the heat flux. The double ellipsoid is used in many papers.

Adaptive meshing techniques concentrate the elements in regions with large gradients, obtaining increased computational efficiency without sacrificing accuracy. Lindgren et al. [125] developed an automatic 3D remeshing algorithm using a graded hexahedral element. They based on the work of McDill and co-workers for the basic hexahedral graded elements [126], the adaptive remeshing technique [127, 128], and the data transfer between meshes [129], and applied it to the study of welding large copper canisters by electron beam reducing the CPU-time 60% compared with a model of the same accuracy without remeshing. Runnemalm and Hyun [130] based upon the same work and included an error estimator that evaluates both the thermal and mechanical fields, to control the mesh refinement/coarsening. Andersen [131] used a similar dynamic remeshing procedure and combined it with substructuring in order to reduce the computational requirements. He modelled a ship subassembly in ANSYS using linear, elastic shell elements for creating a global model, and employing several elastoplastic local models with 3D elements and nonlinear material properties for computing each weld pass separately. Then the results of the local models are mapped to the global model, which carries all the information. He also used "birth & death" procedures to simulate the deposition of weld material.

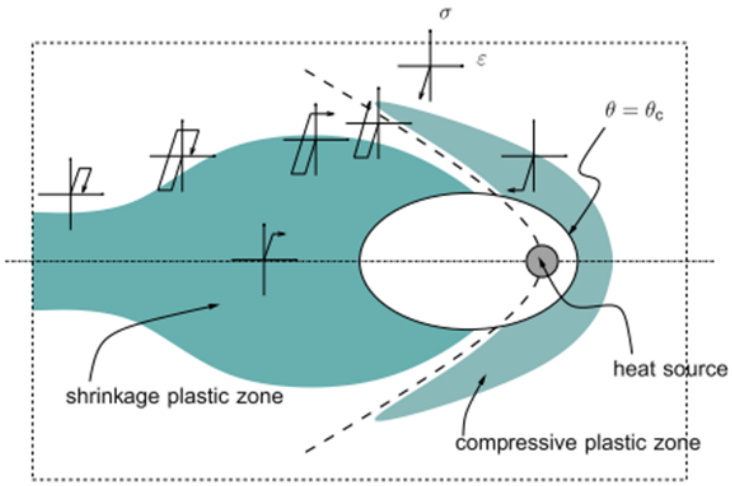

Figure 3.14: Plastic zones during welding. The dashed lines correspond to the line of maximum temperatures *(from [14])*

The modelling of the plastic behaviour of the materials is fundamental due to the high temperatures of the process which create significant plastic strains. The choice of a certain material model influences the final residual stresses. Due to the relatively short time the material spends at high temperatures, rate dependent plasticity is usually neglected [132]. The material suffers stress reversal between the heating and cooling stages (Fig. 3.14), thus the choice of isotropic or kinematic hardening could have some effect on the final stress state. However Devaux et al. [133] studied weld repairs with up to 6 beads and found only small differences. Most of the models use isotropic hardening, some kinematic hardening and a few used combined isotropic-kinematic hardening. However the most important problem is the lack of material property data at high temperatures.

3.2.2 Thermal Models

During 30 years mathematical and numerical CFD models of growing complexity were developed for the detailed study of keyhole dynamics in deep penetration welding. Steady state models were first considered due to computer limitations, although their satisfactory results in predicting temperatures and keyhole shapes make them still useful today. However 3D transient models allow a detailed simulation of the complete process and dynamic effects such as humping, pore formation and also the keyhole formation.

Mazumder and Steen [134] developed the first numerical model for laser welding. They used finite difference techniques to create a 3D steady state model, with a surface heat source, but considering zero reflectivity in the points of the keyhole. Surface heat sources are not well suited for the simulation of deep penetration welding, therefore Goldak et al. [124] introduced the double ellipsoid volumetric heat source, which has the flexibility to be used in shallow or deep welding processes. Yilbas and Sahin [135] and Yilbas [136] developed steady state mathematical models which include phase change, convection and mass removal processes, introducing a numerical approach for solving the energy, momentum and continuity equations, to calculate temperature distributions. Matsunawa and Semak [137] applied the mathematical model developed by Anisimov and Khokhlov [138], which includes the effect of evaporation and recoil pressure, and

studied the keyhole wall dynamics during laser welding, assuming that only the frontal keyhole wall is exposed to the laser beam. Later on Semak et al. [139] improved the model for a transient simulation of the process. They emphasized the importance of recoil-pressure-induced melt ejection in weld pool energy balance, and calculated the keyhole wall velocity for various processing parameters obtaining variations with them. When the keyhole velocity is greater than the beam translation velocity, their model predicted that the frontal keyhole wall has a steplike profile, leading to the formation of humps. Solana and Ocaña [140] presented a 3D finite difference model to determine the weld pool geometry, including ablation losses and evaporation effects in the energy and pressure balances but neglecting fluid flow. Their model predicts the temperature field, electronic density, degree of ionization and absorption coefficient within the plasma, as well as maximum penetration depth. Sudnik et al. [141, 142] presented models with similar capabilities, including a semiempirical approach to model fluid flow in a simplified way. Models which include a keyhole with parallel walls in the geometry were presented by Brüggemann et al. [143], who used a 2D model but without including some factors as Marangoni and natural convection, and Mahrle and Schmidt [144] who used a 3D model to investigate the influence of different fluid dynamic conditions in the weld pool shape and temperature distribution in deep penetration welding.

Thermocapillary flow or Marangoni convection has a fundamental role in the melted fluid flow and heat transport, therefore it is included in all the following CFD models. Ye and Chen [145] developed 2D and 3D steady state models based on finite volumes, and studied the effect of welding velocity, Marangoni convection and natural convection, pointing out the unsatisfactory results obtained with 2D models. Du et al. [146] presented a 3D model based on finite differences to study the full penetration laser welding for titanium alloys. They discussed the effect of Marangoni convection in the molten metal fluid flow, and the typical hourglass shape of the weld pool. Wang et al. [147] developed a 3D steady state model using the control volume method with a rotary Gaussian volumetric heat source plus a double ellipsoid heat source. Abderrazak et al. [148] presented a 3D transient finite volume model for FLUENT. They use a double ellipsoid heat source to study the effect of several parameters on the weld pool formation in keyhole laser welding of AZ91 magnesium alloy sheets. Tobar et al. [149] developed a 3D steady state model, to study conduction welding of aluminium alloys using CFX. They determined that the flow is primarily driven by Marangoni convection instead of buoyancy.

Raytracing procedures involving multiple reflections in the keyhole walls were included in some models to simulate accurately the evolving power distribution inside the piece. Fabbro and Chouf [150] studied the keyhole geometry as a function of the main process parameters such as welding speed, laser power or sample material. They showed that the combination of drilling velocity and beam speed causes the inclination of the front keyhole wall. In their work they used a raytracing procedure taking into account multiple reflections inside the keyhole and determined the dynamics and keyhole geometry, showing that only some combination of parameters can make the rear keyhole wall stationary. Ki et al. [151, 152] presented a 3D transient model with fluid flow and heat transfer including multiple reflections in the keyhole. They simulated the complete keyhole evolution for several cases, showing the effect of including evaporation, a self-evolving L/V interface and multiple reflections. They concluded that the evaporation recoil pressure is the main factor that differences conduction from keyhole welding. Otto, Schmidt and coworkers [13] developed a 3D transient model with the free software OpenFOAM (Fig. 3.15), capable of simulating different laser material processing techniques: deep penetration welding, drilling or cutting. Their model is state of the art, and is based on finite volumes, using the volume of fluid method to deal with free surfaces (Fig. 3.16) and adaptive remeshing strategies

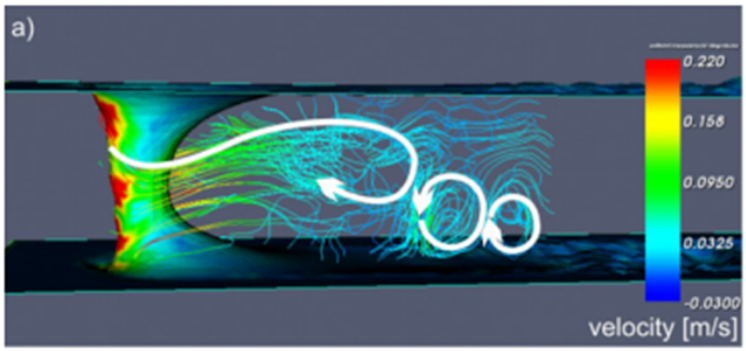

(a)

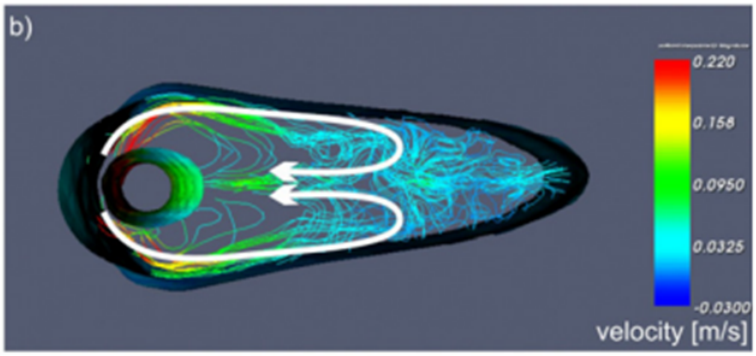

(b)

Figure 3.15: Fluid dynamics of the melt pool during laser beam deep penetration welding of stainless steel: (a) vertical view; (b) horizontal view. Laser power: 3 kW; wavelength: 10.6 μm; beam radius: 200 μm; profile: Gaussian; feed rate: 6 m/min *(from [13])*

to reduce computation time. Latent heats, vaporization, recoil pressure and droplet ejection are included in the model. They calculated the beam propagation with COMSOL Multiphysics as a stationary diffusion problem until the first reflection, and then coupled it with raytracing procedures. Koch et al. [153] also studied the effect of wavelength dependent Fresnel absorption with this model, simulating CO2 and Yb:YAG lasers.

Other researches in laser welding carried out with CFD models focus on different topics apart from keyhole welding. Loredo et al. [154] developed a 3D finite volume model for the optimization of the lap pulsed laser welding of zinc-coated sheets, due to the zinc low boiling point (1180 K), which is lower than the steel melting point (1800 K) and produces a violent boiling during the process. They optimized the parameters for ablate the zinc in one spot and generate the keyhole in the next. Medale et al. [155] developed a model for studying a single laser pulse in laser spot welding. They considered fluid flow, thermo-capillary, evaporation-recoil pressure and multiple reflections in the keyhole by raytracing. Gatzen and Tang [156] presented a 3D steady state model to study laser welding of aluminium under the influence of a coaxial magnetic field, using CFX. They created the geometry with a predefined keyhole shape, and obtained significant effects due to the magnetic field in the upper part of the melt pool. Chakraborty [157] developed a 3D model for laser welding in conduction mode of two dissimilar metals: copper and nickel. Their model included a turbulent k-ε model, which showed a better correlation with experimental tests than a laminar model.

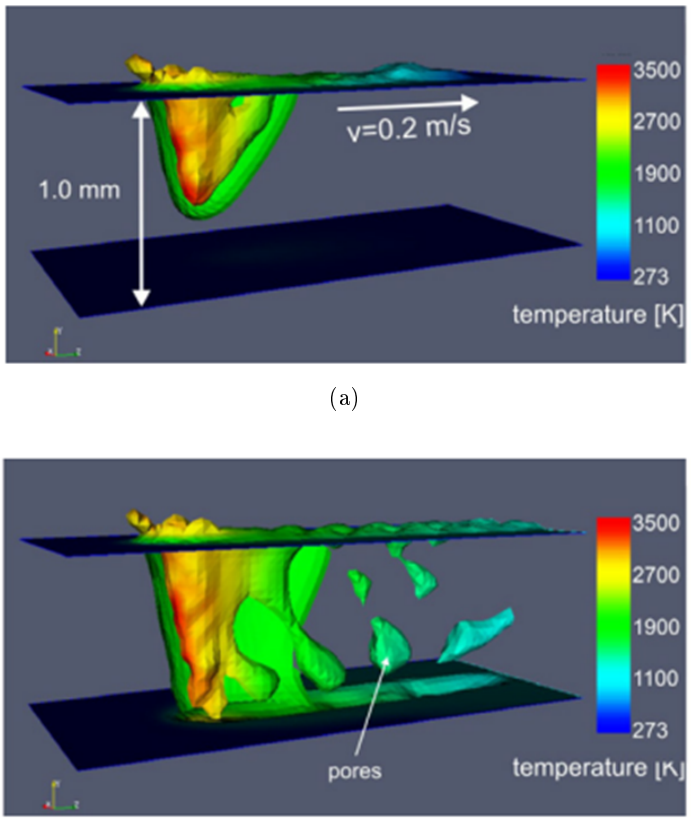

(a)

(b)

Figure 3.16: Pore formation during laser beam deep penetration welding of stainless steel at high feed rates. Laser power: 6 kW; wavelength: 10.6 μm; beam radius: 200 μm; profile: Gaussian; feed rate: 12 m/min *(from [13])*

FEM models have also been used for the simulation of temperature fields and weld profiles, having the advantage of being easily coupled with subsequent mechanical analyses. These models require the use of volumetric heat sources based on some assumptions directed to imitate the heat distribution produced due to fluid flow. Calibration of the heat source with experimental tests is required. GuoMing et al. [158] estimated the transient temperature distribution in keyhole welding using a very simple model with a volumetric heat source in ANSYS. Balasubramanian et al. [159] developed a 3D transient model for studying stainless steel welding, using SYSWELD. They used a conical Gaussian volumetric heat source and calculated temperature profiles and weld pool dimensions. Belhadj et al. [160] developed a 3D transient model for the laser welding of AM60 magnesium alloy plates, using the CAST3M code. They used a volumetric heat source and also a surface heat source to model the heating produced by the plasma. Shanmugam et al. [161] presented a 3D transient model to study T-joint laser welds of stainless steel, using SYSWELD. They used a combination of the double-ellipsoidal heat source and a conical Gaussian heat source. Salonitis et al. [162] study the welding of sandwich materials using a 3D model in ANSYS. They used a semiempirical volumetric heat source and simulate one side and two side weldings, calculating the degree of bonding and the damage to the sensitive core material. Wu et al. [163] analyzed the High Power Direct Diode Laser (HPDDL) welding of metal sheets with a 3D transient model, which beam profile is a rectangular strip with a Gaussian intensity distribution, tilted a certain angle over the laser travel direction. Sabbaghzadeh et al. [164] based on the finite difference model developed by Solana and Ocaña [140] and used their results

to perform simulations of pulsed welding in ANSYS. Bag et al. [165] developed an axisymmetric FEM model for laser spot welding, neglecting fluid flow and using an adaptive volumetric heat source, which is defined adaptively as the size of the weld pool grows.

3.2.3 Mechanical Models

The mechanical models are based on the finite element method, most of them use commercial codes as platforms for their simulations. Plasticity is included in all the models using kinematic or isotropic hardening laws in most of cases. Carmignani et al. [166] used ABAQUS to model deep penetration welding of thick steel plates. They employed a volumetric heat source and included an elastoviscoplastic material model into a user routine. Moraitis and Labeas [167] developed a 3D FEM transient model in ANSYS. They first predicted the keyhole shape by considering a Gaussian surface heat source but deactivating the vaporized elements and applying the laser power to the surface of the elements below, forming the keyhole. They used this information to apply a conical volumetric heat source in the thermomechanical analysis of the lap-joint of 6061-T6 aluminium plates, using a kinematic strain hardening law. 3D Models for the laser welding of aluminium alloys, using ABAQUS and a conical Gaussian heat source, were developed by Spina et al. [168] and Zain-ul-abdein et al. [169], assuming an isotropic hardening behavior. For the laser welding of the titanium alloy Ti6Al4V Chuan et al. [170] presented a 3D model using a uniform conical heat source, and discussed the effect of the mesh size and boundary conditions. Montalvo-Urquizo et al. [14] developed a 3D transient model based on the Adaptive-FEM toolbox ALBERTA. They used different error estimators for the thermal and mechanical uncoupled problems, to control mesh adaption and maintain low computation times. The thermal model is based on the energy balance, assuming the keyhole shape and taking the temperature inside the keyhole as the evaporation temperature of the material. Deng and Kiyoshima [171] studied the effect of residual stresses present in stainless steel pipes prior to the laser welding process. They used an empirical based volumetric heat source and assumed isotropic hardening law. They found a significant contribution of the initial residual stresses to the final stress state, however they pointed out that this cannot be directly extrapolated to other welding geometries apart from pipes.

The effect of phase transformations is included in some studies but is neglected in the rest or simply not necessary due to the use of materials that do not present phase changes during the process. Grignon et al. [172] studied the laser welding process of steels using SYSWELD, calculating temperatures, phase proportions, strains and stresses and compared them with some experimental investigations. Tsirkas et al. [173] developed a 3D model for SYSWELD to simulate the keyhole welding of butt-joint thick steel plates using different welding parameters. They modeled the heat flux distribution as a volumetric conical heat source, and include the effect of phase transformations.

Hybrid welding is treated in some papers. Capriccioli and Frosi [174] developed 3D models for TIG and laser welding in ANSYS, using birth and death techniques and a kinematic hardening model. Zhang et al. [175] developed a 3D transient model for the laser plus GMAW-P hybrid welding process, using an adaptive volumetric heat source that combines two sources: the double ellipsoidal heat source for the GMAW-P process and a cylindrical heat source for the laser. They used isotropic strain hardening and compared the hybrid technique with the GMAW-P only, obtaining lower stresses and distortions. Kong and Kovacevic [15] developed a 3D transient model for studying the hybrid laser/arc welding of lap joints in ANSYS (Fig. 3.17). They used a semiempirical volumetric heat source, isotropic hardening law, and also found lower residual

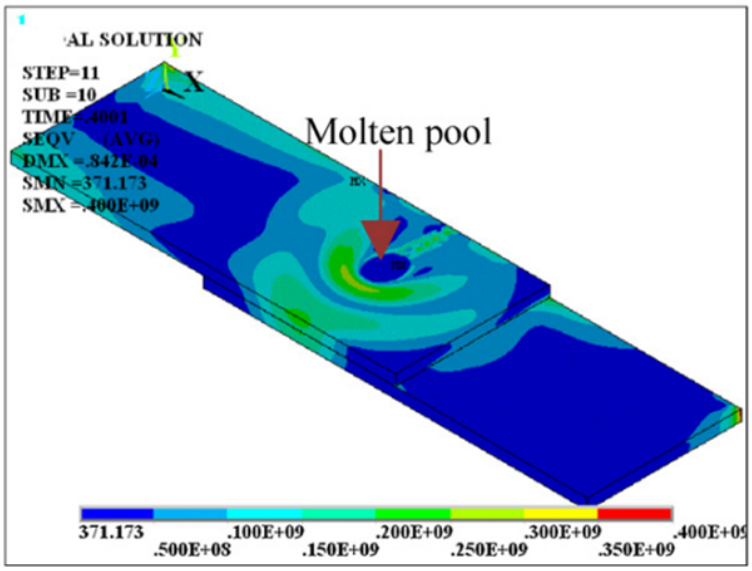

Figure 3.17: Von Mises equivalent stress during hybrid laser-GTAW welding *(from [15])*

stresses with the hybrid method than with the GTAW or laser alone.

Several mechanical models explore laser spot welding. Kang et al. [176] and Chang and Na [177] studied the weldment distortion in laser spot welding of an electronic component using ABAQUS, in order to minimize the residual distortions after the process. Kemal Apalak et al. [178] developed a model to study stresses in adhesively bonded laser-spot welded single lap joints of several metals. They calculated the non-uniform temperature distributions in both metals and obtain the maximum stresses along the sheet interfaces. Martinson et al. [179] developed 3D transient models for laser spot welding of steel sheets, using ABAQUS. They tried different strategies for the welds: ring welds, C-welds and Brezel. Their model includes a conical Gaussian heat source, an isotropic hardening model but they ignored the phase transformations during the process.

3.3 Laser Cladding

3.3.1 Introduction to Laser Cladding

Laser cladding is a versatile technique which consists in the overlay of one metal alloy with another, creating a sound metallurgical bond between them in order to assure good adherence and mechanical properties, achieving low values of porosity and dilution which degrade the special properties of the covering alloy [55]. Both the adherence of the coating and the tribological behaviour are superior to the ones obtained by other techniques such as Atmospheric Plasma Spraying (APS) or High Velocity Oxy-Fuel (HVOF) [180]. In addition, there is a low thermal load transferred to the substrate, generating a smaller heat affected zone and lower distortions in the piece. Laser cladding has a great potential and a growing industrial interest. It is increasingly used for the deposition of protective coatings and the refurbishment of worn off tools and valuable components [181], especially in the aerospace, energy and automotive industries. Turbine blades, engine casings, dies, molds, axles, valve seats... are examples of components repaired or coated

by this technique. New applications of laser cladding are the rapid tooling and rapid prototyping techniques [182] for the fabrication of pore free complex components and tools with excellent mechanical properties.

Several methods for laser cladding have been developed [181]. However, the blown powder method by a coaxial laser cladding nozzle has demonstrated superior flexibility and quality over the rest of the methods, and therefore most of the studies and applications are focused on this method.

The stresses generated during the process are one of the fundamental concerns in this technique. They arise due to the high thermal gradients involved in the process, and the mismatch in material properties between the overlay alloy and substrate, leading to unacceptable distortions in the workpiece or even the appearance of cracks and delamination.

Because of the complexity of the process and the large number of parameters involved, numerical models have been developed to study the thermal and mechanical fields, some of them coupled with metallurgical phase transformation models. Other studies were focused on the blown powder distribution and heating after exiting the nozzle, or the prediction of the clad bead shape.

3.3.2 Thermal Models

The first model of laser cladding is the pioneering work of Weerasinghe and Steen [183] in the early 1980's. They calculated the laser induced temperature field by means of 3D finite difference methods and estimated the required process parameter values using empirical relations, considering also the laser beam attenuation caused by its interaction with the metal powder. Kar and Mazumder [184, 185] and Agrawal et al. [186] solved the one-dimensional heat and mass transfer equations for binary systems in order to calculate the solid solution that is formed by fast cooling process in laser cladding. They also carried out parametric studies correlating several process variables.

2D models were developed to the study of energy and momentum transfer in the melt pool. Hoadley and Rappaz [187] presented a 2D FEM model for laser cladding with powder injection which simulates the quasi-steady temperature field for the longitudinal section of the clad track, taking into account the melting of the powder in the liquid pool, which was considered to be a circumferential arc. Pirch et al. [188] used a 2D non-stationary model for a longitudinal section and studied the melt dynamics and surface deformation, reporting that above a critical velocity intermixing in the melt pool is suppressed. Picasso and Hoadley [189] developed a 2D model for both laser remelting and laser cladding, which considers the fluid motion in the melt pool by thermocapillary forces and the deformation of the liquid-gas interface. Picasso [190] also developed an efficient 2D FEM algorithm with adaptative remeshing using a Delaunay mesh generator, for a stationary Stefan-like problem. Picasso et al. [191] presented 3D analytical solutions of the heat flow equations in order to study the effects of laser beam velocity and powder feed rate. The shadowing effect and the dependence of the absorption coefficient on the angle of incidence were considered. Han et al. [192] and Choi et al. [193] developed models which include the evolution of the free surface, powder injection, powder heating, laser power attenuation and Marangoni flow as well as laser-substrate, laser-powder and powder-substrate interactions, considering melting, solidification and evaporation. They studied the dynamic behaviour of the melt pool and the effect of the momentum transfer by the powder injection in the melt pool shape. Kumar and Roy [194] developed a 3D CFD heat transfer model, incorporating Marangoni

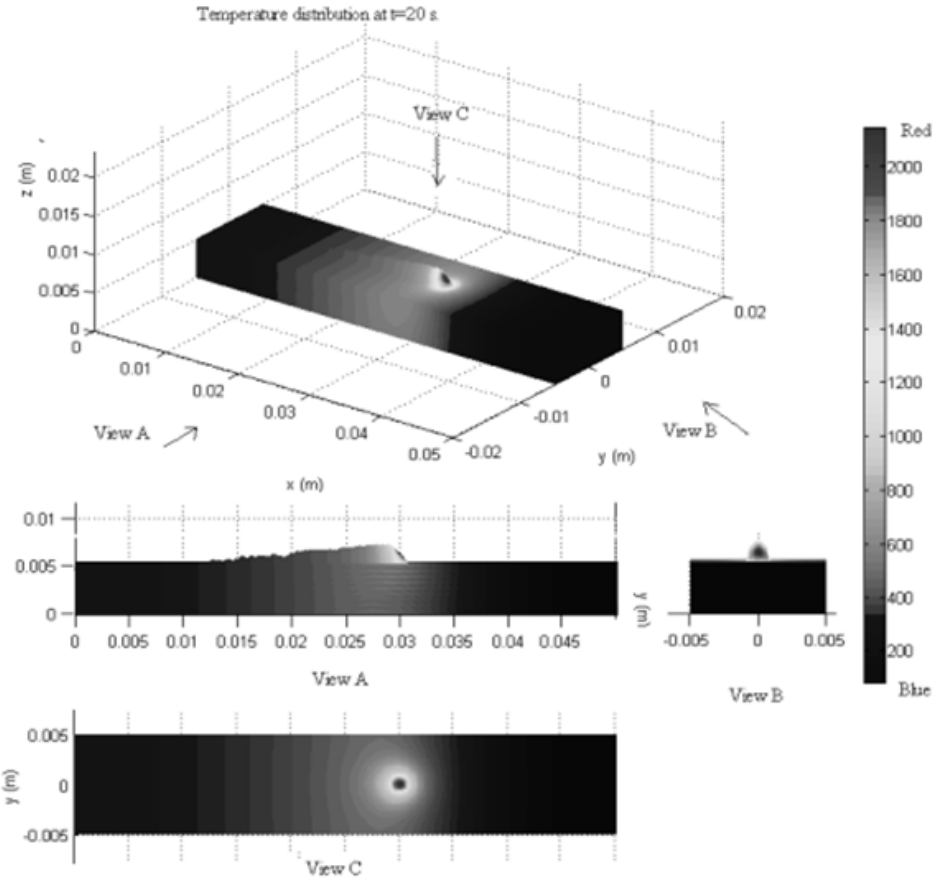

Figure 3.18: Temperature distribution (in Kelvin) at t=20 s for a multistep laser pulse energy *(from [16])*

convection, addition of powder particles and phase changes. They used it to study the influence of several input parameters as well as the Marangoni number, on the laser cladding process.

2D and 3D FEM models were chosen by many researches to calculate the steady state and transient temperature distributions, and study the influence of several parameters. Some of them upgraded their models to calculate the stresses or phase transformations based on the precalculated temperature distributions. Kim and Peng [195, 196] developed a 2D FEM model with adaptative meshing to study laser cladding with wire feeding, for a transversal section near the end of the melt pool. They investigated the effect of laser power and scanning speed on melt pool shape and dilution. Zhao et al. [197] developed a 3D FEM model in ABAQUS, with adaptive meshing, in order to study the dilution control. Cho et al. [198] studied the influence of including the latent heat in the simulations running several 2D models in ABAQUS, finding significant its contribution. Kumar and Roy [199] created a 2D steady state model based on the finite volume method to study the effect of powder preheating and flow rate in the dilution and clad height. Lei et al. [200] simulated laser cladding with preplaced powder and a Gaussian laser heat source using a simple model in ANSYS. Wang et al. [201] also created a simple model in ANSYS for the calculation of the temperatures during the process for several cladding alloys. They correlated the temperatures to the crack formation, detected by acoustic emission, and study whether they are hot or cold cracks. Hofman et al. [202] developed a FEM based model using the commercial

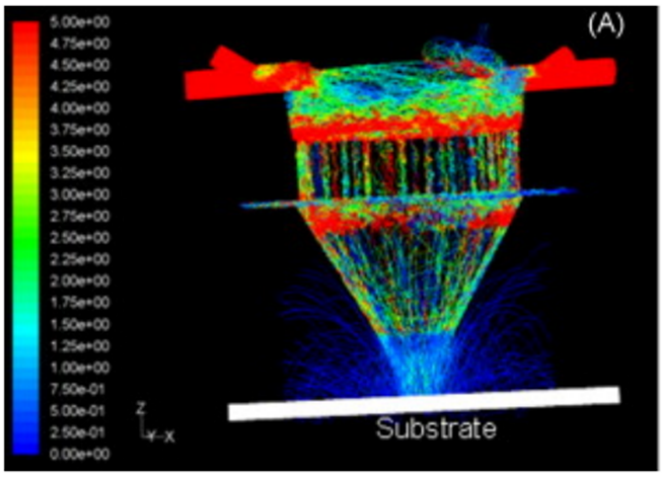

(a)

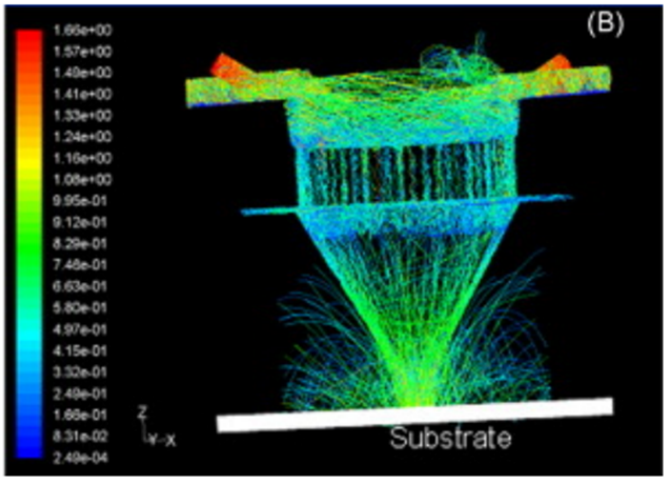

(b)

Figure 3.19: Coaxial laser cladding: (a) particle concentration; (b) particle velocity *(from [17])*

software COMSOL Multiphysics to determine the melt pool, clad geometry and dilution. Their model involves a mathematical transformation of the balance equations describing the physical effects in order to use a simplified geometrical domain with a fixed shape. They also correlate several parameters to dilution. Jendrzejewski et al. [203] studied the temperature distribution in laser cladding of multi-layers of Stellite, by means of a 2D FEM model. Toyserkani et al. [16] developed an interesting 3D FEM model for the study of pulse shaping in the laser cladding process. Their model builds up the clad bead activating elements without a predefined clad geometry (Fig. 3.18). The laser first creates a melt pool, then a fine layer of elements is added above the melt pool. The process is repeated in a series of small time steps until the clad is finished. Their model made good predictions of the clad shape in several conditions.

Interaction between the laser beam and the flying powder particles was studied by Li et al. [204], and later on by Lin [205, 206], Lin and Hwang [207, 208], and Liu and Lin [209] who considered the heat exchange between particles and the carrier gas, influence of the nozzle geometry and the evaporation of strongly heated particles. Also the powder distribution of coaxial nozzles has received some attention. Tabernero et al. [17] modelled the powder flux distribution of a coaxial

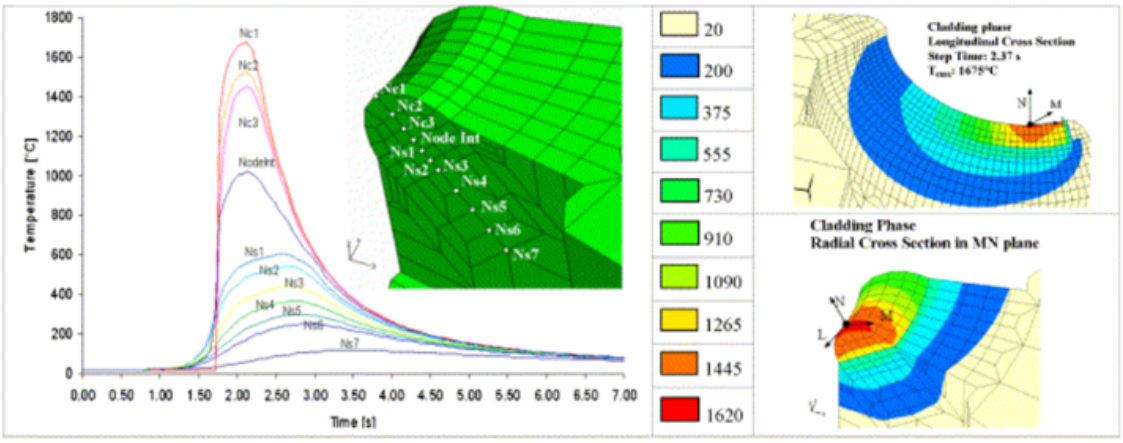

(a)

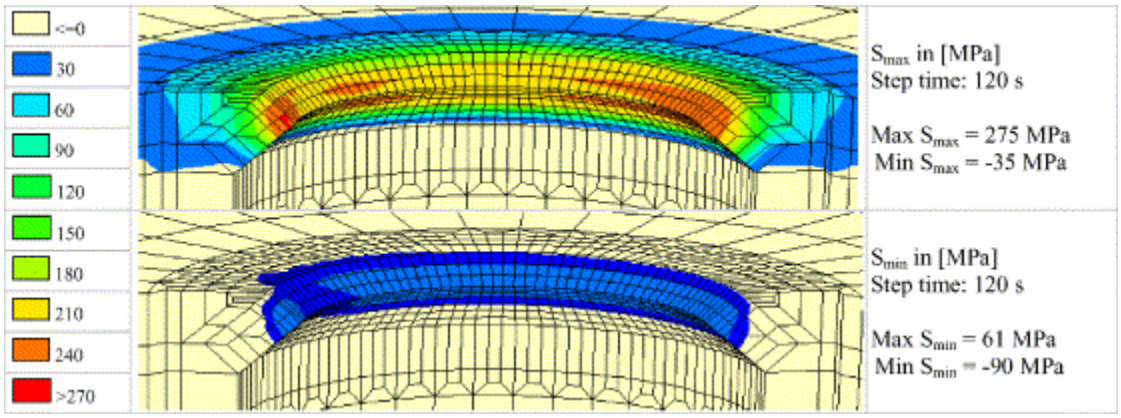

(b)

Figure 3.20: (a) Temperature distribution for several points in the cladding and workpiece, during the laser cladding of a valve seat; (b) Principal residual stresses *(from [18])*

laser cladding nozzle (Fig. 3.19), by means of a CFD model developed for FLUENT, but without considering the heating of the particles. Zhu et al. [210] also studied the powder flow using a 2D CFD model for FLUENT.

3.3.3 Mechanical Models

Numerous models based on the finite element method were developed to tackle with the problem of calculating the stresses during the laser cladding process. Nickel et al. [211] used ABAQUS for creating a model to study the effect of the deposition pattern in layered manufacturing processes on the deflection of the manufactured part. They found that for a beam, a raster pattern with lines oriented 90° from the longitudinal axis produces the lowest deflections; whereas for plate geometry, a spiral pattern scanned from the outside to the inside produces low and uniform deflections. However they did not added material to model the deposition process, only applied a heat flux boundary condition. Dai and Shaw [212] developed a model in ANSYS to calculate the thermal and stress fields in Multi-Material Laser Densification. Simple geometries and cubic elements for the layers were considered. Higher scanning speeds were found to lead higher residual stresses. Kathleen and Kar [213] presented a 1D analytical model for the calculation

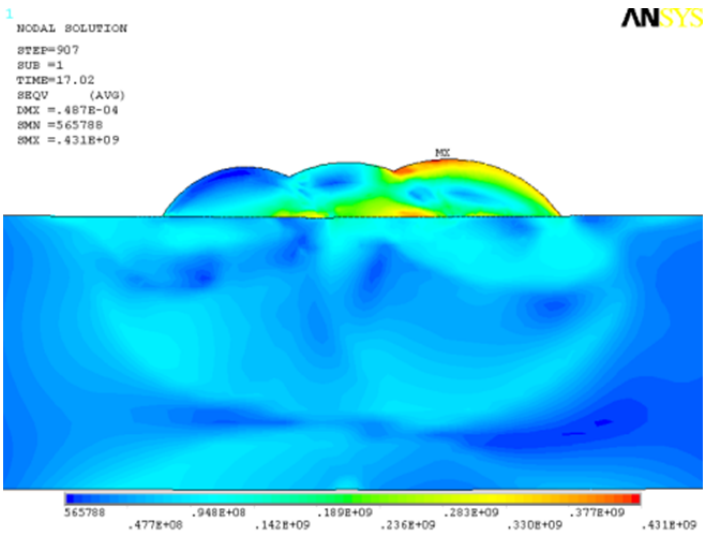

Figure 3.21: Von Mises residual stresses after the cladding process of 3 overlapped clad tracks *(from [19])*

of temperatures and residual stresses. Their thermal model takes into account the laser beam absorption in the metal vapour-plasma plume above the workpiece. Vasinonta et al. [214] developed process maps for the Laser Engineered Net Shaping (LENS) process using ABAQUS to create a 2D model and obtain correlations between process variables, evaluating the effect of preheating temperature, laser power and scanning speed. Labudovic et al. [215] developed a 3D model for ANSYS using cubic shaped elements for the clad track. They compared the predictions of the model with experimental measurements in tests with Monel 400 deposited on AISI 1066 steel.

2D and 3D models using ABAQUS were developed by De Deus [216] for the calculation of thermal and stress/strain fields, allowing a simple simulation of dilution using very simple assumptions for the mixing of the alloys. He also pointed out the convergence issues in the mechanical analysis. Palumbo et al. [18] created a 3D model using ABAQUS, for studying the treatment of ring geometries in the laser cladding of valve seats (Fig. 3.20). Ringsberg et al. [217] simulated with ABAQUS the laser cladding of a disc with a Co-Cr alloy. They used an isotropic-kinematic hardening model for the plastic behaviour of the substrate. In their work, they also simulate the grinding and a twin disk test, comparing the stresses and fatigue life against a non-treated component. Jendrzejewski and Sliwinski [218] and Jendrzejewski et al. [219] investigated the temperature and stress fields in single and double layer laser cladded coatings with the commercial software ADINA. They modelled the coating using cubic shaped elements but they obtained unrealistic high stresses because plasticity was not included in their material model. Tobar et al. [19] developed 2D and 3D models for ANSYS, modelling the clad beads with curved geometries and studying the effect of several parameters on the maximum stresses and maximum bending angles of the cladded plates due to the residual stresses, either for single tracks as for several overlapped tracks (Fig. 3.21). Zhao et al. [220] developed a 3D model for the calculation of the thermal fields in multitrack laser cladding with ANSYS. They also performed calculations of stress fields with one clad track. The authors mention that the method was based on genetic algorithms and neural networks. However, they do not seem to use them in any way. Suárez et al. [221] developed 2D and 3D models for ANSYS. They calculated temperatures, strains and stresses for one single track with and without preheating, and also for several tracks, modelling the clad

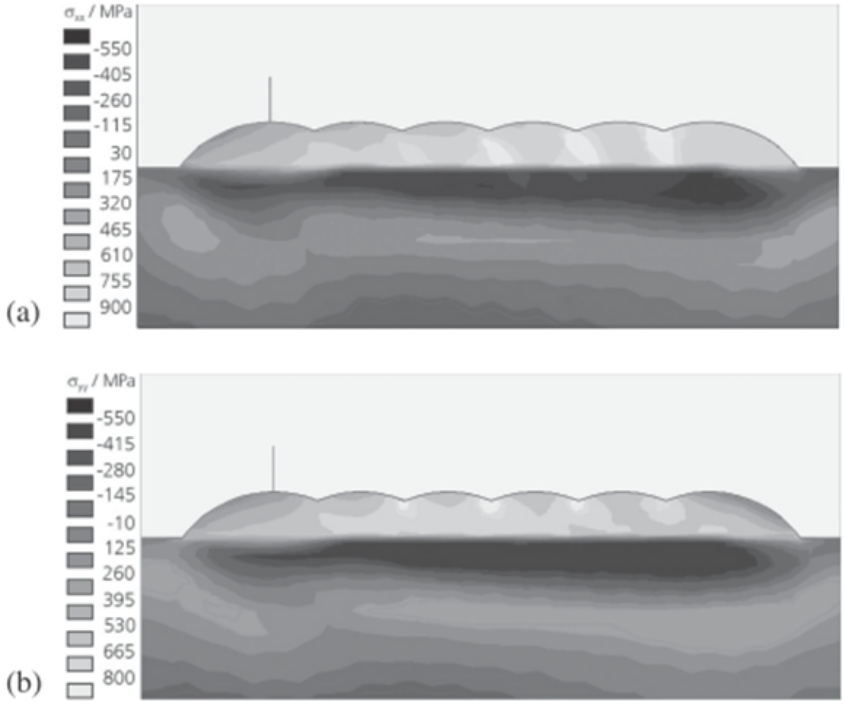

Figure 3.22: Distributions of longitudinal (a) and transverse (b) residual stresses on a cross section through six overlapping beads of Stellite 21 on AISI 1045, including phase transformations *(from [20])*

bead geometry from experimental observations. Their work includes stress measurements using synchrotron radiation for the validation of these models.

3.3.4 Phase Transformations

Several authors coupled phase transformation models to their thermal or thermomechanical models in order to simulate laser cladding on carbon steels and martensitic stainless steels. Gosh and Choi [222] presented a model for the simulation of the direct metal deposition process in order to study the macroscopic and microscopic stresses developed. A phase transformation model, which even includes TRIP, was implemented and the significance of including phase transformations in the analysis was demonstrated by comparison with a model which does not take them into account. Brückner et al. [223, 20] developed 3D models using the commercial software SYSWELD to study laser cladding of cobalt base alloys in AISI 1045 steel, using the phase transformation models of the software and performing analysis for single clad tracks, and multitracks (Figure 23). They pointed out the time consuming calculations required for the solution of these models. In other studies [224, 225] they also explored the effect of an induction preheating coil coupled to the cladding nozzle, finding lower stresses compared with the conventional technique an also lower thermal strains compared with a traditional uniform furnace preheating method.

Costa et al. [21] developed a 3D model for the simulation of rapid tooling by laser powder deposition of a ten layer AISI 420 stainless steel part. They modelled the layers with cubic shaped elements, and coupled a complete phase transformation model based on kinetic data and semiempirical relations, including also martensite tempering. They studied the heat

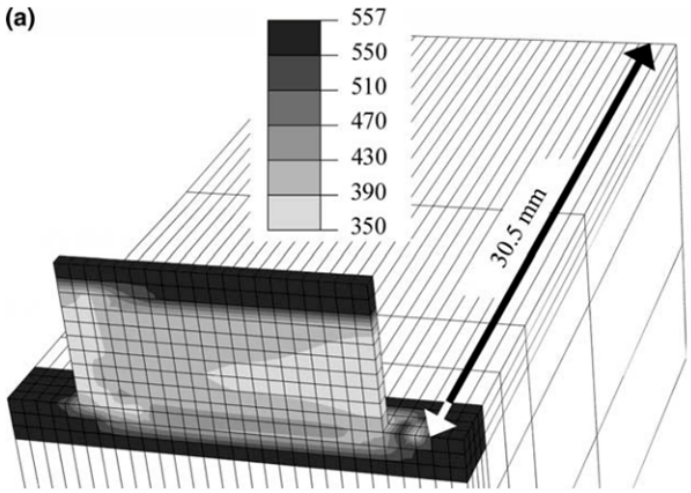

(a)

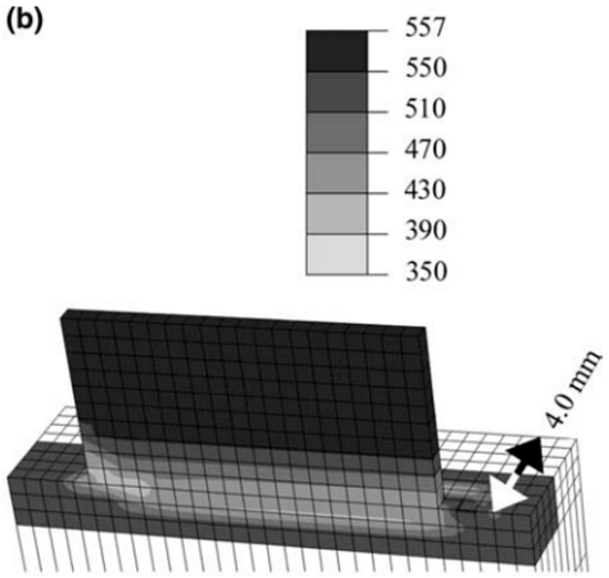

(b)

Figure 3.23: Vickers hardness distribution after cooling to room temperature, for a substrate of: (a) $m = 102.8g$, (b) $m = 13.5g$ *(from [21])*

accumulation during laser prototyping due to short idle times or small substrates, calculating the phase distributions and hardness profiles for several cases. They obtained a more uniform hardness distribution with higher hardness values when the substrate is small, due to the heat accumulation in the workpiece, which maintains the austenitic structure until the final cooling down of the workpiece to produce martensite. Bigger substrates effectively cool down the clad tracks obtaining a tempered martensite microstructure.

Crespo et al. [226] developed a 3D thermokinetic model for the laser powder deposition of titanium alloys. They modelled straight tracks as well as L-shaped tracks with sharp and smooth corners. Wang et al. [227] used SYSWELD to develop a model for the LENS process, simulating 10 superposed clad tracks using elements with cubic shapes, and using as the thermal input a

moving heat source with a Gaussian profile. They applied the model for the deposition of AISI 410 stainless steel, simulating the phase transformations and studying the laser power required to obtain a steady melt pool, finding an almost linear decrease in the power. Afterwards, they also used the model to simulate the mechanical analysis [228] and measured the residual stresses in the experimental samples using neutron diffraction; finding no significant effect of the travel velocity on the vertical component of the stresses, but an increase with the laser power.

3.4 Additional Information

The field of the numerical modelling of laser hardening, welding and cladding includes three decades of studies and thousands of papers. It is too broad to be treated in this only document. The aim of this work was to give a review of the physical processes involved in these techniques and the most important methods and equations used to simulate them, as well as the work of many authors that have researched in these fields. The characteristics of their models are briefly summarized in this review. However, for additional information, other reviews are available. Mackerle [229] compiled an extensive list of over 800 published papers dealing with the finite element simulation of welding, up to the year 1996. Mackwood and Crafer [230] published a review of the modelling of laser welding and related processes, with information up to the year 2002. Lindgren published a comprehensive review about the numerical modelling of welding in three parts [231, 232, 233] updated to the year 2004.

Part II

Numerical Modelling and Simulation

The second part of the thesis is entirely devoted to the numerical modelling of laser hardening and laser metal deposition processes.

Finite element theory is presented, including some analyses carried out for testing element performance and problematic element behavior. The most important aspects of material modeling are treated subsequently: plasticity and phase transformations, explaining in detail the kinetic models developed for steels and titanium which are implemented in the simulation models.

These chapters establish the foundations of the numerical models. Important aspects are treated in detail. The last two chapters of this part explain the numerical models developed for laser hardening and laser metal deposition are treated, with special emphasis in the key aspects. Results from simulations are also presented and thermomechanical stresses discussed.

Chapter 4

Thermomechanical Finite Element Analysis

The second rule was to divide each difficulty which I examined into as many parts as possible and as might be necessary to resolve it better.

René Descartes (*Discourse on the Method for Reasoning*).

Abstract: The constitutive equations for the numerical analysis of thermal and mechanical processes with finite elements, are derived in this chapter. Methods for the iterative solution of the nonlinear problems are described as well along with equation solvers, remarking their performance. At the end of the chapter problematic element behavior is discussed, including a study regarding element performance. Phase transformations and its coupling with thermomechanical analyses will be treated in the next chapter.

4.1 Couplings

Heat transfer, solid mechanics and phase transformations are all coupled in the thermomechanical modelling of laser processes (Fig. 4.1). However, not all the couplings have the same importance. The effect of the stress and strain fields is usually ignored for the heat transfer calculations, and is generally not taken into account in the kinetic models.

The solution of the thermal and mechanical fields simultaneously is not recommended, as this means to solve a large un-symmetric system of equations which is computationally demanding. A staggered solution procedure is much more common and requires less computational power [234]. The usual approach is the split of each time step into a pure thermal analysis followed by a mechanical analysis with the resulting temperature field as load. The heat generated due to deformation in the mechanical analysis can be calculated and applied in the next thermal time step, but it is usually neglected. If phase transformations are going to be simulated, a metallurgical model has to be included within this procedure.

Due to the weak coupling from the mechanical to the thermal field, another approach is to perform a sequentially coupled analysis, which involves the solution of the complete thermal

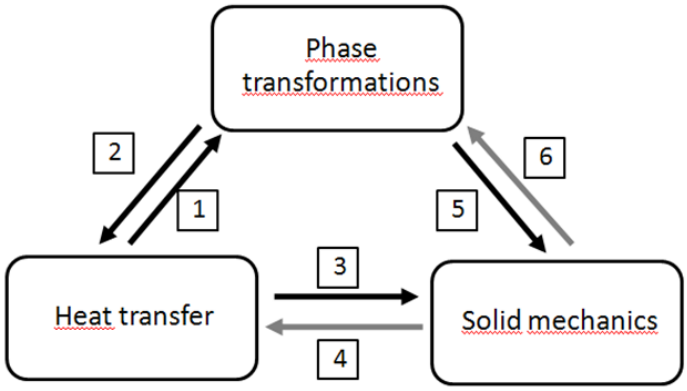

Figure 4.1: Couplings between all the relevant fields in LTH simulations. Weak couplings are in grey (4, 6)

problem first, and then with the calculated temperatures as load, the mechanical analysis. If a metallurgical model is used, it should be included in each of these separate simulations using a staggered procedure.

4.2 Thermal Analysis

The representative equations for the thermal analysis using the Finite Element Method are obtained by the discretization of the energy conservation equation [235, 236, 237, 238].

Applying energy conservation to a differential control volume, the following well known equation is obtained:

$$\rho c \frac{\partial T}{\partial t} + \nabla \cdot \mathbf{q} = Q \tag{4.1}$$

Where Q is the heat generation rate per unit volume, and $\mathbf{q}$ the heat flux vector, which is related to the thermal gradients by the conductivity matrix $[K]$ using Fourier's law:

$$\mathbf{q} = -[K]\nabla T \tag{4.2}$$

The following boundary conditions can be considered:

1. Specified temperatures on surface S_1: $T = T^*$
2. Specified heat flows acting on surface S_2: $\mathbf{q}\hat{\mathbf{n}} = -q^*$
3. Convection on surface S_3: $\mathbf{q}\hat{\mathbf{n}} = h_f(T - T_f)$

Where $\hat{\mathbf{n}}$ is the unit outward normal vector, h_f is the convection coefficient and T_f is the bulk temperature of the fluid.

Applying the finite element discretization, the variation of the temperature field along the element depends on the nodal temperatures T_n by means of an element function $\mathbf{N}$.

$$T = \mathbf{N}\mathbf{T}_n \tag{4.3}$$

Leading to the following equation:

$$\rho \iiint_V c\mathbf{N}\mathbf{N}\dot{\mathbf{T}}_n dV + \rho \iiint_V [B][K][B]\mathbf{T}_n dV = \iint_{S2} \mathbf{N} q^* dS + \iint_{S3} \mathbf{N} h_f (T_f - \mathbf{N}\mathbf{T}_n) dS + \iiint_V \mathbf{N} Q dV \tag{4.4}$$

Which could be rewritten as an algebraic equation:

$$[C_e]\dot{\mathbf{T}}_n + [K_e]\mathbf{T}_n = \mathbf{Q}_e^f + \mathbf{Q}_e^c + \mathbf{Q}_e^g \tag{4.5}$$

Where:

$[C_e] = \rho \iiint_V c\mathbf{N}\mathbf{N}\dot{\mathbf{T}}_n dV$: element specific heat capacity matrix.

$[K_e] = \rho \iiint_V [B][K][B]\mathbf{T}_n dV + \iint_{S3} h_f \mathbf{N}\mathbf{N}\mathbf{T}_n dS$: element conductivity matrix

$\mathbf{Q}_e^f = \iint_{S2} \mathbf{N} q^* dS$: element thermal flux vector

$\mathbf{Q}_e^c = \iint_{S3} \mathbf{N} h_f T_f dS$: element convection surface heat flow vector

$\mathbf{Q}_e^g = \iiint_V \mathbf{N} Q dV$: element heat generation load

The procedure employed for the temporal integration of this set of equations during a transient analysis is the generalized trapezoidal rule:

$$\frac{\mathbf{T}_{n+1} - \mathbf{T}_n}{\Delta t} = (1-\theta)\dot{\mathbf{T}}_n + \theta \dot{\mathbf{T}}_{n+1} \tag{4.6}$$

Where θ is the transient integration parameter. Depending on the value of this parameter, different methods arise:

1. For $\theta = 0$ the equation system is explicit (Forward Euler method).
2. For $\theta > 0$ the equation system is implicit.
   (a) For $\theta > 0.5$ the solution of these equations is unconditionally stable (stability does not depend on the time step).
   (b) If $\theta = 0.5$ the method is called Crank - Nicholson, which is second order accurate.
   (c) if $\theta = 1$ the method is called Backward Euler.

The implicit methods are better in terms of robustness and accuracy than the explicit ones [235, 239]. The Backward Euler method is a robust but first order accurate algorithm, useful in difficult problems. Further details about stability of the time stepping can be found in [236, 240, 241]. Rewriting the governing equation (4.5) for the time t_{n+1}:

$$[C]\dot{\mathbf{T}}_{n+1} + [K]\mathbf{T}_{n+1} = \mathbf{Q} \tag{4.7}$$

Substituting $\dot{\mathbf{T}}_{n+1}$ from the equation (4.6) in equation (4.7):

$$\left(\frac{1}{\theta\Delta t}[C]+[K]\right)\mathbf{T}_{n+1}=\mathbf{Q}+[C]\left(\frac{1}{\theta\Delta t}\mathbf{T}_n+\frac{1-\theta}{\theta}\dot{\mathbf{T}}_n\right) \tag{4.8}$$

Solving the equation (4.8) T_{n+1} is obtained, then $\dot{\mathbf{T}}_{n+1}$ is updated using the generalized trapezoidal rule (4.6). For the initial conditions, the initial temperature T_i could be entered. The temperature formulation is the most used formulation for computing thermal fields in laser surface treatments, but the enthalpy formulations have less numerical problems in the presence of latent heats [242, 241, 237] working even for a pure metal. Also the fictitious heat source method [243] used by Murty et al. [244] has less numerical problems due to latent heats. Lindgren et al. [123] and others [245, 236] employed a time-averaging procedure of the enthalpy h, for calculating the average heat capacity, which is taken as:

$$c_{n+1}=\frac{h_{n+1}-h_n}{\Delta T} \tag{4.9}$$

4.3 Mechanical Analysis

As the inertial effects in these processes are negligible, a full transient mechanical analysis is not necessary; a quasistatic analysis is adequate to simulate them. However, large deformations are important because, although strains are small, residual deformations sometimes are visible to the naked eye.

The derivation of the equations for the mechanical analysis starts with the stress-strain relationship:

$$\boldsymbol{\sigma}=[D]\boldsymbol{\varepsilon}_n \tag{4.10}$$

Where $\boldsymbol{\sigma}=[\sigma_x\ \sigma_y\ \sigma_z\ \sigma_{xy}\ \sigma_{yz}\ \sigma_{xz}]^T$ is the stress vector, $[D]$ the elasticity matrix, and ε_e the elastic strain vector.

The total strain vector is:

$$\boldsymbol{\varepsilon}=\boldsymbol{\varepsilon}_n+\boldsymbol{\varepsilon}_{th}=[\varepsilon_x\ \varepsilon_y\ \varepsilon_z\ \varepsilon_{xy}\ \varepsilon_{yz}\ \varepsilon_{xz}]^T \tag{4.11}$$

And the thermal strain vector:

$$\boldsymbol{\varepsilon}_{th}=\Delta T[\alpha_x\ \alpha_y\ \alpha_z\ 0\ 0\ 0]^T \tag{4.12}$$

Where α_x is the coefficient of thermal expansion in the x direction, and $\Delta T=(T-T_{ref})$, being T the current nodal temperature, and T_{ref} the reference temperature for stress calculation. The strains are related to the nodal displacements by:

$$\boldsymbol{\varepsilon}=[B]\mathbf{u} \tag{4.13}$$

Where $[B]$ is the strain-displacement matrix, based on the element shape functions, and $\mathbf{u}$ is the nodal displacement vector. Using the principle of virtual work for all the internal and external sources of strain energy, with the considerations for a quasistatic process, and applying the finite element discretization [237, 235], the following system of equations is obtained:

$$[K_e]\mathbf{u}-\mathbf{F}_e^{th}=\mathbf{F}_e^{ext} \tag{4.14}$$

Where:

$[K_e] = \iiint_V [B][D][B]\mathbf{u}dV$: element stiffness matrix

$\mathbf{F}_e^{th} = \iiint_V [B][D]\boldsymbol{\varepsilon}_{th}dV$: element thermal load vector

$\mathbf{F}_e^{ext}$: element vector of external nodal forces

The quasistatic formulation does not require any temporal discretization. The updating of the current geometry is done using the following equation:

$$\mathbf{u}_{n+1} = \mathbf{u}_n + \Delta\mathbf{u}_n \tag{4.15}$$

The equilibrium is reached at iteration $n+1$ when the residual equals zero:

$$\mathbf{R}_{n+1} = \mathbf{F}_{n+1}^{ext} - \mathbf{F}_{n+1}^{int} = 0 \tag{4.16}$$

$$\mathbf{R}_{n+1}(\mathbf{u}) = \mathbf{F}_{n+1}^{ext} - [K]_{n+1}\mathbf{u}_{n+1} = 0 \tag{4.17}$$

In non-linear problems the solution of the previous equation requires an incremental iterative approach for solving the displacements in each time step. Usually the Newton-Raphson method is chosen, being recommended to combine it with line search techniques [237, 235, 240].

4.4 Nonlinear Solution Techniques

In a non-linear analysis the non-linear system of equations cannot be solved directly, it is necessary to use some iterative procedure. Rootfinding algorithms like regula falsi, secant, quasi-Newton or Newton-Raphson can be employed, but the most widely used for this task is the last one.

4.4.1 Newton-Raphson Method

The Newton-Raphson method consists in the iterative solution of a linear approximation of the nonlinear system of equations, until a specific convergence criterion is fulfilled. The solution starts with a predictor step that is followed by the correction steps. The goal of the Newton-Raphson algorithm is to reduce the unbalanced load R, which in a structural system represents the out of balance load between external and internal forces, until a certain convergence tolerance is reached.

If the initial solution chosen for the iterative process is within the zone of attraction, divergence does not occur, and the asymptotic rate of convergence is quadratic [237, 235].

The generalized nonlinear equation to solve is:

$$\mathbf{R}_{n+1}^{i} = \mathbf{F}_{n+1}^{ext} - \mathbf{F}_{n}^{int} = 0 \tag{4.18}$$

Assuming $\mathbf{u}_n$ is the converged solution from the previous time step, then: $\mathbf{u}_{n+1}^0 = \mathbf{u}_n$.

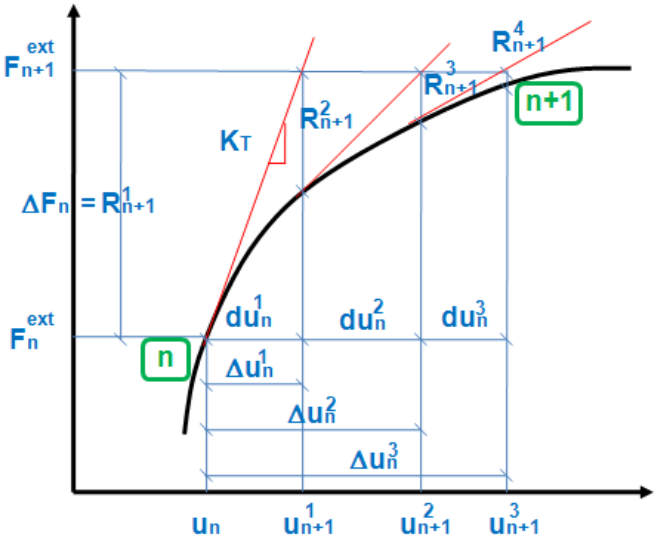

Figure 4.2: Scheme of the Full Newton-Raphson method in 1D.

The method consists of the following steps:

FOR i = 0,1,. . . , UNTIL CONVERGENCE, DO:

1. Compute the vector of unbalanced loads:

$$\mathbf{R}^i_{n+1} = \mathbf{F}^{ext}_{n+1} - [K^T_i]\mathbf{du}^i_n \tag{4.19}$$

2. Compute the Jacobian or tangent stiffness matrix: $[K^T_i]$

3. Calculate the Newton update Δu^i_n from:

$$\Delta \mathbf{u}^i_n = \sum_{k=1}^{i} \mathbf{du}^k_n \tag{4.20}$$

4. Add Δu^i_n to u_n in order to obtain the next approximation:

$$\mathbf{u}^{i+1}_{n+1} = \mathbf{u} + \Delta \mathbf{u}^i_n \tag{4.21}$$

ENDDO

An expensive part of the process is the formation of the tangent stiffness (Jacobian) matrix $[K^T_i]$. Time savings could be obtained by updating it only a few times. This variant is called a Modified Newton - Raphson method. When robustness and accuracy are more important, the Jacobian matrix must be updated every iteration, constituting which is called a Full Newton - Raphson method (Fig. 4.2).

4.4.2 Line Seach Procedures

Line search procedures are regarded as the foundation of the non-linear optimization techniques and are used today for global multidimensional optimization. They are widely used to accelerate the convergence of iterative procedures and prevent its divergence in a wide variety of nonlinear problems [246]. Line search can be used in an attempt to improve a Newton - Raphson solution $\Delta \mathbf{u}_n^i$ by scaling the solution vector with a scalar value, called the line search parameter. Considering the equation (4.21) again, the use of the full $\Delta \mathbf{u}_n^i$ in some situations leads to solution instabilities, therefore it is convenient to scale it with the line search parameter s, for trying to prevent the divergence when strong nonlinearities are present. Hence, the equation (4.21) is modified to be:

$$\mathbf{u}_{n+1}^{i+1} = \mathbf{u} + s\Delta \mathbf{u}_n^i \tag{4.22}$$

The line search parameter is usually determined by minimizing the energy of the system. Then, the scaled solution $s\Delta \mathbf{u}_n^i$ is used to update the current DOF values $\mathbf{u}_{n+1}^{i+1}$, and the next equilibrium iteration is performed.

4.4.3 Adaptive Descent

The adaptive descent technique switches to a *stiffer* matrix if convergence difficulties are encountered, and switches back to the full tangent matrix as the solution converges, resulting a fast convergence rate.

The technique is employed along with the iterative method used to solve the non-linear problem, like the Newton - Raphson method. The tangent matrix used in the equations will be described as the sum of two matrices: $[K_S]$ secant matrix (most stable), and $[K_T]$: tangent matrix.

$$[K_T] = \xi[K_S] + (1 - \xi)[K_T] \tag{4.23}$$

The descent parameter ξ is adjusted during the equilibrium iterations, starting each substep using the tangent matrix, and monitoring the residual over the equilibrium iterations. If it increases, indicating possible divergence, switches to the secant matrix. Then, when the iterations converge, gradually switch to the tangent matrix by decreasing the descent parameter.

4.5 Equation Solvers

The finite element discretization procedure leads to a linear system of equations:

$$[K]\mathbf{u} = \mathbf{F} \tag{4.24}$$

Where $[K]$ is the global stiffness/conductivity matrix and $\mathbf{F}$ the global load vector applied.

This system of linear equations can be solved using either direct methods or iterative methods, in order to calculate the unknown vector of variables $\mathbf{u}$. The method used for the solution is called *solver*.

4.5.1 Direct Equation Solvers

Direct equation solvers involve the decomposition (factorization) of the matrix $[K]$ into lower $[L]$ and upper $[U]$ triangular matrices, and the use of forward and backward substitutions to

compute the solution vector:

$$[L][U]\mathbf{u} = \mathbf{F} \tag{4.25}$$

Making the substitution:

$$\mathbf{w} = [U]\mathbf{u} \tag{4.26}$$

The following triangular matrix system is solved by forward substitution:

$$[L]\mathbf{w} = \mathbf{F} \tag{4.27}$$

And then the solution vector $\mathbf{u}$ is computed using backward substitution (4.26).

If the matrix $[K]$ is symmetric, the Cholesky decomposition can be used:

$$[K] = [L][L]^T = [L'][D][L']^T \tag{4.28}$$

$$[L'][D][L']^T\mathbf{u} = \mathbf{F} \tag{4.29}$$

$$\mathbf{w} = [D][L']^T\mathbf{u} \tag{4.30}$$

$$[L']\mathbf{w} = \mathbf{F} \tag{4.31}$$

Since $[K]$ is normally sparsely populated with coefficients located around the main diagonal, the direct solvers (like the Sparse) are designed to use only the nonzero values in $[K]$. Reordering algorithms for the equations in $[K]$ minimize the fill-in of the matrices obtained in the decomposition process, optimizing the performance of the solver.

4.5.2 Iterative Equation Solvers

Iterative solvers do not factorize the matrix $[K]$, instead they obtain the solution iterating on a series of vectors:

$$\mathbf{u} = \alpha_1\mathbf{v}_1 + \alpha_2\mathbf{v}_2 + \ldots + \alpha_m\mathbf{v}_m \tag{4.32}$$

Where m is smaller or equal to the matrix size n. The method converges in n or few iterations on an infinite precision machine. However for ill-conditioned problems (where the values of $[K]$ vary several orders of magnitude) and nearly singular matrices, they could fail. In these situations direct solvers are preferred because of their robustness.

Most of the iterative solvers are based on the Conjugate Gradient method, which has a convergence rate proportional to the square root of the conditioning number of $[K]$. This number is defined as the ratio between the maximum and the minimum eigenvalues of $[K]$ [237, 247]. For this reason, a preconditioning procedure is used to reduce the conditioning number $[K]$ and improve the convergence.

Iterative solvers require much less computer memory than direct solvers, and are more scalable for parallel computing, resulting in a much lower computing time required for problems with a large number of degrees of freedom (DOF's), compared to direct solvers.

Several tests with transient thermomechanical models of laser cladding were performed to assess the performance of different solvers. Fig. 4.3 shows a comparison between the computing time required to solve the thermal and mechanical analyses, for three models with different number of nodes. The memory requirements for an in-core run are represented in Fig. 4.4.

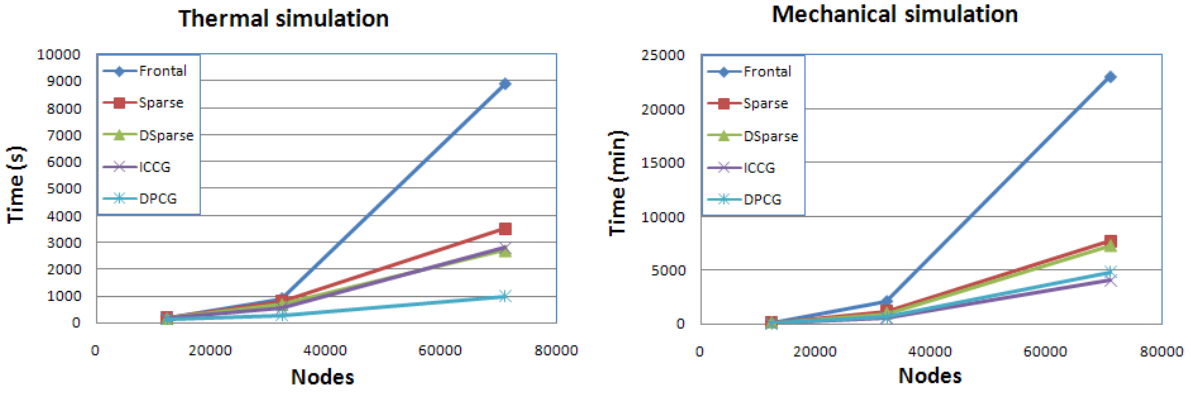

(a) (b)

Figure 4.3: Computing time vs number of nodes for several solvers in: (a) thermal analysis; (b) mechanical analysis.

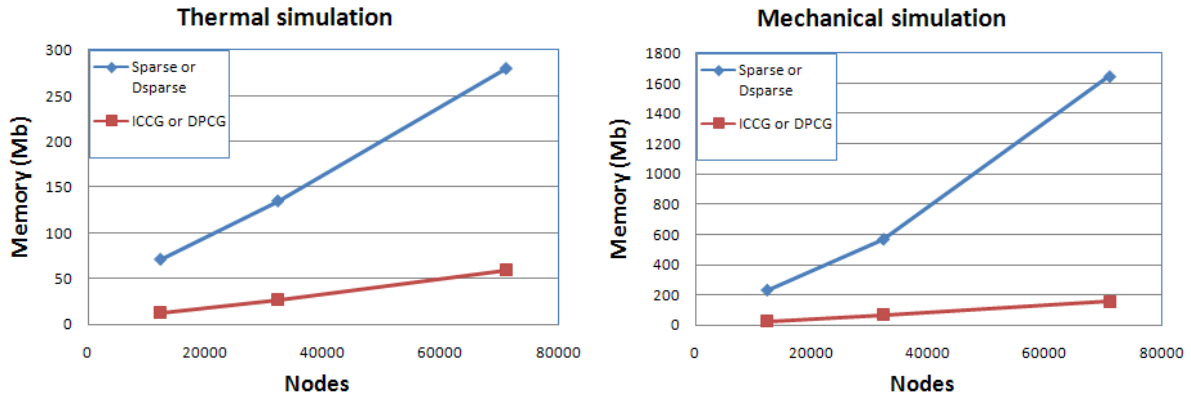

(a) (b)

Figure 4.4: Computer menory vs number of nodes for several solvers during: (a) thermal analysis; (b) mechanical analysis.

4.6 Problematic Element Behavior

Some elements display anomalies under certain mechanical conditions due to the finite element approximation. The most important anomalies are shear locking, volumetric locking and hourglassing.

4.6.1 Shear Locking

Shear locking occurs in linear elements with full integration of the strain and stress fields, subjected to bending deformation. Their behavior is overly stiff, being incapable of modelling the curvature appropriately. In an ideal situation a block of material under a pure bending moment develops a curved shape. The angle α between the previous horizontal and vertical lines drew on the surface of the block, remains as 90° after bending (Fig. 4.5a), just as predicted by classical beam theory.

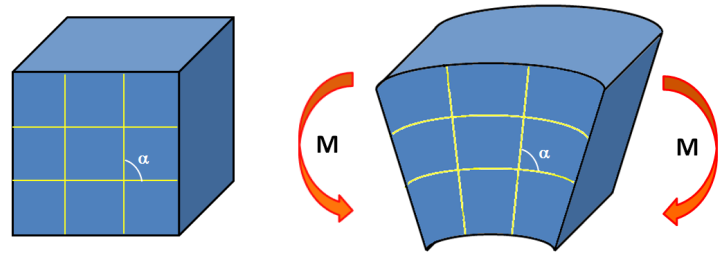

(a)

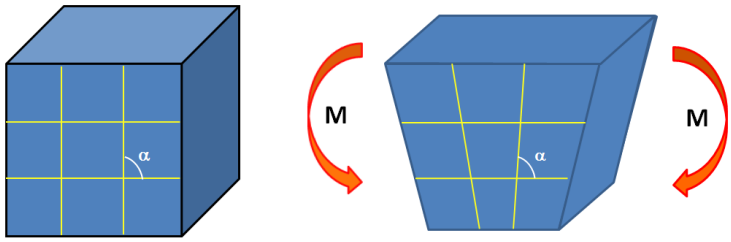

(b)

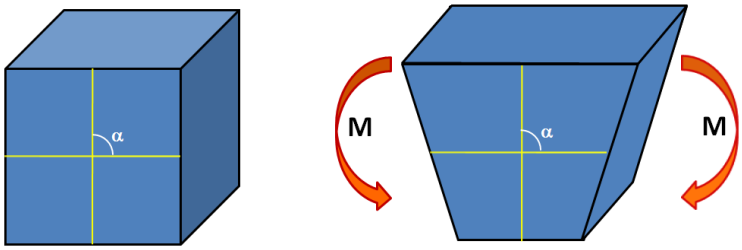

(c)

Figure 4.5: Shape changes under a bending moment: (a) ideal situation; (b) fully integrated first order element; (c) reduced integration first order element

To correctly model the shape change the element should have the ability to assume the curved shape, however the edges of a linear element are not capable of bending to curves, so the element develops the shape shown in Fig. 4.5b, where the angle α can no longer remain at 90°. To change the angle α, a shear stress has been artificially introduced, so the strain energy of the element is generating a shear deformation instead of a bending deformation, and the element becomes locked or overly stiff.

A solution to this problem is to use reduced integration instead of full integration. For a quadrilateral, this means that instead of 4 integration points, only 1 located at its center is now considered. For an hexahedral element also 1 integration point is taken, instead of 8. Now the shear stresses in pure bending are zero at the integration point (Fig. 4.5c).

Reduced integration also traduces in an important decrease of the computation time, and additionally the elements with reduced integration have a better tolerance to shape distortions. It is only available for quadrilaterals and hexahedrals. Tetrahedrals do not have reduced integration schemes. However, linear quadrilaterals and hexahedrals also have another way of treating this

problem: the enhanced strain formulations. They are designed to cope with shear locking and volumetric locking by introducing additional internal DOF's, at the expense of increasing the computation time.

Fully integrated second order elements do not present shear locking, as they are able to bend, remaining the angle α as 90°.

4.6.2 Hourglassing

The reduced integration elements have several advantages. However, they also have some problems. The existence of only one integration point at the center of the element makes it excessively flexible, which sometimes results in non-physical deformations through zero-energy modes. The normal and shear stresses at the integration points are zero, therefore there is no strain energy generated by the deformation, creating non-physical zero-energy modes, which results in correct strains and stresses, but wildly varying displacements [248].

Commercial FEM software have hourglass control methods implemented that alleviate the problem and reduce the propagation of these spurious modes throughout the mesh. With linear hexahedrals, using a mesh with sufficient elements usually solves the problem. Quadratic elements do not tend to have problems with hourglassing unless the mesh has only one element across the thickness.

4.6.3 Volumetric Locking

Volumetric locking occurs for incompressible or nearly incompressible behavior. Fully integrated elements become excessively stiff resulting in a zero deformation field: the element locks. The use of reduced integration elements is one way to avoid locking. Another option is the use of hybrid elements, in which the pressure is an additional variable because, in truly incompressible behavior, an increase in the hydrostatic pressure does not change the displacements, therefore the pressure cannot be derived from the displacement fields [235].

4.6.4 Element Tests

In order to test the element behavior and the convergence of the results through a mesh refinement, a simple example was studied. The case consists of a cantilever beam of 1 m length and square cross section of 5 cm side. The displacements of the nodes at one end were completely constrained, and two concentrated loads of 3500 N were placed at the lower vertexes of the free end. The material of the beam is stainless steel AISI 304 with a bilinear isotropic hardening model. The load is sufficient to cause significant yielding and bending in the beam.

Hexahedral and tetrahedral meshes with different refinements and element integration were tested in the study. The meshes were classified according to element size into three main cases: case 1 has an element size of 5 cm, and therefore there is only one element across the thickness of the beam. Case 2 has an element size of 2.5 cm, and case 3 of 1.25 cm. They are represented in Fig. 4.6.

The results of the simulations were compared with the converged solution of the problem, and the relative errors calculated are included in Table 4.1. Several conclusions can be extracted:

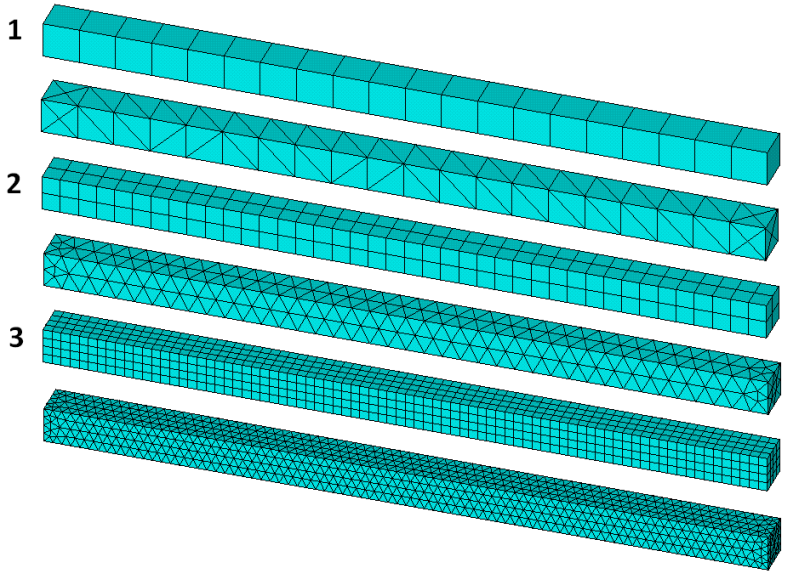

Figure 4.6: Different meshes for the element behavior and convergence study.

	Linear			Quadratic	
Model	**Full Int.**	**Red. Int.**	**Enh. Str.**	**Full Int.**	**Red. Int.**
1 Hex.	70.44	1069	-90.25	110.2	Not Conv.
1 Tet.		-96.85		-42.76	
2 Hex.	-64.46	-18.87	-6.289	-5.660	-4.088
2 Tet.		-93.081		-6.289	
3 Hex.	-24.84	-5.66	-0.943	-2.830	-1.887
3 Tet.		-89.62		-2.201	

Table 4.1: Error percentage (%) of the different tests with respect to the converged solution. Negative values represent results below the solution value.

- With only one element across the thickness of the beam the results are completely wrong with all meshes, and the reduced integration hexahedrals show an extremely flexible behavior.
- With two layers of elements, the quadratic elements, both full or reduced integration hexahedrals and also tetrahedrals, give fairly good results.
- There is very little difference between reduced and fully integrated quadratic hexahedrals.
- Fully integrated linear hexahedrals are too stiff and gave worst results than reduced integration linear hexahedrals.
- Reduced integration linear hexahedrals give results as good as a mesh composed of quadratic hexahedrals with half the density of elements, and still compute much faster,

while enhanced strain linear elements give results comparable to a mesh of the same density of quadratic elements with lower computation times.

- Linear tetrahedrals are extraordinarily stiff and gave poor results in all cases, while quadratic tetrahedrals surprisingly performed extraordinary well, likewise their hexahedral counterparts, being worth to be considered.

Linear 2D quadrilaterals or 3D hexahedrals are usually the elements chosen for plasticity problems [249, 250]. They perform much better than linear triangles and tetrahedrons. Reduced integration or enhanced strain formulations are required in order to avoid shear locking in bending dominated problems or volumetric locking in case of large plastic strains in nearly incompressible problems. However, quadratic reduced integration elements show an excellent performance in all kinds of problems, and are the standard elements in some commercial packages [238].

The final recommendation for thermomechanical analyses is to use linear reduced integration hexahedrals, with a fine mesh density, and quadratic tetrahedrals in the zones that cannot be meshed with hexahedrals. The results should be accurate and fast.

Chapter 5

Material Modelling: Plasticity And Phase Transformations

We know very little, and yet it is astonishing that we know so much, and still more astonishing that so little knowledge can give us so much power.

Bertrand Russell.

Abstract: The key aspects of material modelling are discussed in this chapter. Especial emphasis was placed in the simulation of metal plasticity and the kinetic models developed to compute phase transformations in steels.

5.1 Plasticity

Plastic deformation in metals is usually a consequence of the motion of a large number of dislocations.

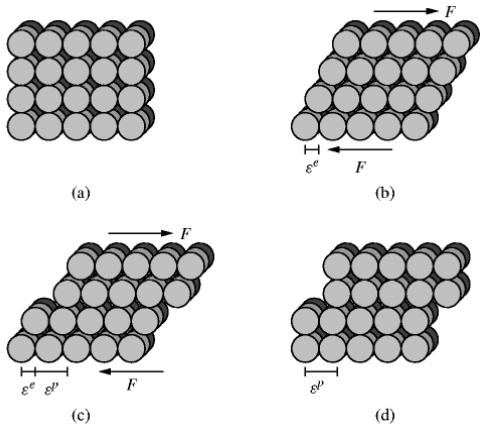

Figure 5.1: Deformation of a metal: (b) pure elastic; (c) elastic-plastic; (d) pure plastic

During the process the number of dislocations in the material increases dramatically, spawning from existing dislocations, defects, grain boundaries and interfaces. Their motion occurs by sequential bond breaking and bond forming along preferential slips systems [251], which in polycrystalline materials vary from grain to grain, generating non-recoverable deformations in the material (Fig. 5.1).

The dislocation movement is thermally activated and gets faster at high temperatures, and therefore plasticity increases with temperature. The deformation by slipping system does not change the volume of the material thus a pure plastic deformation does not alter the volume, as opposed to an elastic deformation. and the same happens with pure plastic deformation

5.1.1 Rate Independent Elastoplasticity

This section is focused on the description of the constitutive equations of rate independent elastoplasticity, thereby viscoplastic phenomena like creep are not included. This is justified because of the relatively short time the material spends at high temperatures during laser treatments. Rate dependent plasticity is generally used only if subsequent heat treatments are simulated.

The yield function, which governs the onset of plastic deformation at every position of the material [252], can be described as a function of stress components σ_{ij}, yield surface translation components (or backstress) α_{ij}, and plastic work κ:

$$f = f(\sigma_{ij}, \alpha_{ij}, \kappa) = 0 \tag{5.1}$$

The direction of plastic straining is given by the flow rule established by the Prandtl-Reuss equation:

$$\dot{\varepsilon}_{ij}^{pl} = \lambda \frac{\partial f}{\partial \sigma_{ij}} \tag{5.2}$$

Where $\frac{\partial f}{\partial \sigma_{ij}}$ is the component of the outward unit vector of the yield surface in stress space, and λ is the plastic multiplier, which determines the amount of plastic straining. The plastic work over the entire loading history is:

$$\kappa = \int \sigma : d\varepsilon^{pl} \tag{5.3}$$

The translation of the yield surface is calculated with a material parameter C, that depends on the rate independent plasticity model chosen:

$$\alpha = \int C d\varepsilon^{pl} \tag{5.4}$$

Differentiating the yield criterion (5.1), taking into account the elastic stress-strain relationships and dividing the strain increment into the elastic and plastic parts:

$$\sigma = D : d\varepsilon^{el} \tag{5.5}$$

$$d\varepsilon^{el} = d\varepsilon - d\varepsilon^{pl} \tag{5.6}$$

The plastic multiplier can be obtained:

$$\lambda = \frac{\frac{\partial f}{\partial \sigma} D : \varepsilon}{\frac{\partial f}{\partial \sigma} D \frac{\partial f}{\partial \sigma} - \frac{\partial f}{\partial \kappa} \sigma \frac{\partial f}{\partial \sigma} - C \frac{\partial f}{\partial \alpha} \frac{\partial f}{\partial \sigma}} \tag{5.7}$$

And the plastic strain can be computed with the flow rule (5.2). The implementation in a numerical code requires an iterative procedure for the calculation of the plastic strain increment [237, 253]. The procedure starts evaluating the yield strength at the current temperature and time step, and guessing a trial strain from a previous time step to calculate if the stress exceeds the material yield. In that case λ is calculated through an iterative procedure, and the plastic strain updated:

$$\varepsilon_n^{pl} = \varepsilon_{n-1}^{pl} + \Delta\varepsilon^{pl} \tag{5.8}$$

The plastic work and the displacement of the yield surface are updated afterwards.

5.1.2 Hardening Model

The yielding of the material was assumed to follow the Von Mises yield criterion, as is usually assumed in most metals:

$$f = (\sigma_1 - \sigma_2)^2 + (\sigma_2 - \sigma_3)^2 + (\sigma_1 - \sigma_3)^2 - 2\sigma_Y^2 \tag{5.9}$$

Where σ_i is the principal stress (eigenvalue of the stress matrix) in the i direction. This equation can also be expressed using the deviatoric stresses $\mathbf{s}$:

$$f = \mathbf{s} : \mathbf{s} - \frac{2}{3}\sigma_Y^2 \tag{5.10}$$

Where the deviatoric stresses are obtained extracting the hydrostatic part σ_H form the stress tensor, being I the identity matrix:

$$\mathbf{s} = \boldsymbol{\sigma} - \sigma_H I \tag{5.11}$$

Isotropic hardening (5.12) is usually considered sufficient to describe the plasticity during laser heat treatments because at high temperatures recovery occurs and plastic history disappears [254]. With this assumption the yield function expands isotropically in the stress space with an increasing stress (Fig. 5.2a).

$$f = \mathbf{s} : \mathbf{s} - \frac{2}{3}\sigma_Y^2(\varepsilon^{pl}) \tag{5.12}$$

In tension-compression, during the stress reversal the yield stress does not reach in compression the same absolute value as in tension before, thus the material softens when the load is reversed (Fig. 5.2b). This phenomenon, called Bauschinger effect, is modelled with a translation of the elasticity domain in stress space, defining a kinematic hardening model:

$$f = (\mathbf{s} - \boldsymbol{\alpha}) : (\mathbf{s} - \boldsymbol{\alpha}) - \frac{2}{3}\sigma_Y^2(\varepsilon^{pl}) \tag{5.13}$$

The yield surface translation is defined as:

$$\boldsymbol{\alpha} = \frac{1}{3}G\boldsymbol{\varepsilon}^{sh} \tag{5.14}$$

Where G is the shear modulus, and $\boldsymbol{\varepsilon}^{sh}$ is the shift strain, defined as:

$$\boldsymbol{\varepsilon}_n^{sh} = \boldsymbol{\varepsilon}_{n-1}^{sh} + \Delta\boldsymbol{\varepsilon}^{sh} \tag{5.15}$$

And the shift strain increment calculated as follows:

$$\Delta\boldsymbol{\varepsilon}^{sh} = \frac{C}{2G}\Delta\boldsymbol{\varepsilon}^{pl} \tag{5.16}$$

Where the material parameter C can be calculated through the Young's modulus and the tangent modulus E_T:

$$C = \frac{2}{3}\frac{EE_T}{E - E_T} \tag{5.17}$$

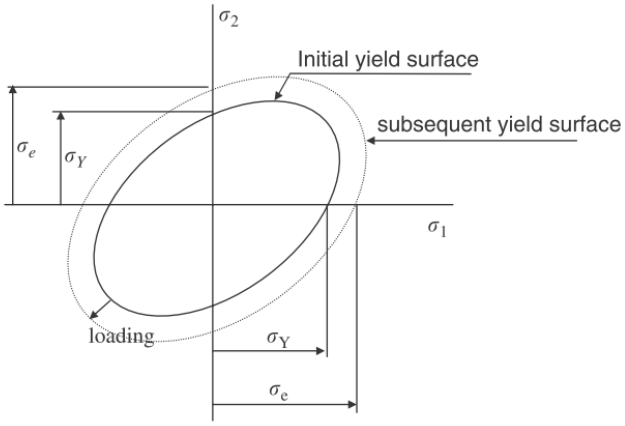

(a)

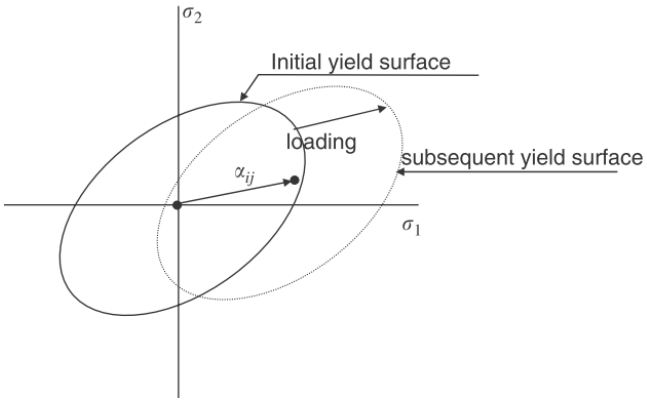

(b)

Figure 5.2: Schematic 2D diagrams showing: (a) isotropic hardening; (b) kinematic hardening

5.2 Phase Transformations In Steels

Hardening processes are usually performed on hypoeutectoid steels composed of a ferritic-pearlitic microstructure. The carbon content of pearlite (0.8% aprox.) is much higher than in ferrite, therefore the austenite grains start to nucleate in the pearlite colonies. Ferrite will transform at higher temperatures. Transformation of pearlite to austenite takes place when the material is heated above the austenitization temperature. During the transformation, the crystalline lattice changes from ferrite's BCC to austenite's FCC, which has a higher atomic packing factor, hence the phase change implies a density increase (Fig. 5.3a).

The rest of material properties change accordingly during the phase change, showing in the case of the thermal conductivity a different behavior between the α phases and the γ phase, as depicted in Fig. 5.3b.

Austenitization is regarded as a two step process [22, 85]. The first stage is the intragranular diffusion of carbon in pearlite, which is fast due to the short diffusion distances. During this stage cementite lamellae in the pearlite colonies start to dissolve and carbon diffuses from cementite lamellae into the surrounding ferrite lamellae (Fig. 5.4a). Additionally, part of the ferrite grains transform to austenite, with negligible carbon content. Afterwards takes place the second stage, the intergranular diffusion of carbon from high concentration to low concentration regions,

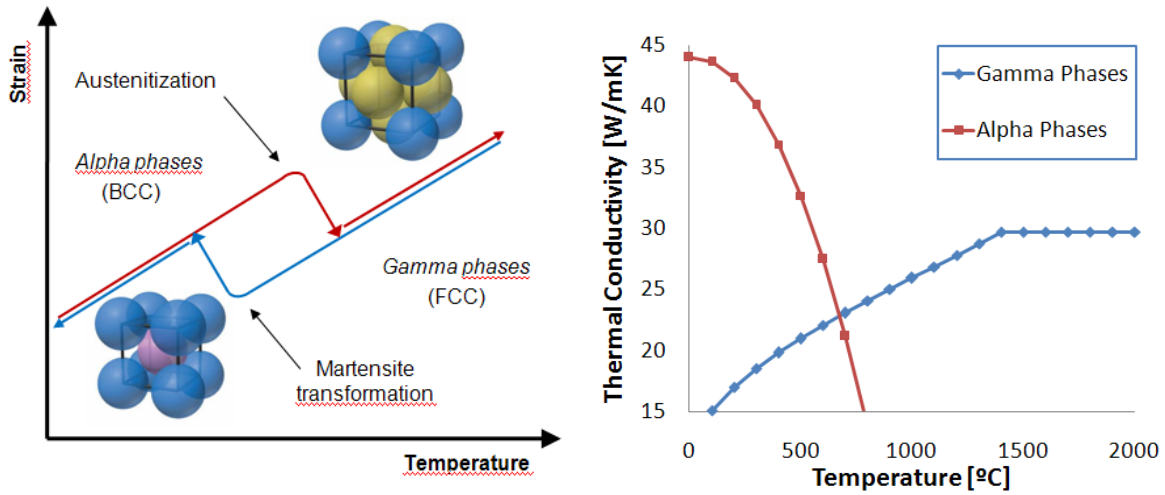

(a) (b)

Figure 5.3: (a) Strain during phase transformation austenite ferrite; (b) thermal conductivity of bcc and fcc iron phases

homogenizing the carbon distribution (Fig. 5.4b). The latter implies larger diffusion distances being a slower process.

During the subsequent cooling, the austenite with carbon content above a critical value transforms to martensite, which is a supersaturated solid solution of carbon on α-Fe. The martensitic transformation changes the crystal structure from FCC to BCT by means of a displacive transformation, hence without diffusion, depending only on the degree of subcooling below the martensite start temperature (M_s).

During laser transformation hardening the laser beam induces a thermal cycle in the material surface. Heating and cooling times are very short in comparison with other hardening processes,

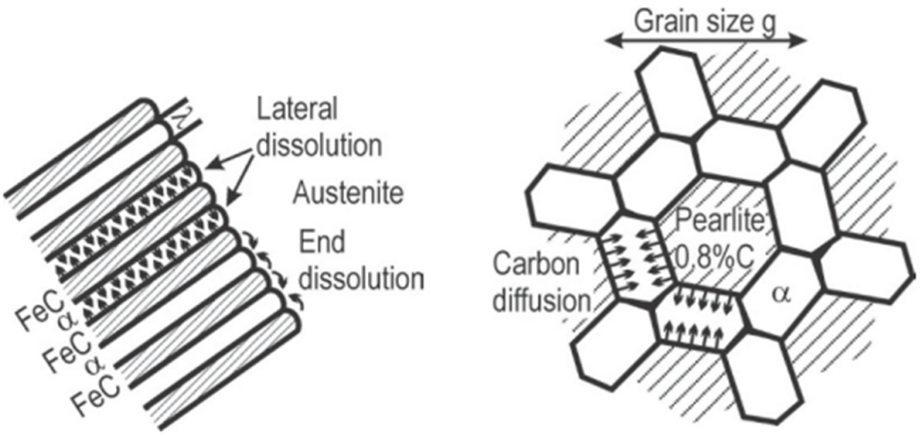

(a) (b)

Figure 5.4: Carbon diffusion during austenitization: (a) fast intragranular diffusion in pearlite; (b) slow homogenization of a hypoeutectoid steel *(from [22])*

and therefore usually only the most superficial zone is completely austenitized, resulting in homogeneous martensitic structures after quenching of this zone. Below this area, due to the short heating time which limits the carbon diffusion reactions, the base material transforms into austenite without reaching the equilibrium weight fraction, resulting in undisolved carbides and an austenitic matrix with reduced carbon content [10]. At high heating rates a superheating is also necessary to enhance the austenitization due to the finite carbon diffusion rate. The lower carbon content in this zone produces an increase in the martensite start transformation temperature (M_s) during the subsequent quenching process, having an appreciable impact on the final martensite morphology and mechanical properties of the hardened structure [10]. Hence the martensite start and martensite finish temperatures depend on the heating and cooling rates.

Usually not all the austenite transforms during the cooling, remaining a certain fraction of retained austenite in the microstructure, which is dependent of the carbon content in carbon steels, and specially the alloyants and its quantities in alloyed steels.

The cooling stage is very fast, caused by conduction of the heat deposited on the surface of the workpiece to the rest of the material, in a process called "self-quenching", which results in high cooling rates. Typical values vary between 1000 K/s and 10000 K/s.

5.2.1 Calculation Of Diffusion Controlled Transformations

5.2.1.1 Kinetics Of Austenitization

During the heating stage, when the temperature surpasses A_1 in the Fe-C diagram (Fig. 5.5), the equilibrium fraction of pearlite is cero: $f_p = 0$. The pearlite colonies transform to austenite with a high carbon content during the first stage of austenitization. Between temperatures A_1 and A_3 austenite and ferrite coexist in percentages given by the phase diagram. Above A_3 temperature only austenite can exist, and if the second stage of the austenitization was not completed, the previously untransformed ferrite will become austenite with negligible carbon content.

To model the austenitization, Temperature Time Austenitization (TTA) diagrams (Fig. 5.6) are available for some steels. However they are not available for all the steels and usually include heating rates much lower than those encountered in laser material processing.

To avoid the use of TTA diagrams, a model based on carbon diffusion was developed in this thesis. Several authors [98, 87, 8, 106] use simple 1D diffusion models based on Ashby and Easterling pioneering work [22]. A 2D kinetic model was used by Skavarenina and Shin [94], however 1D models are fast and seem to be in good agreement with experimental results, being therefore better suited for industrial environments than 2D and 3D models.

Haidemenopoulos used two simple 1D models, for simulating the two steps of austenitization [91]. Based on the same idea, the model proposed in this thesis simulates the two steps of the austenitization process with two separate 1D models.

The first model simulates the intragranular diffusion of carbon in pearlite. Given the pearlite interlamellar spacing, the cementite and ferrite lamellae widths (Fig. 5.7) are calculated from the carbon concentrations of pearlite (0.8%), cementite (6.67%) and ferrite (0.005%). The diffusion distance is subdivided in smaller intervals (e.g. 100 intervals) and the carbon concentration calculated for these intervals, considering complete austenitization when the carbon concentration

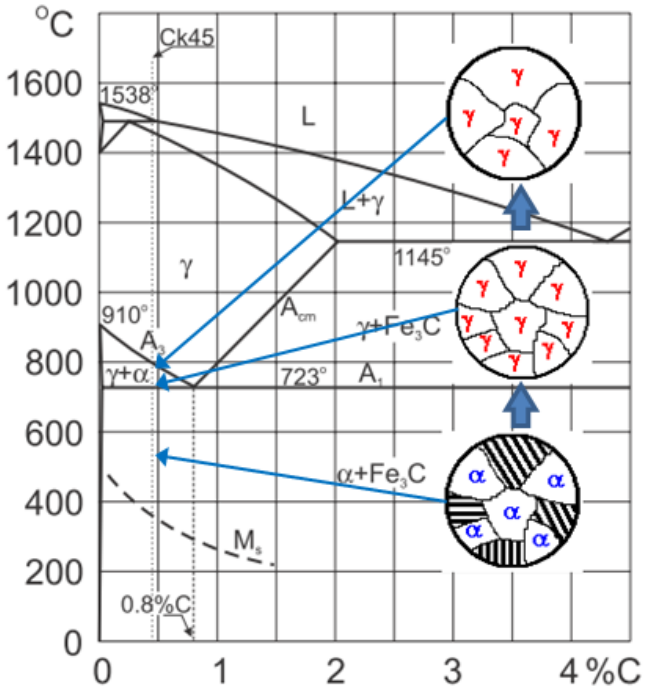

Figure 5.5: Iron-Carbon phase diagram showing the medium carbon steel CK45 and a representation of the different microstructures during austenitization

reaches the 90% of the pearlite carbon concentration in all the intervals.

The second model simulates the intergranular diffusion of carbon within the proeutectoid ferrite grains, during the homogenization of the austenitic structure. Pearlite grain size and carbon content are an input for the model, in order to calculate the diffusion distance between pearlite grains (Fig. 5.8). Afterwards the distance is subdivided in smaller intervals and the carbon concentration calculated for those intervals, considering austenitized the ones with a carbon content above the austenite critical carbon content (0.05%).

Both models are based on the carbon diffusion from a homogeneous phase of width h and an initially constant carbon content C_0, from which carbon diffuses to a region of lower carbon content.

The process is governed by the 1D diffusion equation [255, 256]:

$$\frac{dC(x,t)}{dt} = D(T)\frac{\partial C(x,t)}{\partial x} \tag{5.18}$$

With the previous initial condition, and considering a symmetry boundary condition at the origin and one reflection at the end of the cell ($x = LT$), the following equation results:

$$C(x,t) = \frac{C_0}{2}\left[errf\left(\frac{(h-x)}{2\sqrt{D(T)t}}\right) + errf\left(\frac{(h+x)}{2\sqrt{D(T)t}}\right) + \right. \\ \left. + errf\left(\frac{(h-(2LT-x))}{2\sqrt{D(T)t}}\right) + errf\left(\frac{(h+(2LT-x))}{2\sqrt{D(T)t}}\right)\right] \tag{5.19}$$

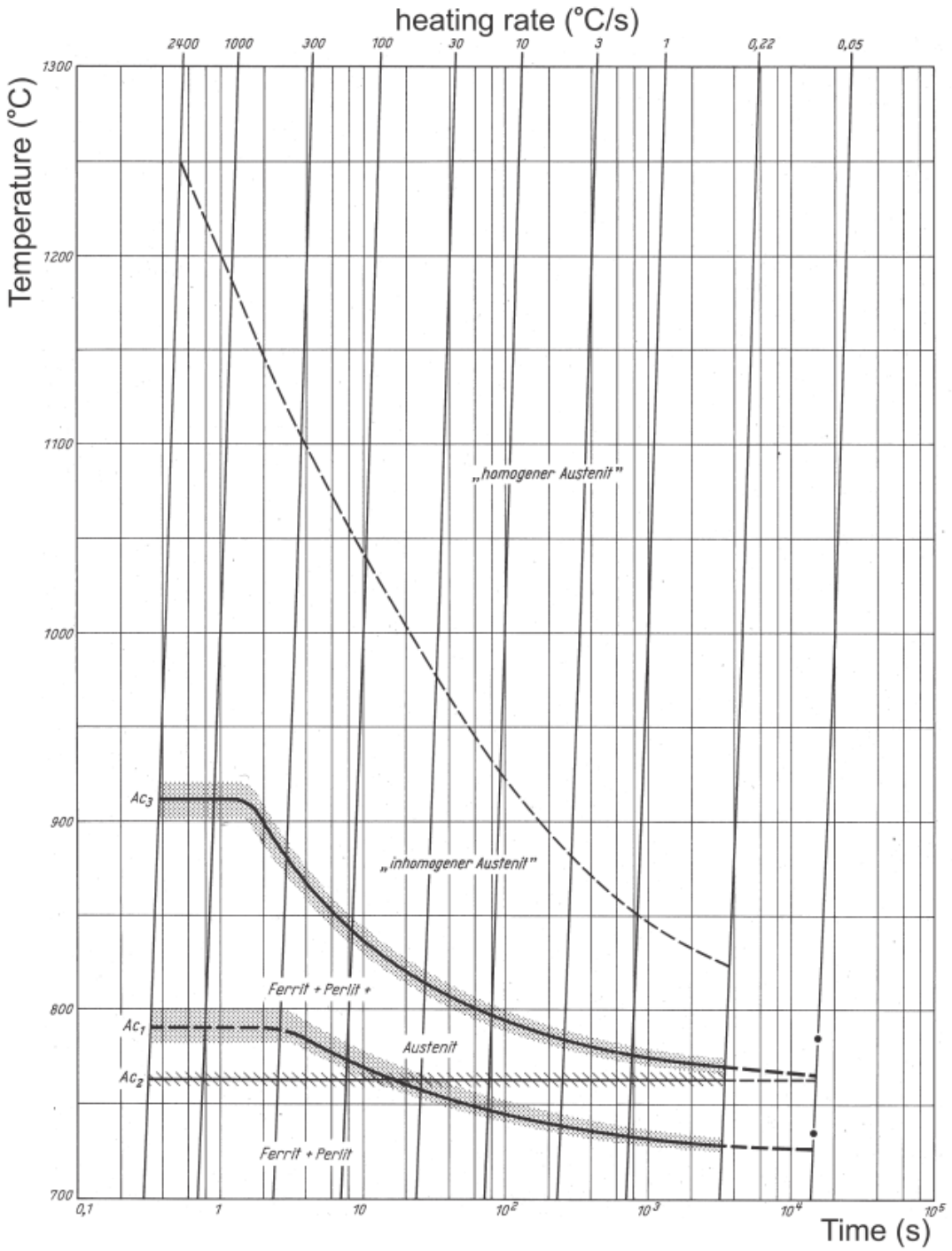

Figure 5.6: TTA diagram for CK45 carbon steel

The diffusion coefficient, which is temperature dependent, is calculated as follows:

$$D(T) = D_0 \, exp\left(-\frac{Q}{RT}\right) \tag{5.20}$$

Where D_0 is the preexponential diffusion coefficient of carbon, Q is the activation energy of carbon diffusion, R $(8.314 J/molK)$ is Boltzmann's constant and T is the absolute temperature.

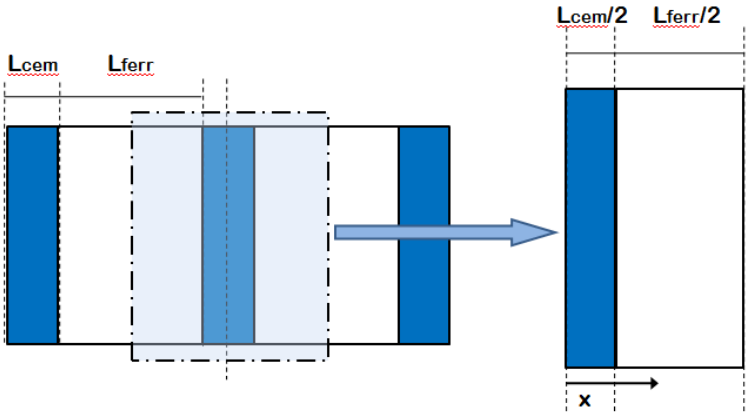

Figure 5.7: Schematic of the geometrical model for the pearlite dissolution

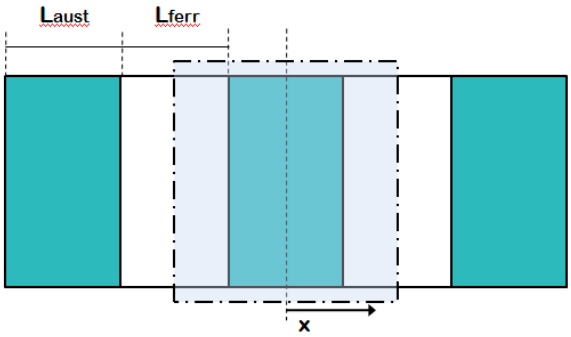

Figure 5.8: Schematic of the geometrical model for the austenitization of proeuctectoid ferrite

The carbon diffusion profiles from 20 μm pearlite grains at a temperature of 1000 K, are represented in Fig. 5.9 for several times. The line at the highest time represents the carbon content of the steel, which is 0.2%.

5.2.1.2 Kinetics Of Diffusive Transformations Of Austenite

During the cooling stage, phase transformations are usually simulated using the information given by the Time-Temperature-Transformation (TTT) diagrams or Continuous-Cooling-Transformation (CCT) diagrams. The procedure for calculating the volume fractions during an arbitrary non-isothermal process for diffusion controlled transformations [257] is to consider the process as composed of many isothermal stages of a small duration (Fig. 5.10).

Each isothermal stage is usually modelled using the Johnson-Mehl-Avrami equation:

$$f = 1 - exp(-bt^n) \tag{5.21}$$

Where f is the volume fraction of the new phase, t is the isothermal time duration, b is a constant dependent on the temperature, composition of parent phase, and grain size, n is also a constant dependent on the type of phase transformation, which ranges from 1 to 4.

The constants b and n at different temperatures can be calculated from the TTT diagrams. Taking the starting and final volume fractions as: $f_s = 0.01$ and $f_f = 0.99$, and using the

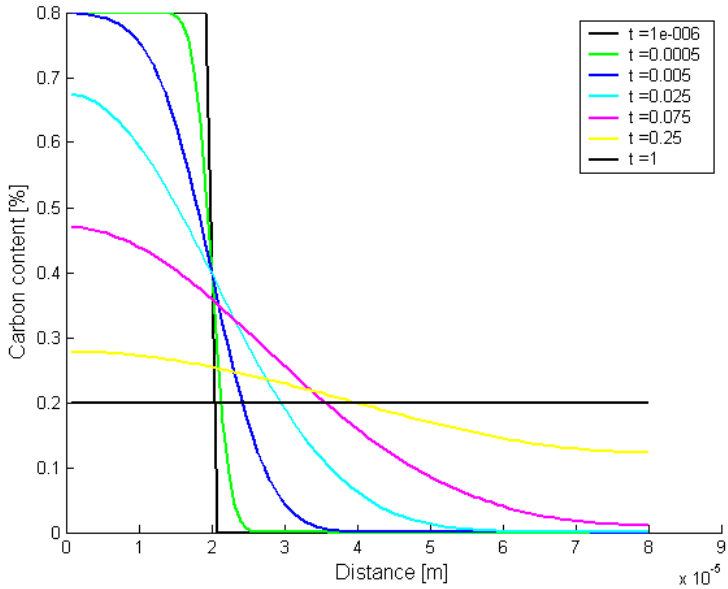

Figure 5.9: Carbon diffusion from homogeneous austenite to ferrite calculated for several times.

following equations [23, 258]:

$$n(T) = \frac{Ln\left(Ln(1-f_s)\right) - Ln\left(Ln(1-f_f)\right)}{Ln(t_s) - Ln(t_f)} \approx \frac{6.1273}{Ln(t_s) - Ln(t_f)} \tag{5.22}$$

$$b(T) = \frac{Ln(1-f_s)}{t_s^{n(T)}} \approx \frac{0.01}{t_s^{n(T)}} \tag{5.23}$$

After the calculation of these parameters for a series of temperatures, the dependence with the temperature can be calculated using a curve fitting algorithm. The effect of the isothermal stages can be added according to Scheil's additivity rule, which allows the calculation of both the time required to attain a certain fraction transformed t_m and the incubation time t_s which is the time period before the transformation starts, in a non-isothermal transformation. The general form of the Scheil's additivity rule can be expressed as:

$$S = \int_0^{\tau} \frac{dt}{t_i^{TTT}} = 1 \; or \; S = \sum_{i=1}^{n} \frac{\Delta t_i}{t_i^{TTT}} = 1 \tag{5.24}$$

Where if τ is t_s, then t_i^{TTT} is the incubation period under a certain isothermal temperature. If τ is t_m then t_i^{TTT} is the time to reach the transformed fraction f_m at the isothermal temperature, which can be obtained using the Avrami equation 5.21. In the incremental form of the additivity rule, Δt_i is the time step. When S equals unity, the incubation time or the desired transformation, is complete.

Scheil's additivity rule can be modified to account for the differences between the incubation time in TTT and CCT diagrams [259], by the introduction of a parameter ϕ_i as follows:

$$\sum \frac{\Delta t_i}{t_{s(i)}^{TTT}} \frac{1}{\phi_i} = 1 \tag{5.25}$$

Where:

$$\phi_i = \int_0^{t_{s(i)}^{TTT}} \frac{dt}{t_s^{TTT}} \tag{5.26}$$

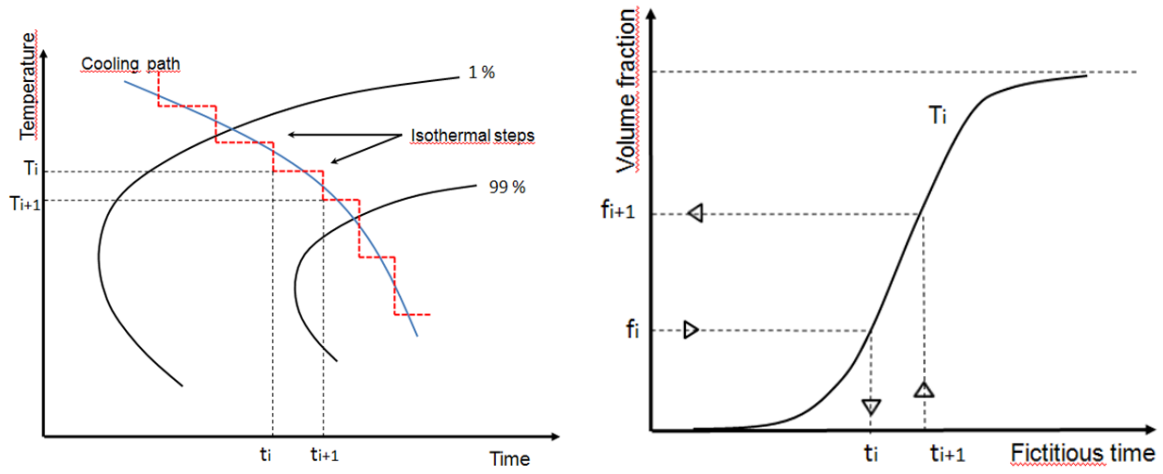

(a) (b)

Figure 5.10: Calculation of anisothermal growth kinetics by using Scheil's additivity principle and JMA equation *(from [23])*.

After the calculation of the incubation time, the growth kinetics can be calculated. For the implementation of these equations into a calculation method, it is common [257] the use of the fictitious time and fictitious transformed volume fraction for a time step Δt:

$$t_i^* = \left(\frac{-Ln(1-f_{i-1})}{b_i}\right)^{\frac{1}{n_i}} \tag{5.27}$$

$$f_i^* = 1 - exp(b_i(t_i^* + \Delta t)^{n_i}) \tag{5.28}$$

The fictitious time represents the time required for the formation of the volume fraction f_{i-1} at the temperature T_i, considering an isothermal transformation. Then, the transformed fraction is corrected to take into account the amount of austenite available for the transformation, and reactions that do not reach full completion:

$$f_i = f_i^* f_{max}^{\gamma} f_{max} \tag{5.29}$$

Where f_{max}^{γ} is the maximum austenite fraction at the start of the transformation, and f_{max} is the maximum possible transformed fraction for this type of transformation. In order to account for the incubation period t_s the Avrami equation and its coefficients need to be modified [260]:

$$f = 1 - exp(-b(t-t_s)^n) \tag{5.30}$$

$$n(T) = \frac{Ln\left(Ln(1-f_1) - Ln(1-f_2)\right)}{Ln(t_1 - t_s) - Ln(t_2 - t_s)} \tag{5.31}$$

$$b(T) = \frac{Ln(1-f_1)}{(t_1 - t_s)^{n(T)}} \tag{5.32}$$

5.2.1.3 Tempering Model

The previously formed martensite undergoes a heating process during the next laser passing, which causes its tempering. Martensite is a metastable structure produced by the insufficient time for carbon to diffuse in the iron lattice during the cooling down. The increased temperatures during the tempering speed up the diffusion process, decomposing the martensite into a stable microstructure composed mainly by ferrite with fine carbides dispersed within. This microstructure offers excellent mechanical properties, showing good strength, toughness and higher hardness than a ferritic-pearlitic microstructure. However the lower resultant hardness compared to a fully martensitic microstructure is the main disadvantage in hardening processes.

The tempering starts at temperatures as low as 100°C and continues till the A_1 temperature (727°C). At low temperatures, between 100°C and 200°C a finely dispersion of ε carbide and transition metal carbides is formed [261]. At temperatures between 200°C and 300°C takes place the transformation of retained austenite into ferrite and cementite. At higher temperatures the martensite looses its tetragonality and the cementite precipitates. The carbides coarsen in this range of temperatures softening the microstructure.

However, in high alloyed steels there are some differences. The retained austenite volume fraction is higher in these steels, and it is much more stable (several temperings are requiered for some tool steels). Also for steels containing refractory elements such as tungsten, vanadium, molibdenum and chromium, in the range of temperatures above 500°C these elements are able to diffuse and precipitate as a finely dispersion of carbides, generating the secondary hardness peak.

The volume fraction of martensite transformed during laser back-tempering will be modeled like in conventional tempering processes [262, 103] using the Johson-Mehl-Avrami equation, as it was previously done by Lakhkar et al. [10]:

$$f_{TM} = f_M \left(1 - exp\left(-kt\right)^n\right) \tag{5.33}$$

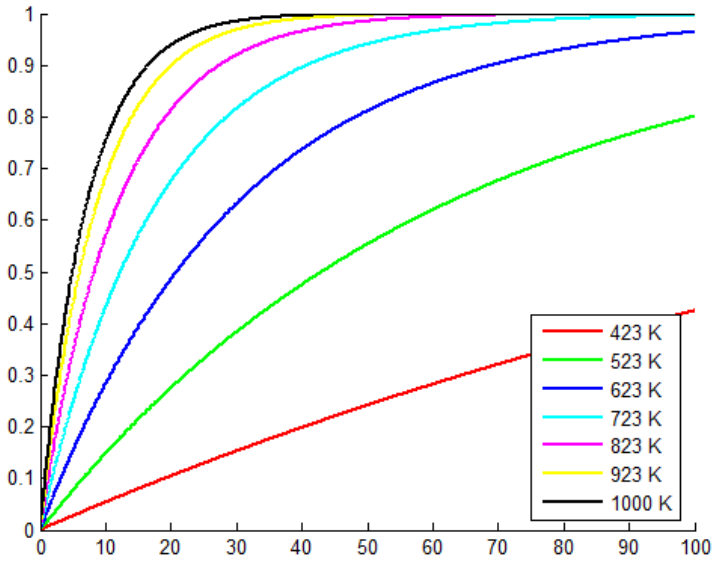

Figure 5.11: Tempered martensite volume fraction calculated for several temperatures and times.

Where:

$$k = k_0 exp\left(-\frac{Q}{RT}\right) \tag{5.34}$$

being f_M the maximum fraction of martensite reached, Q the activation energy and n and k_0 experimentally derived constants.

The equation is valid for isothermal processes, therefore the anisothermal process is subdivided into isothermal steps, and the effect of each step is added according to the Scheil's additivity rule, as seen before. The tempered martensite volume fraction predicted by the model for several temperatures is represented in Fig. 5.11.

5.2.2 Calculation Of Martensitic Transformation

The martensitic transformation is independent of the cooling rate, depending only on the temperature. The Koistinen-Marburger equation describes the evolution of the transformed volume fraction of martensite f_M:

$$f_M = 1 - exp(-\alpha(M_s - T)) \tag{5.35}$$

Where M_s is the martensite start temperature, T is the temperature and α is a constant dependent on the transformation rate and the steel composition. Usually, for steels with carbon content lower than 1.1 % $\alpha = 0.011$ [23]. For low carbon and low alloy steels, there are some modifications to the Koistinen-Marburger equation proposed to take into account the effect of carbon diffusion [263].

The M_s temperature for carbon steels and some alloyed steels can be obtained by the following empirical equations [264]:

$$M_s(^\circ C) = 520 - 320C$$

$$M_s(^\circ C) = 512 - 453C - 16.9Ni + 15Cr - 9.5Mo + 217C^2 - 71.5CMn - 67.6CCr \tag{5.36}$$

The hardness of the final microstructure is commonly calculated by means of a linear combination of the hardness of each phase, called the rule of mixtures:

$$H = \sum_{i}^{k} f_i H_i \tag{5.37}$$

Where k is the number of phases present in the final microstructure, f_i is the volume fraction of phase i, and H_i its hardness.

Chapter 6

Model For Laser Transformation Hardening

The usual approach of science of constructing a mathematical model cannot answer the questions of why there should be a universe for the model to describe. Why does the universe go to all the bother of existing?

Stephen Hawking.

Abstract: The FEM models developed for Laser Transformation Hardening (LTH) are explained in this chapter. Notes on convergence and material properties are included. At the end of the chapter, thermal stresses developed during LTH and similar processes are discussed, as well as the effect of phase transformations.

6.1 Introduction

For the modelling of LTH with ANSYS several macros and input files were developed. The whole set of files consists of:

- Input files with:
  - The meshing algorithm
  - The thermal analysis
  - The mechanical analysis
- Macros, consisting of:
  - The laser irradiance function generator and the laser path generator
  - The heating and cooling stages of the thermal and mechanical analyses
  - The phase transformation model
  - Macros for capturing images and postprocessing results
- Material properties

The macros and input files were coded in the own ANSYS programming language, APDL (*Advance Programming Design Language*). The input files contain the parameters defining the analyses and the callings to the macros, which are designed for carrying out specific functions. All the files are organized into a set of folders: *Input*, *Macros*, *Materials*, *Simulations* and *Images*. The last folder contains the images captured during the analysis, which are useful to monitor the results of the ongoing simulation and generate high quality videos. The *Simulations* folder stores the simulation databases, solution files and results.

The model is designed to simulate the thermo-mechano-metallurgical phenomena of laser surface heat treatments. It is not limited only to LTH, laser bending and laser surfaceremelting, both with or without phase transformations, can be easily simulated. Laser spot welding or laser conduction welding can be simulated as well, however to fully describe processes in which large volumes of melted material are generated, a fluid dynamics simulation (CFD) including convection processes in the melted pool by buoyancy and thermocapillary will be more accurate.

6.2 Geometry And Meshing

ANSYS has a wide set of tools for geometry creation and mesh generation, as well as importing/exporting capabilities from other programs. However the most common geometry used in experimental tests is the metal plate or sheet. Therefore a versatile algorithm for the fast and easy creation of plate geometries with adapted structured hexahedral meshes given a set of predefined input parameters, helps and eases the simulation process.

Hexahedral meshes are preferred over tetrahedral meshes due to their advantageous numerical properties. They are better in terms of numerical convergence of the solution and they can calculate results with the same accuracy of a tetrahedral mesh using a lower number of elements. Their behavior in mechanical analyses, especially when plasticity is important, is usually better. However, the behavior of quadratic tetrahedrons is surprisingly fine, constituting a serious option for this kind of simulations.

The geometry and meshing input file allows the creation of plates with or without planar

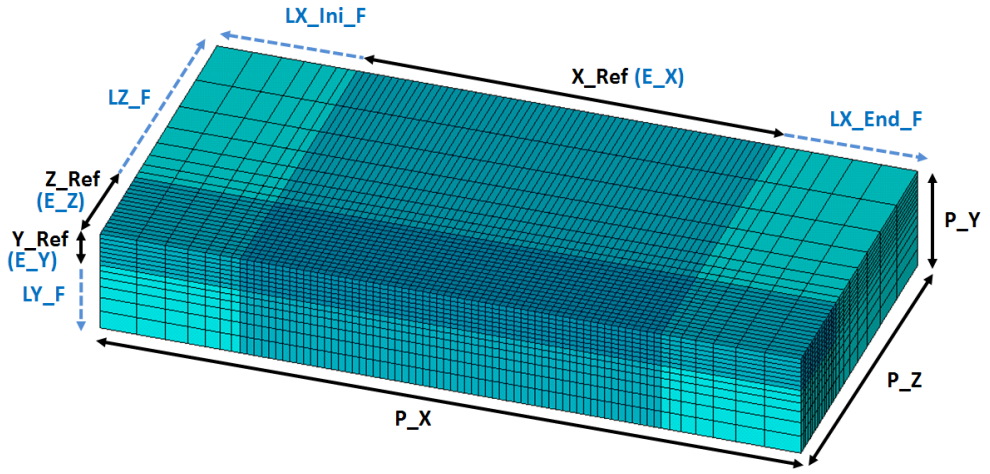

Figure 6.1: Mesh with planar symmetry, showing the input parameters for its generation

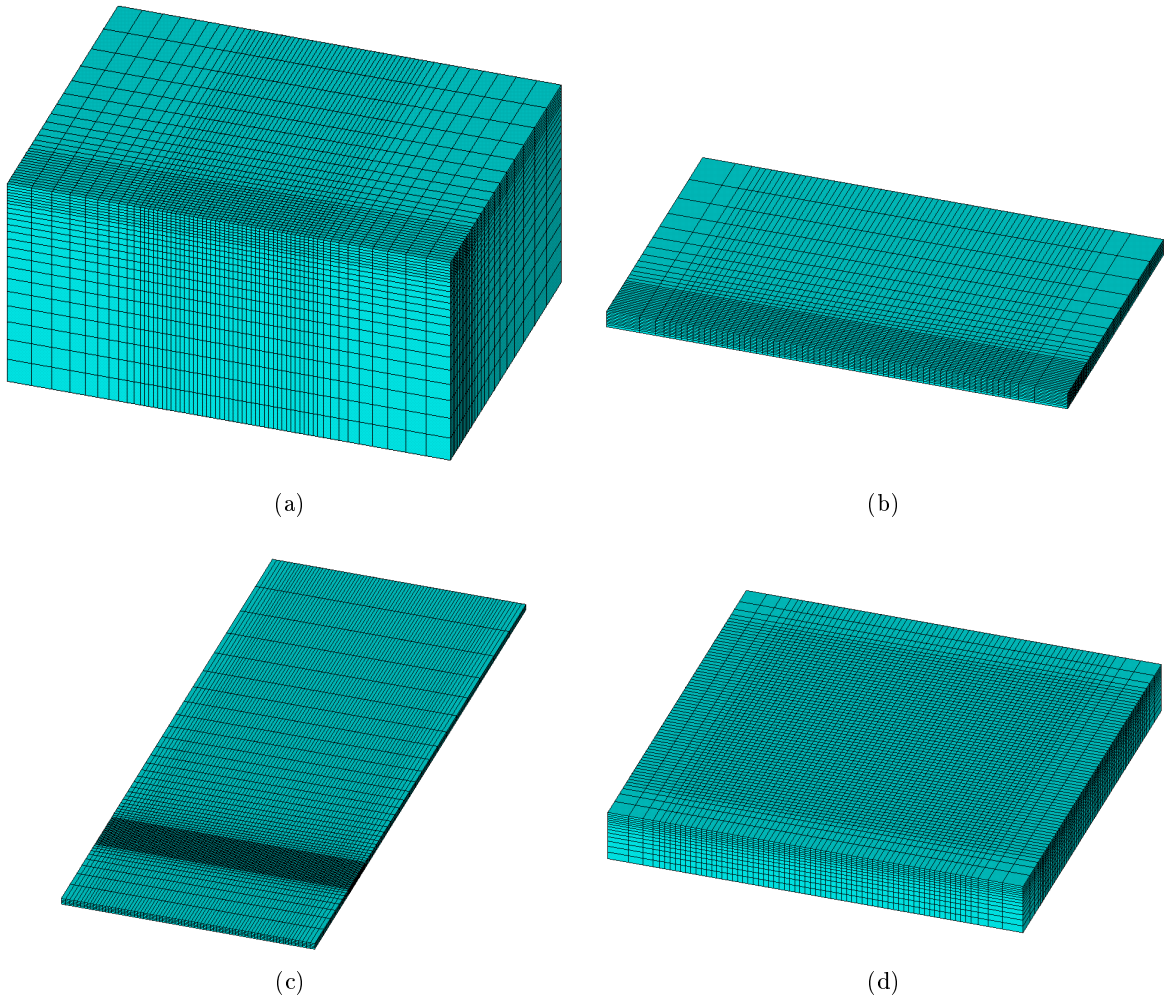

Figure 6.2: Different meshes for LTH with (a,b) and without (c,d) planar symmetry

symmetry along the laser path. The input geometrical parameters for the mesh generation with planar symmetry are represented in black in Fig. 6.1, and consist of the dimensions of the plate: *P_X, P_Y, P_Z*, and the dimensions of the refined area: *X_Ref, Y_Ref, Z_Ref*.

The input parameters for the mesh generation are represented in blue in Fig. 6.1, and comprise the element dimensions in the refined zone: *E_X, E_Y, E_Z*, and the ratio between the first element of a non-refined line, and the last one: *LY_F, LZ_F, LX_Ini_F, LX_End_F*. With these parameters the number of elements of each different volume are calculated, increasing the element size in the non-refined zones following a geometric progression based on the element size of the refined zones and the ratios between the elements of the different lines. In Fig. 6.2 are represented meshes generated with the algorithm using different plate dimensions and parameters, with and without planar symmetry.

The nodes belonging to the exterior areas of the model are named with the aim of selecting them during the simulation and the application of loads and boundary conditions, as shown in Fig. 6.3. The nodes of the top area of the plate have the laser irradiance applied, and are named *N_Laser*. The nodes of the symmetry plane are named *N_P_Sym*. All the nodes of the areas experiencing convection heat transfer with the surrounding air are grouped withing the

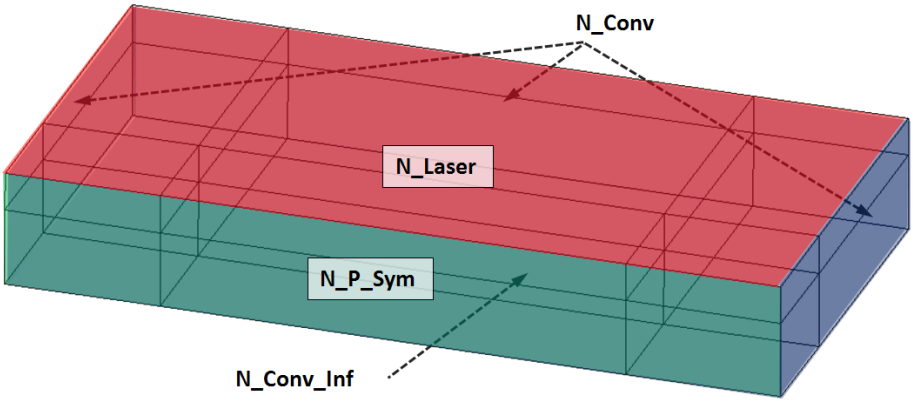

Figure 6.3: Naming conventions for the different areas of the plate

component *N_ Conv*, with exception of the nodes of the area located at the bottom of the plate *N_ Conv_ Inf*, in order to apply a higher convection coefficient to simulate heat transfer with a possible supporting plate, if desired. More complex geometries can be modeled and simulated as long as these naming conventions are maintained.

The reason to apply the loads directly to the nodes instead of applying them to the areas, and letting the program transfer them to the elements and thereafter to the nodes, is to avoid certain convergence problems related with convection. Elements that have the same temperature as the ambient air sometimes pose difficulties during solution, which results in an unphysical cooling down below the ambient air temperature. In order to avoid this problem, a nodal based loading scheme was adopted. The nodes of the previous components that have a temperature higher than the ambient air temperature, are selected to apply convection over them. The rest of the nodes, which were not heated yet, do not need to have convection applied. Additionally the nodes located at the top of the plate are subjected to the laser irradiance, applied as a heat flux boundary condition. In order to apply convection to the nodes that were heated but are not receiving laser power, it is necessary to select them based on their heat applied flux. If it is zero, they will suffer convection cooling.

6.3 Laser Irradiance

The laser irradiance is the only load during the LTH simulation. The macro developed simulates three laser modes: TEM 00 (Gaussian), TEM 01* (annular) and Top Hat (uniform). In Fig. 6.4 are represented these modes and cross sections of their irradiance profiles. The mathematical equations, given in polar coordinates, are:

$$TEM_{00} : I = \frac{2P}{\pi\omega^2} exp\left(-\frac{2r^2}{\omega^2}\right) \tag{6.1}$$

$$TEM_{01^*} : I = \frac{4Pr^2}{\pi\omega^4} exp\left(-\frac{2r^2}{\omega^2}\right) \tag{6.2}$$

$$Top\ Hat : I = \frac{P}{\pi\omega^2} \tag{6.3}$$

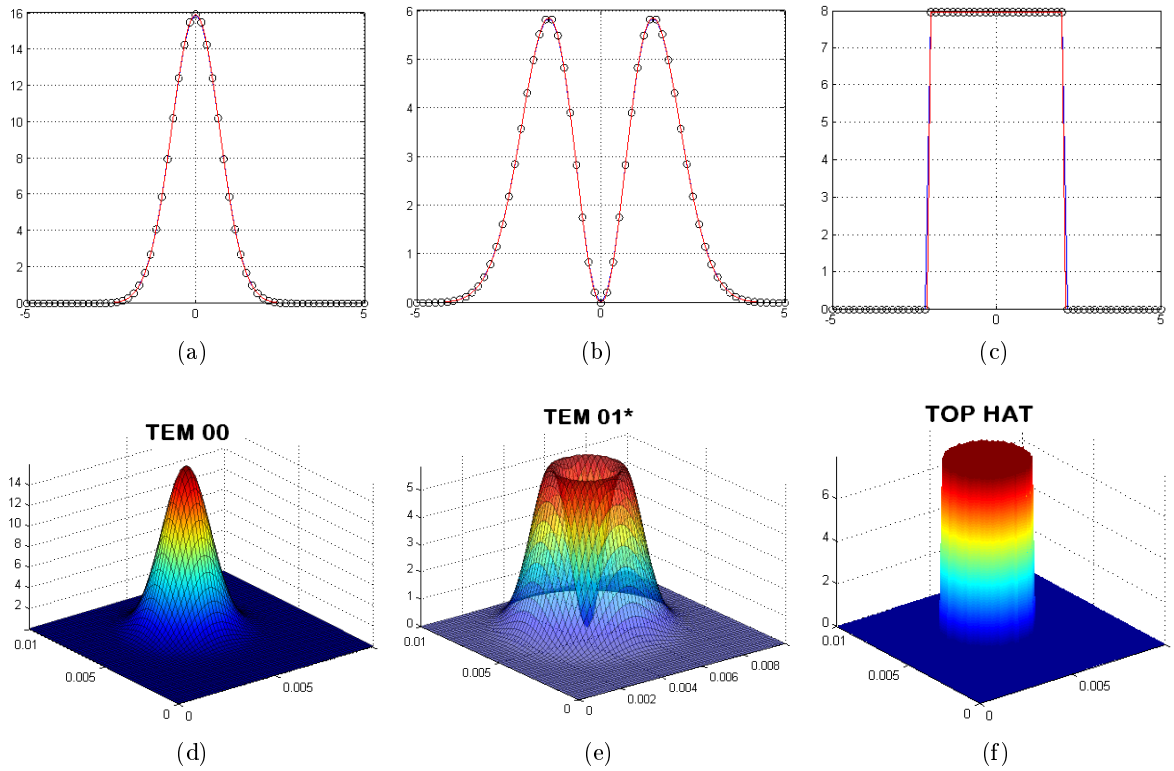

(a) (b) (c)

(d) (e) (f)

Figure 6.4: Different laser modes: (a,d) TEM00 (Gaussian); (b,e) TEM01* (Annular); (c,f) Uniform (Top Hat)

Where P is the laser power and ω is the radius at which the irradiance drops to $1/e^2$ of the maximum value for the TEM modes, and the radius of the laser beam for the Top Hat mode.

The laser power is partially absorbed by the material through its absorption coefficient, which is temperature dependent. In order to include this coefficient and its dependency with the temperature, a table array is defined with the values of the absorptivity at different temperatures. A table array is a special kind of array in ANSYS. A one dimensional table array will have the x points of a function at the axis of the table and the y corresponding values in a vector. The concept of the table array is like a linear spline: there is linear interpolation between the points located between the x points of the table, while maintaining constant the values for variables outside the lowest or highest limits of the table to the lowest or highest values respectively, as it is represented in Fig. 6.5a. The concept of table array can be extended to higher dimensions.

The laser macro generates a 3D Table, which is composed by several 2D planes, each of them containing the values of the laser irradiance under the selected laser mode, multiplied by the absorption coefficient for the temperature index of the plane (Fig. 6.5b). Therefore the values are interpolated through the X, Z, T variables when applied to the nodes, being X and Z the axis parallel to the top surface of the plate and T the temperature of each node with laser irradiance applied.

The table generated corresponds to the current load step, being centered at the X and Z coordinates given by another macro which contains the laser path function. This macro is called from the laser heating macro, with the current load step number, and generates the coordinates

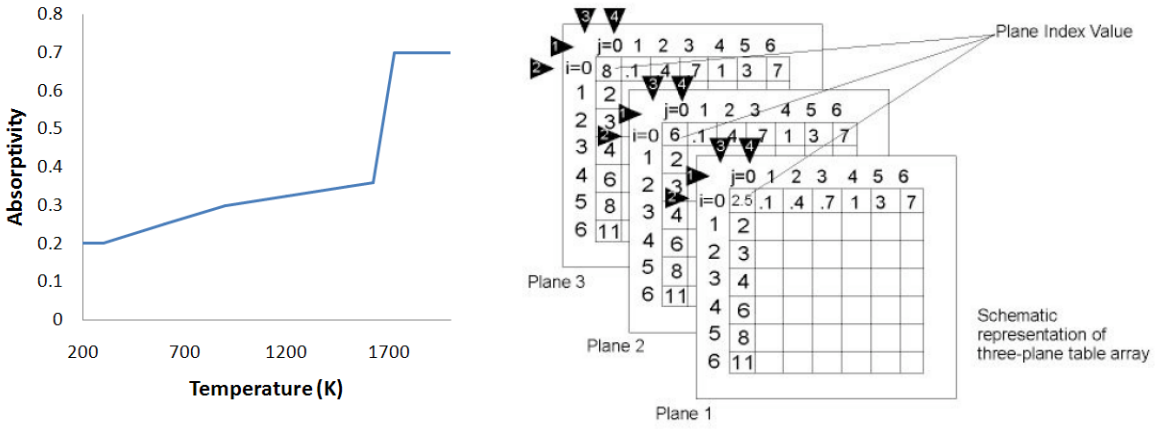

(a) (b)

Figure 6.5: (a) Representation of a temperature dependent absorptivity in an ANSYS Table; (b) scheme of a 3D ANSYS Table

of the laser position for the calculation of the laser irradiance by the laser macro. Complex trajectories can be implemented (e.g. Fig. 6.6).

6.4 Laser Heating And Cooling Stages

The macro in charge of the laser heating stage *LH_Heat* is called directly from the input thermal analysis file. This file contains all the required parameters for the simulation, including: convection coefficients, ambient air temperature, initial temperature of the workpiece, absorptivity, laser parameters, material parameters, equation solvers, etc.

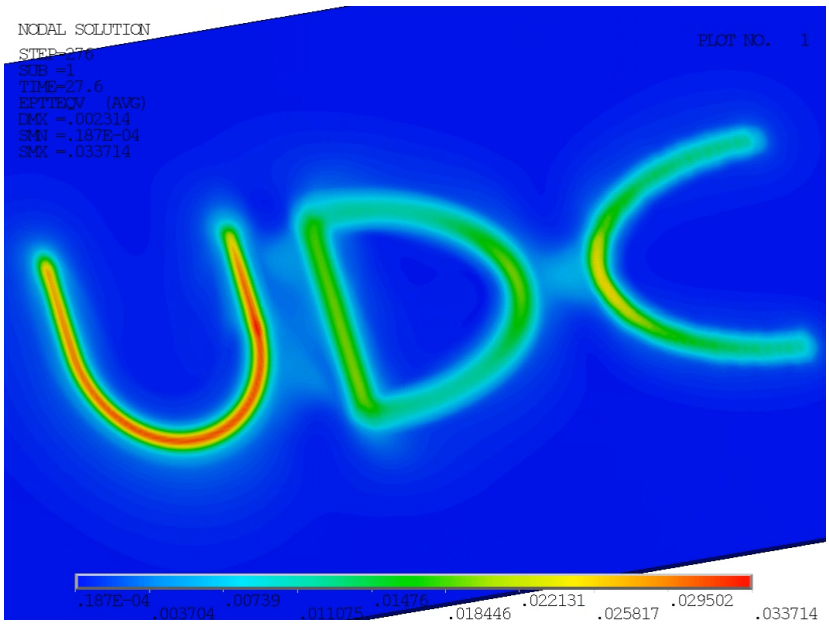

Figure 6.6: Residual plastic strains during a simulation of LTH with complex trajectories

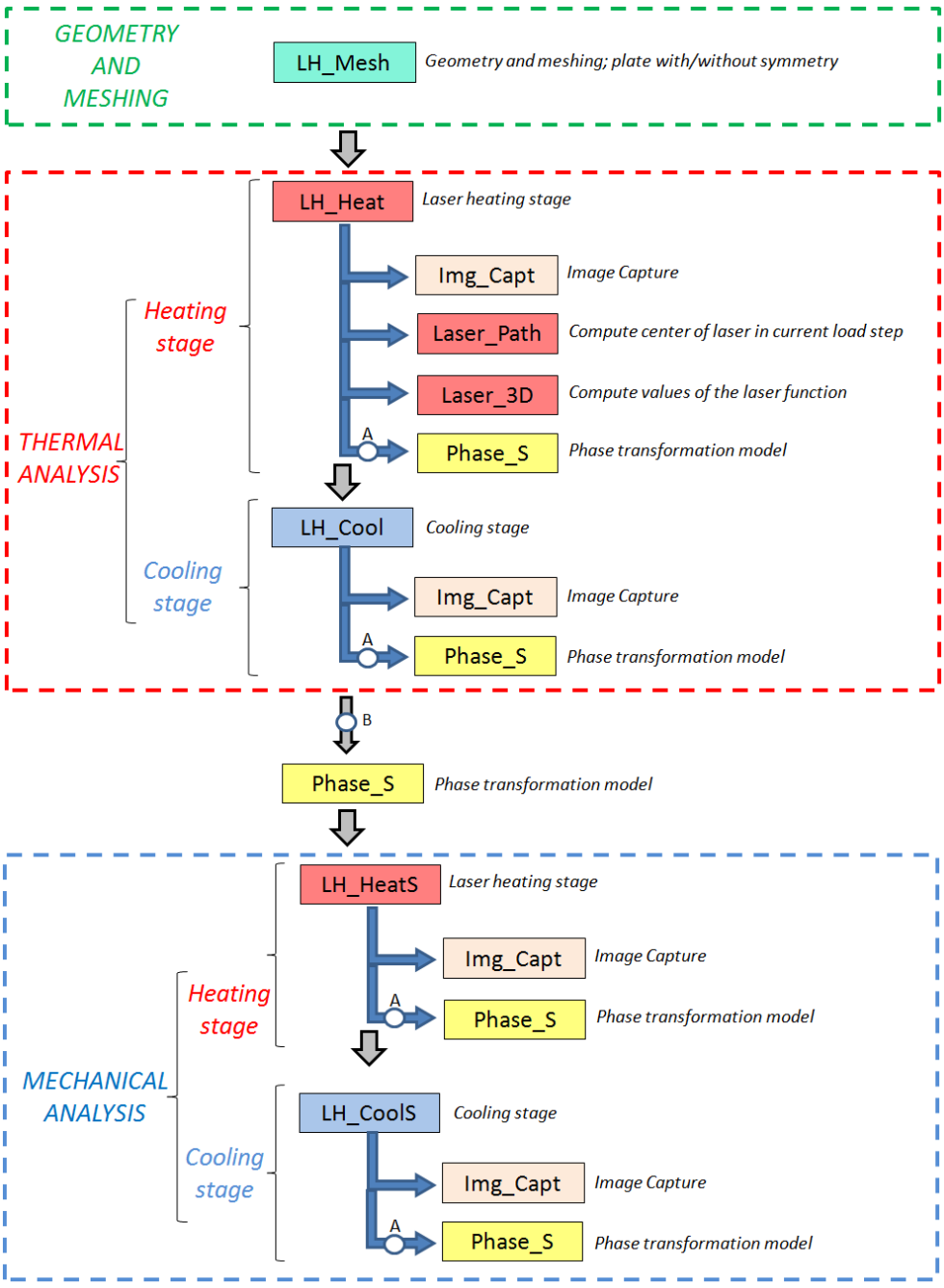

Figure 6.7: Scheme of the macros used for the LTH simulations. Phase transformation model can be used in each load step (A) or after the thermal simulation (B).

The laser heating macro can be controlled by time steps or load steps (for complex trajectories), and can be called as many times as laser passings are needed. During the first load step of the analysis, the macro defines a transient thermal analysis using some algorithms for the nonlinear solution: full Newton-Raphson, DOF Predictor, Line Search and automatic time stepping. Also the equation solver is selected, which by default is recommended the Incomplete Cholesky Conjugate Gradient (ICCG) as it proved to be the fastest solver for this kind of analysis in several tests performed (Fig. 4.3a). Afterwards, the laser path macro is called and the laser irradiance calculated and applied to the model; then, the current load step is solved.

The following time steps commence postprocessing the results of the previous one. The nodes of the components N_Conv and N_Conv_Inf that have a temperature higher than the ambient temperature, are selected, and convection is applied over them. The nodes of the component N_Laser with a laser heat flux applied zero or close to zero, are selected too in order to apply convection to them.

The elements with a temperature higher than the melting temperature of the material are selected and stored in individual components in each load step of the analysis, as they will be required during the mechanical simulation. Finally, there is the possibility of capturing contour images of the temperatures of the plate, to monitor the analysis as it progresses during the simulation, and/or make a high quality video using these images after the analysis finishes.

After the postprocessing, if the phase transformation model was selected, the analysis calls the corresponding macro before entering in the solution process again.

The cooling stage is simulated by the macro LH_Cool, which selects the nodes of all the surfaces of the plate heated above the ambient air temperature, and applies convection over them. During this stage the load steps are increased following a geometric progression in order to efficiently simulate the exponentially decaying cooling down with a low number of load steps.

The set of macros is represented in Fig. 6.7. Phase transformations can be included in the simulation in two ways: in each load step using staggered procedure (A), or after the complete thermal analysis (B). This will be explained with more detail in the next section.

6.5 Phase Transformations

The phase transformations for steels were described in Chapter 5. This section of the present chapter is dedicated to the numerical implementation of the equations presented before for the calculation of phase transformations.

In the next section the adaptability of the code to model other phase transformations will be discussed and demonstrated with titanium alloys.

The model of phase transformations consists of a set of macros fully coupled with the thermal analysis, allowing the calculation of the phase transformations during the ongoing transient simulation. Each load step is solved using a staggered solution procedure commenced by a pure thermal analysis and the subsequent metallurgical analysis. It is not a postprocessing code as other phase transformation models, and therefore allows the change of material properties during the analysis, a feature that at present was not necessary to use but it is ready to be used in the thermal simulations if required.

However, a sequentially coupled procedure is also possible, running the model after a thermal analysis finished and before the mechanical one. The phase percentages corresponding to each load step are stored in files for the subsequent postprocessing and the change of material properties during the mechanical analysis.

The model is oriented to an element-wise description of the metallurgy of the materials, considering the microstructure discretized as a set of elements of different homogeneous composition, according to the previous thermal history of the process. This method allows

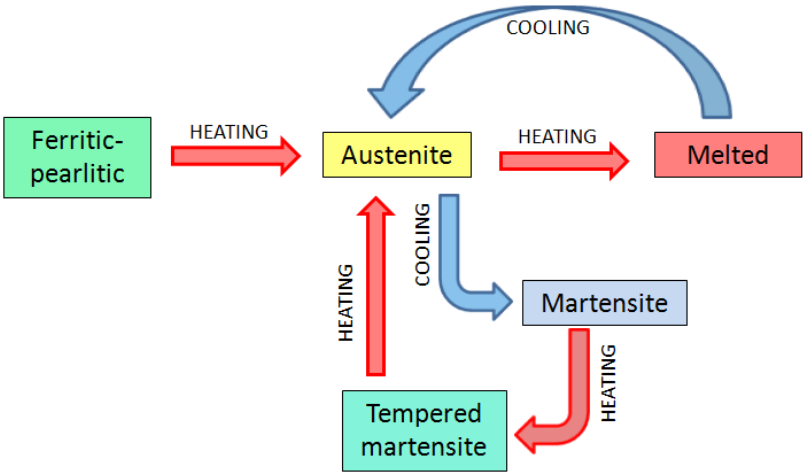

Figure 6.8: Scheme showing the phase transformations in steels and their relationships

to easily change the material properties of each element during the simulation and describe gradients of phases throughout linear interpolation between elements.

It consists of a main subroutine *Phase_S* that controls the transition between the different regions of stability of the different phases, according to the temperature range of each region and the element temperature. Within these regions specific macros containing the kinetic models are called from the main subroutine for computing the phase evolution.

The history of several phase changes is calculated and recorded during the whole transient analysis. In order to do that, each of the elements of the model has assigned a vector in which all the required information is stored: temperatures, residence times within the current phase region, phase percentages, auxiliary variables for the kinetic models and a variable that defines the current state of the element. All these vectors are stored in a matrix in which each row corresponds to one element of the model. All of the subroutines are fully vectorized code, and therefore the whole phase transformation model is computed very fast.

6.5.1 Phase Transformation Model For Steels

The phase transformations in steels and their relationships, are schematized in Fig. 6.8. The model was designed upon the previous scheme. The element vector containing the information required for the phase transformation model of steels is represented in Fig. 6.9. The matrix which contains the vectors is defined during the first step of the analysis and is updated during each load step.

According to the temperature ranges and temporal histories of the phase transformations, the first one to occur is the austenitization, followed by the melting if the temperature goes beyond the melting temperature. During the cooling down only the martensitic transformation is considered due to the high cooling rates of LTH. If the material is subsequently reheated again by another laser passing, then the tempering of the previously formed martensite is simulated, as well as a possible reaustenitization and melting. The set of macros called by the phase transformation macro are represented in Fig. 6.10.

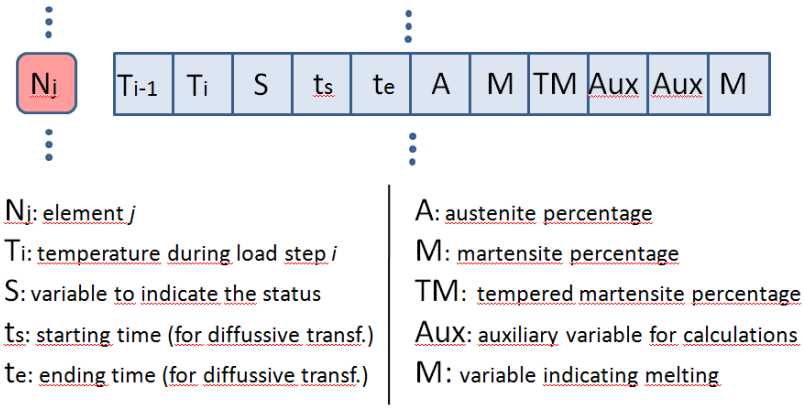

Figure 6.9: Vector for each element containing the information required for the calculation of the phase transformations for steels.

6.5.1.1 Austenitization

The two step process of austenitization of a hipoeutectoid steel is simulated with several macros. The one that controls the process is the *Aust* macro, which calls the rest of the macros and computes the phase percentages.

The first stage intragranular diffusion is partially carried out with the macro $1StCDif$. This macro is used only once. It creates a table array with isothermal diffusion times calculated for the current steel at a range of temperatures between A_1 and melting.

The material data needed as input for the macro are the pearlite lamellar spacing, the carbon content of the steel simulated and its A_1, A_3 and melting temperatures. Additionally the carbon content of ferrite, cementite and pearlite, which are taken as 0.005%, 6.67% and 0.8% from

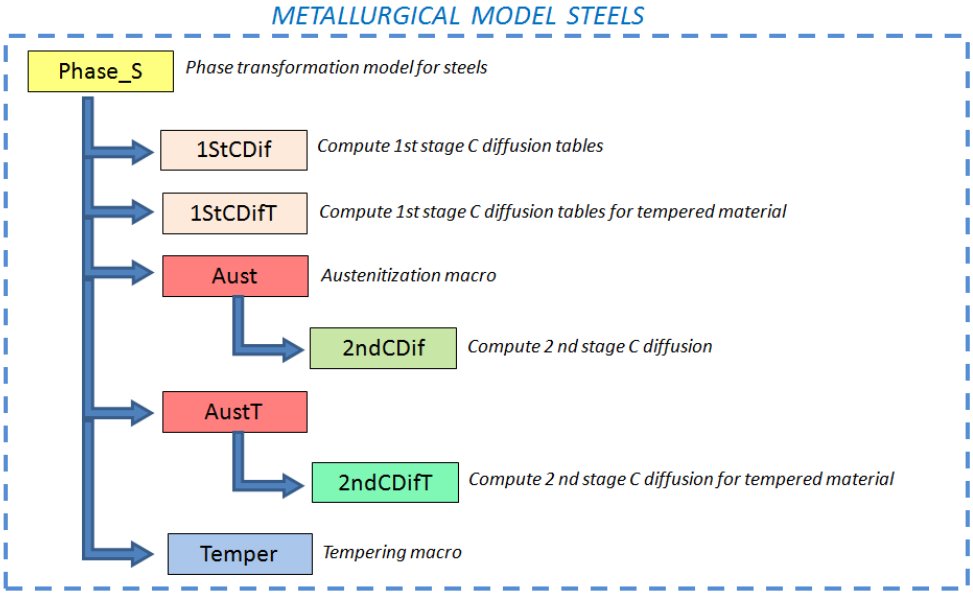

Figure 6.10: Scheme of the macros called by the phase transformation macro for steels.

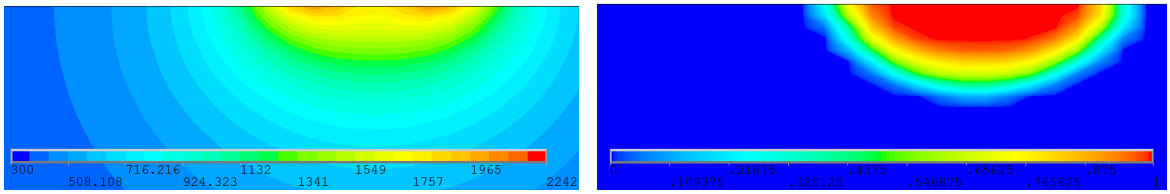

(a) (b)

Figure 6.11: (a) Temperature map in the cross section of a plate during a LTH simulation; (b) corresponding austenite volume fraction.

literature. The diffusion process is simulated with eq. (5.19), taking the preexponential diffusion coefficients of carbon in austenite and ferrite from [10] as $1 \cdot 10^{-5}\ m^2/s$ and $5 \cdot 10^{-5}\ m^2/s$ respectively.

The cementite and ferrite lamellae widths are calculated from the carbon concentrations of pearlite, cementite and ferrite, and the interlamellar spacing. The diffusion distance is considered as half of the pearlite interlamellar spacing. This distance is subdivided into smaller intervals (e.g. 100) in which the evolving carbon concentration is calculated during increasing times at an isothermal temperature. The austenitization is considered complete when the carbon concentration reaches the 90% of the pearlite carbon concentration in all intervals, and the time required for that is stored in the previously mentioned table array. This macro is not needed again.

The first stage is simulated in a simplified and very fast manner. The anisothermal process is considered as composed of several isothermal steps, each of them increases the transformation percentage until the stage is completed. During the simulation, in each load step, the temperature of each element within the austenite stability zone and the time spent at that temperature (which is at most the length of the time step) are stored. Then this time is compared with the required time for a complete first stage austenitization at that temperature, which is stored in the table array created by the macro $1StCDif$. If the transformation is not completed, the percentage of completion is computed and the transformation continues in the next time steps. The starting time of the transformation, which is when the temperature of the element surpasses the A_1 temperature, is calculated through linear interpolation between the times and temperatures of the current and previous load steps. The ending time is calculated in a similar manner.

The maximum volume fraction of austenite between the temperatures A_1 and A_3 is given by the iron-carbon phase diagram. This fraction is extracted from the diagram at several temperatures and stored in another table array, in order to limit the maximum volume fraction of austenite of the elements between both temperatures.

The second stage of the austenitization process is partially carried out by the $2ndCDiff$ macro. The additional parameters required for this macro are the pearlite grain size and the critical carbon content for austenite formation, which is commonly assumed as 0.05%.

The methodology is analog to the previously explained. The macro uses the temperature of the current time step to compute the diffusion coefficient, and then with the time spent at that temperature, the austenite percentage during the current time step of the analysis is increased, using the same equation mentioned before, and the temperatures and times of previous time steps,

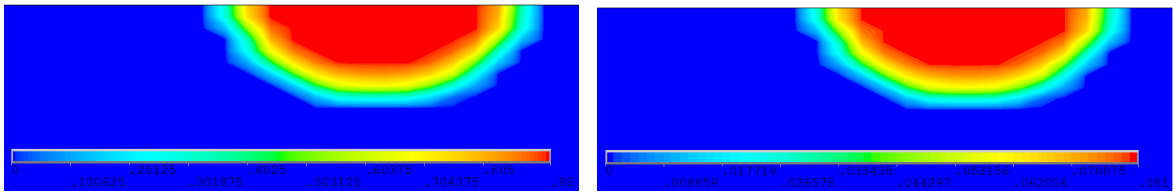

(a) (b)

Figure 6.12: (a) Martensite volume fraction in the cross section of a plate during a LTH simulation; (b) corresponding retained austenite volume fraction.

which are stored in auxiliary positions within the element vector to compute the austenitization in the next time steps. An example of the temperature profile during a LTH simulation and the corresponding austenite volume fraction is shown in Fig. 6.11.

6.5.1.2 Martensitic Transformation

The martensitic transformation is simulated using the Koistinen-Marburger equation 5.35 implemented directly in the main macro. This transformation depends only on the subcooling below the M_S temperature of the simulated steel, therefore no permanence times have to be calculated. The maximum volume fraction of martensite that can be transformed during the analysis is equal to the maximum previous volume fraction of austenite reached for each element. However, not all the austenite is transformed. Usually a small amount remains untransformed as retained austenite. The maximum percentage of retained austenite must be specified for the current steel. The volume fraction of martensite produced in an LTH simulation and the corresponding retained austenite are shown in Fig. 6.12.

6.5.1.3 Tempering

During tempering the metastable martensitic structure experiences a stabilization process due to the effect of time and temperatures below the A_1 point. The process is simulated using a JMA style equation (5.33) (5.34), dividing the anisothermal process into a set of isothermal steps.

The prior microstructure during tempering can be composed of martensite, retained austenite and even initial ferrite-pearlite grains that were not completely austenitized. Only the martensite suffers transformations during this process, decomposing into carbides and ferrite. When the elements containing martensite are heated at a temperature above 100°C the macro *Temper* simulates the tempering process on them. An example of the tempered martensite volume

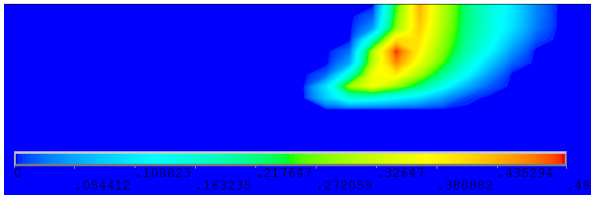

Figure 6.13: (Tempered martensite volume fraction in the cross section of a plate during a LTH simulation.

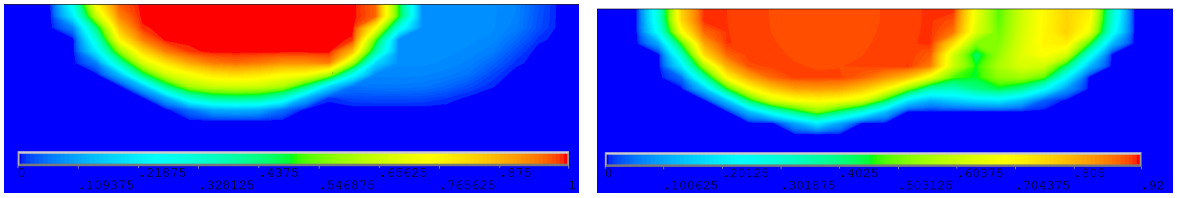

(a) (b)

Figure 6.14: (a) Austenite volume fraction in the cross section of a plate during a LTH simulation; (b) martensite volume fraction at the end of the simulation.

fraction transformed during an LTH simulation is shown in Fig. 6.13, and the martensite volume fraction in Fig. 6.14b.

6.5.1.4 Re-austenitization After Tempering

If the tempered microstructure is heated above the A_1 temperature, the whole microstructure starts to transform into austenite again. The macro $AustT$ controls this process. The unstransformed percentage of base ferritic-pearlitic microstructure, in case it exists, follows the austenitization process explained before. The untempered martensite is considered to transform instantly to austenite. The previously tempered martensite follows again a two step austenitization process: intragranular diffusion and intergranular diffusion.

Tempered martensite grains are assumed to have a certain carbon concentration, with dispersed carbides in a ferritic matrix. Therefore, a first stage is simulated in which the carbides dissolve and homogenize the carbon concentration in the newly forming austenite. A certain carbide radius is input for the macro $1stCDifT$, which computes the diffusion time required for the complete dissolution of these carbides, depending on the temperature and carbon concentration of the tempered martensite. The diffusion times calculated are stored in a table array. Afterwards during the simulation the time needed for the first stage is computed by interpolation with the table array using the temperature and carbon concentration.

The second stage considered is the intergranular diffusion of carbon, which is simulated as before but with the macro $2ndCDifT$. An example of the austenite volume fraction calculated through this process is shown in Fig. 6.14a, and the final martensite volume fraction calculated at the end of the simulation in shown in Fig. 6.14b

6.6 Phase Transformations In Other Alloys

The phase transformation model can be adapted to simulate transformations in other alloys appart from steels, when the transformations follow the Johnson-Mehl-Avrami equation.

The phase evolution of titanium and titanium alloys during laser metal deposition processes was studied adapting the previously explained model to their metallurgy.

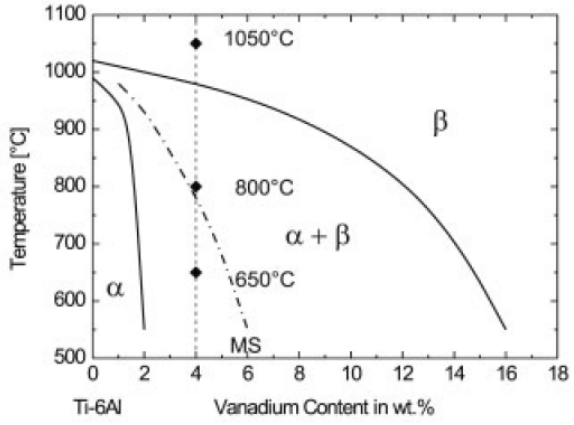

Figure 6.15: Phase diagram for alloys Ti-6Al with different vanadium contents *from [24]*

6.6.1 Titanium And Titanium Alloys

Low density, excellent high temperature mechanical properties and good corrosion resistance of titanium alloys have led to a diversified range of successful applications for the demanding performance and reliability requirements of aerospace, naval, medical, petrochemical, nuclear and power generation industries [265]. Titanium alloys can be used as replacements for aluminum-based materials when the operation temperatures exceed 130°C, the limit for the aluminum in engineering applications [266]. The aerospace sector makes extensive use of titanium alloys, consuming nearly 70% of the global production, mainly for aeroengine components such as casings, compressor blades and rotors, but also in nacelles and structural parts of the planes [267]. Ti6Al4V alloy represents half of the titanium production. Alternatively, as titanium shows very low corrosion rates in human body fluids as demonstrated [268], there are applications relevant to the medical industry like prosthetic devices such as artificial heart pumps, heart valve parts as well as load bearing bone such as for hip bone replacement.

6.6.2 Phase Transformations in Ti and Ti6Al4V

The phase diagram of Ti6Al4V is shown in Fig. 6.15. The phases considered are α, β, martensite α' and melted material. The base microstructure of Ti6Al4V is bimodal, composed mainly by α grains with a low amount of β.

During the heating, above the beta transus temperature, α phases destabilize and start their transformation to β phase according to the phase diagram. Melted material is also deposited in fully β state. During the cooling down, below the beta transus temperatur the β phase starts to slowly decompose in α phase. Two different α phases are usually distinguished: Widmanstätten and grain boundary [269], although in this study they were considered the same phase for simplicity. However, if the temperature goes below the martensite start temperature (M_s), and the cooling rate is sufficiently high, martensite is formed from the previous β phase. Due to permanence at high temperatures the previously formed martensite can be tempered, decomposing to α or $\alpha + \beta$.

Pure titanium presents the transition to β phase and it is even reported to form a quasi-equilibrium martensite with high dislocation density [270]. Therefore, the same transformations

$\beta \rightarrow \alpha$			$\alpha' \rightarrow \alpha$		
T (K)	**K**	**n**	**T (K)**	**K**	**n**
1023	0.0280	1.4	673	0.667	0.0192
1073	0.0260	1.34	773	61.106	0.0147
1023	0.0220	1.38	873	1.252	0.0246
1143	0.0250	1.34	973	1.326	0.0307
1173	0.0460	1.21			
1193	0.0240	1.39			
1223	0.0170	1.41			

Table 6.1: Parameters for the JMA equation during the transformations: $\beta \rightarrow \alpha$ and $\alpha' \rightarrow \alpha$

than in Ti6Al4V were assumed, and due to the lack of experimental kinetic parameters, the same parameters of Ti6Al4V were used.

The element vector containing the information required for the phase transformation model of titanium is represented in Fig. 6.16. The macros controlling the kinetics of the process are explained below.

6.6.3 Diffusional Phase Transformations

Two diffusional phase transformations were included in the model: decomposition of $\beta \rightarrow \alpha$, and martensite tempering: $\alpha' \rightarrow \alpha$. The parameters used for the first transformation were obtained from Sha and Malinov [269] and are included in Table 6.1.

The martensite tempering is assumed to transform the existent α' into α according to the kinetic parameters obtained from Gil Mur et al. [271], which are also included in Table 6.1.

The macros which control the kinetics of both processes are: JMA_MA for the transformation

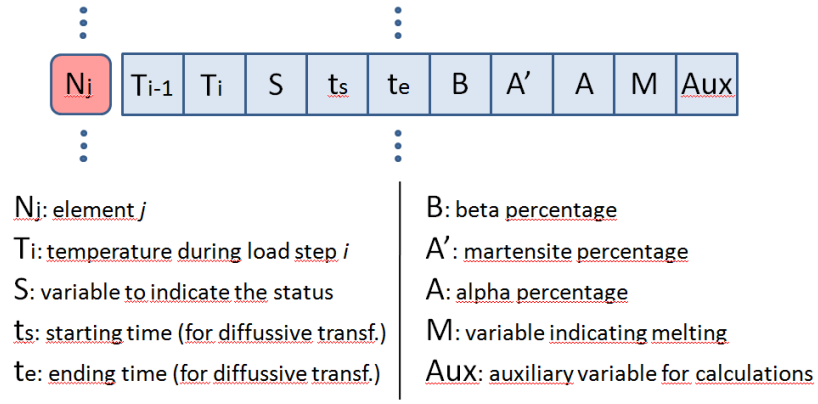

Figure 6.16: Vector for each element containing the information required for the calculation of the phase transformations for titanium.

$\alpha' \rightarrow \alpha$ and JMA_BA for the transformation $\beta \rightarrow \alpha$. Both are generic macros that can simulate any process following a JMA equation given a determined set of parameters.

6.6.4 Diffusionless Phase Transformations

The diffusionless phase transformations considered are the transformation from α and α' to β, which are assumed to transform instantly a volume fraction according to the phase diagram above the beta transus temperature; and the martensitic transformation, which is commonly simulated by the Koinstinen-Marburguer equation (5.35), with a constant $c = 0.003$ for titanium alloys [272].

6.7 Mechanical Analysis

The mechanical analysis is sequentially coupled with the thermal analysis, due to the low influence of the mechanical field on the thermal analysis. It consists of the same two parts of the thermal analysis: heating stage, simulated by the macro LH_HeatS, and cooling stage, simulated by the macro LH_CoolS. The boundary conditions for the mechanical analysis are a symmetry boundary condition applied to the symmetry plane, in case it exists, and then the minimum fixations to avoid solid rigid motion, in order to let the workpiece expand freely and develop stresses just due to the thermal loads, not due to overconstrains. Therefore, the left and right corners of the symmetry plane are selected, constraining all the displacements in one of the nodes and the vertical displacement in the other (Fig. 6.17a). In case the plate does not have symmetry plane, the four lower corners of the plate are selected, constraining all the displacements in one of them and the vertical displacement in the others (Fig. 6.17b).

The load applied during both the heating and cooling parts of the analysis is the temperature field calculated in the previous thermal simulation. During the heating part, the melted elements previously selected and named during the thermal simulation (in case they exist) are reselected at their corresponding load step and killed; a numerical procedure that involves multiplying their stiffness matrix by a low value so they *virtually* disappear from the simulation. Additionally, the plastic history of these elements is completely erased, which is what happens in reality.

If the phase transformation model was selected, the previously calculated phase percentages were stored in a series of files. During the mechanical analysis the material properties of the elements are changed accordingly to their phase content. The macro Mat_PH makes a linear interpolation between the material properties of the phases present during the analysis in order to calculate the new properties of each element.

6.8 Convergence And Material Properties

The material properties play an important role on the numerical convergence during the solution process. Convergence issues are specially important during the mechanical simulations. In this section some guidelines oriented to mitigate these problems are provided.

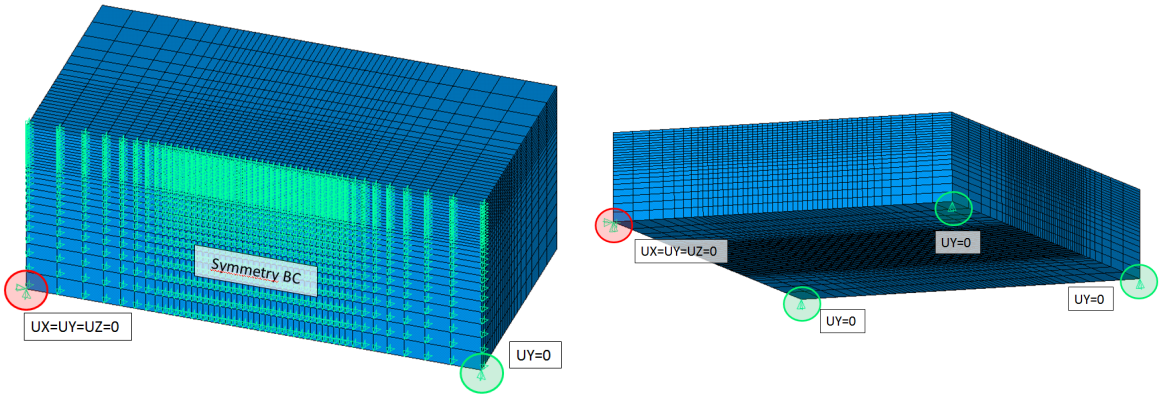

(a) (b)

Figure 6.17: Boundary conditions during the mechanical analysis: (a) model with symmetry; (b) without symmetry.

6.8.1 Thermal Analysis

The main issue in thermal simulations is the melting, in case it exists. Usually, there is a steep change in material properties at this point: density drops, conductivity changes and the specific heat capacity shows a pronounced spike around this transition.

Alloys do not have a unique melting point unless they are eutectic. Usually they have a range of melting temperatures, which alleviates the numerical issues providing a less steep transition. However, if the range is too small, spreading the transition in the thermal properties over a wider range of temperatures will help with the convergence without diminishing accuracy in this kind of analysis.

The problem with the specific heat capacity is solved by using an enthalpy formulation for the analysis, instead of the specific heat formulation. In addition the enthalpy formulation makes easy to include the latent heat of fusion in the simulation.

6.8.2 Mechanical Analysis

Abrupt changes of several orders of magnitude in the mechanical properties often lead to convergence problems. The elastic modulus of steels is about 200 GPa at ambient temperature, and should not decrease lower than 1 MPa after the melting. Poisson's ratio should not be higher than 0.48, and usually values lower than 0.45 give the same results. Otherwise the material is very close to incompressibility and numerical problems could appear.

Yield strength should vary with temperature until melting point, but in the liquid phase plasticity should not be considered. With respect to plasticity, stiffer materials give less problems than softer materials. In the unrealistic case that plasticity is not considered the convergence of the solution is usually not a problem. However, always has to be included, otherwise results would show spurious high stresses. A simple plasticity model based on a bilinear isotropic hardening assumption could be adequate, due to the removal of strain history at high temperatures.

A significant improvement in convergence can be achieved by avoiding the thermal expansions at high temperatures and especially in the liquid region. The aim is to prevent excessive

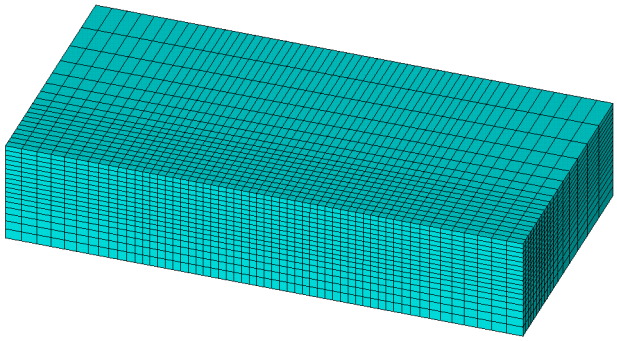

Figure 6.18: Mesh used in the LTH simulation.

distortions in the material. A simple way to counteract thermal expansion at high temperatures is to compensate it with a decrease in the coefficient of thermal expansion proportional to the temperature difference, in order to maintain the volume of the element.

6.9 Thermomechanical Anlysis Of LTH

The LTH simulation of a small plate is included in this section to describe the main characteristics of the process. The mechanical simulation was carried out with and without phase transformations, in order to compare both cases.

A plate of dimensions 20x10x3 mm was modeled with planar symmetry. The FEM mesh is shown in Fig. 6.18. It consists of 17136 hexahedral elements, with 19494 nodes. The laser profile selected was a top hat, with a scanning velocity set to 5 mm/s, being active during 1 s.

6.9.1 Without Phase Transformations

The temperature map during the heating stage and the history of several consecutive nodes located at the symmetry plate, on the surface of the plate, are represented in Fig. 6.19.

Fig. 6.20 shows the calculated vertical displacements. The XYZ directions are defined as length, width and height.

During the heating stage the plate bends slightly in a concave shape, due to the differential thermal expansion. This expansion is higher in the upper part of the plate due to its higher temperatures. The heated material tries to expand, but it is surrounded by the remaining material of the plate, which remains at lower temperatures, and therefore is stronger because its yield strength and elastic modulus are higher. The heated material has low strength, experiencing significant plastic deformations during this stage. It cannot expand much in the X and Z directions, so it expands vertically in the Y direction. Thus an initially cubic volume of the material changes into a rectangular prism.

During the cooling down the material contracts. Those material volumes which had changed their initially cubic shape into a prism during the heating, will now show lower X and Z lengths in the upper side of the plate due to the contraction process; so the corresponding areas of the upper part of the plate shrink in these directions. Distortion of these volumes draws attached volumes

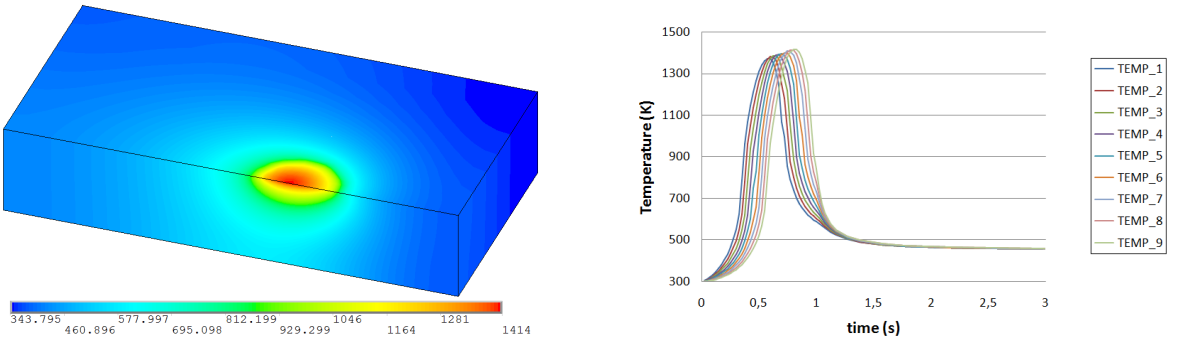

(a) (b)

Figure 6.19: (a) Temperature map during the simulation; (b) temperature histories of several consecutive nodes.

inducing tensile stresses in the material. The result is the bending of the plate in a convex shape. Also the thickness of the plate was affected, increasing in these zone. The distortion of these volumes draw the attached volumes inducing thermal stresses in the material.

The whole process is completely summarized in Fig. 6.21. The bending angle depends on the process parameters as well as the material properties and the dimensions of the plate. It should be minimized during LTH, but it can be exploited in treatments like laser forming, in which metal sheets are laser bended.

In Fig. 6.22 are shown the stresses during the heating stage and the temperature of the

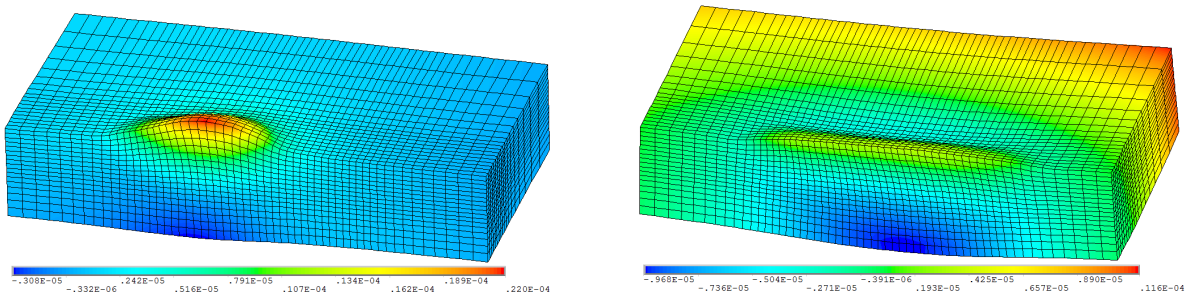

(a) (b)

Figure 6.20: Vertical displacements (deformed shape multiplied by 30): (a) During the heating (t=0.4s); (b) after the cooling.

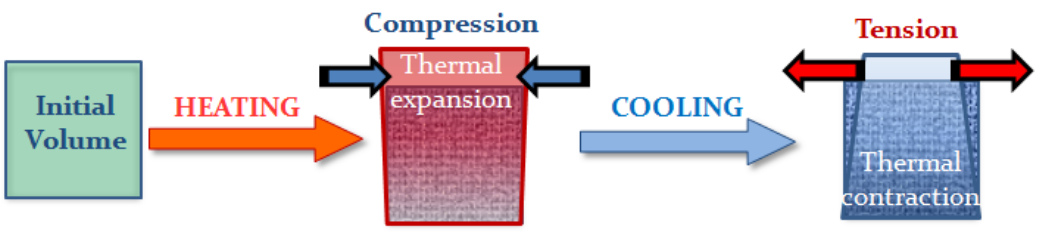

Figure 6.21: Schematic representation of the generation of strains and stresses during LTH.

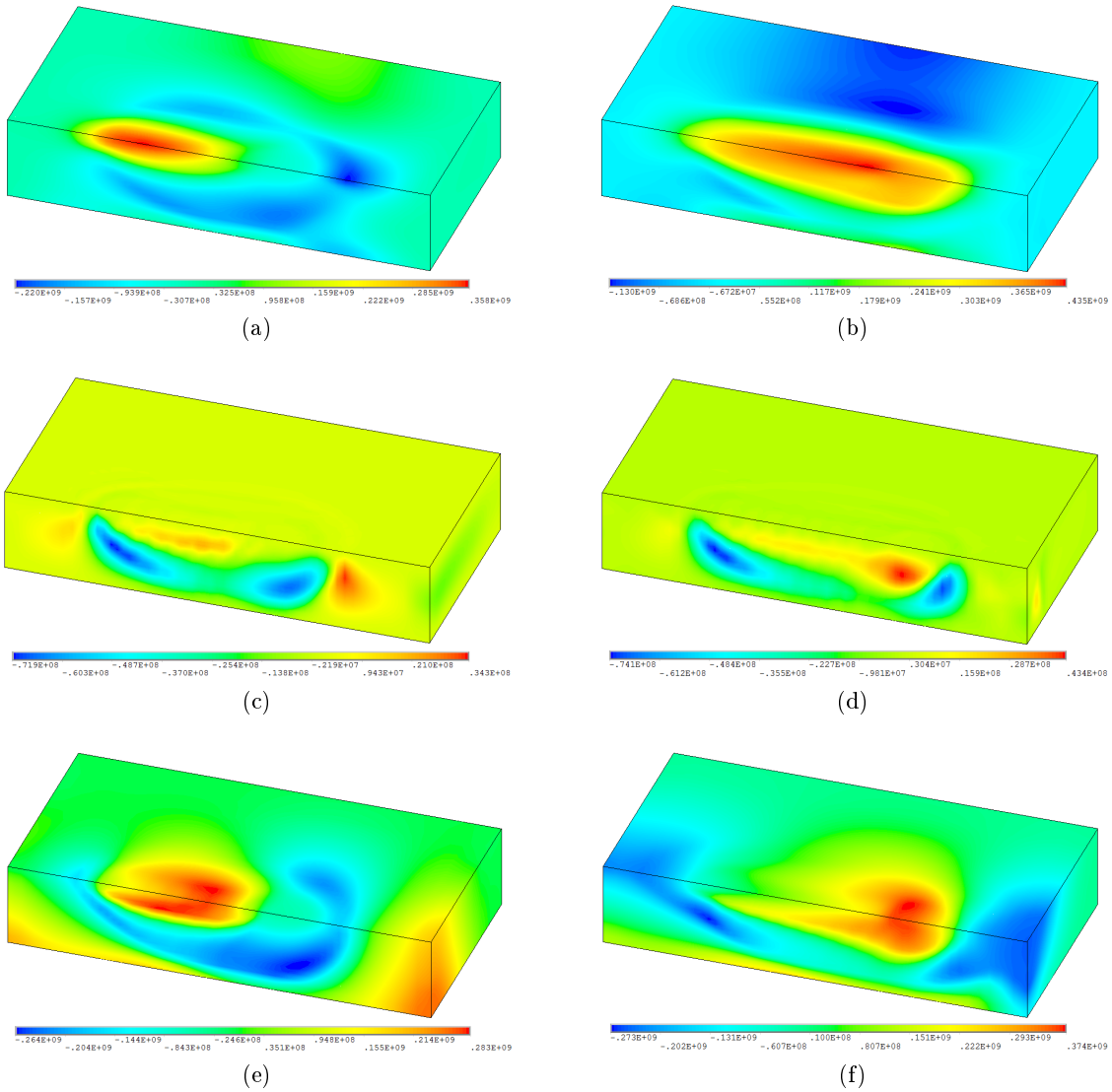

Figure 6.22: Stresses during the heating stage (t=0.8s): (a) X; (c) Y; (e) Z; Stresses after the cooling down (t=100s): (b) X; (d) Y; (f) Z.

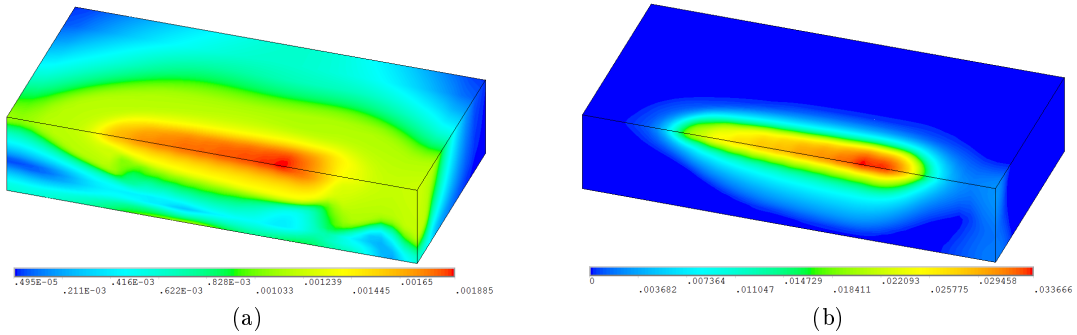

Figure 6.23: Residual strains: (a) elastic; (b) plastic

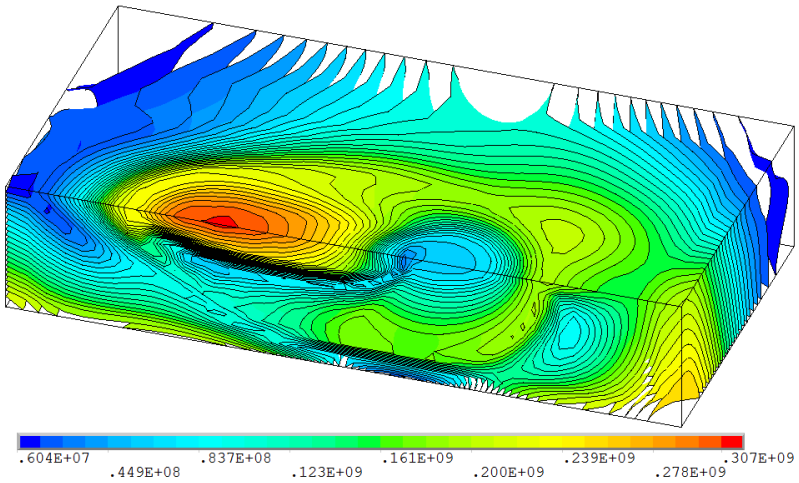

(a)

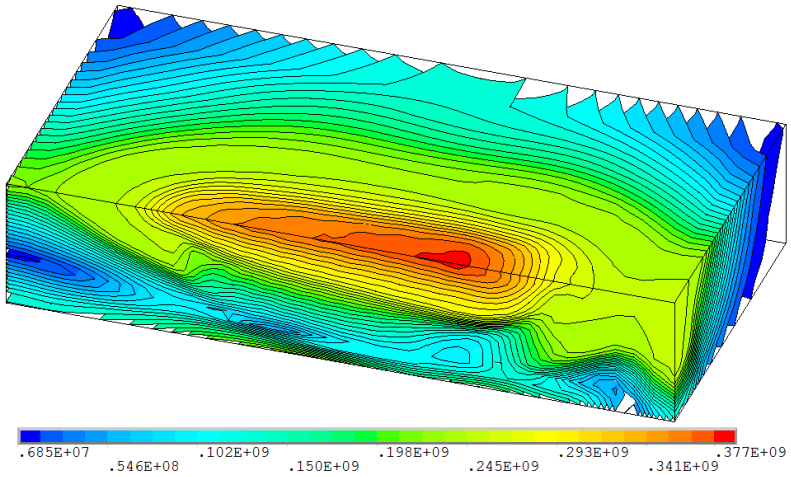

(b)

Figure 6.24: Von Mises equivalent stress (represented in isosurfaces): (a) During the heating (t=0.8s); (b) after the cooling down (t=100s).

corresponding load step. Von Mises equivalent stress is represented in isosurfaces in Fig. 6.24a. The zones with high number of surfaces present high gradients within them. The map of residual elastic strains is shown in Fig. 6.23a, and the map of plastic strains, in Fig. 6.23b.

One node considered representative of the process, located at the symmetry plane, on the upper surface of the plate, was selected to represent its temporal history of strains and stresses. In Fig. 6.25a are represented the XYZ components of the stress as well as the equivalent Von Mises stress. The temperature history is also included as a dotted red line. This figure shows clearly an example of the stress evolution during the process. As explained before, during the heating stage the stresses developed are compression stresses then, there is a point in which the stress reverses and starts to diminish until tensile stresses develop, grow and stabilize. Stresses are lower during the heating stage than during the cooling, because the material is at high temperatures and its mechanical strength is diminished. Besides, not all the components are equally important. The highest stresses develop in the X direction, as it is expected, because it is the traversing direction of the laser beam. Z stresses are lower, but Y stresses are 2 orders of magnitude lower than both

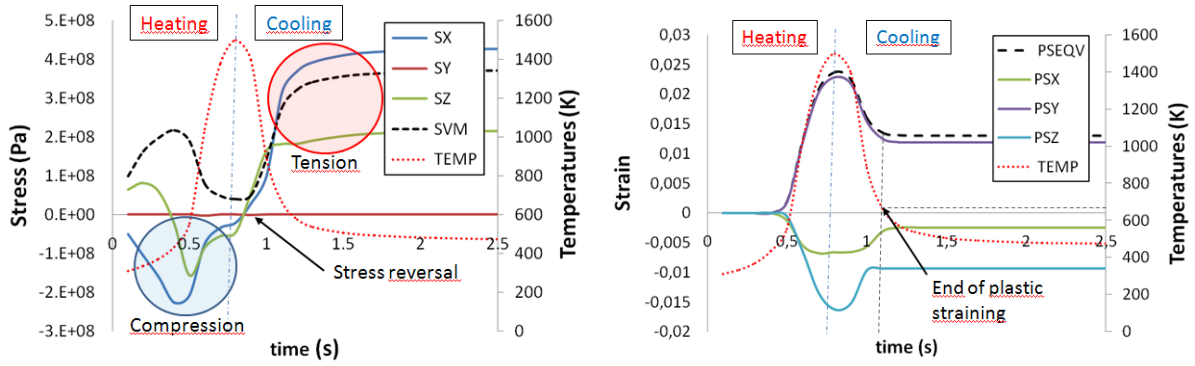

(a) (b)

Figure 6.25: Temporal history of one node heated by the laser beam: (a) stresses; (b) strains.

of them.

In Fig. 6.25b the plastic strains of the same node are represented. During the heating stage, the X and Z plastic strains are negative and lower than the Y strains, which are positive. During the cooling stage, plastic strains diminish in magnitude due to the stress reversal and stabilize at temperatures between 400-500°C remaining as residual plastic strains in the workpiece.

6.9.2 With Phase Transformations

The same model was simulated again including phase transformations. First, some properties of the material used for the plate were changed, like the coefficient of thermal expansion, which was modified in order to simulate the variation of the specific volume due to austenitization, which lowers by 4% approximately. In Fig. 6.26 are represented the previous coefficient and the new one.

Then, the model of phase transformations was included in the simulation, in order to compute the phase evolution and change the material properties in the mechanical analysis according to the different phase percentages of each element.

Fig. 6.27 shows the computed austenite and martensite volume fractions during the heating

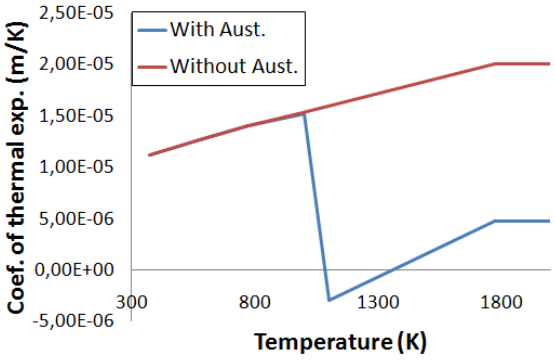

Figure 6.26: Coefficients of thermal expansion, with and without austenitization.

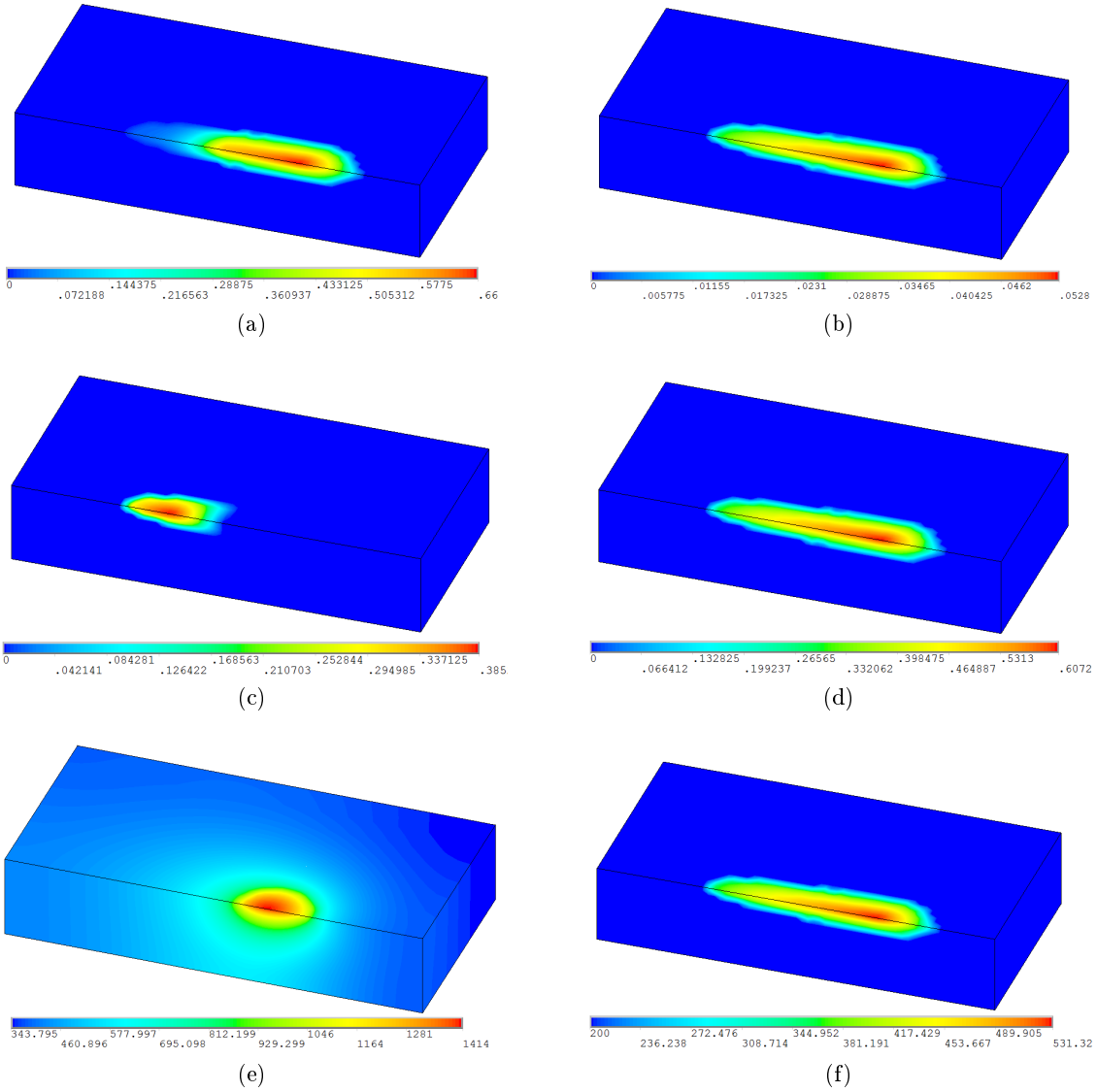

Figure 6.27: Phase volume fractions: (a) austenite (t=1s); (b) austenite (t=100s); (c) martensite (t=1s); (d) martensite (t=100s); (e) temperature map (t=1s); (f) final hardness profile.

stage and after the cooling down. The temperature map corresponding to the load step during the heating stage is also included, as well as the estimated hardness profile after the treatment.

The residual stresses are shown in Fig. 6.28. There are some remarkable differences compared with the previous case. First of all, the stress profiles are much more irregular than before, due to the multiple phases present at different times in the analysis and their different material properties. The stresses in the X direction are still the highest, however, in some areas the stresses in the Y direction are now important, due to the volumetric contraction during the austenitization.

It is reasonable that the strains decrease in magnitude when phase transformations are included. During the heating, when the material is submitted to high stresses and strains due to thermal expansion, austenitization lowers the material specific volume and thus reduces dramatically

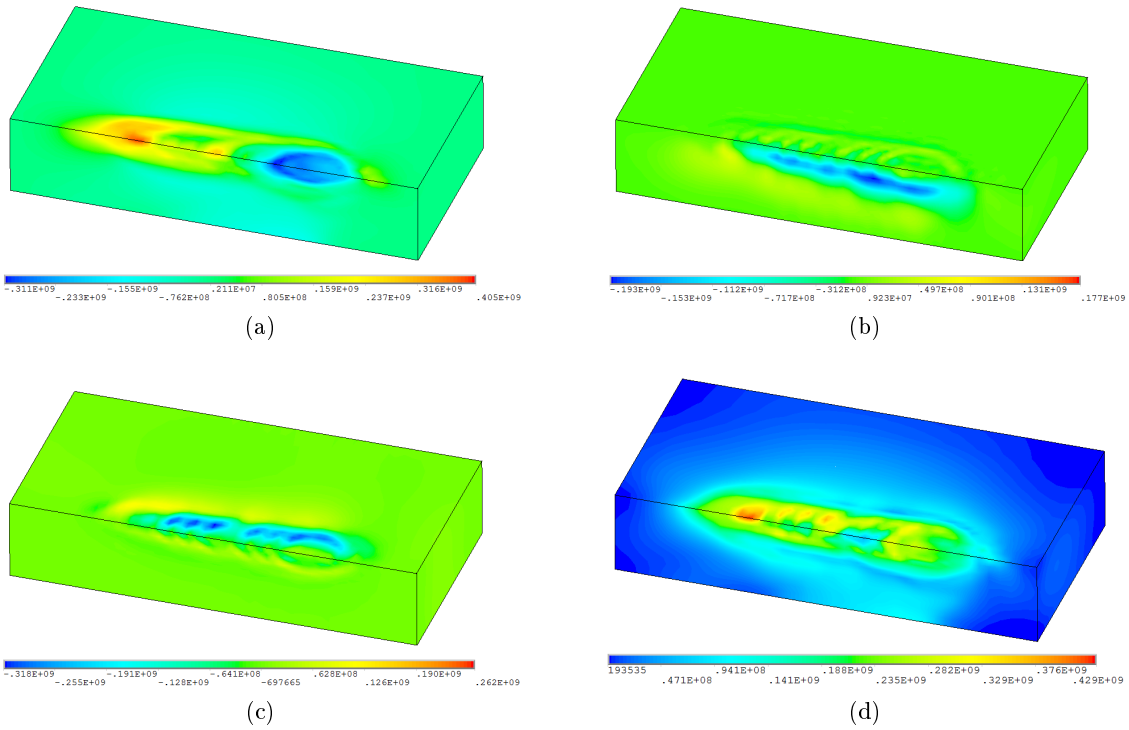

Figure 6.28: Residual stresses in the following directions: (a) X; (b) Y; (c) Z; (d) Von Mises.

the strains and stresses, whereas during the cooling stage, when the material is contracting, austenitization increases its specific volume counteracting thermal contraction to the point of even generating compression stresses in the material. This point is illustrated in Fig. 6.28a. At the starting edge of the track the material that has suffered austenitization is very low, remaining tensile residual stresses, whereas at the end of the track most of the material suffered austenitization, resulting in compressive residual stresses. The strains produced are much lower. However, the stresses, which in this case are also lower, do not have to show the same behavior. Actually, higher yield strength of resultant martensite makes possible to develop higher stresses. The mechanical history of the same node selected before is shown in Fig. 6.30. The phenomena explained above can be seen in this picture.

The map of residual strains is shown in Fig. 6.29. Their magnitude is less than a half of the previously calculated without phase transformations.

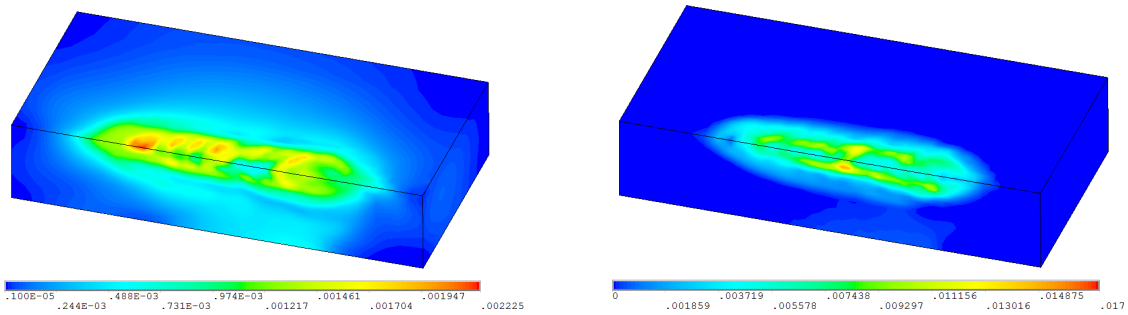

(a) (b)

Figure 6.29: Residual strains: (a) elastic; (b) plastic.

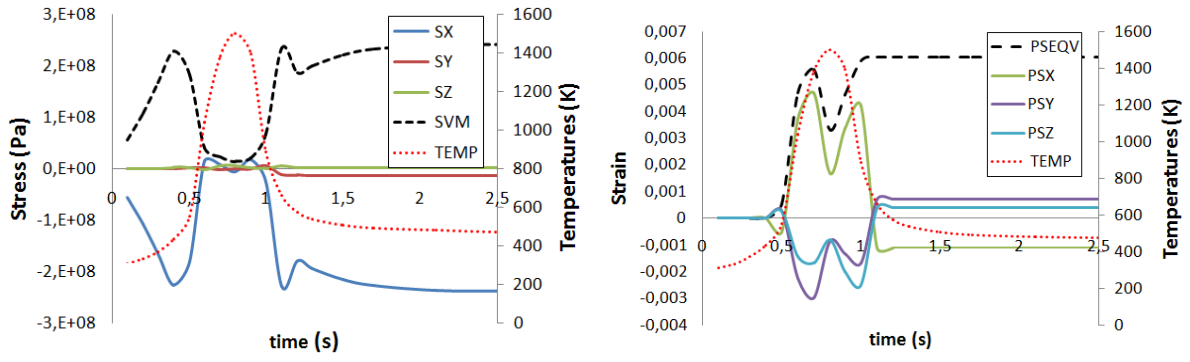

(a) (b)

Figure 6.30: Temporal history of one node heated by the laser beam: (a) stresses; (b) strains.

Chapter 7

Model For Laser Metal Deposition

Everything should be made as simple as possible, but not simpler.
Albert Einstein.

Abstract: The FEM models developed for laser metal deposition techniques, which include laser cladding and prototyping, are explained in detail in this chapter, including at the end of it a discussion of the results during laser cladding with single clad tracks, several overlapped clad tracks and several superposed clad tracks.

7.1 Introduction

For the modelling of laser metal deposition a set of macros and input files was developed, consisting of similar files to the ones developed for LTH and explained in Chapter 6.

The models are designed to simulate the thermo-mechano-metallurgical phenomena of laser metal deposition processes. Phase transformations can be included in the simulations as before.

7.2 Geometry And Meshing

Geometry for the laser cladding model is much more complicated than the simple plate geometry of the LTH model. The clad bead usually has a cross section similar to a section of cylinder, and has rounded start and end. Furthermore it has to be entirely divided into curved slices for the thermomechanical analysis.

Geometry is complex so its creation and meshing is a challenging and time consuming task. A macro for geometry generation and meshing would simplify the whole process. To be useful, it has to be flexible and allow the change of multiple parameters. The generated mesh should have a low number of elements, preferentially hexahedrals.

The macro C_Mesh developed generates the entire FEM model of a single clad track deposited on a plate with planar symmetry. The clad bead is modelled as a section of a cylinder. The

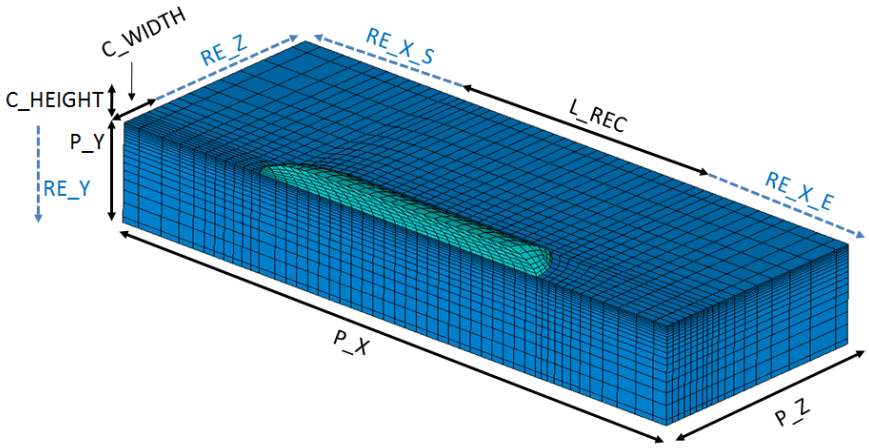

Figure 7.1: Mesh with planar symmetry, showing the input parameters for its generation

start and end of the clad bead are calculated as sections of two different ellipsoids. The entire clad bead is divided into slices, which will be activated during the analysis in each corresponding load step. These slices can be modelled as straight cuts of the cylinder or as ellipsoidal sections of the cylinder.

The input parameters for the macro are:

- Clad dimensions: width, height, length.
- Starting position of the clad bead.
- Curvature of the slices, and its thickness.
- Number of elements of each slice.
- Plate dimensions: width, height, length.
- Number of divisions of each dimension of the plate.
- Ratio between the first and last division.

In Fig. 7.1 are represented most of the input parameters required by the macro.

The meshing algorithm was entirely developed for the laser cladding process. It defines every node of the clad bead and the plate according to sets of equations dependent on the input parameters. Then, it creates hexahedral elements joining the nodes, and afterwards, it names the components for the simulation. No surfaces or volumes are generated during the process, it is a pure FEM mesh.

Like in the LTH macro, the meshing of the plate follows exponential progressions to increase the element size from the refined areas, around the clad track, to the borders of the plate. Element size in the whole model is primarily dependent on the number of elements in which each slice is subdivided.

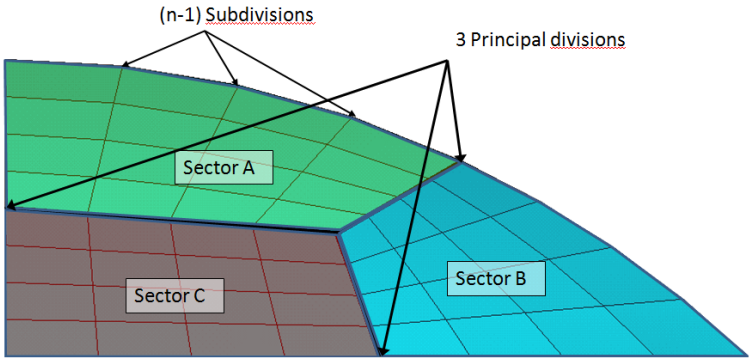

Figure 7.2: Slice division in sectors and elements (n=4).

Meshing of the clad slices is based on the division of each slice in 3 sectors. Then, the three edges of each sector are subdivided by $n-1$ subdivisions, generating n^2 hexahedral elements per sector and $3n^2$ elements per slice as it is represented in Fig. 7.2.

Examples of meshes created by changing some of the input parameters of the macro, in this case

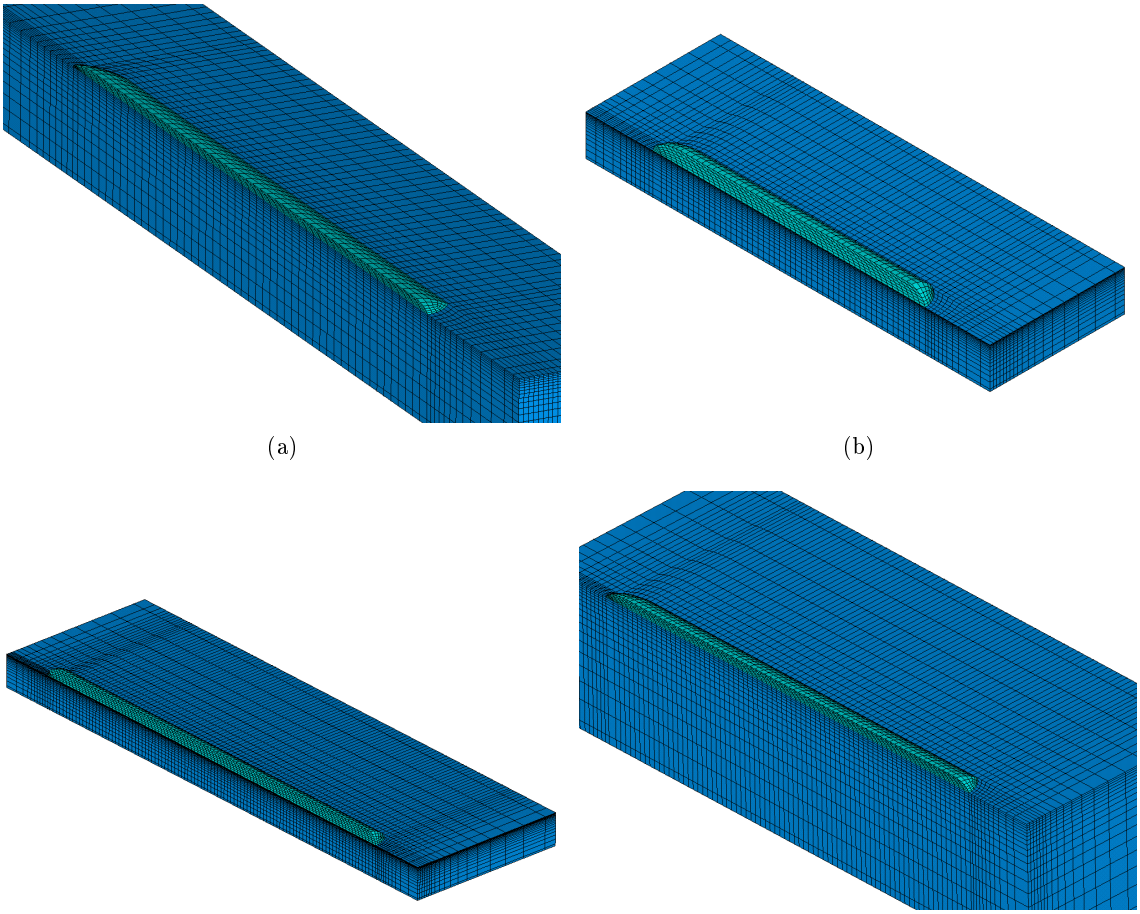

(a) (b)

(c) (d)

Figure 7.3: Different meshes created by the macro C_Mesh

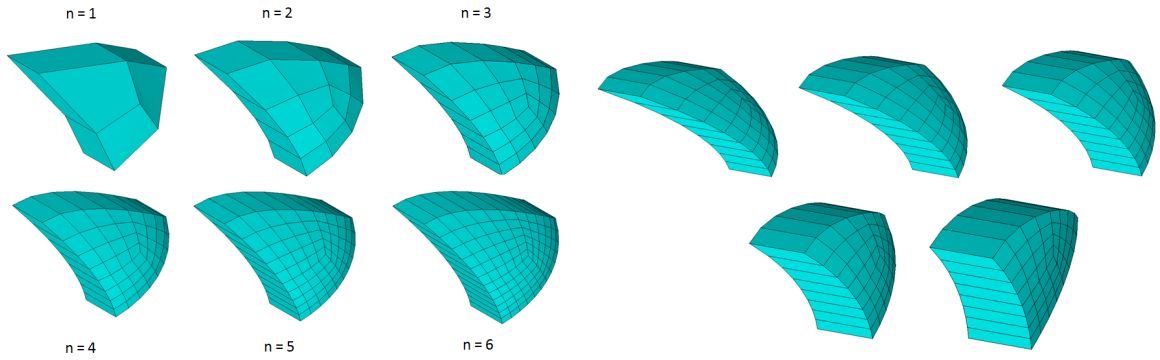

(a) (b)

Figure 7.4: Different slice shapes created changing: (a) number of slice divisions; (b) parameters of the ellipsoid defining their geometry

plate dimensions and clad bead dimensions, are included in Fig. 7.3. Mesh generation takes only seconds and the resultant meshes are almost ready for simulation. The only step required is the assignment of the material properties to the plate and the clad bead.

The number of elements of each slice has special relevance, inasmuch as it controls the element size of some zones of the mesh. Some examples of meshed slices with different number of divisions are shown in Fig. 7.4a.

Slice geometry is important too. As mentioned before, it is computed as an ellipsoidal section of the cylinder defining the clad bead. Ellipsoid parameters can be change, varying the slice shape as shown in Fig. 7.4b. It is important to try to avoid low angles shapes, which are difficult to mesh and produce distorted elements that affect negatively on the solution process.

Unfortunately this macro serves only for models with a single clad bead and planar symmetry. For the simulation of several overlapped clad beads creating a coating on the workpiece, the macro *Cover_Mesh* helps with clad bead geometry generation. It uses the dimensions of the first clad bead, its position, overlapping between clad beads and the plate dimensions as inputs to generate the geometry. Overlapping between subsequent clad beads is used along with an iterative procedure to compute the shape of the next clad beads, maintaining the volume of the first one as it is represented in Fig. 7.5. The macro *Cover_Name* names the different volumes and areas of the model, for their selection during the analysis. The mesh is predominantly formed by linear hexahedrals with quadratic tetrahedrals for the transition zones. A complete model with 4 clad tracks is shown in Fig. 7.6a.

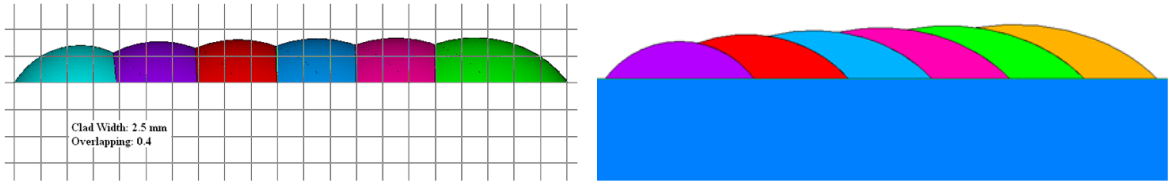

(a) (b)

Figure 7.5: Cross section of 2D clad beads generated with an overlapping of: (a) 40%; (b) 55%.

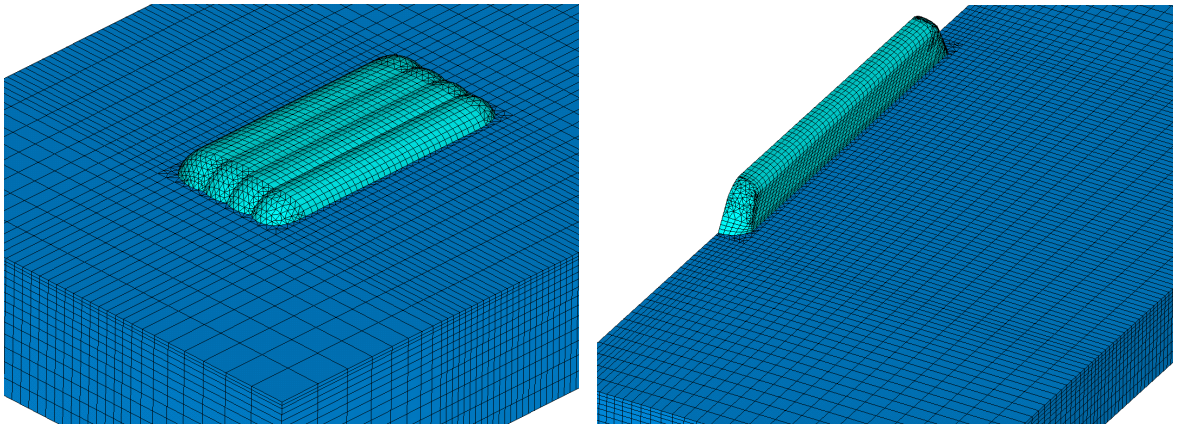

(a) (b)

Figure 7.6: (a) Model with four overlapped clad beads; (b) Model with four superposed clad beads.

The macro *Proto_Mesh* helps with geometry building when several superposed clad tracks have to be simulated. Clad tracks are no longer simulated as sections of a cylinder because that would generate a very poor meshing afterwards. Although, curved shapes are maintained for the upper parts of the clad beads and its starts and ends. Naming of volumes and areas is done with the macro *Proto_Name*. The mesh is predominantly hexahedral based with quadratic tetrahedrals for the transition zones. An example of a model with four superposed clad tracks is shown in Fig. 7.6b

7.3 Thermal Analysis

The macro *C_Heat* controls the heating stage of the process. The analysis starts with all the elements of the clad bead, *killed* (deactivated). The clad deposition is simulated activating each slice of the clad bead at a temperature above the melting point of the coating material which is being deposited. The temperature is calculated using energy conservation. The laser input power is distributed as follows: heating of the slice, heating of the surface of the plate and power losses. However, all of these quantities can only be estimated a priori. Therefore, in order to fine tune power parameters metallographic cross sections can be compared with model predictions.

The laser beam is assumed to have a top hat profile, which is the usual profile after the laser is transmitted through an optical fiber, and it is applied on the surface of the plate with exception of the areas below the already deposited clad slices. In models with several overlapped or superposed clad beads the laser beam is also applied on the surface of the corresponding previously deposited clad beads, which in the model with overlapped clad beads are the clad slices adjacent to the slice being deposited. In the model with superposed clad beads are those situated before and below the clad slice being deposited.

Convection heat transfer is applied in every load step on the nodes of the free surfaces of the plate which were heated above ambient temperature. Therefore, these nodes are previously selected according to the results of the previous load step. The melted elements of the plate are selected as well and grouped into components for the subsequent selection during the mechanical analysis, in order to kill them. The surfaces of the already deposited clad slices, with exception of the

one being deposited, are also selected in order to apply convection on them. The bottom of the plate is selected separately in order to apply a different convection coefficient.

The cooling stage is controlled by the macro *C_Cool*, which applies convection heat transfer with the surrounding air to all the external surfaces that are heated above ambient temperature. This includes the surfaces of the previously deposited elements. Like in LTH process, the cooling time steps are increased following a geometric progression in order to efficiently simulate the exponentially decaying cooling down with a low number of load steps.

Both macros include routines for capturing images during the ongoing simulation in order to monitor its results and create videos if desired. Phase transformations can be included during the simulation or be sequentially coupled after it. Phase transformation macros will calculate the phase evolution and store the phase percentages of each element in a file every load step.

7.4 Mechanical Analysis

Mechanical analysis is sequentially coupled with thermal analysis. Heating stage is simulated by the macro *C_HeatS*, and cooling stage is simulated by the macro *LH_CoolS*. The boundary conditions for the mechanical analysis are the same applied to the LTH simulations. A symmetry boundary condition is applied to the symmetry plane, in case it exists, and then the minimum fixations to avoid rigid body motion, in order to let the workpiece expand freely and develop stresses just due to the thermal loads applied, not due to overconstrains. Therefore, the left and right corners of the symmetry plane are selected, constraining all the displacements in one of the nodes and the vertical displacement in another. In case the plate does not have a symmetry plane, the four lower corners of the plate are selected, constraining all the displacements in one of them and the vertical displacement in the others (Fig. 6.17).

The load applied during both heating and cooling stages is the temperature field calculated in the previous thermal simulation. During the heating part, the melted elements previously selected and named during the thermal simulation, are reselected at their corresponding load step and killed, a numerical procedure that involves multiplying their stiffness matrix by a low value so they virtually disappear from the simulation. Additionally, the plastic history of these elements is completely erased, which is what happens in reality.

If the phase transformation model is selected the previously calculated phase percentages, that were stored in a series of files, are read during the analysis and element material properties are changed according to their phase content. The macro *Mat_PH* makes a linear interpolation between the material properties of the phases present during the analysis in order to calculate the new properties of each element.

7.5 2D Models

Several macros for the creation of 2D models were developed in order to simulate the cross section of one of the 3D models. Large computing times for full thermomechanical analysis are the main disadvantage of 3D models, especially in case of multiple clad bead models. 2D models are very fast, simulating several clad tracks in a couple of hours. The information they provide is limited, nevertheless, they show results very similar to 3D models, so parametric studies can be carried

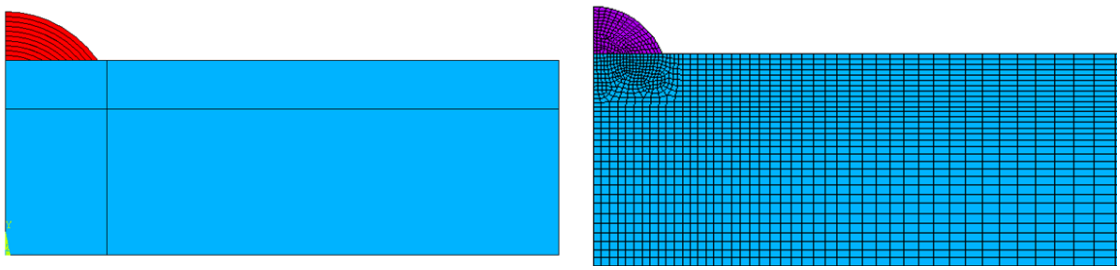

(a) (b)

Figure 7.7: 2D laser cladding models: (a) geometry; (b) mesh.

out with them, whereas with 3D models the time required could be excessive. Although, taking into account the spectacular advances in computer performance, the computing time required is continuously diminishing.

2D models simulate the process discretizing the cross section of the clad bead into several slices (Fig. 7.7). The laser is applied to the surface of the plate at the correct time, and the slices are activated at its corresponding load step. When they are activated, the part of the plate below the slice does not receive laser heating. If several clad tracks are going to be deposited, each of them starts the activation of its slices at the corresponding time.

Convection heat transfer is applied to the external lines, with exception of the symmetry line, in case it exists. The boundary conditions for mechanical analysis are similar to the ones applied to 3D models. They consist of a symmetry boundary condition applied on the symmetry line, the constraining of all displacements of the lower node of the symmetry plane, and the constraining of vertical displacements of the lower vertex of the plate.

7.6 Thermomechanical Anlysis Of Laser Metal Deposition

Simulations of laser metal deposition techniques are presented in this section. Thermomechanical phenomena during the techniques were studied as well as the effect of several parameters in the process. The analyses consists of 2D models and 3D models, either with one clad bead or several overlapped or superposed clad beads.

7.6.1 Laser Cladding

Thermomechanical strains and stresses arise from the same phenomena previously explained for LTH. However, the heat load is higher in laser cladding and furthermore there is always melted material unlike in LTH.

During clad deposition, the plate bends in a concave shape (Fig. 7.8a) due to the differential thermal expansion. The expansion is higher in the upper part of the plate due to its higher temperatures. The non-melted heated material tries to expand, but it is surrounded by the rest of the material of the plate, which remains at lower temperatures, being therefore strongest because its yield strength and elastic modulus are higher. The heated material has lower strength, experiencing significant plastic deformations during this stage. It cannot expand much in the

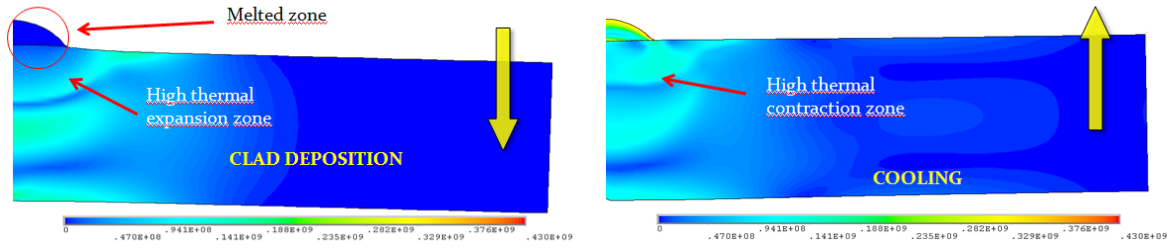

(a) (b)

Figure 7.8: Bending of the plate during the cladding process: (a) during the metal deposition (concave); (b) after cooling down (concave).

X and Z directions, so it expands vertically in the Y direction. Thus, an initially cubic volume of the material changes into a rectangular prism as it is represented in Fig. 6.21. Additionally, there is a significant amount of melted material, corresponding to the alloy being deposited and the melted material of the upper surface of the plate.

During cooling down the previously heated material contracts. Those material volumes which had changed their initially cubic shape into a prism during the heating, will see their X and Z lengths reduced after contraction. Thus, the upper plate surface shrinks in these directions. Distortion of these volumes affects surrounding material, they pull of the rest of the upper plate, creating tensile stresses. The melted material contracts uniformly, creating tensile stresses in all directions, but specially in the X and Z directions due to the larger length of melted material contracting and pulling the plate. As a result of this, the plate bends in a convex shape (Fig. 7.8b). The melted material contracts much more than the surrounding material increasing the strains and stresses with respect to a similar LTH process.

7.6.1.1 Parametric Study

In order to test the influence of several parameters and geometric characteristics in the laser cladding process, a series of tests were performed with the 2D models, simulating a plate of 2.5 cm width of stainless steel AISI 304, with Stellite 6 as coating material. Neither of both materials present phase transformations.

The variables that were study in the tests were:

- Plate height.
- Plate width.
- Clad height.
- Clad width.
- Process velocity.
- Preheating.

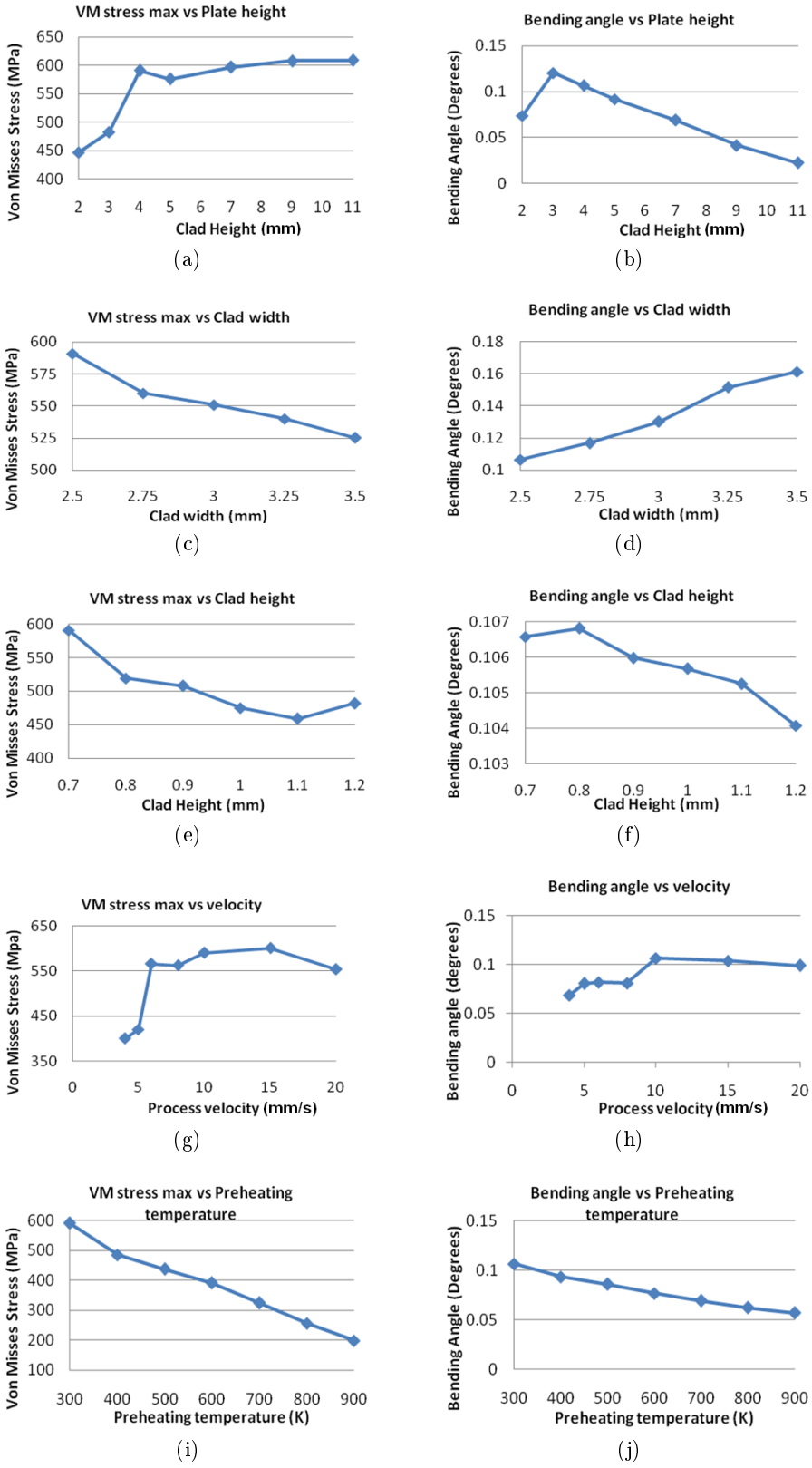

Figure 7.9: Parametrical study of the laser cladding with the 2D model

The results of the study are represented in Fig. 7.9. They show specific trends with the different parameters. The bending angle follows a linear tendency in most of the cases, excepting some anomalies produced mainly due to geometrical parameters of the clad bead or excessive heat accumulation in thin plates. The maximum Von Mises stress follows nonlinear tendencies in the cases of the plate height, clad height and velocity, showing linear trends in the cases of clad width and preheating of the plate.

The study concluded that those parameters leading to lower gradients tend to produce lower stresses and lower distortions on the plate. Specifically the preheating of the plate is the parameter most influential parameter regarding the lowering of the stresses.

According to the results, parameters can be listed from most to least relevan as follows:

- Preheating.
- Process velocity.
- Plate height.
- Clad width.
- Clad height.

7.6.2 Overlapped Clad Tracks

Models with several overlapped clad tracks were also studied. Simulations were carried out again with AISI 304 as substrate and Stellite 6B as coating material. In Fig. 7.10a is shown the temperature mapping during the laser cladding process of several clad tracks, and in Fig. 7.10b the corresponding Von Mises stresses.

Von Mises stresses after deposition of one, two, three and four clad tracks are shown in Fig. 7.11. During the deposition of the next clad tracks, there is a stress rearrangement within the first

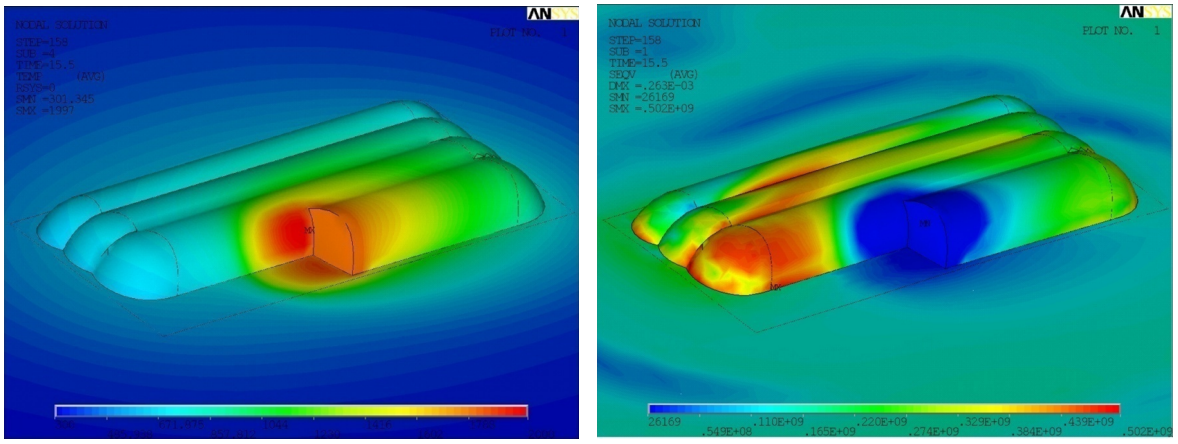

(a) (b)

Figure 7.10: Simulation with several overlapped clad tracks: (a) temperatures; (b) Von Mises stress

clad track. Due to the heating provided by the deposited track there is a stress relaxation on the previous track, and also a change in the stress profile due to the strains and stresses developed during the cooling down of the deposited track.

The highest stresses are located on the surface of the plate, in the zone between both clad tracks, and also in the interphase between both clad tracks and the plate. When another clad track is deposited, the effect is the same. Regarding the distortions of the plate, the bending angle increases almost linearly with every clad track deposited.

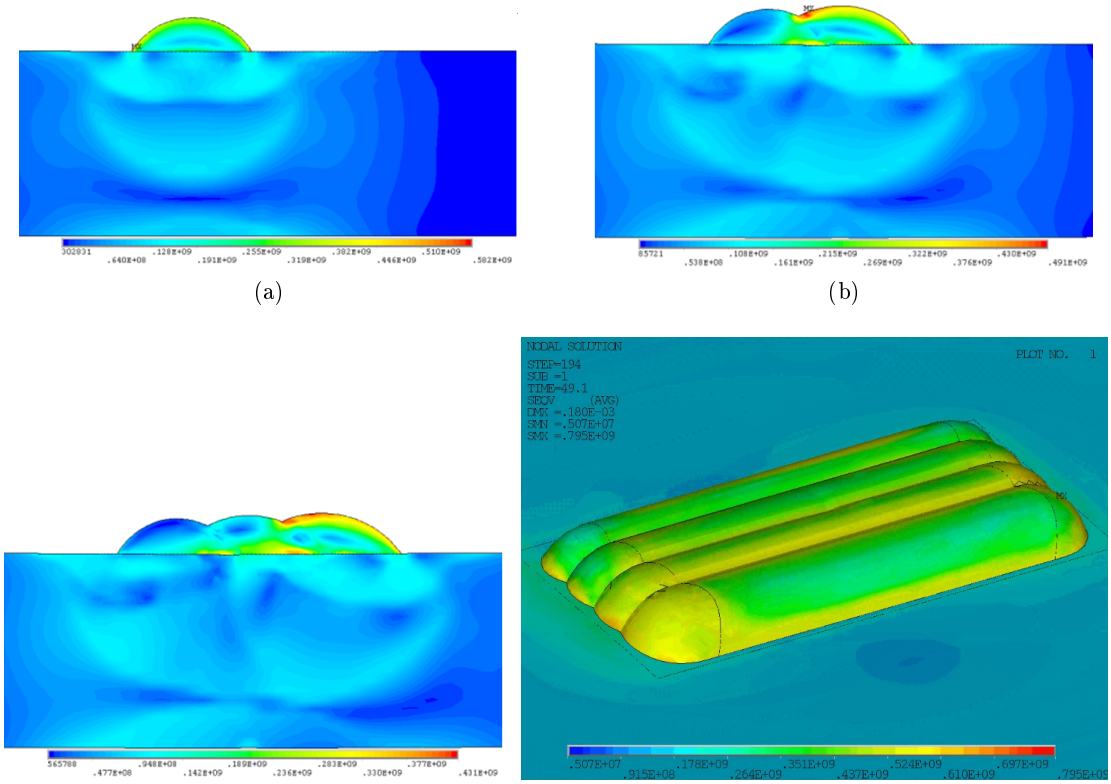

Figure 7.11: Von Mises stress of the cross section of the model with several overlapped clad tracks: (a) one track; (b) two tracks; (c) three tracks; (d) four tracks (external surfaces)

7.6.3 Superposed Clad Tracks

Four superposed clad tracks of Stellite 6B on a plate of AISI 304 were simulated with this model. Temperatures during the analysis and the corresponding Von Mises stresses are shown in Fig. 7.12.

The analysis shows a complete stresses rearrangement in the previously deposited clad tracks during the deposition of each clad track, because an important part of the previous track is remelted in the process, and the zone situated below is heated to elevated temperatures, relaxing the stresses.

Fig. 7.13 shows Von Mises stresses during the deposition of each track. The highest stresses in the cross section are located in the interphases between clad tracks. However, the highest

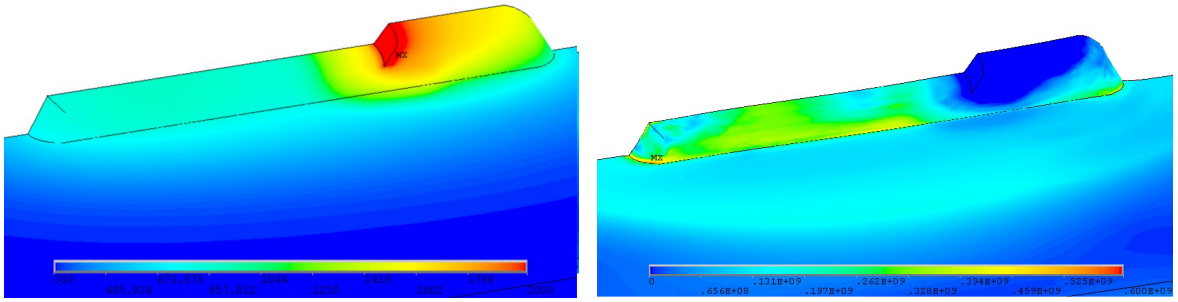

(a) (b)

Figure 7.12: Simulation with several superposed clad tracks: (a) temperatures; (b) Von Mises stress

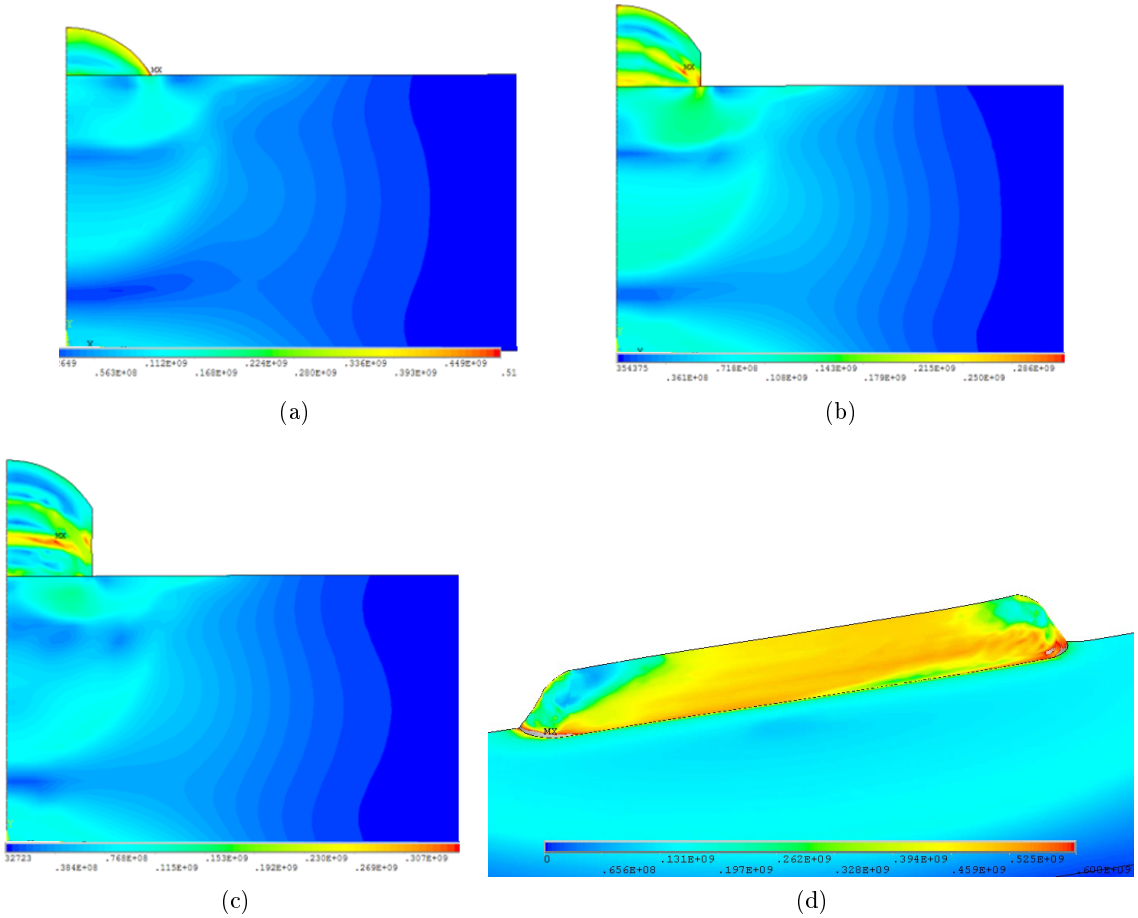

(a) (b)

(c) (d)

Figure 7.13: Von Mises stress of the cross section of the model with several superposed clad tracks: (a) one track; (b) two tracks; (c) three tracks; (d) four tracks (external surfaces)

stresses calculated by the model were located at the start and end of the first clad track, located in the interphase with the plate. The analysis shows that each clad track deposited contributes to the building up of stresses in this zone.

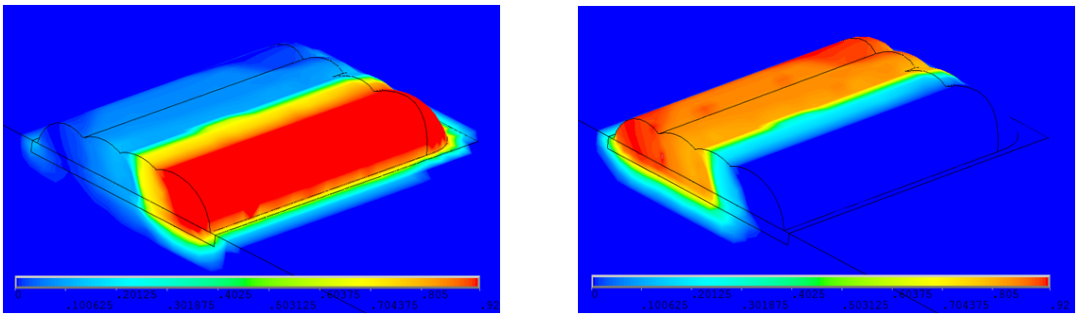

(a) (b)

Figure 7.14: Phase volume fractions calculated with the model with overlapped clad tracks (after final cooling): (a) martensite; (b) tempered martensite.

7.6.4 Overlapped Clad Tracks With Phase Transformations

Simulations were carried out with AISI H13 as both substrate and coating material. Phase transformations are included in the simulations. Therefore, material properties are recalculated for the elements which present phase transformations each load step.

Each clad track is deposited and cooled very fast by heat conduction with the steel plate, producing martensite. During the deposition of the next clad track the reheating produces the tempering of the previously generated martensite, so at the end of the simulation only the last clad track is in fully martensitic state (Fig. 7.14a and Fig. 7.14b). The final hardness map is shown in Fig. 7.15a. With a preheated plate, a smaller plate or more clad tracks, the workpiece could be heated to high temperatures and the slower cooling would allow diffusive transformations of the austenite.

Martensitic transformation has an important impact on the stresses. During the heating the contraction martensitic transformation causes, counteracts the thermal expansion of the material whereas during the cooling, the expansion caused by the transformation, counteracts the thermal contraction even to the point of reversing the stress profile and lead to compressive residual stresses. Thus the strains are lower than without phase transformation. However, the same is not true for stresses: higher yield strength of martensite could lead to higher stresses.

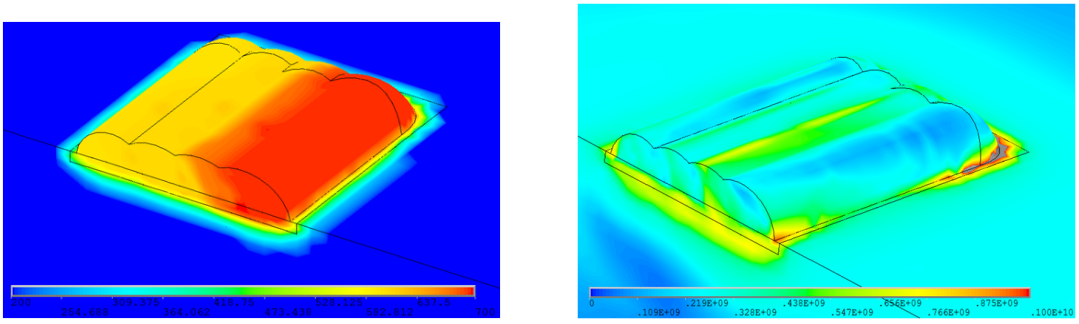

(a) (b)

Figure 7.15: (a) Final hardness map calculated with the model with overlapped clad tracks; (b) Von Mises equivalent stress.

Von Mises equivalent stress is represented in Fig. 7.15b. The last clad track has a high percentage of martensite and shows low compressive stresses. Von Mises stress history of 2 elements is shown in Fig. 7.16. The elements are situated in: 1) clad track; 2) plate (untransformed zone). The temperature history of element 1 was also represented.

The profiles obtained are complex. Element 2 shows a typical profile without phase transformations, during the multitrack deposition process: valleys when the material is hot and peaks when is cold. Element 1 suffers complete martensitic transformation, generating stress reversal from tensile to compression during the cooling, producing two peaks instead of one. Besides, the final stresses are lower than before. Fig. 7.17 shows the stress history of Element 1 in the X, Y and Z directions, including Von Mises equivalent stress and temperature.

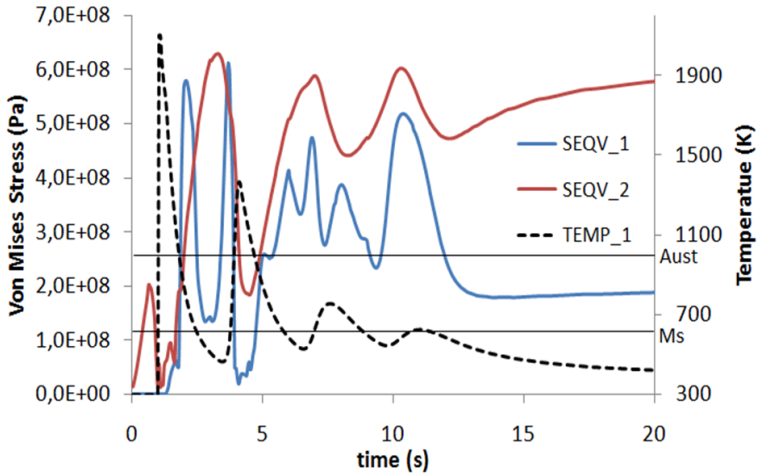

Figure 7.16: Von Mises stress and temperature histories calculated for two elements from the model with overlapped clad tracks.

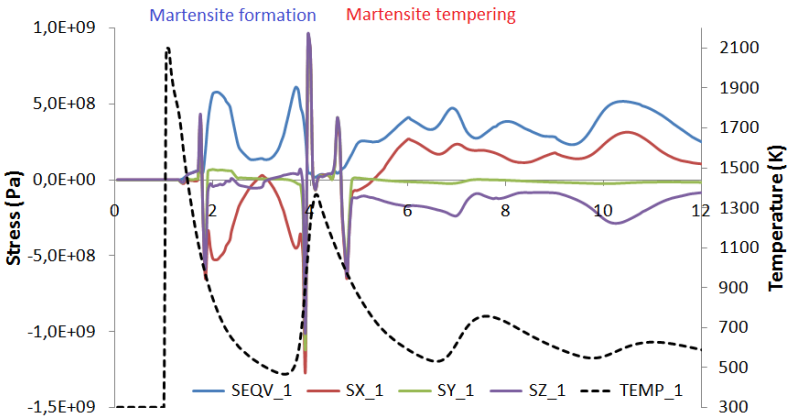

Figure 7.17: Stress and temperature histories calculated for one element of the first clad track from the model with overlapped clad tracks.

Part III

Experimental Validation Of The Models

Part III deals with experimental methods used for the validation of the models. These methods include the measurement of temperatures, residual stresses, distortions and the characterization of microstructures in metal plates. The scope of this part is to validate the predictions of the models.

Chapter 8

Measurement Of Residual Strains And Stresses

Humanity needs practical men, who get the most out of their work, and, without forgetting the general good, safeguard their own interests. But humanity also needs dreamers, for whom the disinterested development of an enterprise is so captivating that it becomes impossible for them to devote their care to their own material profit.

Marie Curie.

Abstract: This chapter explains briefly the nature of residual strains and stresses, and gives an outline of some of the techniques available to measure them, introducing some of the methods used for the experimental part of this thesis.

8.1 Introduction

Residual strains and stresses are those which remain in a body that is at equilibrium with its surroundings and without external loads applied.

Residual strains are responsible for workpiece deformation and material hardening, whereas residual stresses can be very detrimental to the material service performance, including an increase susceptibility to corrosion, and to the fatigue life of a component.

Different types of stress are characterized according to the characteristic length scale over which they self-equilibrate (Fig. 8.1). Type I stresses or macrostresses vary continuously over large distances (e.g. the workpiece). They are mainly thermally or mechanically induced. Type II stresses vary over the grain scale, existing nearly always in polycrystalline materials simply from the fact that the elastic and thermal properties vary for different grain orientations. Type III stresses have a characteristic length scale in the range of the atomic scale, and comprise stresses produced due to coherency at interfaces between equal lattices with different parameters and dislocation stress fields.

From an engineering perspective, the relevant residual stresses are type I. The stresses measured in the subsequent chapters and those predicted by the models belong to this type.

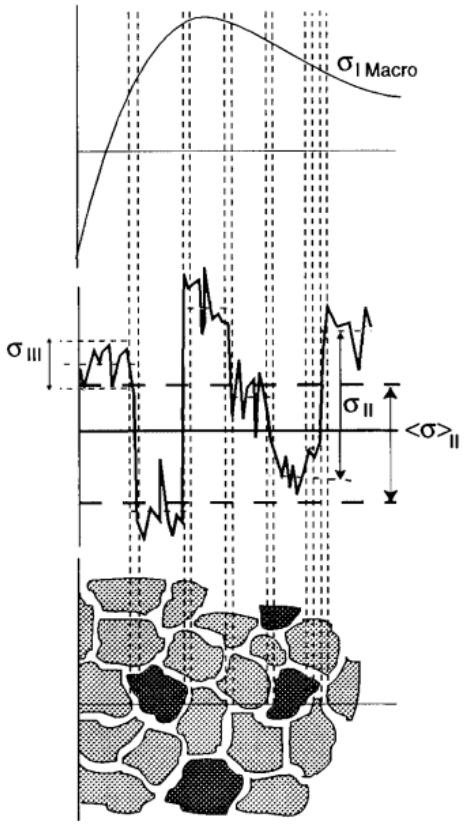

Figure 8.1: Residual stress types and their characteristic length scales in which they self-equilibrate (*from [25]*)

8.2 Techniques To Measure Residual Stresses

The techniques available to measure residual stresses can be divided into two groups: mechanical methods and physical methods [25].

Mechanical methods are based in the stress relaxation produced by the deliberate removal of material, which generates distortions in the workpiece that can be monitored to estimate the previous residual stress state through a back-calculation process. The main mechanical methods are hole drilling, saw cutting or layer removal techniques. They use strain gauges (in the shape of rosettes or film strips) to measure the distortions after the material removal. In some cases strain gauges can be used during the process that causes the residual stress (e.g during the deposition of a coating).

Hole drilling and saw cutting techniques are cheap and widely used for the task. They give the equivalent stress by measuring two stress components, obtaining unreliable measurements in certain cases [273]. Layer removal techniques measure the curvature of the plate after removing a layer of material, however, the relationship between curvature and residual stress is not unique, existing some ambiguity on the measurements.

Physical methods are based on the change of some physical properties due to the presence of residual stresses. They include X-ray diffraction, neutron diffraction, ultrasonic methods, magnetoacustic Barkhausen emission, Eddy currents and piezospectroscopic methods.

Among the diffraction methods, neutron diffraction has the advantage of higher penetration than X-rays for wavelengths comparable to the atomic spacing of materials. They usually penetrate many centimeters in engineering materials [274]. However, hard X-rays produced by large synchrotrons can penetrate from several millimeters to a few centimeters inside the materials, having a higher lateral resolution than neutrons. On the other hand, laboratory X-rays cannot penetrate the material and therefore their measurements are restricted to the surface of the workpiece.

8.3 Techniques Selected For The Validation Of The Models

Usually the experimental validation of numerical models is a challenging task. To validate the models developed for this thesis, a series of measurements of different nature were performed.

For the thermal models direct temperature measurements using thermocouples were compared with the simulated thermal histories. In laser cladding the analysis of the microstructure of the samples allowed the determination of dilution zones and heat affected zones, which are indicative of isotherms at characteristic temperatures that can be compared with the temperature field predicted by the model.

Validation of kinetic models involved microstructural studies on hardenable steel samples along with microhardness measurements. Laser cladding samples with Ti6Al4V deposited on pure titanium were studied as well.

For mechanical models several laser bending tests were done, in which deflection of thin plates was measured after several laser passings. However, direct measurement of stresses requires the use of the techniques introduced in the previous section. As an starting point, the capabilities of nanoindentation techniques to assess residual stress profiles were explored in order to obtain a qualitative picture of the residual stresses at the surface. However, to fully characterize the stress field inside the samples, measurements using diffraction of synchrotron radiation were performed at the European Synchrotron Radiation Facility (ESRF).

Chapter 9

Measurement Of Temperatures And Distortions On Steel Plates

A scientist can discover a new star, but he cannot make one. He would have to ask an engineer to do that.

Gordon L. Glegg.

Abstract: This chapter presents the results of laboratory measurements performed in several experimental tests with different materials for the validation of the models. The measurements include temperatures and bending angles during the laser heating of stainless steel and carbon steel plates.

9.1 Measurement Of Temperatures

Measurements of temperature histories during the heating and cooling phases of experimental tests can be directly compared with the ones calculated by the thermal model, and hence check the accuracy of its predictions.

The measurement of temperatures can be performed with several methods: using thermocouples attached to several locations of the workpiece, using a pyrometer aimed to a certain point of the surface of the workpiece, using a thermal camera to measure the whole temperature map in the surface of the workpiece and the cutting of the samples to study the melted zones and/or heat affected zones, in order to correlate their shapes with the calculated ones.

The last method will be discussed in the next chapter, applied to the validation of the metallurgical model and the laser cladding model. In this chapter measurements performed with thermocouples during the laser heating of two different materials are presented.

9.1.1 Experimental Tests

Experimental tests consist in the laser irradiation of plates with a laser spot aimed at the middle of the plates, that is with zero velocity, and two or three laser pulses with a certain cooling time

Material	Composition
ST-52	**C** 0.22-0.28%, **Mn** 0.3-0.6%, **P** $<$ 0.04%, **S** $<$ 0.05%, **Fe** bal.
In 718	**Ni** 50-51%, **Cr** 17-21%, **Fe** bal., **Nb** 4.75-5.5%, **Mo** 2.8-3.3%, **Ti** 0.65-1.15%, **Co** 1% max., **Al** 0.2-0.8%, **C** 0.08% max., **Mn** 0.35 max., **Si** 0.35% max., **Cu** 0.3% max., **S** 0.015% max., **P** 0.015% max., **B** 0.006% max.

Table 9.1: Chemical composition of carbon steel ST-52 and nickel base superalloy Inconel 718

between them. The tests were performed with a 1 kW CW Nd:YAG laser, shooting laser pulses of several seconds at low laser power. The whole temperature measurement time ranges between 90-100 seconds.

The materials chosen for the tests were the carbon steel ST-52 and nickel base superalloy Inconel 718. In Table 9.1 is included the chemical composition of both materials, and in Fig. 9.1 are represented the material properties used for the thermal simulations. The geometry of the samples is represented in Fig. 9.2, in which is also shown the location of the thermocouples on the surface of the samples along one of their symmetry planes. In order to establish a good contact between the thermocouples and the plate, they were welded to the surface of the plate using a laser pulse.

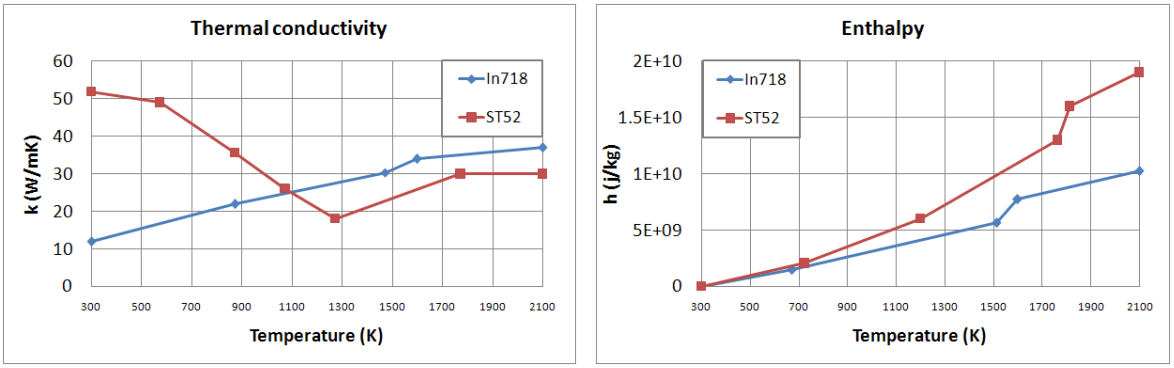

(a) (b)

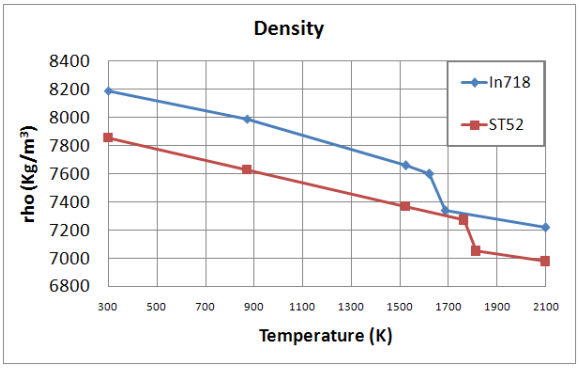

(c)

Figure 9.1: Material properties of Inconel 718 and steel ST-52 used in the thermal simulations: (a) Thermal conductivity; (b) Enthalpy; (c) Density

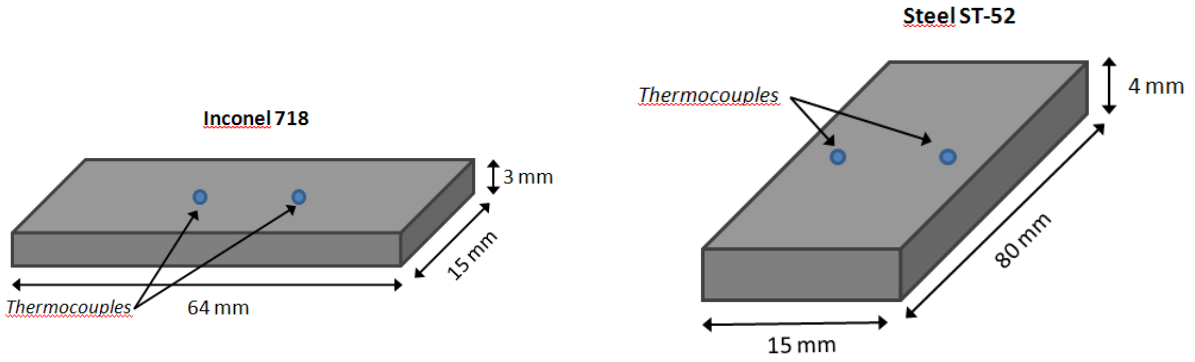

(a) (b)

Figure 9.2: Geometry of the samples and location of the thermocouples: (a) Inconel 718 (b) Steel ST-52

The parameters for the different tests, regarding laser pulse characteristics, thermocouple distance to the center of the plate and time interval between pulses are summarized in Table 9.2.

9.1.2 FEM Model

Several models were created for the simulation of the experimental tests. Taking advantage of the symmetries of the problem, in order to reduce the computing time, only one quarter of the sample was modelled (Fig. 9.3). The symmetry planes were considered adiabatic, and the rest of the surfaces of the samples had convection heat transfer with the surrounding ambient, except for the area submitted to the laser irradiation.

The two different geometries of the samples were meshed with linear hexahedral elements, studying convergence of the results with different levels of refinement. Computing time for the coarser models varied between 10-20 minutes, whereas with the refined models it ranges between 1-3 hours, in a 2.4 GHz Intel Dual Core PC, with 2Gb of RAM. The results converged in a satisfactory manner with increasing mesh refinement, selecting from these tests a suitable

Sample	**1**	**2**	**3**
Material	In718	In718	ST-52
Beam diameter (mm)	1.6	1.6	1.6
Power (W)	300	300	250
TC distance (mm)	±2.8	±2.8	±4
N° of shots	2	3	3
Shot duration (s)	7,7	7,7,3	5,5,5
Time between pulses (s)	5	5,5	20,20

Table 9.2: Parameters used in the experimental tests for the measurement of temperatures

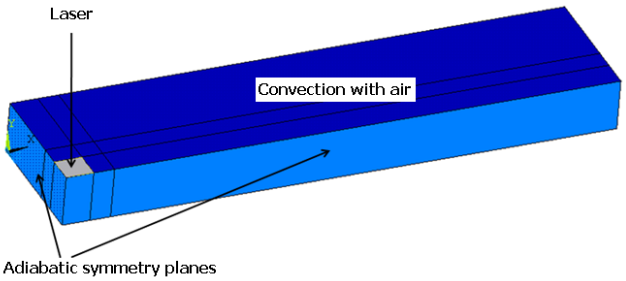

Figure 9.3: Geometry of the samples used in the FEM models

element size for the simulations.

Additionally, a different model was created to simulate with greater accuracy the cooling part of the process. This model includes a plate situated under the sample in order to simulate the heat transfer from the bottom of the sample to the supporting plate, by conduction heat transfer with a certain thermal resistance between both materials (Fig. 9.4). However, this method introduces more elements into the problem, thus a different approach was tried, simulating this part of the heat transfer assuming convection heat transfer with ambient air with a fictitious convection coefficient.

The laser used for the experimental tests was a fiber guided Nd:YAG laser, having an output beam with a top hat profile. The absorptivity of the samples was taken from bibliography [51] and fine tuned with the experimental tests. The convection coefficient was previously measured in laboratory, resulting a value of $h = 40\ W/m^2K$, which is a typical value for air. The initial temperature of the samples as well as the temperature of surrounding air, was set to 27°C (300 K).

The fictitious convection coefficient h_B for simulating the heat transfer from the bottom of the plate was calibrated with one sample, being $h_B = 120\ W/m^2K$.

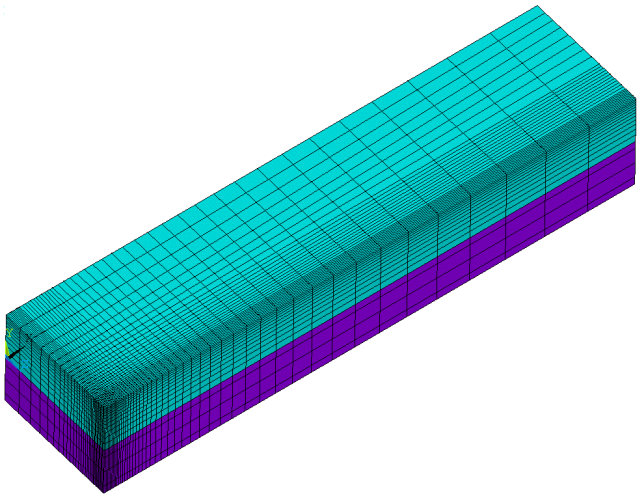

Figure 9.4: One of the models having a plate underneath the sample

9.1.3 Results And Discussion

In Fig. 9.5a and Fig. 9.5b are represented the results from the tests with the Inconel 718 plates. The simulated temperature histories are in good correlation with the temperatures measured by the two thermocouples and within the experimental errors, both in heating and cooling.

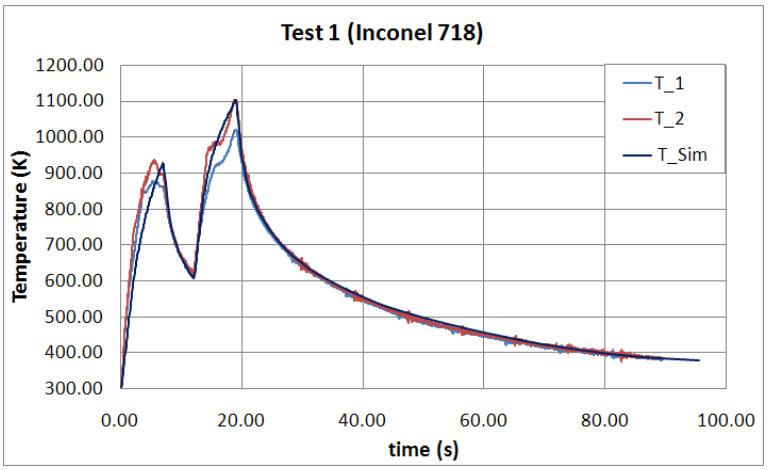

(a)

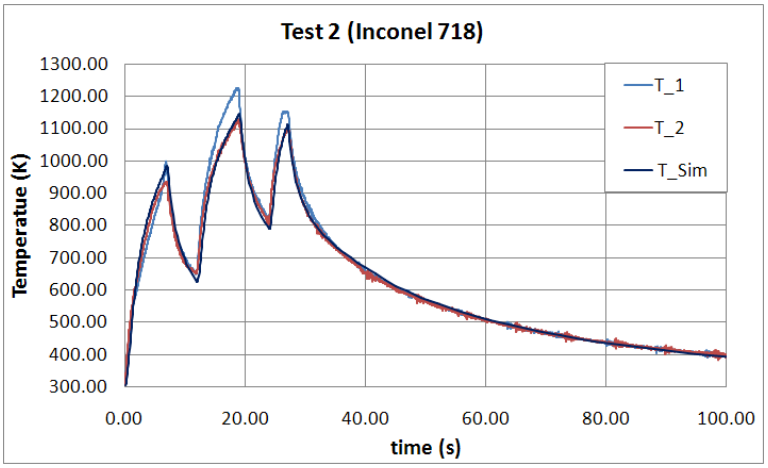

(b)

Figure 9.5: Temperature histories, measured and simulated, from the experimental tests with Inconel 718 plates: (a) Test 1; (b) Test 2

Fig. 9.6 shows the temperature histories for the test with the steel ST-52. The measurements and the simulated results are in excellent agreement.

In both cases the application of a fictitious convection coefficient for the simulation of the heat transfer from the bottom of the plate show very good results during the cooling stage of the process in all the samples, saving calculation time and model complexity compared to the model with a supporting plate underneath.

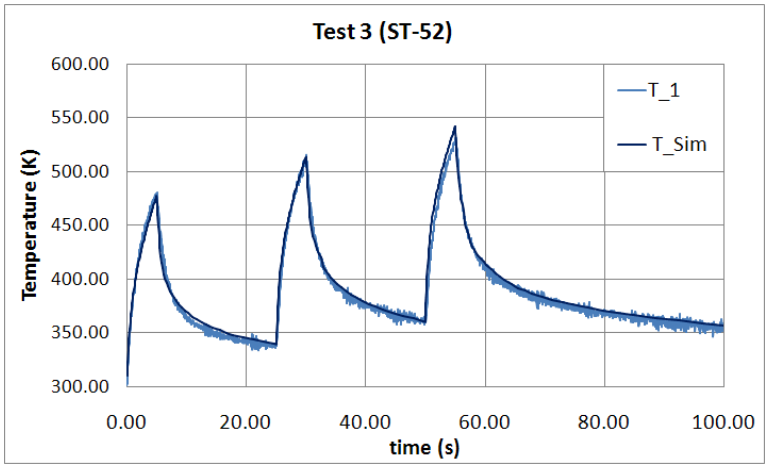

Figure 9.6: Temperature histories, measured and simulated, from the experimental tests with steel ST-52 plates: Test 3

9.2 Measurement Of Bending Angles

In the following tests, several plates of two different steels were submitted to several laser passings with different parameters in order to produce measurable distortions on them. Specifically, the measured quantity was the bending angle of the plates.

There are three main bending mechanisms. The most important is the thermal gradient mechanism (TGM) which is the mechanism explained in Chapters 6 and 7 for LTH and laser cladding. It is primarily caused by the thermal gradients along the thickness of the plates. They generate a differential expansion in that section, which coupled with the increased plasticity of the material at high temperatures, leads to significant cumulative plastic deformations during the heating phase. Afterwards, the plastically deformed material will have a thermal contraction during the cooling phase, pulling the surface of the plate and making it bend. The direction of the bending angle is always positive (towards the laser beam).

Other bending mechanisms are the buckling mechanism (BM) and the upsetting mechanism (UM). The buckling mechanism is encountered during the bending of thin sheets with a laser beam which is several times larger than the thickness of the plate. There is no steep temperature gradient through the sheet thickness. Due to heating, thermal compressive stresses develop in the sheet which results in a large amount of thermo-elastic strain which in turn results in local thermo-elasto-plastic buckling of the material. This buckle is generated along the moving direction of the laser beam scanning. The direction of the bending angle is not defined by the process itself as it is for the TGM. The part can be made to bend in either the positive or the negative directions depending on a number of factors including the process parameters, the pre-bending orientation of the sheet and the pre-existing residual stresses [275].

For the UM the process parameters are similar to the BM but the dimension of the heated area is much smaller compared to the sheet thickness. Due to nearly homogeneous heating of the sheet and the restrictions in thermal expansion from the surrounding material, the sheet is compressed with an almost constant strain along its thickness, causing its shortening and an increase in thickness.

Material	Composition
DC01	**C** 0.05%, **Mn** 0.2%, **P** 0.024%, **S** 0.01%, **Si** 0.01%, **Al** 0.041%, **Fe** bal.
AISI 304	**Cr** 18-20%, **Ni** 8-10.5%, **Fe** bal., **Mn** 1% max., **Si** 1% max., **C** 0.08% max., **P** 0.045% max., **S** 0.03% max.

Table 9.3: Chemical composition of very low carbon steel DC01 and stainless steel AISI 304.

9.2.1 Experimental Tests

The materials selected were the stainless steel AISI 304, and the very low carbon steel DC01. The composition of both materials is listed in Table 9.3.

The material properties used in the thermal simulations are represented in Fig. 9.7, and in the mechanical simulations in Fig. 9.8.

Sheets 1 mm thick of both materials were used in the experimental tests. The dimensions of the samples were the same in both cases: 160x40x1 mm. The samples were clamped at one end, overhanging like a cantilever beam. In the stainless steel samples the laser trajectory is close to the clamped end, situated at 40 mm of it (Fig. 9.9a), whereas in the carbon steel samples the

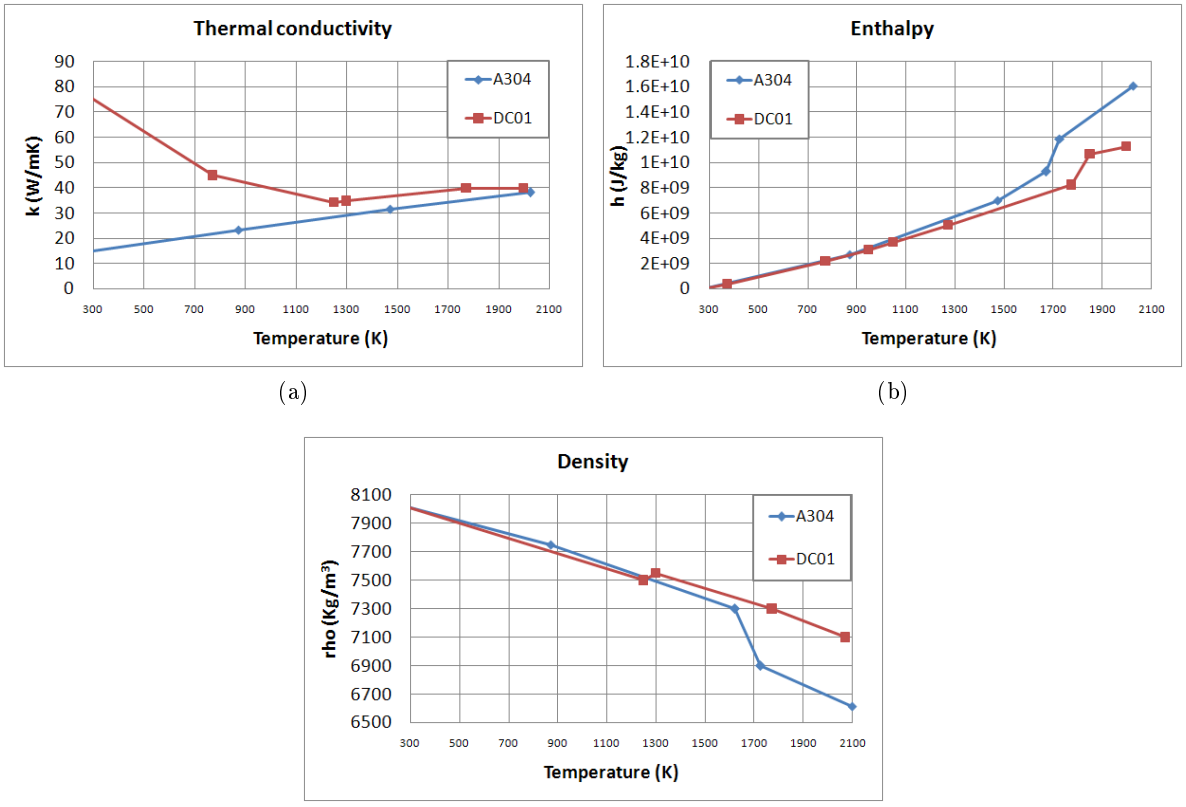

Figure 9.7: Material properties of AISI 304 and DC01 used in the thermal simulations: (a) Thermal conductivity; (b) Enthalpy; (c) Density

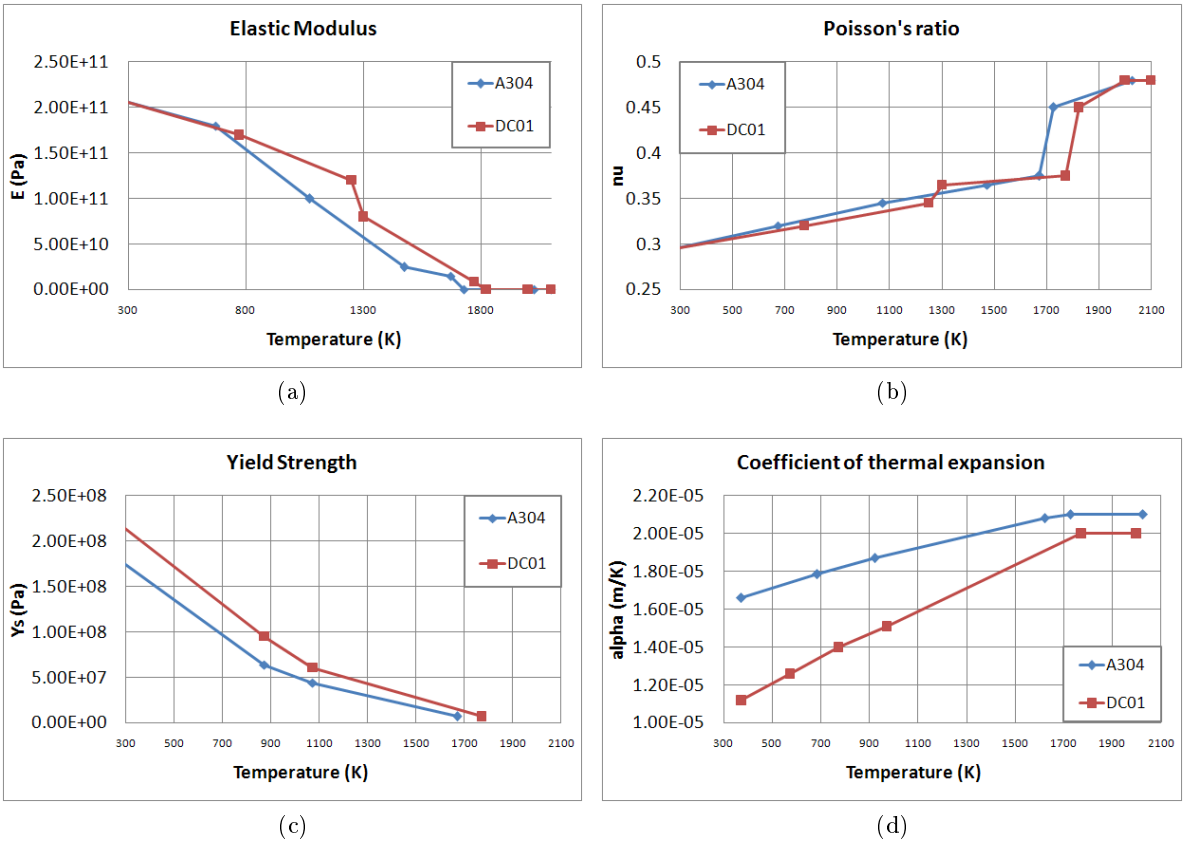

(a) (b) (c) (d)

Figure 9.8: Material properties of AISI 304 and DC01 used in the mechanical simulations: (a) Elastic modulus; (b) Poisson modulus; (c) Yield strength; (d) Coefficient of thermal expansion

laser trajectory was situated at the middle of the samples (Fig. 9.9b). The only reason for this difference was the intention to simulate the process assuming planar symmetry along the laser path and therefore reduce the number of elements of the model, which had a smaller laser spot applied and consequently a smaller element size.

The tests were done with different parameters regarding laser power, laser velocity, laser spot diameter and number of laser scans. The time between laser scans was maintained constant at 3 seconds. The parameters used for the tests are summarized in Table 9.4.

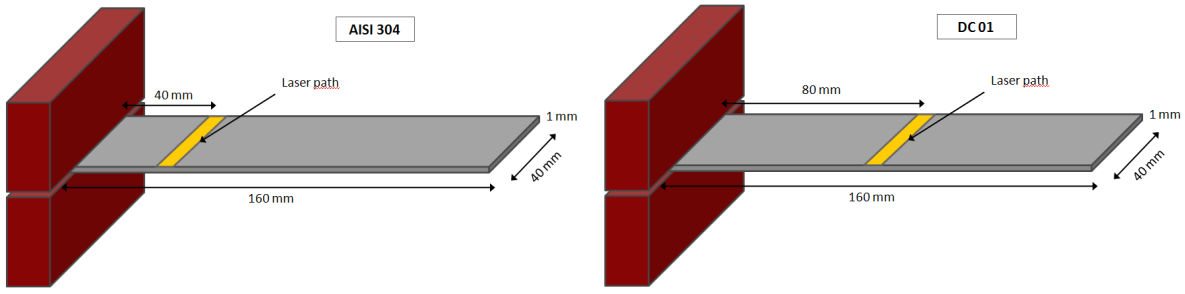

(a) (b)

Figure 9.9: Scheme of the experimental setup for the bending tests: (a) AISI 304; (b) DC 01

Material	**AISI304**			**DC01**		
Sample	**1**	**2**	**3**	**4**	**5**	**6**
Beam diameter (mm)	2.2	2.2	2.2	2.2	1	1
Power (W)	800	550	350	800	190	310
Velocity (mm/s)	15	10	5	15	5	5
N^o of laser scans	8	8	5	3	3	6

Table 9.4: Parameters used in the experimental tests for the measurement of temperatures

9.2.2 FEM Model

Two models were created for the simulation of the experimental tests. The tests with the stainless steel plates have 4 elements across their thickness. They do not present symmetry so the complete sheet was modelled, with a refinement in the area close to the laser path (Fig. 9.10a). Vertical displacement of the external nodes of the elements located at the shorter end were constrained to simulate the clamping condition.

Models for carbon steel have 5 elements across the thickness. They have planar symmetry along the laser path, so only half of the plate was modelled (Fig. 9.10b). The nodes of the symmetry plane have a symmetry boundary condition, with exception of a node located on the lower part of that plane, that has restricted all the displacements in order to prevent rigid body motion.

9.2.3 Results And Discussion

Fig. 9.11 shows the calculated Von Mises stresses and plate deformations corresponding to the tests with the AISI 304, at two representative times of the analysis.

Results of the bending tests are summarized in Table 9.5. The agreement between simulations

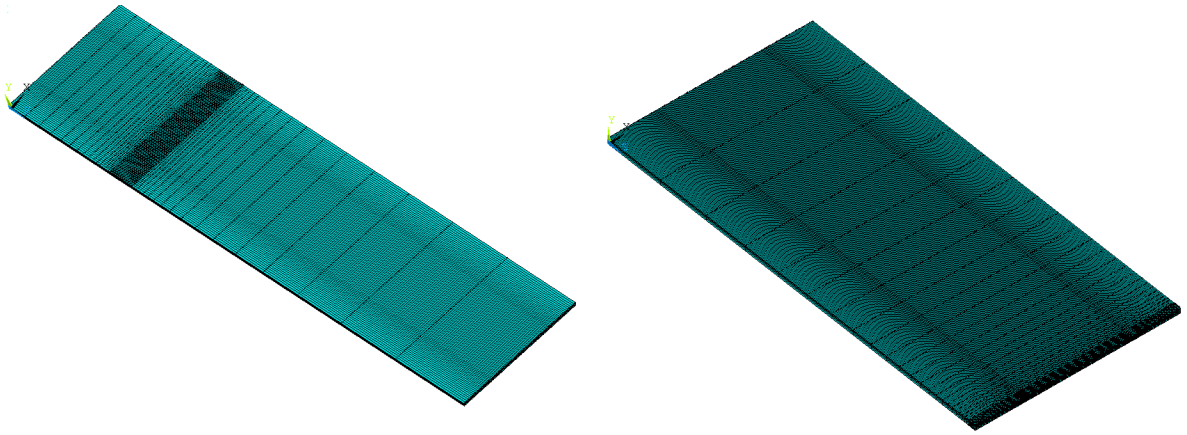

(a) (b)

Figure 9.10: FEM meshes used for the bending tests: (a) AISI 304; (b) DC 01.

Material	**AISI304**			**DC01**		
Sample	**1**	**2**	**3**	**4**	**5**	**6**
Measured bending angle (°)	15.00	11.66	6.91	0	2.92	8.26
Calculated bending angle (°)	14.56	11.32	7.24	0.21	3.01	8.58

Table 9.5: Results from the bending tests.

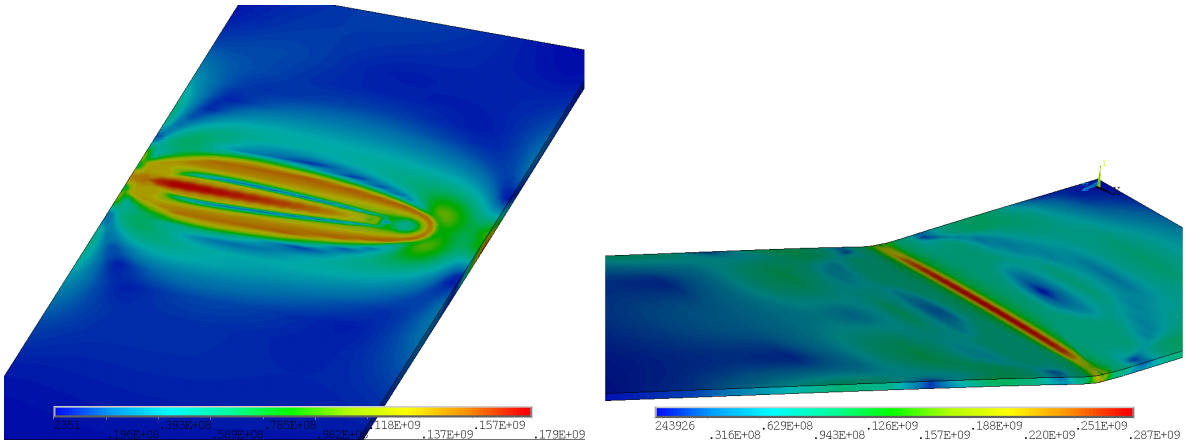

(a) (b)

Figure 9.11: Deformations and stresses of the AISI 304 bending samples: (a) during the first laser passing; (b) during the final cooling down.

and experimental results is good. The calculated values are close to the experimental ones in all cases.

It should be remarked the test 4, in which the experimental results showed a zero deformation of the plate. This is partially caused by the high thermal conductivity of DC01 steel, which minimizes thermal gradients that are already lower than in the next cases due to the higher diameter of the laser spot. Besides, phase transformations compensate thermal expansion during both heating and cooling, leading to the resulting zero bending angle. The rest of the tests with DC01 steel were performed with a smaller laser spot, inducing a very superficial melting of the plate and causing significant distortions due to the pronounced contraction of the material.

Chapter 10

Microstructural Analysis

We see only what we know.
Johann Wolfgang von Goethe.

Abstract: In this chapter the microstructure and hardness profiles calculated by the LTH model with phase transformations are presented and compared with experimental tests on carbon steel plates. The tests consist in the laser surface melting of a steel plate performing several tracks, with similar parameters and different spacing between them. Additionally, samples prepared using laser metal deposition of titanium alloys were studied and compared with the predictions of the titanium phase transformation model. The samples include single tracks as well as overlapped and superposed multitracks.

10.1 Carbon Steel Tests

Several laser surface melting (LSM) tests were carried out using carbon steel plates of AISI 1045 and a 2 kW CO_2 laser, with nitrogen as shielding gas. The tests consist of 3 laser tracks with the same parameters separated a certain distance between them, in order to study martensite generation and its tempering. The laser power was sufficient to melt the surface of the plate. Therefore, the following phases are present in the samples:

- Previously melted material.
- Retained austenite.
- Martensite.
- Tempered martensite.
- Initial ferritic-pearlitic microstructure.

The material properties of AISI 1045 carbon steel used in the simulations are represented in Fig. 10.3. The different properties between alpha and gamma phases and also phase transformations

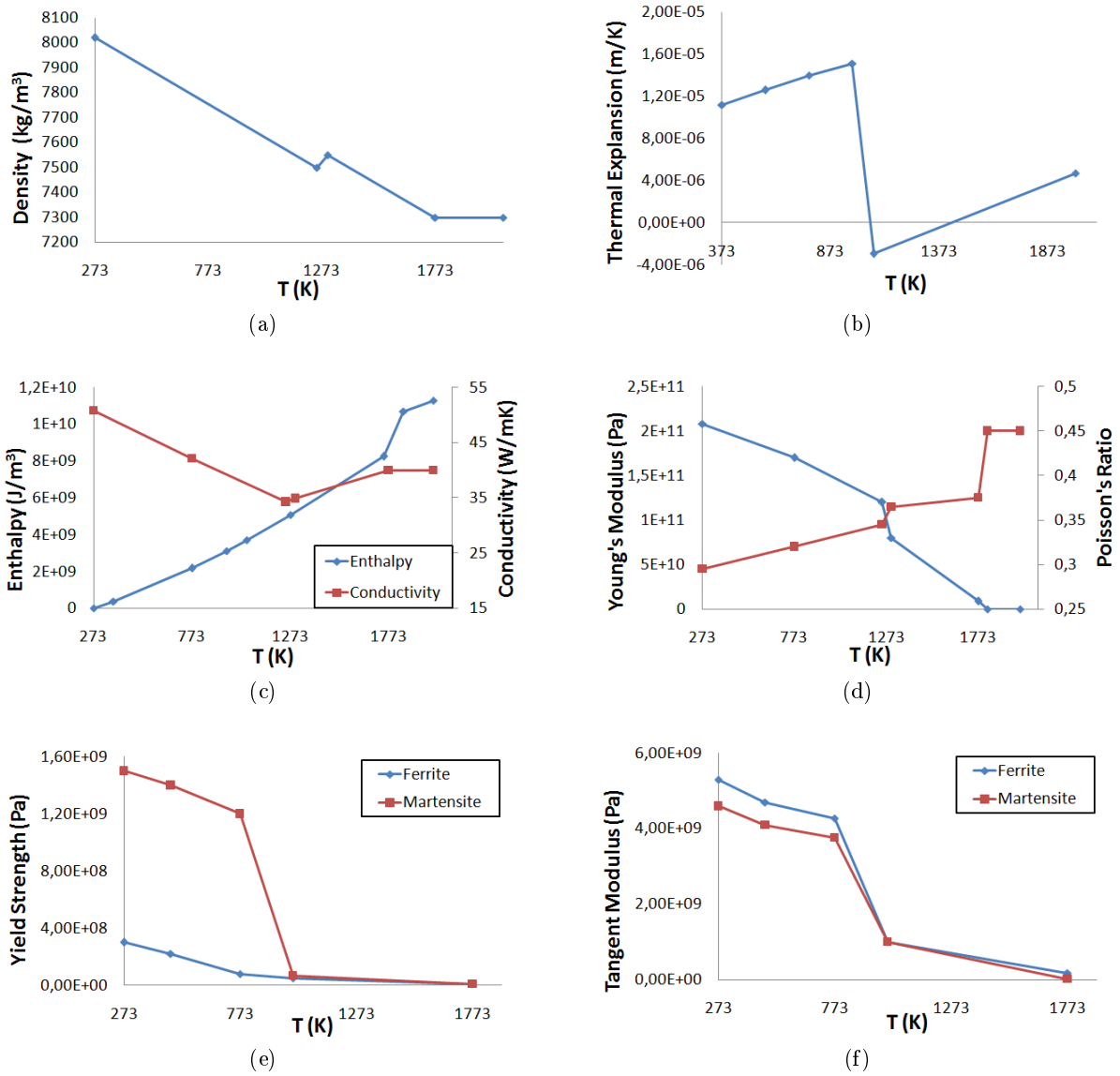

Figure 10.1: Properties of the carbon steel AISI 1045 used in the simulations.

at certain temperatures, are included. Besides, regarding mechanical properties, a distinction between martensite and the rest of the phases was made.

Test	1	2	3
Laser spot (mm)	4	4	4
Velocity (mm/s)	5	5	5
Laser power (W)	1200	1200	1200
Interspace (mm)	4	3	2

Table 10.1: Parameters of the experimental LSM tests with AISI 1045.

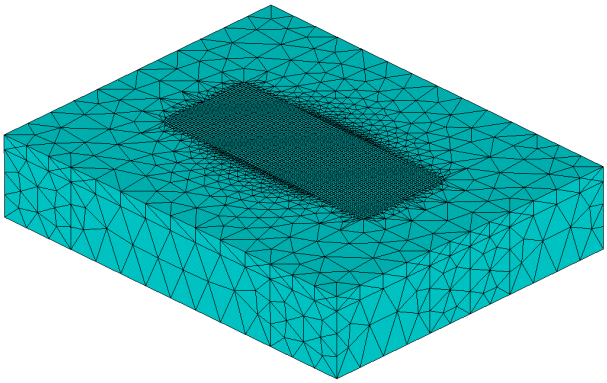

Figure 10.2: FEM mesh for the LSM tests with AISI 1045.

The mesh used in the simulations is shown in Fig. 10.2. It consists of hexahedral elements in the zone below the laser passings and coarse tetrahedral elements in the rest of the plate, in order to minimize the number of nodes. The mesh is composed of 126590 elements and 89468 nodes.

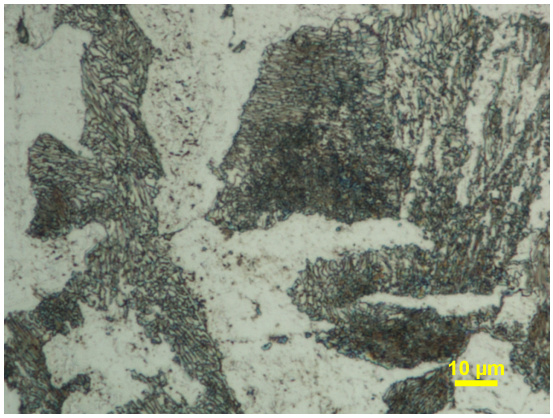

(a)

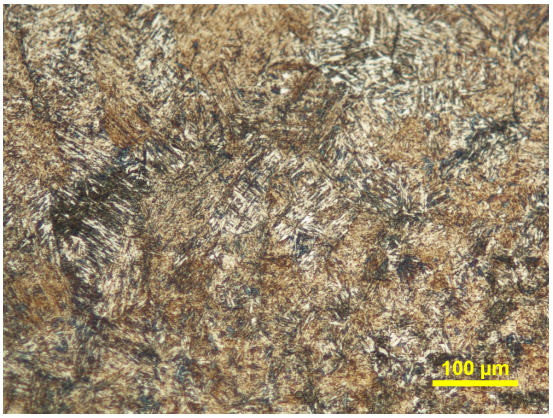

(b)

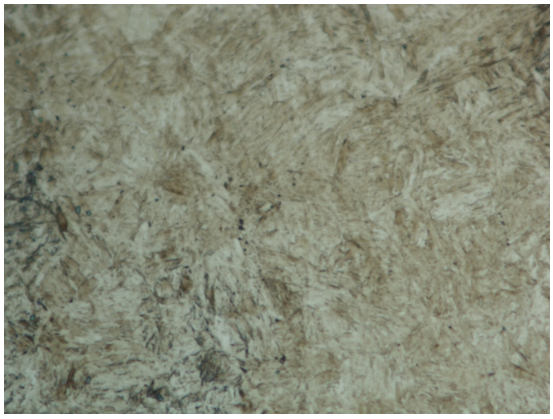

(c)

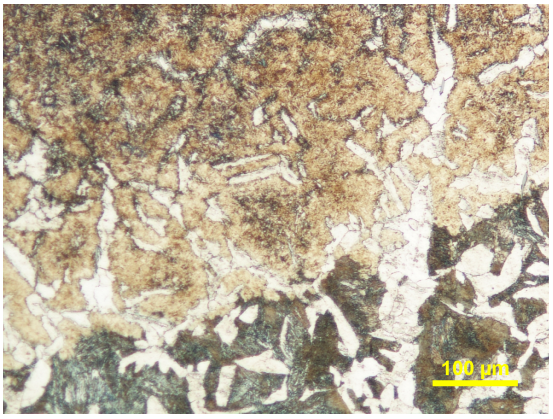

(d)

Figure 10.3: Different microstructures of AISI 1045 steel: (a) ferritic-pearlitic; (b) martensite; (c) tempered martensite; (d) interphase between ferrite-pearlite and HAZ.

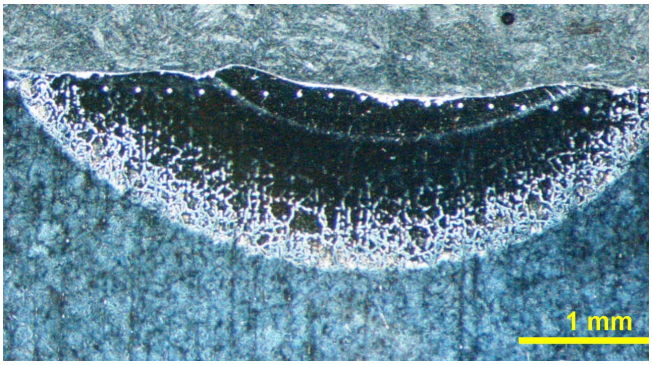

Figure 10.4: Cross section of one laser melted track, showing microindentation marks.

The tests were done with a laser velocity of 5 mm/s, laser power of 1200W and a laser spot of 4 mm with a TEM01* laser profile. The space between passings was varied in the different tests in order to produce different amounts of of tempered martensite. The parameters of the tests are summarized in Table 10.1.

After the tests the samples were cut, mechanically grounded, polished and etched to reveal their microstructural features. The base microstructure of the steel plates is composed of a ferritic-pearlitic mixture as it is shown in Fig. 10.3a. The white grains are ferrite and the black grains are pearlite in which it can be distinguised the internal ferrite/cementite lamellae. The needlelike martensite obtained after the process is shown in Fig. 10.3b. Slightly tempered martensite is shown in Fig. 10.3c, and the interphase between the base microstructure and the martensite based HAZ is shown in Fig. 10.3d.

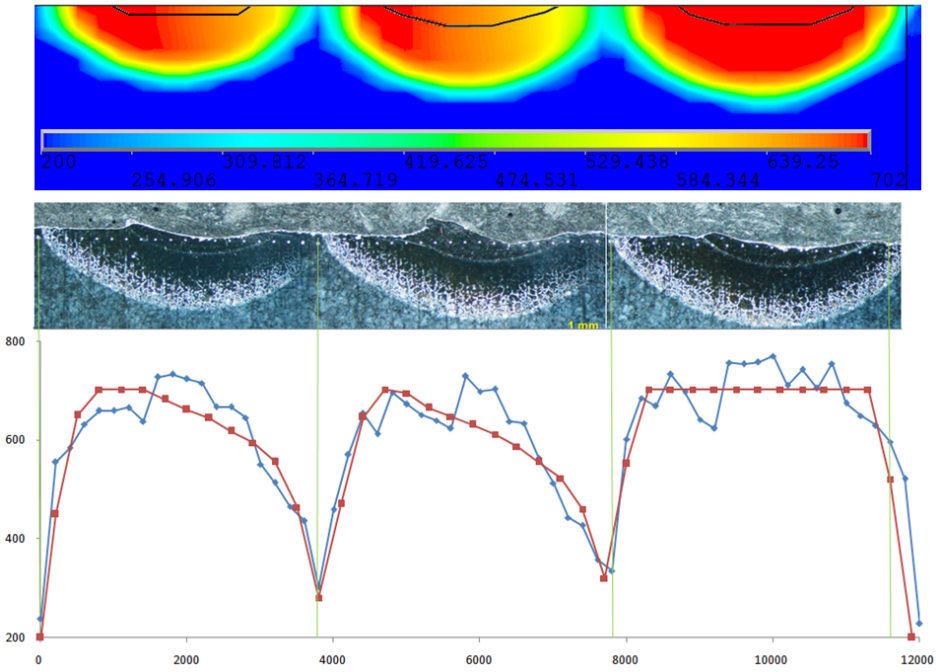

Figure 10.5: Results of Test 1. First track at left.

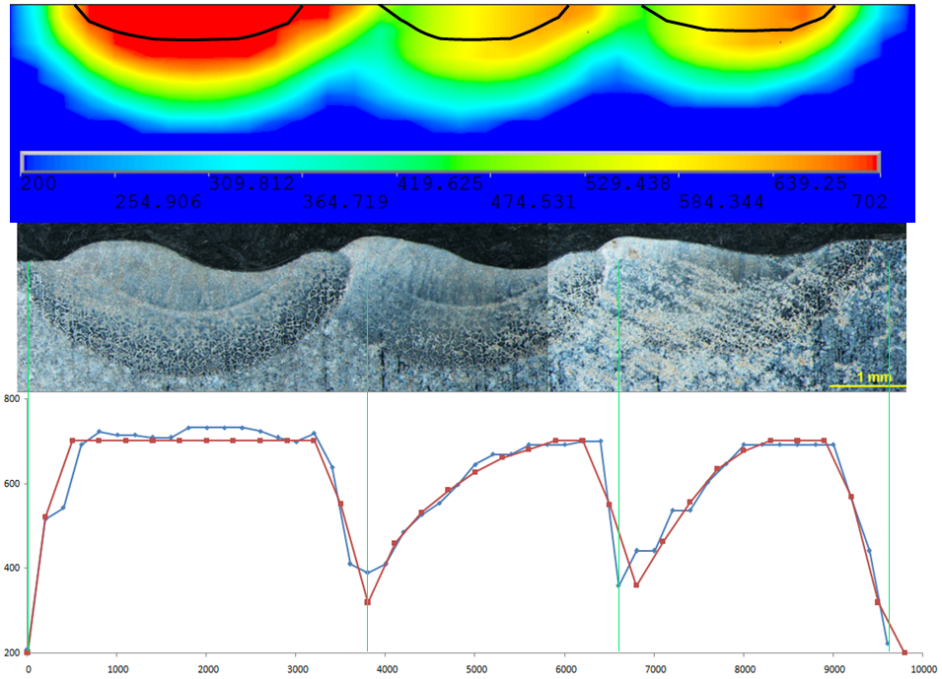

Figure 10.6: Results of Test 2. First track at right.

10.1.1 Results

In Fig. 10.4 is shown one of the laser melted tracks. The image was taken after microhardness measurements so the indentation marks are clearly visible. The different zones are easily

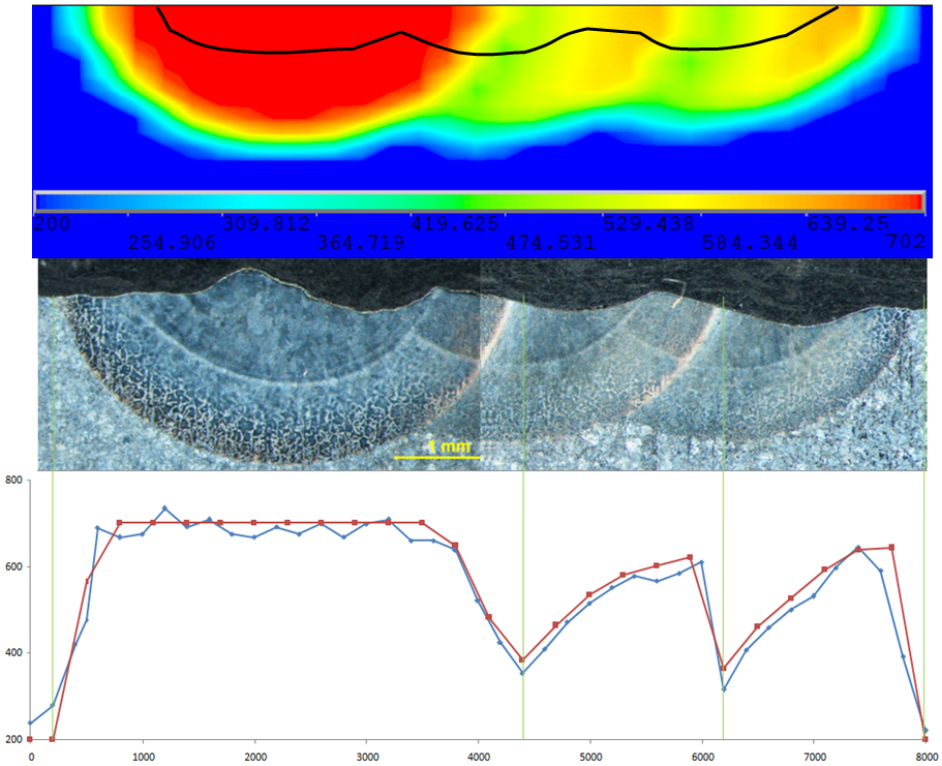

Figure 10.7: Results of Test 3. First track at right.

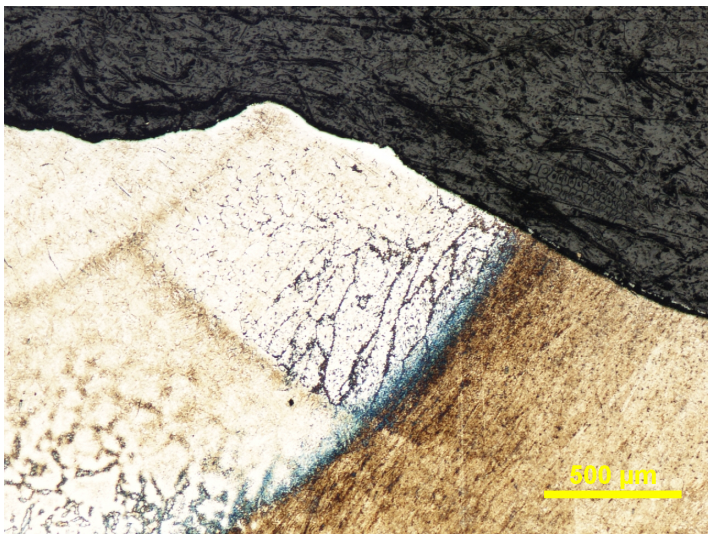

Figure 10.8: Several microstructures present in the samples.

distinguishable in the picture: melted zone, HAZ and base microstructure.

A comparison between results is shown in Figs. 10.5, 10.6, 10.7. The pictures include the

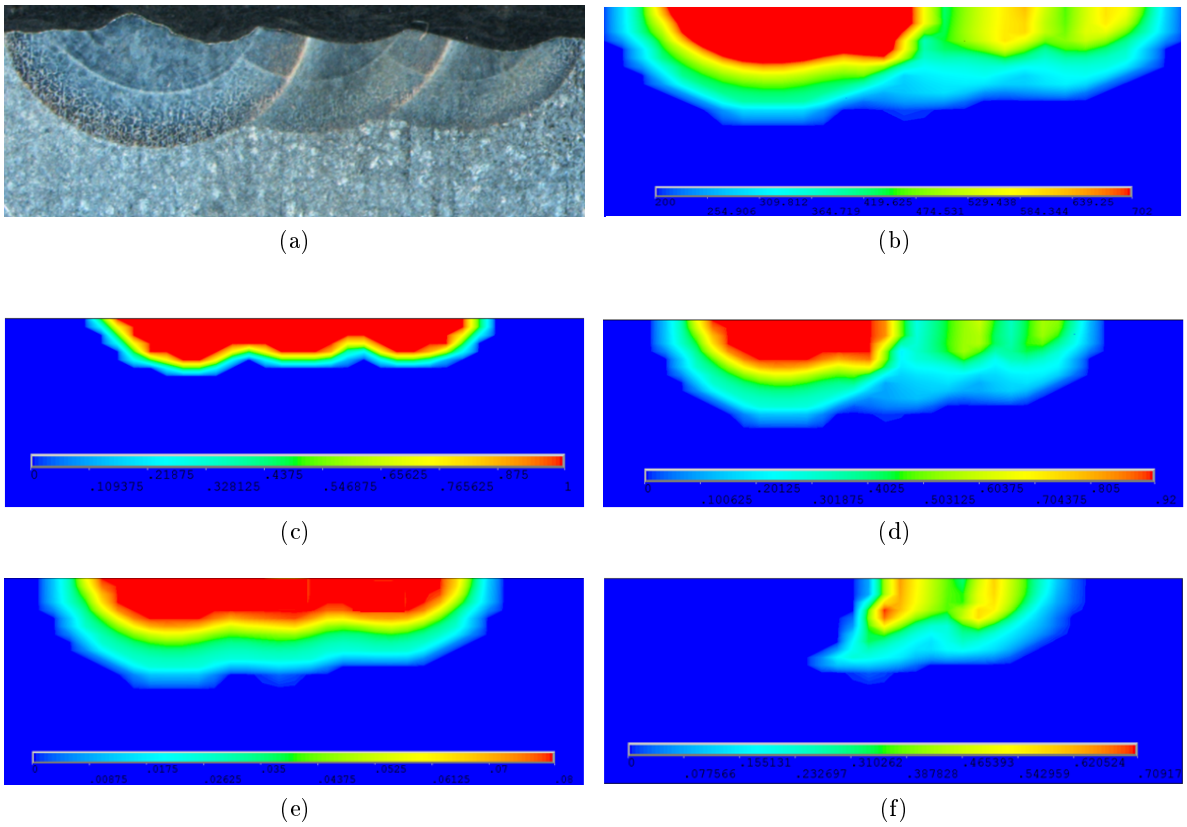

(a) (b)

(c) (d)

(e) (f)

Figure 10.9: (a) Microstructure of the experimental sample; data predicted by the model: (b) hardness profile; (c) melted zones; (d) martensite volume fraction; (e) retained austenite volume fraction; (f) tempered martensite volume fraction.

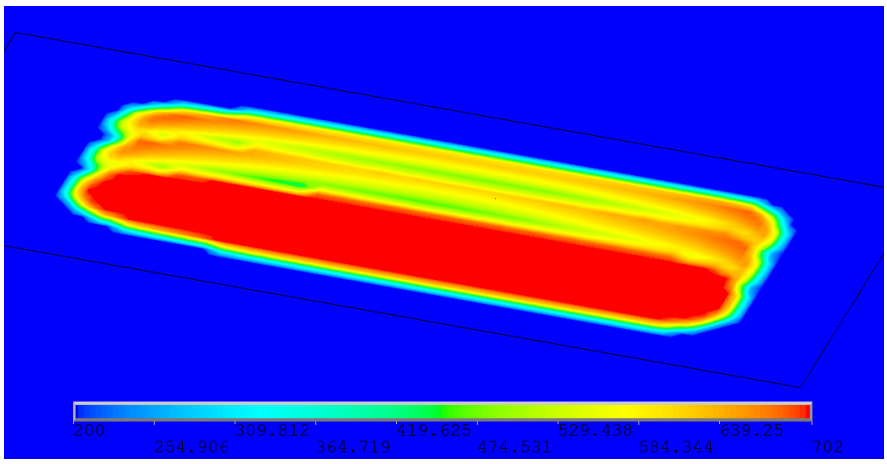

Figure 10.10: Hardness map calculated for Test 3.

hardness map predicted by the model, as well as the measured and calculated hardness profiles along an horizontal line situated between 100-200 μm below the surface. The predicted melted zones are marked with solid black lines in the calculated hardness map.

The microstructure is complex and it is composed of several phases. An example of a zone in which several phases are present, is shown in Fig. 10.8, where it can be distinguished: melted zones, zones previously austenitized and transformed to martensite from the base ferrite-pearlite microstructure, zones with tempered martensite, and finally, zones where the previously formed martensite was subsequently reaustenitized due to the heating of the next laser passing and subsequently transformed to martensite.

Fig. 10.9 includes several pictures taken from the model and the cross section of the experimental sample to which they correspond (Test 3). The pictures include the hardness map, melted zones and volume fractions: martensite, retained austenite and tempered martensite. The hardness profile on the top surface is shown in Fig. 10.10

Calculated and measured profiles agree well, showing only minor differences. Melted zones, heat affected zones and tempered zones calculated in the simulations, are similar to the obtained in the experimental tests. However, the tests which have deeper melted zones present higher differences regarding melted depths compared with the calculated ones. This is something expected because the model neglects the fluid dynamic convection processes that take place in the molten pool, simulating only heat transfer by conduction.

10.2 Titanium

Several tests comprising the laser metal deposition of Ti6Al4V on Ti grade 2 (pure titanium) plates were carried out in the laboratory. The dimensions of the titanium plates were 40x10x3 mm and the length of the clad tracks deposited was 30 mm. All the samples were preheated to 822 K. The shielding gas was helium, and the powder feed rate was 2 g/min. The specimens were processed using a Nd:YAG laser working in continuous wave mode and a coaxial laser cladding nozzle. The laser profile was a top hat with a 2 mm beam diameter on the surface of the workpiece. Beam power varies in the interval between 600 and 900 W, and process velocity shifts between 8 and 12 mm/s.

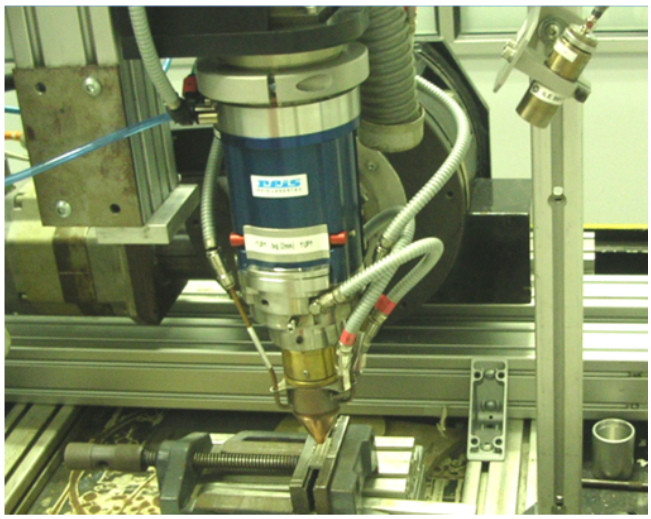

Figure 10.11: Experimental setup for the laser cladding of Ti6Al4V on pure Ti.

Temperature of a fixed spot on the surface of the workpiece was measured during the process by means of a two-color pyrometer. Experimental setup is shown in Fig. 10.11. The process parameters used for the tests are summarized in Table 10.2.

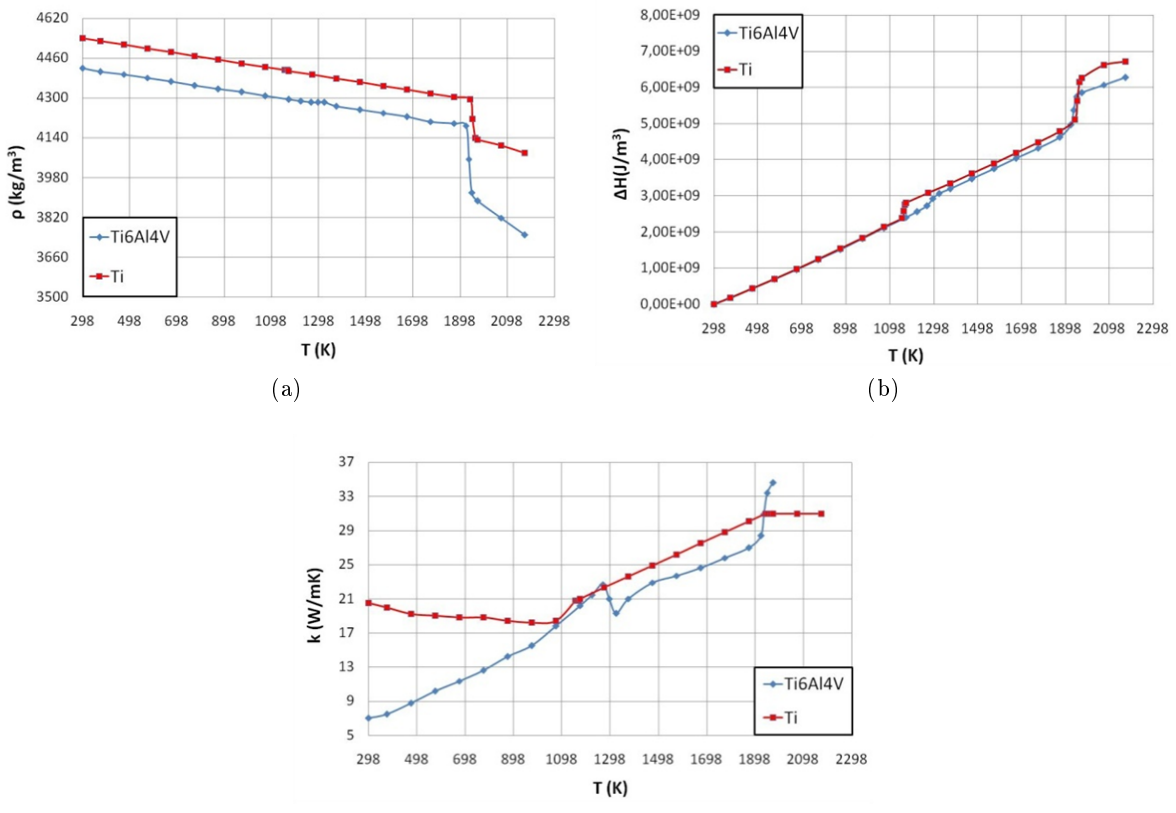

(a) (b)

(c)

Figure 10.12: Thermal properties of Ti6Al4V and pure Ti.

Test	Power (W)	Velocity (mm/s)
1	700	12
2	600	8
3	900	12

Table 10.2: Parameters of the experimental tests carried out with titanium.

The thermal material properties used in the simulations were taken from [276] and are represented in Fig. 10.12.

10.2.1 Single Clad Tracks

Models with single clad tracks were created for this study. Their meshes have a high density of elements in the zones with higher gradients, with an element size that ranges between 0.1-2 mm. The models are entirely meshed with linear hexahedral elements. All the models have 20721 elements and 24010 nodes. An example of the mesh is shown in Fig. 10.13.

During the process the two-color pyrometer aimed at a fixed point on the plate and registered a signal which is proportional to the temperature of the measured area. The pyrometer was calibrated with furnace tests, however on the measured area the estimated spot size was between 1.5-2 mm, which is of the approximate same size of the clad tracks. In this measurement area there are points with very different temperatures and emissivities and therefore the measurements cannot be considered precise in any manner. For the comparison with the simulated temperatures, the thermal histories of several nodes were integrated over the area of the pyrometer spot, accounting for the changing geometry and clad deposition. This comparison is shown in Fig. 10.14, showing an acceptable agreement between both.

All samples prepared during the experimental tests in the laboratory were transversally cut, mechanically grounded, polished with silica suspension and etched with Kroll's etch. Cross-

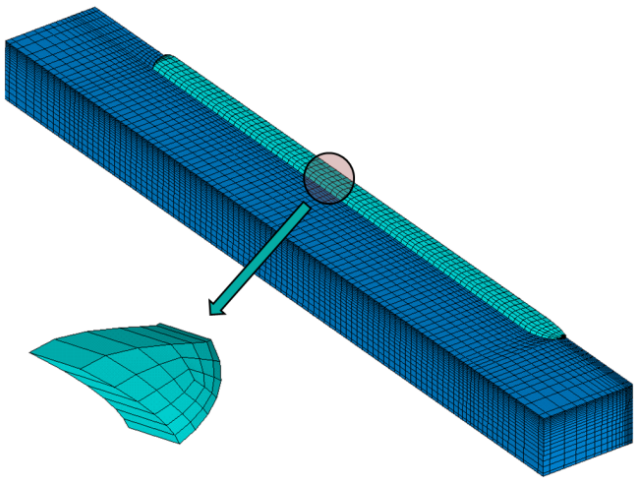

Figure 10.13: Mesh used in the simulations of laser cladding of Ti6Al4V on pure Ti.

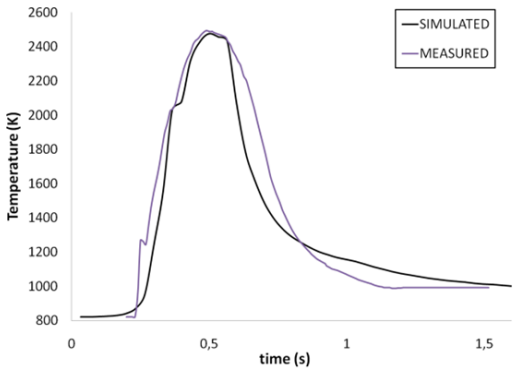

Figure 10.14: Comparison between measured and simulated temperature histories.

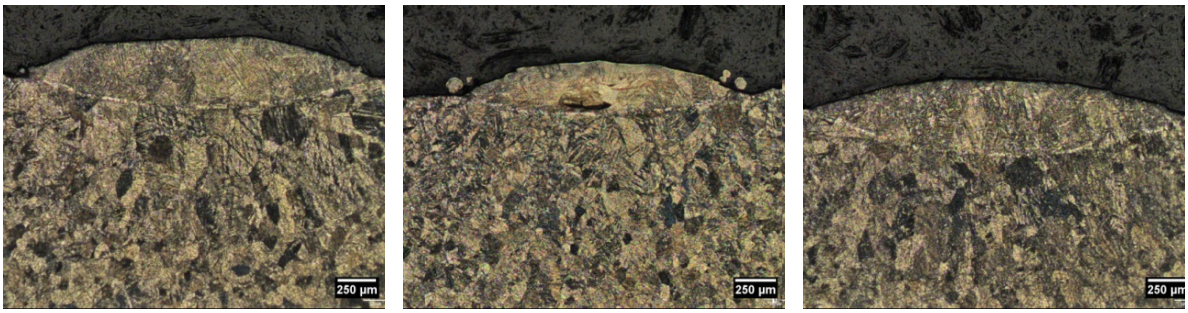

(a) (b) (c)

Figure 10.15: Microstructure of the different samples of Ti6Al4V on pure Ti.

sections of the resulting claddings were examined by optical and scanning electron microscopy (SEM). Fig. 10.15 shows the metallography of the cross sections of the samples with single clad tracks. Fig. 10.16a shows the SEM image of the upper part of the clad track in sample 1, with a typical martensitic structure. EDX analyses were carried out in several parts of the clad track to study dilution. In Fig. 10.16b is represented the semiquantitative analysis of the 2 boxes marked in Fig. 10.16a.

(a)

Processing option : All elements analysed (Normalised)

Spectrum	Al	Ti	V	Total
Spectrum 1	5.30	90.87	3.83	100.00
Spectrum 2	5.27	90.74	3.99	100.00
Mean	5.28	90.81	3.91	100.00
Std. deviation	0.02	0.09	0.11	
Max.	5.30	90.87	3.99	
Min.	5.27	90.74	3.83	

All results in weight%

(b)

Figure 10.16: (a) SEM image of the Ti6Al4V deposited; (b) EDX semiquantitative measurements.

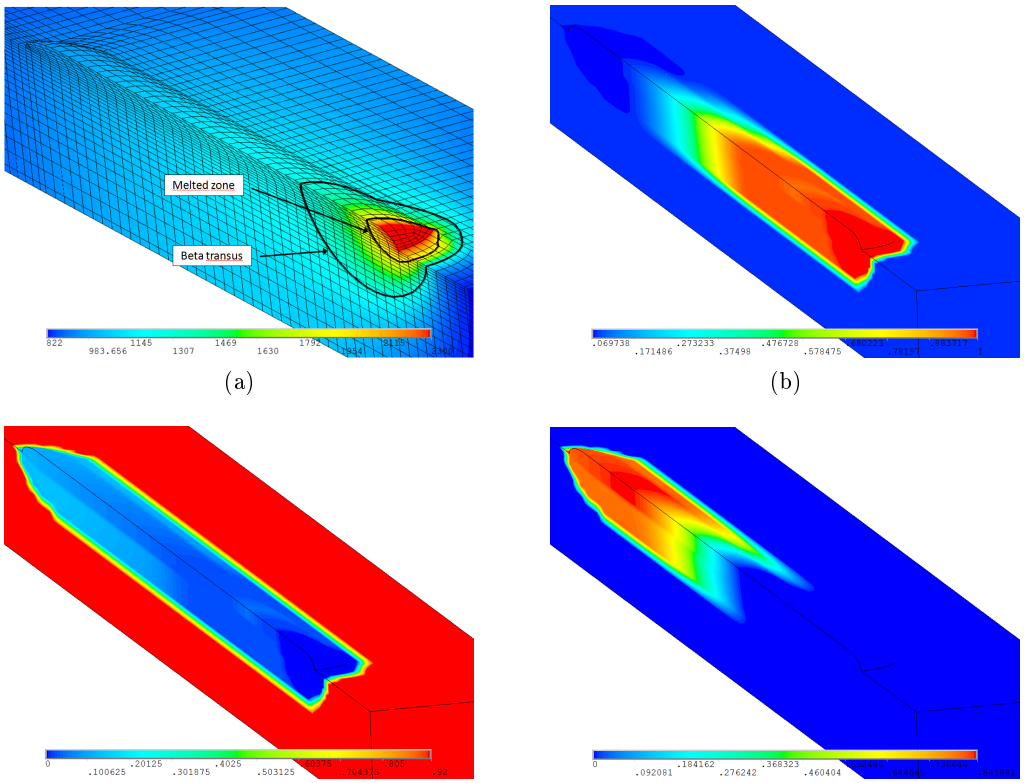

Figure 10.17: Model with single clad tracks of Ti6Al4V on pure Ti, load step at the end of deposition process: (a) temperatures; (b) beta phase; (c) alpha phase; (d) martensite.

In Fig. 10.17a is shown the temperature map at the end of the clad deposition process, before the cooling stage. The boundaries with the melting and beta transus temperatures are marked with black solid lines. Figs. 10.17b, 10.17c and 10.17d show contour maps of the calculated phase volume fractions of beta phase, alpha phase and martensite, respectively, at the same load step of the previous figure. Therefore, a significant portion of the clad track is still in beta phase,

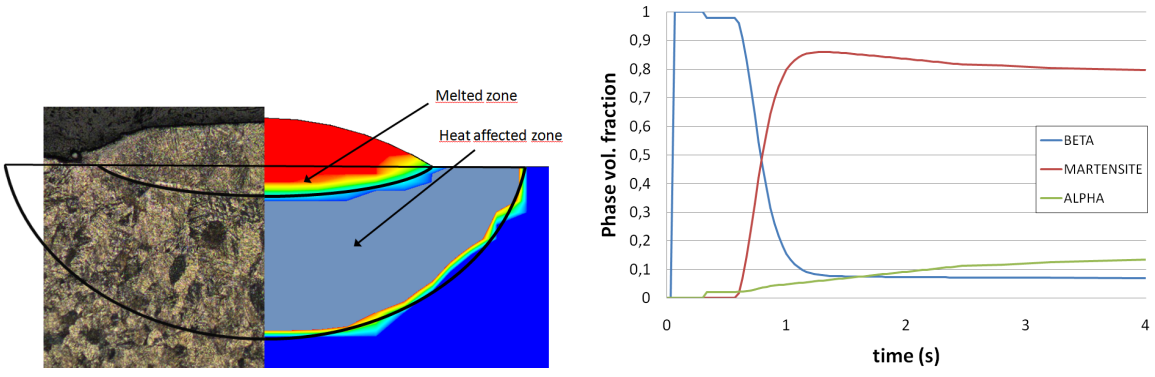

Figure 10.18: (a) Comparative between the microstructure of the experimental sample and the calculated one; (b) curves indicating phase evolution in the model.

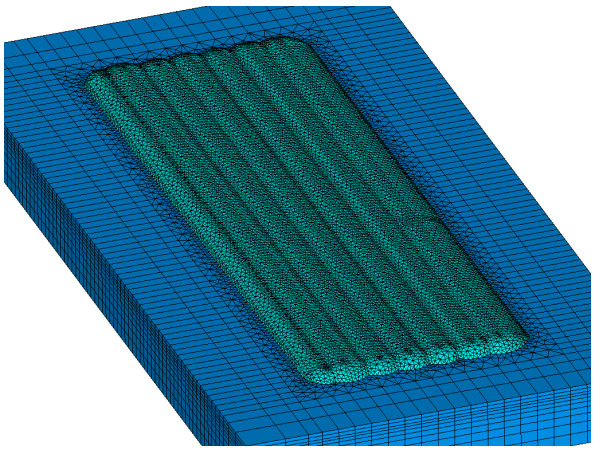

Figure 10.19: FEM model of seven overlapped clad tracks.

whereas the rest has already transformed into martensite, due to the fast cooling rate, and into a small volume fraction of alpha phase.

A comparison between the experimental results and the predictions of the model regarding melted zones and heat affected zones is shown in Fig. 10.18a. Both, the melted zone and the heat affected zone are in agreement between them.

The phase history of one element from the clad track is represented in Fig. 10.18b, showing the temporal evolution of all the considered phases. The element is deposited in β phase and starts to transform into martensite below the martensite start temperature. Additionally, some β phase transforms into α, as well as a low amount of martensite, which is slightly tempered due to the high residual temperatures at the end of the process. When the simulation ends, there is a small residual fraction of retained β phase untransformed, which was limited to the typical values present in quenched samples.

10.2.1.1 Overlapped Clad Tracks

Seven overlapped clad tracks of Ti6Al4V were deposited on a plate of Ti grade 2, with dimensions: 40x20x3 mm. The clad tracks had a length of 30 mm and an overlapping of 37%, being deposited without a time delay between them and all in the same direction. The parameters selected for the process were the corresponding to Test 1 in Table 10.2.

The FEM model is composed of 141778 elements and 110199 nodes. The elements are mostly

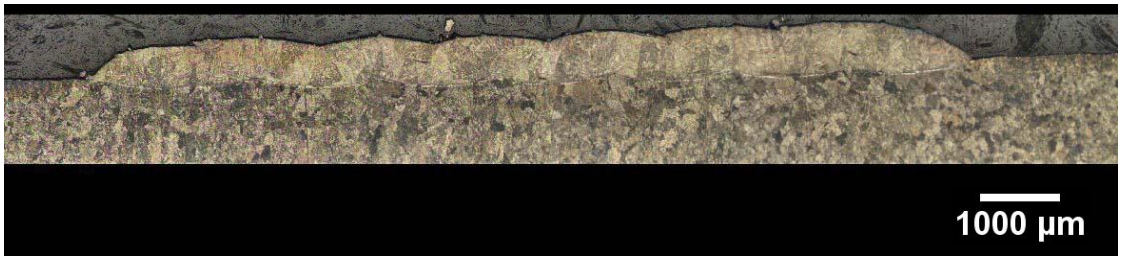

Figure 10.20: Metallography of the cross section of the test with seven overlapped clad tracks.

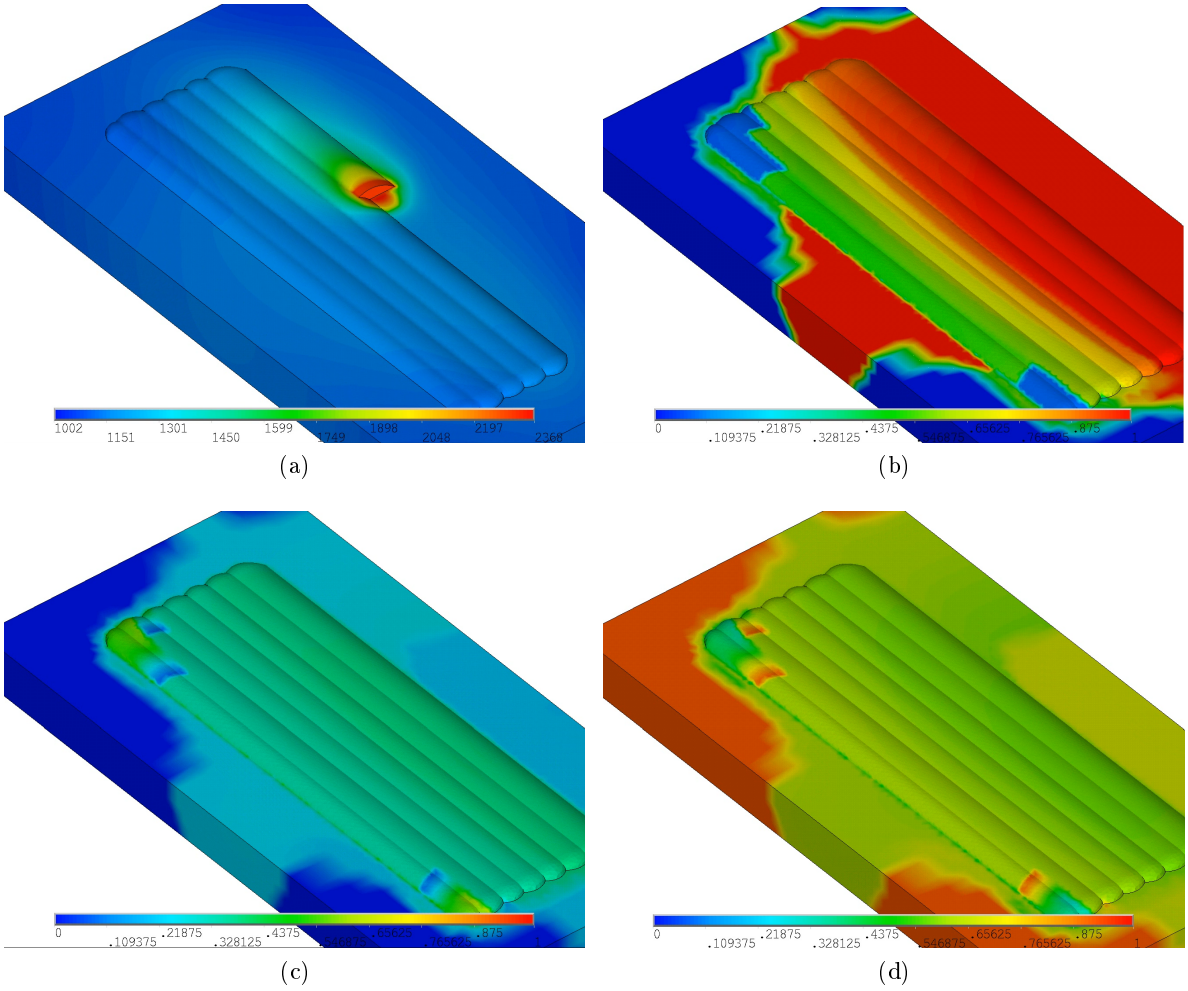

Figure 10.21: Several images from the simulation with seven overlapped clad tracks: (a) temperature field; volume fractions: (b) beta; (c) martensite; (d) alpha.

quadratic tetrahedrals due to the complex geometry. A picture of the mesh is shown in Fig. 10.19. The transient simulation consists of 460 load steps in order to complete the laser metal deposition and cooling stages.

In Fig. 10.21a is shown a contour picture of the temperature field during the analysis. Fig. 10.21b shows the calculated beta phase volume fraction at the last load step of the laser metal deposition process. Fig. 10.21c and 10.21d show the final volume fraction of martensite and alpha phase, respectively.

The first clad tracks cool down faster than the next ones so martensite is able to form before the heating induced by deposition of the next tracks. Each clad track continuously increase the temperature of the titanium plate and also of the previously deposited. Therefore, the previously formed martensite at the ends of the first tracks is partially tempered during the deposition of the subsequent tracks. On the other hand, the remaining parts of the tracks reach a temperature above beta transus, so martensite is transformed back to beta phase. From the third track and forth, this material in beta phase is no longer able to cool down below the martensite start temperature, so it starts forming alpha phase. When all the tracks are deposited, all the material

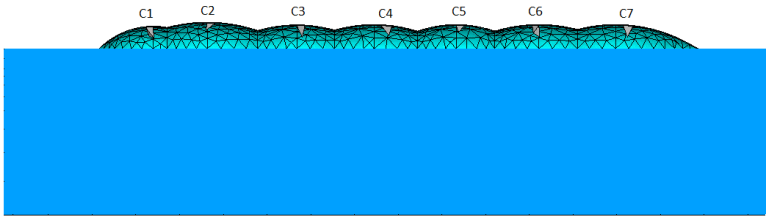

Figure 10.22: Elements selected for the history charts in the model of seven overlapped clad tracks.

with untransformed beta phase cools down to form martensite.

In the previous figures it is clearly distinguished the effect of the heat accumulation in the right part of the plate, due to the continuous deposition of clad tracks. This part of the plate has reached a temperature above the beta transus during the analysis, while only a small part of the plate surpassed this temperature in the left side. Additionally, the differences in the beta transus temperatures between the Ti6Al4V of the clad tracks and the pure titanium of the plate, can be distinguished in the figures.

The sample obtained during the experimental tests performed in the laboratory was cut down

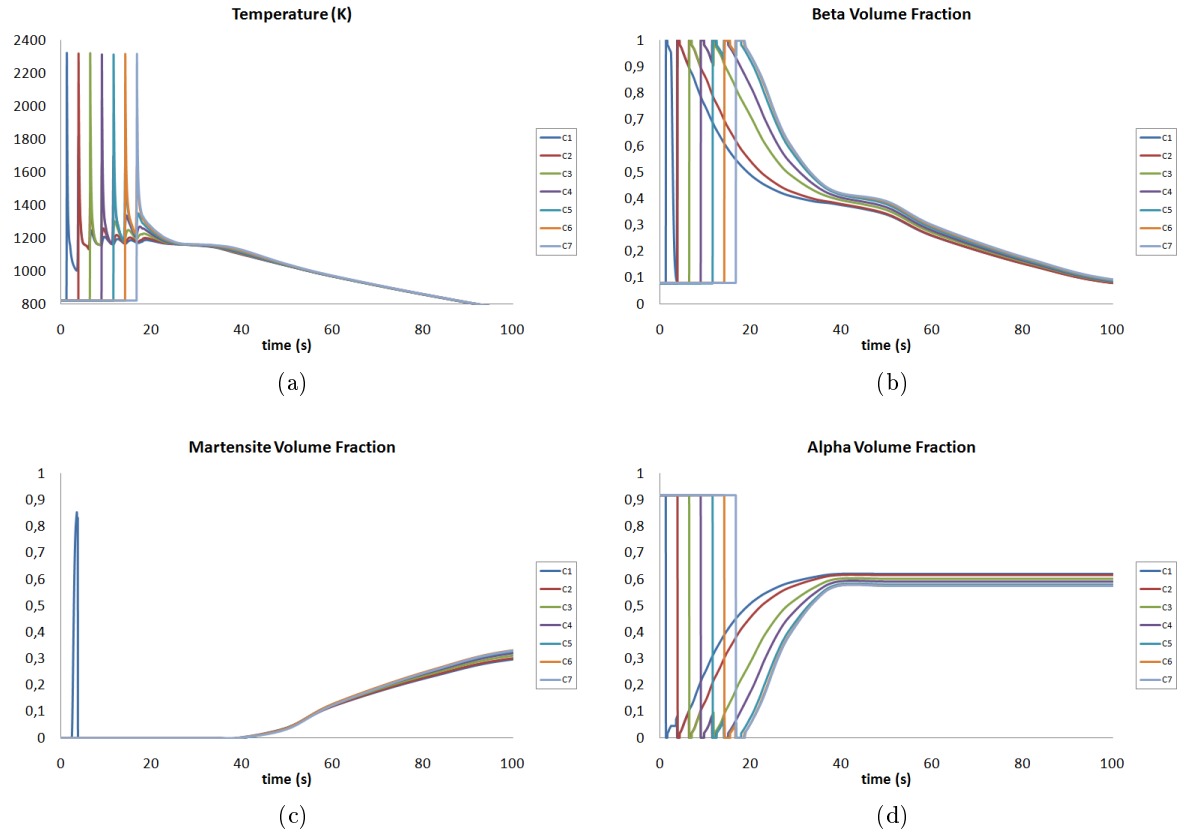

Figure 10.23: History charts from the simulation with seven overlapped clad tracks: (a) temperature field; volume fractions: (b) beta; (c) martensite; (d) alpha.

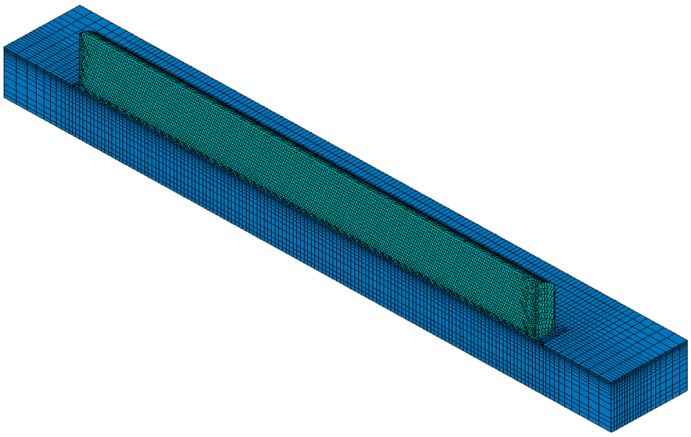

Figure 10.24: FEM model with ten superposed clad tracks.

and metallographically prepared. A picture of the cross section of the sample is shown in Fig. 10.20. The grain size in the right part of the plate is slightly larger than in the left part, which is in accordance with the simulated temperatures. Heat affected zones below the clad tracks span all the thickness of the plate, like in the simulation. Martensite volume fractions seem to be lower than in the samples with only one clad track; however, the martensite content should be measured with some technique to get an accurate comparison.

Several elements were selected for history charts, one from the middle section of every clad track, as it is represented in Fig. 10.22. The thermal history of these elements is shown in Fig. 10.23a. The volume fractions of beta phase, martensite and alpha phase are shown in Fig. 10.23b, 10.23c and 10.23d, respectively. Most of the elements follow the same pattern, with exception of the first track, which cools down below the martensite start temperature and martensite starts to form before the deposition of the next track, when it heats above the beta transus temperature. All the subsequent tracks do not reach the martensite start temperature during the cooling down before the deposition of the next track; they start to form alpha phase until the seven clads are deposited and the workpiece cools down enough to initiate the martensite formation process.

10.2.1.2 Superposed Clad Tracks

Ten superposed clad tracks of Ti6Al4V were deposited on a plate of Ti grade 2, with dimensions: 40x10x3 mm. The clad tracks had a length of 30 mm being deposited without a time delay between them and all in the same direction. The laser cladding nozzle was displaced upwards

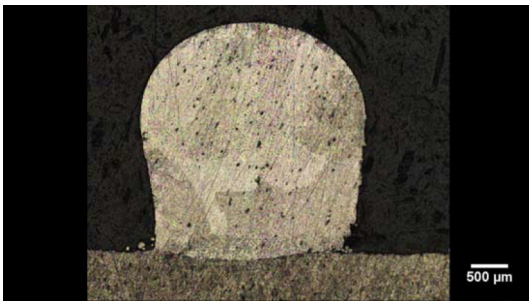

Figure 10.25: Cross section of the sample wit ten superposed clad tracks.

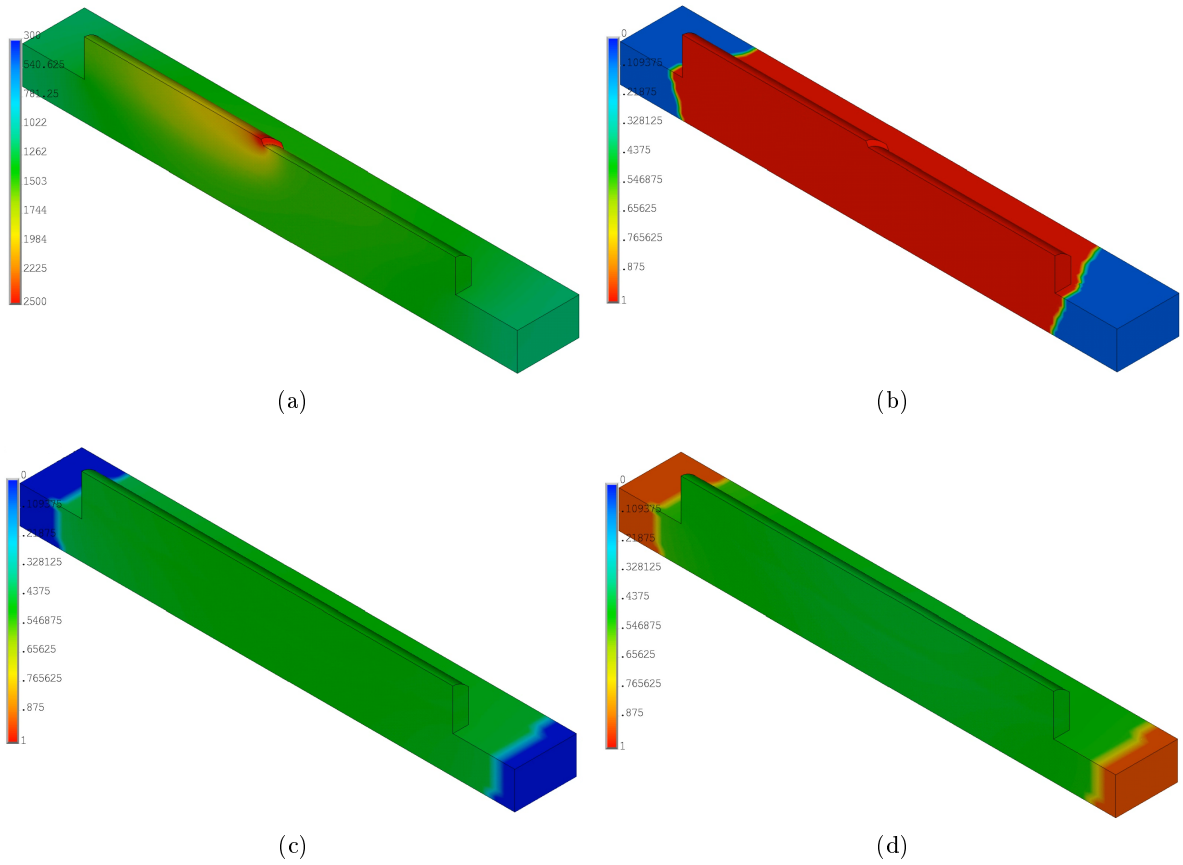

Figure 10.26: Several images from the simulation with seven overlapped clad tracks: (a) temperature field; volume fractions: (b) beta; (c) martensite; (d) alpha.

150 μm with each clad track. The parameters selected for the process were the corresponding to Test 1 in Table 10.2.

The FEM model is composed of 141778 elements and 110199 nodes. The elements are mostly linear hexahedrals, with quadratic tetrahedrals in zones with complex geometries. A picture of the mesh is shown in Fig. 10.24. The transient simulation consists of 640 load steps in order to complete the laser metal deposition and cooling stages.

In Fig. 10.26a is shown a contour picture of the temperature field during the analysis and in fig. 10.26b the calculated beta phase volume fraction at the corresponding load step. Fig. 10.26c and 10.26d show the final volume fraction of martensite and alpha phase, respectively.

The first clad track cools down faster than the next ones so martensite is able to form before the heating induced by the deposition of the next tracks. Each clad track continuously increase the temperature of the titanium plate and also of the tracks previously deposited. The heat accumulates in the workpiece and at the end of the deposition process all the deposited clad tracks as well as most of the plate remain in beta phase. They cool down together forming an almost constant volume fraction of alpha phase and martensite in the whole zone.

The phase and temperature history of one element from the first clad track are represented in Fig. 10.27. This figure has a time scale that spans only until 35 seconds, instead of the 1000

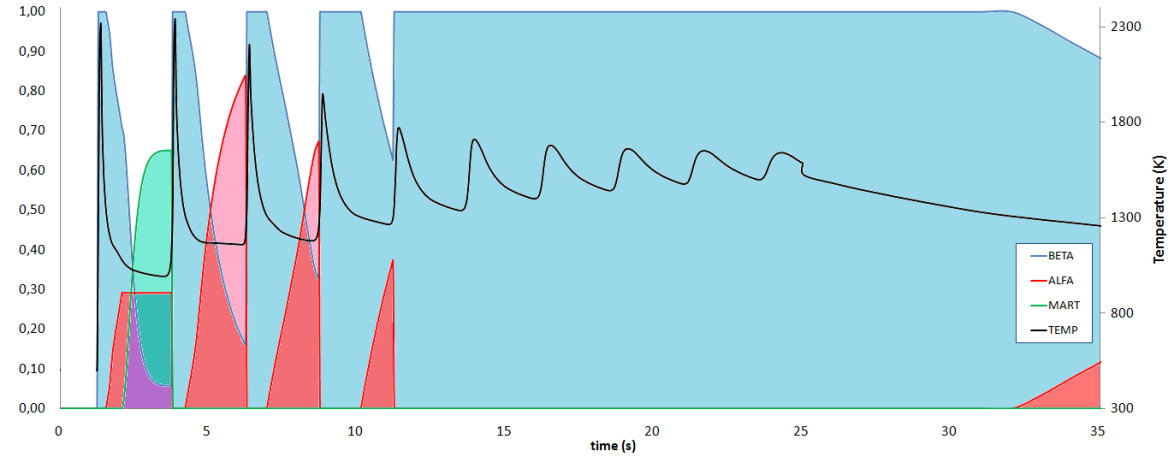

Figure 10.27: Phase and temperature history of one element of the first track from the model of ten superposed clad tracks.

seconds of the simulation, in order to have a detailed view of the deposition process. The graph summarizes the behavior explained before: the deposition of additional clad tracks increase the temperature and the element remains in beta phase, being unable to transform to alpha phase or martensite until the end of the deposition process.

In this test, the major part of the plate was transformed during the process. The use of a larger plate will act as a more effective heat sink, thus it will extract heat from the deposited clad tracks more efficiently and its temperature will not rise above the beta transus.

10.3 Conclusions

In this chapter were presented metallographies obtained from experimental tests performed in the laboratory, for the validation of the phase transformation models. The tests consisting in the laser surface melting of carbon steel AISI 1045 show a good agreement in the melted zones, heat affected zones and predicted hardness profiles, in all the cases studied.

Phase transformation model for Ti6Al4V and Ti was compared with metallographies obtained from experimental samples prepared using laser metal deposition process with single clad tracks as well as overlapped and superposed multitracks. The comparison show accordance between the different zones. The models with several clad tracks give all the information needed to understand the phase evolution during the processes.

Both phase transformation models seem to work properly. Several experimental tests were carried out, with carbon steel AISI 1045 and with laser cladding of Ti6Al4V on pure Ti. In both cases the comparison between tests and model predictions showed good agreement.

Chapter 11

Estimation Of The Residual Stresses With Nanoindentation Techniques

There are two possible outcomes: if the result confirms the hypothesis, then you've made a measurement. If the result is contrary to the hypothesis, then you've made a discovery.

Enrico Fermi.

Abstract: The influence of residual stresses on nanoindentation measurements is studied in this chapter. Experimental nanoindentation tests were performed on samples taken from laser cladded plates of stainless steel AISI 304 with Stellite 6B, showing differences in the loading/unloading curves in areas with different levels of stress. FEM simulations of the nanoindentation process with tensile, compression and no stress reproduce the experimental curves. A complete thermomechanical simulation of the laser cladding process and the subsequent cutting of the samples is compared with the hardness map measured, showing a similar profile. However, no attempt of relating the hardness values with the residual stresses was made.

11.1 Introduction

In the past decades several studies have been devoted to try to measure residual stresses with nanoindentation. This technique has proven to be a powerful tool for estimating the mechanical properties of materials at sub-micrometer scales. Residual stresses have some influence on the properties measured with instrumented indentation techniques. The load/unload curves measured by the indenter at the same penetration are shifted towards higher or lower loads, depending on the magnitude and sign of the residual stresses, and thus affecting the measured properties. The contact area between the indenter and the specimen is also affected by residual stresses. In presence of tensile stresses, the contact area increases whereas with compressive stresses diminishes.

The first attempt to measure residual stresses with nanoindentation techniques was made by Tsui et al. [277] applying stresses of known magnitude to a fine-grained, high-strength aluminium

alloy, and using a sharp Berkovich indenter for hardness measurements. Their experiments show a good correlation between hardness and stress, however, careful examination of their data showed that the hardness changes were not real, but an experimental artifact caused by the influence of the stress on the geometry of the pile-up around the hardness marks. Finite element simulations support these observations [278]. In spite of the fact that there was no change in the true hardness of the material, the "apparent hardness" measured by nanoindentation is indeed affected in a way that might be useful in the characterization of residual stresses. However, the effect is small. Tsui et al. [277] reported a change in the hardness of no more than 10%.

Based on these results, Suresh and Giannakopoulos [279] suggested a method for sharp indenters founded on the difference in contact areas of stressed and unstressed materials indented to the same depth, and the invariance of the contact pressure. The contact areas can be measured indirectly through the contact stiffness, relating it to the contact area. They describe the equibiaxial residual stresses through a hydrostatic stress plus an uniaxial component in the indenter direction that induces a differential indentation force. With several assumptions they derive equations restricted to this particular stress state.

The small effect of residual stresses on indentation with sharp indenters led Taljat and Pharr [280] to study nanoindentation with spherical indenters, using FEM simulation models. Their studies revealed a significant effect on the indentation load. This effect was experimentally tested on several commercial aluminium alloys with different levels of equibiaxial tension and compression stresses by Swadener et al. [281], who developed two methods for measuring residual stresses with spherical indenters based on the onset of yielding and the contact pressure. Liepinski et al. [282] tested the method developed by Swadener et al. in thin films, comparing the nanoindentation with X-ray diffraction measurements of the stresses. They found difficulties and serious obstacles to the practical implementation of the method.

Carlsson and Larsson [283, 284] recognized that the residual stresses do not have an effect on hardness, but on the other hand, residual plastic strains have a substantial influence on it. Therefore, the ratio between the actual and nominal contact areas at indentation depends on the residual stresses as well as the residual plastic strains present in the material. Hence, the accuracy of the methods using this ratio to obtain the residual stresses deteriorates with residual plastic strains. Their work is also based on this ratio and is restricted to equibiaxial stress fields.

Lee and Kwon [285, 286], based on the work of Suresh and Giannakopoulos, analyzed the load shift induced by the residual stresses and modified its model by dividing the residual stress tensor into a mean and a deviatoric part, and considering the effect of the residual stresses as the normal component in the deviatoric part. They extended the equibiaxial model to a general stress state by introducing the stress ratio κ as the ratio of the minor residual stress component σ_3^{res} to the major σ_1^{res}. They also applied their method to the assessment of residual stresses in P12 steel welds in power plant facilities before stress relaxation annealing [287].

The present work is focused in the study of the influence of the residual stresses on nanoindentation hardness measurements using a Berkovich indenter. The samples have a general stress state. Thermomechanical FEM simulations of the complete laser cladding process and the subsequent cutting of the samples were used to obtain the stress distribution on the surface of the samples. Several zones with different levels of stress were selected in order to simulate the indentation process and compare the simulated load/displacement curves with the experimental ones.

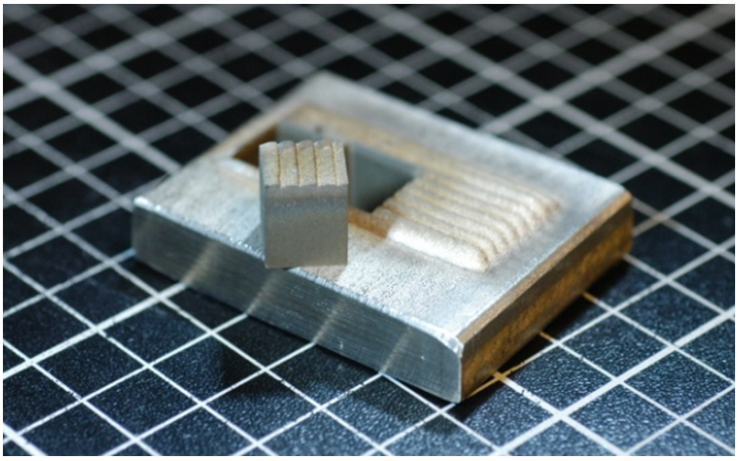

Figure 11.1: Sample cut by means of EDM

11.2 Experimental

11.2.1 Materials

The Co-based alloy Stellite 6B was deposited on a substrate of austenitic stainless steel AISI 304. This alloy is one of the most commonly used stainless steels, offering high toughness and ductility over a wide range of temperatures. The plates used for the experiments were cut down from a rolled plate with a thickness of 10 mm. Strain hardening due to the rolling of the plate is estimated using the Tabor equation 11.1, which relates hardness H and elastic limit σ_Y for a wide range of steels:

$$H = C\sigma_Y \tag{11.1}$$

The Co-based alloy Stellite 6B is characterized by its high temperature properties, showing high strength, hardness, corrosion and wear resistance at elevated temperatures, being used mainly in high requirement applications, and also in free lubricating equipment due to its low friction coefficient.

Composition and properties used for the simulations were taken from sources [276] and [288], and are represented in Table 11.2. Data available does not cover the entire range of temperatures up to the melting, so at high temperatures, above 600-800°C, their values were linearly extrapolated from the solid ones or taken constant.

Mechanical behaviour of the materials for the FEM models is assumed to follow an elastoplastic rate independent bilinear isotropic hardening model.

11.2.2 Laser Cladding Experimental Setup And Sample Preparation

Stellite 6B powder was deposited on the stainless steel plates using a computer controlled 2.2kW Nd:YAG Rofin Sinar laser in continuous wave mode.

The parameters used for the process were: power of 1500W with a defocused laser spot of 2.2 mm, speed of 5 mm/s and powder flow rate of 0.37 g/s. Three samples were selected for the study:

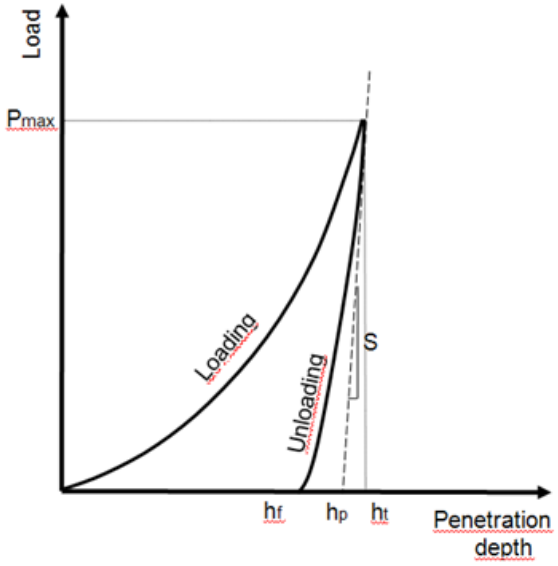

Figure 11.2: Load vs penetration curve for a typical nanoindentation measurement

- Stainless steel plate at room temperature, one clad track
- Stainless steel plate preheated to 300°C, one clad track
- Stainless steel plate at room temperature, several clad tracks with an overlapping of 34% of the clad width.

The single clad tracks resulted in an average width of 3.2 mm, a height of 1.4 mm and a dilution of about 9-10%, obtained in micrographs as the ratio between the melted area of the plate and the sum of this area and the area of the clad bead.

For the measurement of the samples cubes of 10 mm side were cut down from them between the center and the end of the clad tracks, by means of Electro-Discharge Machining (EDM), in order to not induce stresses in the samples. In Fig. 11.1 is depicted one of these samples.

11.2.3 Nanoindentation Measurements

Several tests were conducted with different loads and penetrations, in order to select the optimum parameters for the nanoindentation measurements. Before the tests, the equipment was calibrated using high loads and performing a series of indentations on a AISI 1045 carbon steel with a known elastic modulus. The resulting load vs displacement curves and the known elastic modulus were used to fit the area function to an eighth degree polinomial.

The tests performed with low penetrations did not show a significant difference in the measured properties along the surface of the sample. However, increasing penetration depth up to 10 μm by using the highest loads available on the equipment, the differences are clear. This penetration is closer to the grain size of the material.

The measurements were done using the dynamic CSM module of the nanoindenter. This allows to obtain multiple values of load/unload in each point of the load vs displacement curves. The

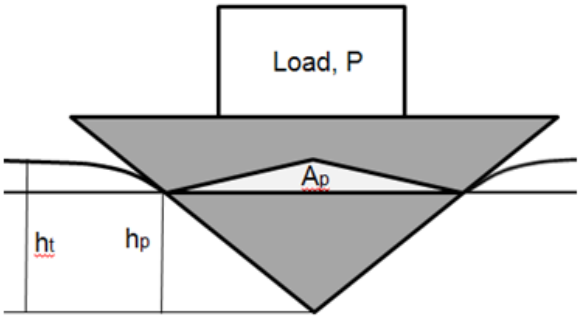

Figure 11.3: Indentation depths and contact area during a nanoindentation test.

frequency of the dynamic analysis was set to 45 Hz.

The nanoindenter measures penetration depth and indentation force continuously, generating the load displacement curve (Fig. 11.2). From this curve it is possible to calculate parameters used to estimate several material properties.

The contact stiffness S is a parameter obtained as the initial slope of the unloading curve:

$$S = \left.\frac{dP}{dh}\right|_{h=h_t} \tag{11.2}$$

The contact depth h_p can be calculated from this parameter, the maximum load P_{max}, and the maximum penetration depth h_t:

$$h_p = h_t - \varepsilon \frac{P_{max}}{S} \tag{11.3}$$

Where ε is defined as:

$$\varepsilon = \frac{2(\pi - 2)}{\pi} \tag{11.4}$$

The contact area can be calculated from the contact depth:

$$A_p = m_0 h_p^2 + m_1 h_p + m_2 h_p^{1/2} + m_3 h_p^{1/4} + m_4 h_p^{1/8} + m_5 h_p^{1/16} + \ldots \tag{11.5}$$

Now the hardness can be obtained by the following equation:

$$H = \frac{P_{max}}{A_p} \tag{11.6}$$

Also the reduced elastic modulus:

$$E^* = \frac{\sqrt{\pi}}{2\sqrt{A_p}} S \tag{11.7}$$

From which the elastic modulus can be calculated using the properties of the diamond indenter:

$$E = \left[\left(\frac{1}{1 - \nu^2} \right) \left(\frac{1}{E^*} - \frac{1 - \nu_D^2}{E_D} \right) \right] \tag{11.8}$$

Where $\nu_D = 0.07$ and $E_D = 1140$ GPa, are the Poisson coefficient and elastic modulus of the diamond indenter, respectively. The complete surface of the samples was measured, in order to create a mapping of the material properties. The points of the mapping are 1 cm interspaced, except in the upper 2 cm of the plate, where they are spaced 0.5 cm for a better resolution in

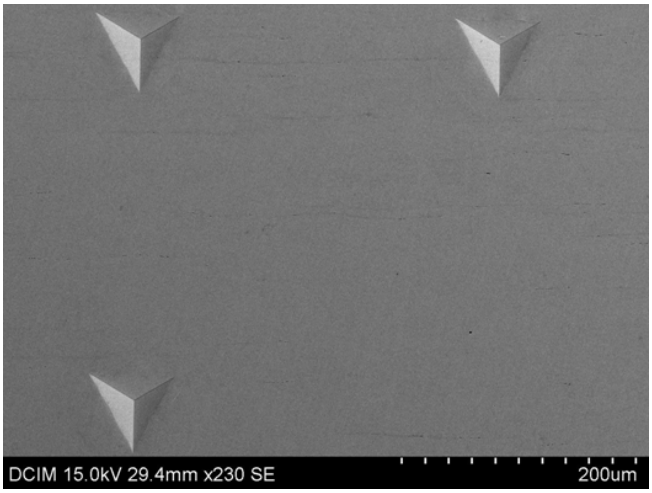

Figure 11.4: Three Berkovich indentation marks. Their averaged properties constitute one point in the mapping matrix.

this area. In each point of the mapping matrix, four indentations were carried out, separated 350 μm from the centre of the previous indentation mark. However, due to equipment faults, only three indentations were performed in most of these points (Fig. 11.4). The mean value of the four indentations is assigned to each point of the mapping matrix.

11.3 FEM Models

11.3.1 Laser Cladding Model

The model developed for the simulation of this process is a nonlinear transient thermomechanical model under the software ANSYS. Thermal and mechanical fields are sequentially coupled. The simulation starts with a transient thermal analysis to calculate the temperature field. The results are applied as a load in the subsequent quasistatic mechanical analysis. Birth & Death techniques are used for the simulation of the material deposition. More details of the model can be found in Chapter 7.

The measurements performed with nanoindentation penetrate only about 10 μm in the samples. Therefore, it is necessary to simulate the cut off, because the residual stresses will redistribute near the cut surfaces, in order to equilibrate the internal stresses.

To simulate this, the elements of a cube with the dimensions of the sample were selected in the FEM model. At the end of the previous thermomechanical analysis, in a new load step, these elements were kept "alive" while the rest of the elements of the plate were "killed". One node in the middle of the plate was fixed as the boundary condition, and no load was applied. Using a very small time step the solution converged after a few iterations.

11.3.2 Nanoindentation Model

The indentation process was simulated by another FEM model, in order to compare the simulation results with the experimental measurements. This model is a quasistatic mechanical

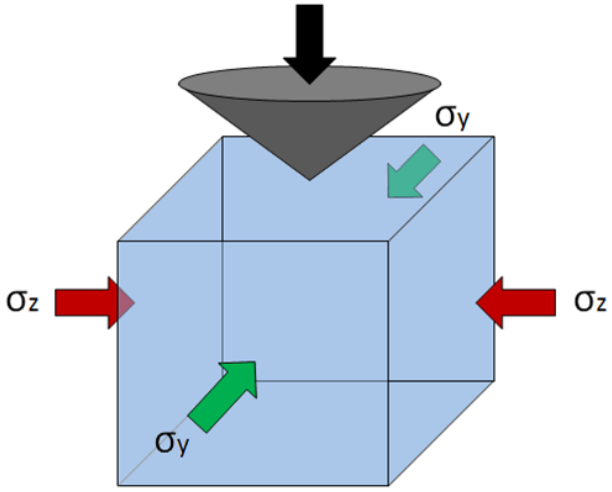

Figure 11.5: Volume for the nanoindentation FEM simulations, and biaxial stresses applied.

analysis, also under the software ANSYS. A small cubic volume is simulated in a 3D model. The nanoindentation volume is biaxially prestressed with stresses obtained from the laser cladding model. The stresses are selected in a determined point and are applied homogeneously to the corresponding faces of the nanoindentation volume, perpendicular to the indenter (Fig. 11.5). No stress is applied in the normal direction.

The Berkovich indenter is modelled as an equivalent cone indenter, with a rounded tip. Taking advantage of the symmetry of the problem, only one quarter of the volume is simulated, which corresponds to a cube of 150 μm. Symmetry boundary conditions are applied to the corresponding faces. The mesh consists of linear reduced integration tetrahedral elements, refined close to the indenter (Fig. 11.5). The indentation depth is 10 μm, and the indentation velocity is 0.1 μm/s, although the material model cannot simulate rate dependent effects, the velocity affects the selected time steps.

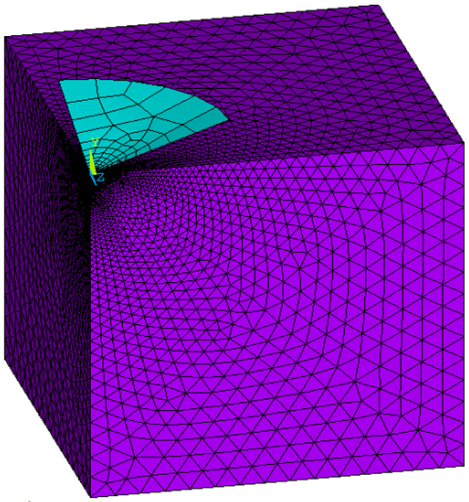

Figure 11.6: Geometry and mesh of the nanoindentation FEM model.

The contact simulated was surface-to-surface, based on the Augmented Lagrange method using contact detection on Gauss points with a tight penetration tolerance. Friction was neglected. The model is composed of 97972 elements, consisting of 94859 solid elements and 3113 surface elements for modelling the contact.

Three cases, corresponding to determined areas of the surface of the laser cladding model, having the following stresses, were simulated:

- Tensile stresses: $\sigma_x = -200MPa, \sigma_y = -100MPa$
- Compression stresses: $\sigma_x = 300MPa, \sigma_y = 200MPa$
- Zero residual stresses

11.4 Results And Discussion

11.4.1 Residual Stresses After The Cutting Of The Samples

The samples are cubes of 10 mm edge which were cut off from the laser cladded plates, by means of Electro Discharge Machining (EDM) in order to not induce additional stresses due to the cutting process. Material removal changes the residual stress profile in a volume which ranges from the surface of the samples to some depth within them, as the residual stresses inside the samples need to be compensated. Thus, after the cutting of the plate, in some zones the stresses shift from tensile to compression and the opposite.

Nanoindentation techniques cannot penetrate inside the material more than a few tens of micrometers. Therefore, the measurements are restricted to the zone in which the stresses shifted due to the cut off.

Residual stresses in the samples were calculated using the FEM model. The results of the stresses in the Z direction for one single clad bead before the cutting are shown in Fig. 11.7a, and after the cutting in Fig. 11.7b, were the stress reversal can be appreciated.

11.4.2 Hardness Measurements By Nanoindentation

Although it is accepted that the intrinsic material hardness is invariant, the apparent hardness measured by nanoindentation is affected by the residual stresses. The load required to reach the same penetration depth is higher in presence of compression stresses than in the stress free condition, and lower in the case of tensile stresses. Suresh and Giannakopoulos [279] explain this effect as the creation of a hydrostatic stress that generates a differential force in the indentation direction, which supports or opposes to the indentation force.

The load vs penetration curves obtained in the measurements present this shift in the maximum load required for the same penetration. In Fig. 11.8a are represented the curves obtained for the areas with tensile, compression and zero residual stress from section 11.3.2.

The simulations reproduce similar load vs penetration curves with the same maximum values. In Table 11.1 are included the maximum indentation loads measured experimentally in the

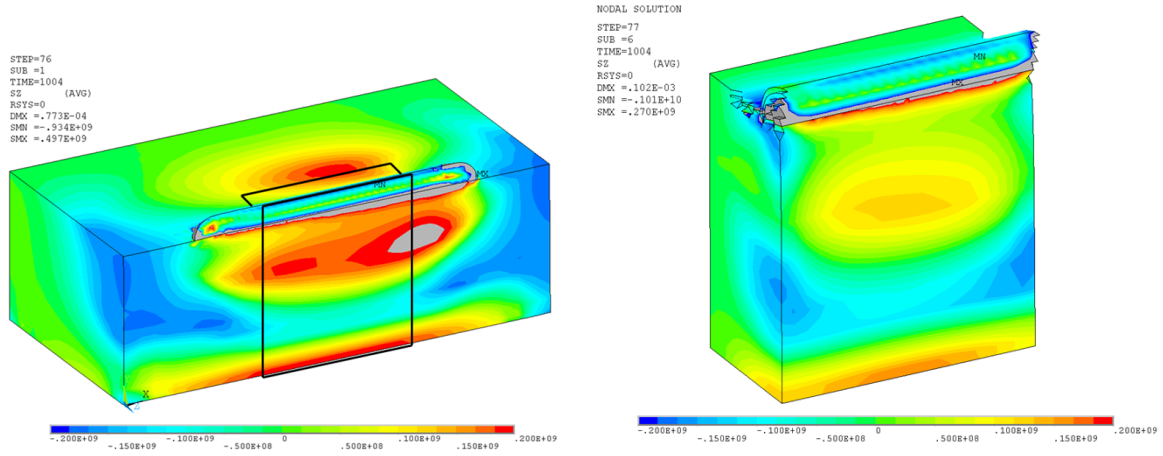

(a) (b)

Figure 11.7: (a) Geometry of the samples including the coordinate system used for the stresses; (b) Cross section of one of the samples.

nanoindentation tests, the maximum penetration depth, and the maximum values calculated for the corresponding penetration depth using the nanoindentation FEM model. The comparison between the measured load vs penetration curve and the simulated, for the tensile stress region is shown in Fig. 11.8b.

Fig. 11.9a shows a complete mapping of the hardness of the entire surface of the samples. A comparison between the hardness profile and the residual stresses present in the surface, simulated using the laser cladding FEM model, is shown in Fig. 11.9b. The stresses represented are those Z direction stresses, which are the highest. The stresses in the Y direction are much lower, and in the X direction, in the surface, are zero.

Although the simulation of the exact residual stress profile in the surface of the samples is a very complex task, there are significant similarities between the simulated stresses and the hardness map. The areas with highest apparent hardness are located below the clad bead, where the model predicts the highest residual compression stresses. Also the areas with the lowest apparent hardness are located in the zones where the model predicts residual tensile stresses.

In Fig. 11.10a is represented the apparent hardness map measured for the sample with one clad bead and preheating to 300°C. The profile is similar to the previous sample, although the

Residual stresses	**Penetration (nm)**	**Max. value (nN) measured**	**Max. value (mN) simulation**
Compression	9500	4653	4681
Zero	9500	4321	4280
Tensile	9629	4008	3990

Table 11.1: Maximum values measured from the experimental curves and calculated in the simulations, in three different cases of residual stress.

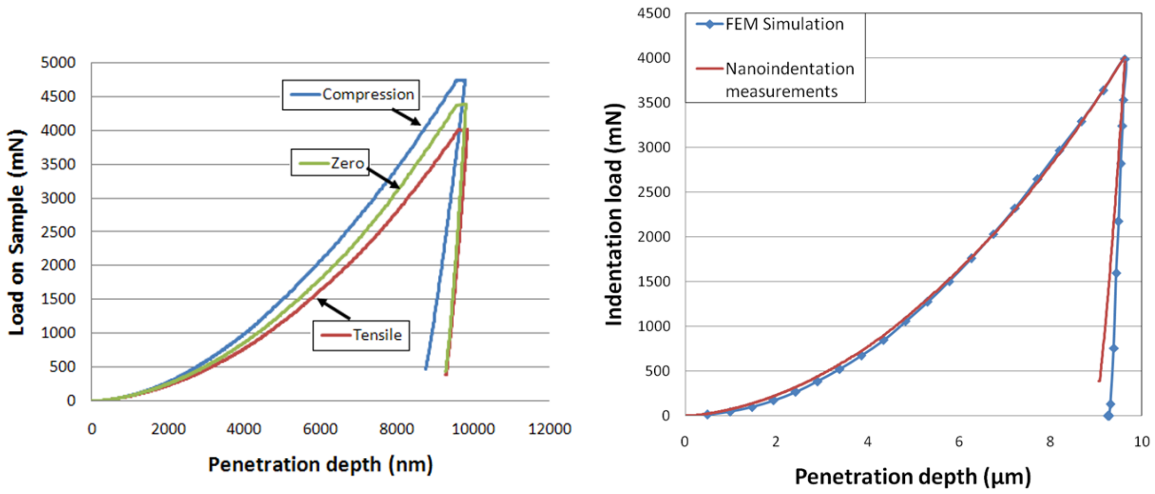

(a) (b)

Figure 11.8: (a) Load vs penetration curves, for areas with different levels of residual stresses, obtained from the experimental measurements; (b) Load vs penetration curves measured and simulated, for an area with tensile stresses.

maximum and minimum apparent hardness values are higher and lower, respectively, compared with the sample without preheating. This is in agreement with the lower level of residual stresses in this sample due to the effect of the preheating, which seems to be reflected in lower maximum tensile/compression stresses.

Fig. 11.10b shows the apparent hardness map measured for the sample with several clad beads without preheating. The maximum apparent hardness values are higher than the measured in the sample with only one clad bead, which is in agreement with the higher residual stress levels present in this sample. The maximum apparent hardness values are located in a wider zone at the top of the plate, as it would be expected from the presence of several clad beads.

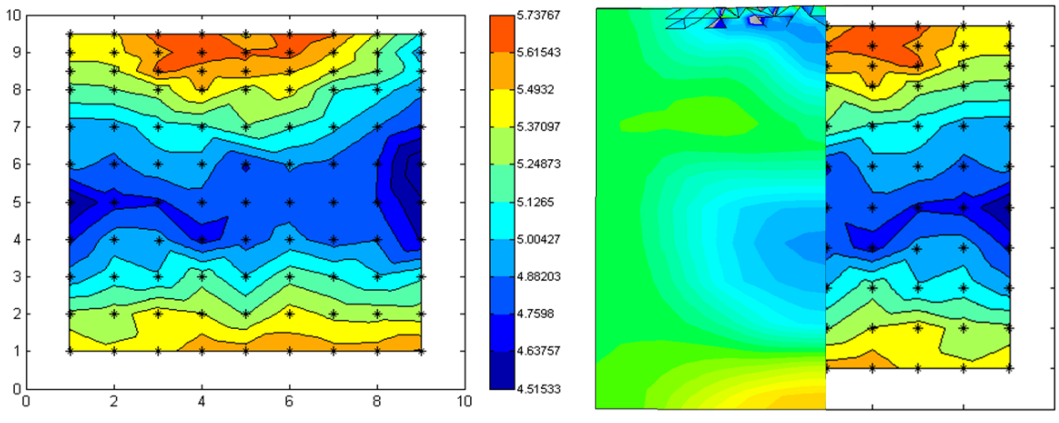

(a) (b)

Figure 11.9: (a) Apparent hardness map from the sample with one clad bead; (b) Comparison between the Z direction stresses from the FEM model (left) and the apparent hardness map from the measurements (right).

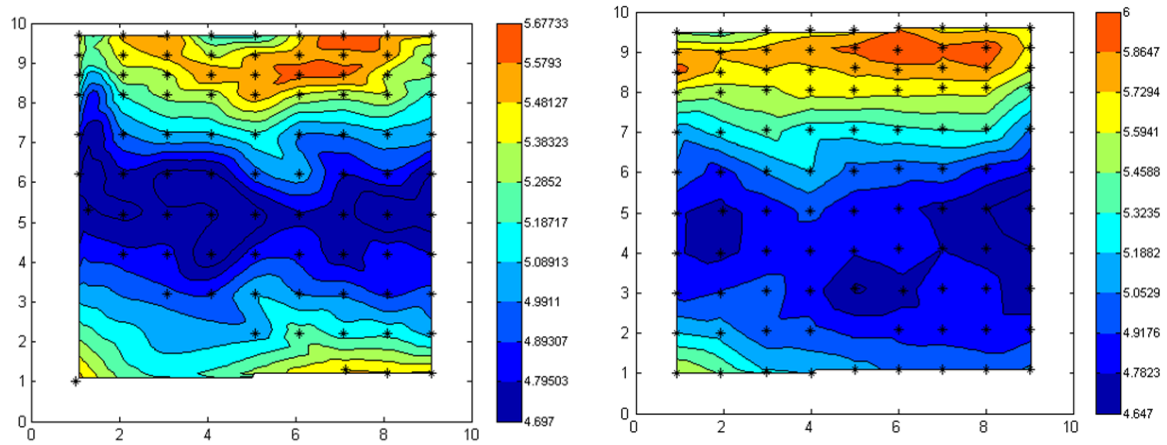

(a) (b)

Figure 11.10: (a) Apparent hardness map from the sample 300°C of preheating, one clad bead; (b) Apparent hardness map from the sample with several clad beads.

11.4.3 Conclusions

The influence of residual stresses on nanoindentation measurements was studied in this chapter. Experimental nanoindentation tests were performed on samples taken from laser cladded plates of stainless steel AISI 304 with Stellite 6B, showing differences in the loading/unloading curves in areas with different levels of stress. FEM simulations of the nanoindentation process with tensile, compression and no stress reproduce the experimental curves. A thermomechanical simulation of the laser cladding process and the subsequent cutting of the samples was compared with the hardness map measured, showing a similar profile. However, no attempt of relating the hardness values with the residual stresses was made.

Table 11.2: Composition and thermomechanical properties of AISI 304 and Stellite 6. Extrapolated values are in italics.

Composition	C	CO	Cr	Fe	Mn	Mo	Ni	P	S	Si	W
AISi 304	max. 0.08	–	18–20	Bal.	max. 2	–	8–10.5	max. 0.045	max. 0.03	max.1	–
Stellite 6	0.9–1.4	bal.	28–32	max. 3	max. 2	max. 1.5	max. 3	–	–	max. 2	3.5–5.5

AiSi 304

Temperature (°C)	25	100	200	400	600	650	800	1000	1200	1400	1454	1600	1800
Density (kg m^{-3})	8020		7950	7860	7750		7645	7530	7430	7300	6900	6780	6615
Thermal conductivity (W m^{-1} K^{-1})	14.85		18.41	22.41	26.41		30.41	34.41	38.41	42.41		46.41	50.41
Specific heat (J kg^{-1} K^{-1})	500		535		*616*			*696*		*776*			*856*
Coef thermal exp. (μm m^{-1} K^{-1})		1.66E−05		1.79E−05		1.86E−05				*2.08E−05*			*2.10E−05*
Latent heat fusion (J g^{-1})	265.2												
Elastic modulus (Pa)	2.08E+11		1.95E+11	1.80E+11	1.50E+11		1.00E+11	*1.00E+10*	*1.00E+10*	*1.00E+10*	*1000*		*1000*
Poisson ratio	0.295		0.308	0.32	0.335		0.345	*0.365*	*0.375*	*0.375*	*0.45*		*0.45*
Yield strength (Pa)	1.80E + 08		1.30E + 08	8.70E + 07	6.40E+07		4.40E+07	*1.70E + 07*	*7.00E + 06*	*7.00E + 06*			
Ultimate tensile strength (Pa)	5.86E + 08		4.96E + 08	4.39E + 08	3.50E + 08		2.00E + 08	*5.00E + 07*	*5.00E + 07*	*5.00E + 07*			

Stellite 6

Temperature (°C)	25	200	400	600	800	1200	1355	1628	1800
Density (kg m^{-3})	8380								
Thermal conductivity (W m^{-1} K^{-1})	14.85		22.41		30.41	38.41			*50.41*
Specific heat (J kg^{-1} K^{-1})	456	482		573	629	741			*909*
Coef. thermal Exp. (μm m^{-1} K^{-1})	1.39E−05		1.45E−05		1.58E−05		*1.85E−05*		*1.85E−05*
Latent heat fusion (J g^{-1})	266								
Elastic modulus (Pa)	2.10+11		1.65E+11		*9.50E+10*		*2.73E+10*	*1000*	*1000*
Poisson ratio	0.33		0.36		*0.39*		*0.45*	*0.45*	*0.45*
Yield strength (Pa)	6.40E + 08		4.95E + 08		2.80E + 08		*8.34E + 07*		
Ultimate tensile strength (Pa)	1.06E + 09		1.00 + 09		5.00E + 08		*6.06E + 07*		

Chapter 12

Measurement Of Residual Stresses With Synchrotron Radiation

There is a single light of science, and to brighten it anywhere is to brighten it everywhere.

Isaac Asimov.

Abstract: In order to validate the mechanical predictions of the FEM models, measurements using the Energy Dispersive X-Ray Diffraction (EDXRD) technique were performed at the European Synchrotron Radiation Facility (ESRF), for several samples of laser cladded plates of AISI 304 stainless steel with the Stellite 6B alloy, and compared with the predictions.

12.1 Introduction

The EDXRD technique is a versatile and powerful tool that has enormous potential for material science and engineering. The penetration capabilities of very high energy X-rays combined with the ability to collect whole diffraction spectra and high brilliance, make possible the measurement of residual strains and stresses inside materials [289].

Previous measurements using synchrotron radiation in laser cladded samples were performed by U. de Oliveira et al. [290]. They used a different technique to measure the stresses inside clad beads of Stellite 6 with a fixed energy and monitoring the γ-Co (311) peak, also with the so called 3D X-ray microscopy technique [291], showing important hydrostatic stresses in the clad, near to 500 MPa.

In the present work the measurements were performed inside the stainless steel plates, in order to characterize the stresses generated in the workpiece by the laser cladding technique, studying samples either with one and also with several overlapped clad tracks.

12.2 Experimental

12.2.1 Materials

The Co-based alloy Stellite 6B was deposited on a substrate of austenitic stainless steel AISI 304. The plates used for the experiments were cut down from a rolled plate with a thickness of 10 mm. The samples are the same previously used for the nanoindentation measurements.

Composition and properties used for the simulations were taken from sources [276] and [288], and are represented in Table 11.2. Data available does not cover the entire range of temperatures up to the melting, so at high temperatures, above 600-800°C, the values were linearly extrapolated from the solid ones or taken constant.

12.2.2 Laser Cladding Experimental Setup And Sample Preparation

The Stellite 6B powder was deposited on the stainless steel plates using a computer controlled 2.2kW Nd:YAG Rofin Sinar laser in continuous wave mode.

The parameters used for the process were: power of 1500W with a defocused laser spot of 2.2 mm, speed of 5 mm/s and powder flow rate of 0.37 g/s. Three samples were selected for the study:

- Stainless steel plate at room temperature, one clad track
- Stainless steel plate preheated to 300°C, one clad track
- Stainless steel plate at room temperature, several clad tracks with an overlapping of 34% of the clad width.

The single clad tracks resulted in an average width of 3.2 mm, a height of 1.4 mm and a dilution of about 9-10%, obtained in micrographs as the ratio between the melted area of the plate and the sum of this area and the area of the clad bead.

For analyzing the samples in the synchrotron a cube of 10 mm side was cut down from them between the center and the end of the clad tracks, by means of Electro-Discharge Machining (EDM), in order to not induce stresses in the sample. In Fig. 11.1 is depicted one of these samples and in Fig. 12.1 the cross section of another sample with the coordinate system to which the stresses will be referred to.

12.2.3 Synchrotron Experimental Setup And EDXRD Stress Measurement Technique

The experiments were conducted on the high energy beamline ID15A at the European Synchrotron Radiation Facility (ESRF) in Grenoble, France. This particular beamline is able to produce a high photon flux beam with energies up to 300 KeV, and thus having enough penetration depth to allow the measurement of the residual stresses inside the samples and also with a high spatial resolution.

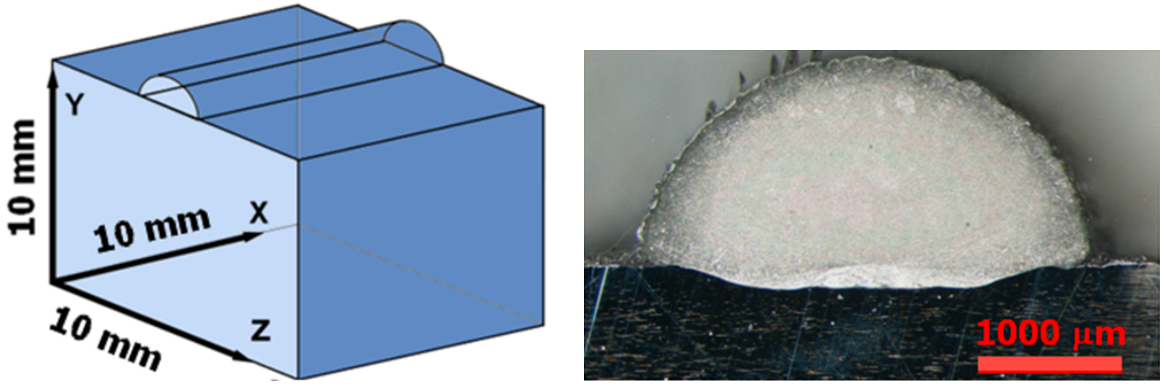

(a) (b)

Figure 12.1: (a) Geometry of the samples including the coordinate system used for the stresses; (b) Cross section of one of the samples.

Diffraction is described by Bragg's Law:

$$n\lambda = 2dsin\theta \tag{12.1}$$

Where n is an integer, λ is the wavelength of the incident radiation, d is the distance between atomic planes and θ is the angle between the incident ray and the scattering plane which equals the diffraction angle. Considering the use of a high energy beam this implies a relatively small diffraction angle and in turn a relatively elongated gauge volume, which favours the application of the technique to essentially 2D problems. A more detailed description of this technique can be found in [274].

Fig. 12.2 shows a scheme of the experimental setup. The specimens were placed on a motorized XY platform, the coordinates of the samples were previously measured for subsequently mapping them with the beam in order to obtain the strains on the $Y-Z$ plane. The incident X-ray white beam shaped by the incident slits impinges on the samples causing diffraction in all directions. Two diffracted beams are selected through a pair of slits and then arrive at the horizontal and vertical detectors, respectively, in order to measure the lattice spacing in two orthogonal directions. The detectors are energy-discriminating and placed at a scattering angle of $2\alpha = 5°$. They are used to measure several peaks simultaneously. Between the slits and the detector the beams traveled through copper tubes shielded with lead. The whole setup is shown in Fig. 12.3.

Only the plate was measured, because with its grain size of about 20 μm a large number of grains are contained inside the gauge volume, which is necessary for the diffraction in all directions. The comparatively large grain size of the clad bead made impractical this technique. The measurements were made in transmission with a gauge volume of dimensions: 0.2x0.2x2 mm^3. The energy dispersive spectrum covered the range 30-250 keV which, in practice, means the first 6-7 reflections in the bcc systems. Whole pattern refinement was performed using the software General Structure Analysis System (GSAS) [292], therefore several reflections were fit simultaneously. Following the conclusion of Daymond et al. [293] this allows the use of the engineering values of the elastic constants for the stress calculation. The samples were rotated 90° around the y axis for the stress measurements in the x direction, so the beam impinges on the longitudinal section ($X-Y$ plane) of the samples. Note that in the $Y-Z$ section the stress state is quite similar to a plain strain configuration, so sections of the sample along the x axis by $Y-Z$ planes at different positions should have similar stresses, however the $X-Y$ sections do

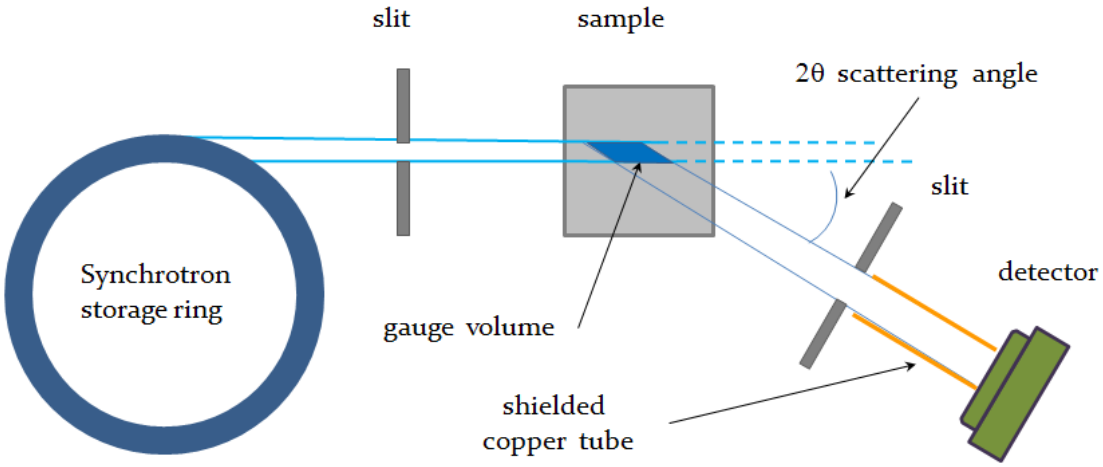

Figure 12.2: Scheme of the experiment

not have a plane strain stress state, so the measurements average the stresses along the 2 mm of the gauge volume length.

The strain ϵ in the direction i is directly obtained by the equation:

$$\epsilon_i = \frac{d - d_0}{d_0} \tag{12.2}$$

where d_0 is the unstressed lattice parameter and d is the stressed one. Parameter d0 was determined from maps in uncladded samples, taking the averaged lattice spacing over the entire sample. The phase used was austenite. Different values of d_0 were determined, one for each detector and for each direction in the sample, to account for variations in the experimental setup between measurements. Changes in d_0 could lead to severe errors in the residual stress values, therefore some points measured in the dilution zone were rejected because differences in chemical composition influence this parameter. Other sources of variation of d_0 were not evaluated. When the principal directions are known only 3 measurements are sufficient to define the complete strain tensor at a point. Otherwise measurements in 6 different directions are necessary. It is commonly assumed that the principal directions are coincident with the coordinate directions X, Y, Z, so the principal stresses are given by [294]:

$$\sigma_x = \frac{E}{(1+\nu)(1-2\nu)} \left[(1-\nu)\epsilon + \nu(\epsilon_y + \epsilon_z)\right] \tag{12.3}$$

where $\nu = 0.295$ and $E = 208$ GPa, being the Poisson ratio and elastic modulus respectively, with corresponding equations for σ_y and σ_z. The typical strain error estimated is about $6 \cdot 10^{-5}$, corresponding to stress uncertainty of 20MPa.

12.3 FEM Model

A nonlinear transient thermomechanical model was developed for the simulation of the laser cladding process, under the software ANSYS. In the model the thermal and the mechanical fields are sequentially coupled. Therefore, the temperature field inside the material during all the process is computed first with a transient thermal analysis, and then these results are given

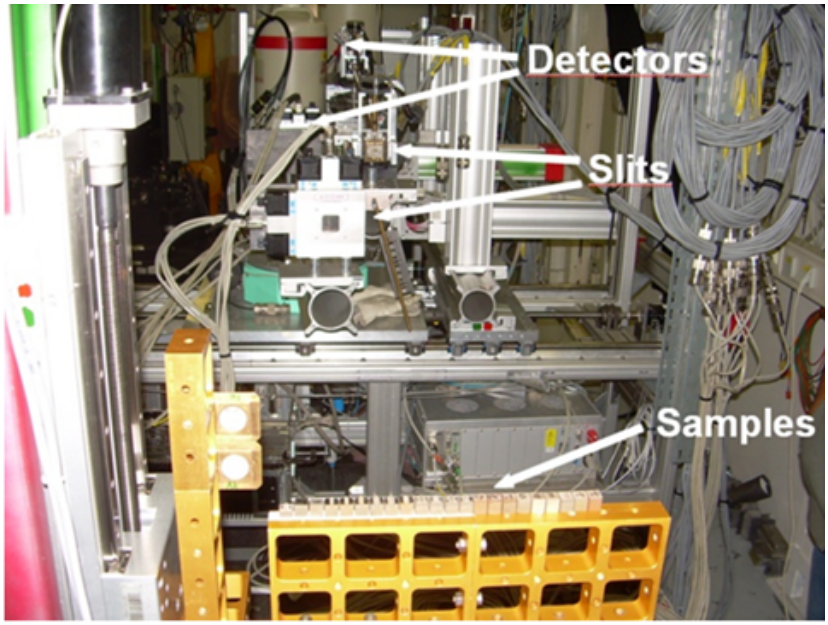

Figure 12.3: Setup of the experiment inside the experimental hutch of the beamline ID15A at ESRF.

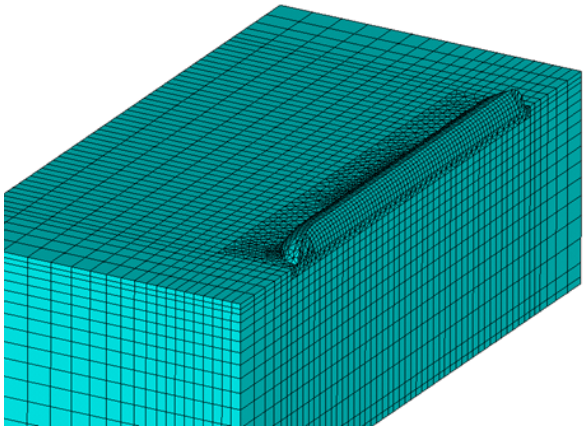

Figure 12.4: Mesh used in the simulations with one clad track

as a thermal load to the mechanical analysis. For modeling the clad deposition process, the whole clad track was divided into slices of 0.5 mm thickness. Then, using the Birth & Death feature, all the elements of the clad track were "killed", a process which multiplies the heat capacity matrix or the stiffness matrix of these elements by a very small value, usually 10−6, so they virtually disappear from the simulation. Afterwards the elements of each slice are activated during the corresponding load step with its nodes constrained at the temperature of the melted material. applying conservation of energy, the remaining laser power is calculated and applied to the surface of the plate excepting the surface underneath the clad bead already deposited, with a top hat profile concentric to the slice being activated. This power is previously multiplied by the absorptivity of the surface. The laser is applied as a heat flux boundary condition on the surface of the elements. Convection heat transfer was applied to the remaining external surfaces with a value of 40 $Wm^{-2}K-1$ and a fluid temperature of 300 K, except for the bottom of the plate, which has a coefficient of 120 $Wm^{-2}K-1$ to take into account in a simple way the faster

cooling rate with the piece in which the sample is supported. This value was obtained using measurements with thermocouples in previous tests, and comparing the temperatures with the model. Radiation was neglected due to its low relevance, but the enthalpy of fusion was included. For the model with preheating, the initial temperature of the nodes of the piece was set to 600 K.

The quasistatic mechanical analysis has the previous results as the thermal load and as constraints only the minimum necessary to prevent rigid body motion, so only one corner is fixed and the others have their vertical displacement constrained. The models with one single clad track take advantage of the symmetry of the problem modeling only half of the piece in order to reduce the computing requirements. The mechanical behaviour of these materials is assumed to follow an elastoplastic rate independent model, in particular a bilinear model with isotropic hardening was selected. The election of a creep model has only minor effect on the residual stresses [295]. More complicated material models could represent the mechanical behavior near the melted zone more accurately [296], but the lack of material data, especially at high temperatures is the major drawback.

2D plane strain and full 3D models were developed. In cases with several clad tracks the 2D models show reasonably good agreement with the 3D models in the prediction of the $Y-Z$ plane stresses of the piece.

A mesh adapted to the zones of higher gradients was used (Fig. 12.4), with a refinement in the clad bead and the zone of the plate underneath it, and an increase in the element size from these zones to the borders of the plate. Most of the plate is meshed with quadratic reduced integration hexahedra, except the transition zone between the clad bead and the plate, as well as the start and end of the clad track, which are meshed with tetrahedra due their complex geometry. The element size ranges between 0.2-2 mm.

12.4 Results And Discussion

12.4.1 Single Track Samples

Fig. 12.5a shows the results of the stress measurements by EDXRD in the Z direction for the sample without preheating. Note that the measurement points are depicted in the image (with exception of the ones discarded because they correspond to the dilution zone) and start at 1 mm of each border, using a mapping spacing of 1 mm between points, excepting the area below the clad track, which is refined in order to achieve a higher detail.

Fig. 12.5b shows the predicted stresses in the z direction by the 3D FEM model. In both pictures the zone with the higher stresses is located below the clad track and has important tensile stresses, as it was expected. The shape of this zone is similar in both cases, but the FEM model predicts a wider and deeper zone. Below, there is a compression area, and in the bottom, the model predicts an area of tensile stresses, but in the measurements there is a lack of results in this area. The model also predicts very small zones of compression just below both ends of the clad bead, but again these zones were not fully covered in the mapping. However the few points measured show a similar pattern. It is noteworthy that although there are differences in the stress patterns, the values of the stresses are very similar for the most important areas. It is worth to mention the presence in all samples of an area with important tensile stresses just in

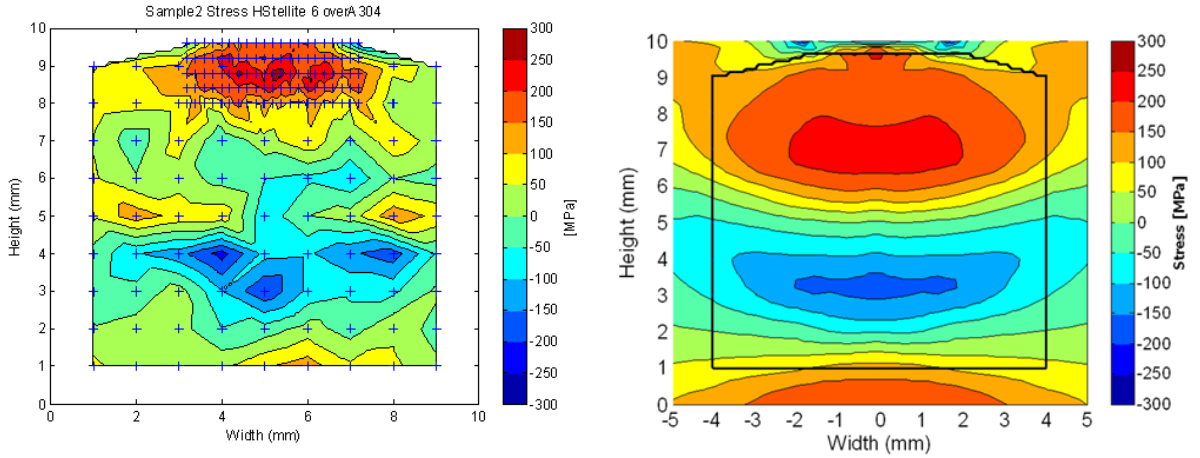

(a) (b)

Figure 12.5: (a) Residual stresses in the Z direction measured by EDXRD, for the sample without preheating (b) Predicted by the 3D model

the middle of the plate, in all directions, but especially in the Y and Z. It is possible that these stresses were present before the laser procedure, maybe due to the rolling process.

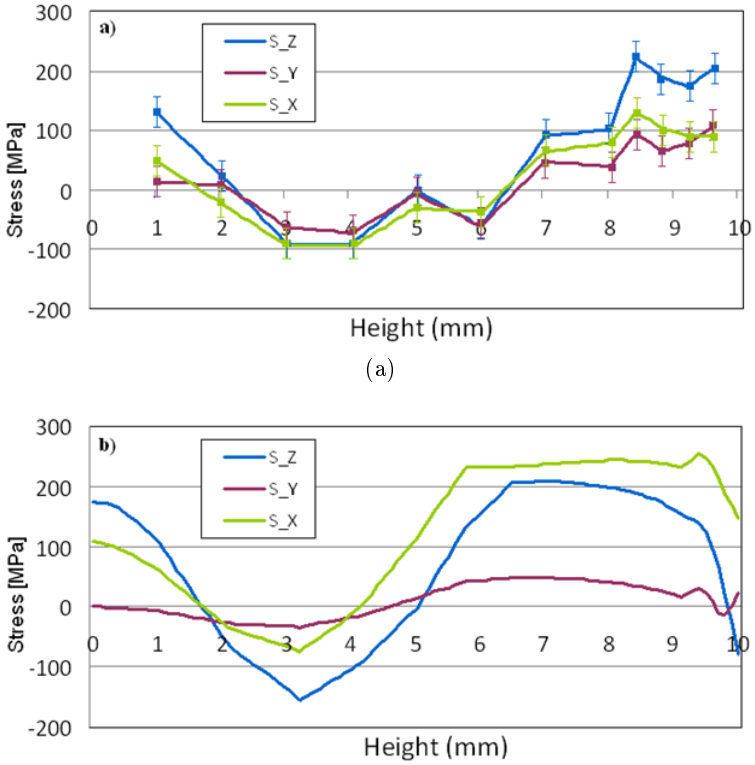

(a)

(b)

Figure 12.6: (a) Residual stress profile over the height of the sample near its center, starting at the bottom of the plate, for the sample without preheating, measured by EDXRD, (b) predicted by the 3D model.

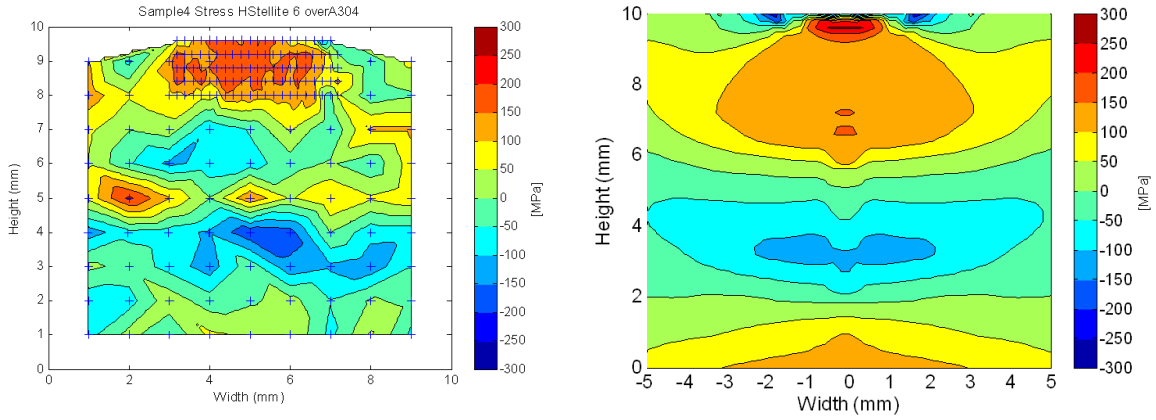

(a) (b)

Figure 12.7: (a) Residual stresses in the Z direction measured by EDXRD, for the sample with preheating (b) Predicted by the 3D model

In Fig. 12.6a the profile of stresses measured along a vertical line near the center of the sample, is represented, and in Fig 12.6bis shown the same profile for the 3D model. The stresses in the y direction show a similar pattern in both cases, although they are higher in the measurements. The X direction stresses are predicted as the highest but show up lower measured values. As it was explained before, in this direction the stress state cannot be considered as plane strain.

The preheated sample shows stresses of lower magnitude (Fig. 12.7), as was expected, both in the simulation model and in the measurements with an agreement similar to the previous sample. The preheating of the substrate reduces the temperature differences in the process, lowers the mismatch between the melted material and the substrate, and also slows down the cooling stage. It is, therefore, a successful way to lower the stresses in laser cladding and welding processes.

12.4.2 Multitrack Sample

The 2D model was used instead of the full 3D for modeling this sample, because with several clad tracks the 3D model needs too much time to complete the simulations and the 2D models seem to provide good results when compared with the 3D ones.

Fig. 12.8a shows the results of the stress measurements by EDXRD in the Z direction and Fig. 12.8b shows the model predictions. The positions of the high stressed areas seem to be similar, as well as the magnitude of the stresses. The model predicts that the highest stresses will be located near the last clad track deposited, suffering the previous tracks a stress relaxation due to the thermal heating when new clad tracks are being deposited and, therefore, lowering the stresses, something that could not be fully checked with the measurements because there is a lack of detailed mapping over the entire upper part of the plate.

Fig. 12.9 shows a comparison between the stress profiles in the $Y - Z$ plane predicted and measured, along a vertical line near the center of the sample, showing a similar pattern and values.

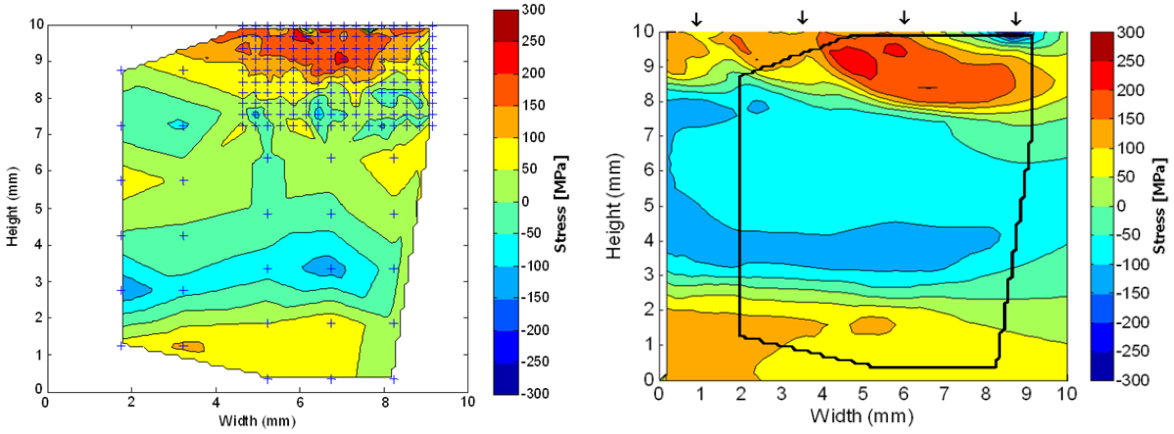

(a) (b)

Figure 12.8: (a) Residual stresses in the Z direction measured by EDXRD, for the sample with several overlapped clad tracks; (b) Predicted by the 3D model, (positions of the clad tracks indicated through arrows)

12.4.3 Conclusions

The EDXRD technique with synchrotron radiation was applied to the measurement of residual stresses in cladded samples with one or several clad tracks. The results of the measurements were compared with the predictions of the model, showing a reasonably good agreement both qualitatively and quantitatively. Potential improvements for the differences could include a more complex material model, the precise measurement of the temperatures of the clad track, and the use of samples completely without stress before the cladding process. A mapping of the pieces including additional zones that have been missed would be interesting in order to compare the entire $Y - Z$ plane, and also taking measurements inside the clad bead using a different combination of materials.

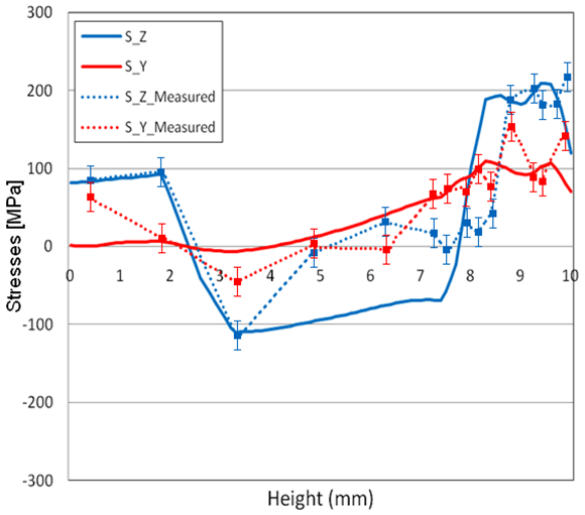

Figure 12.9: Residual stress profile over the height of the sample, near its center, starting at the bottom of the plate, predicted by the 2D FEM model (solid lines) and measured by EDXRD.

Conclusions

Anyone who has never made a mistake has never tried anything new.

Albert Einstein.

The development of high stresses and distortions is one of the main concerns in laser surface heat treatments. The objective of the present thesis is to contribute to the better understanding of the thermomechanical behavior during laser transformation hardening and laser metal deposition techniques, including as well the development of a flexible tool with customizable models for the numerical calculation of the thermomechanical variables, and the microstructural evolution through phase transformation models.

Such a tool will be useful for the prediction of the residual strains and stresses after these processes as well as the phase changes, helping with its optimization and understanding, thus reducing the number of test trials necessary to achieve the desired results.

The thesis includes a bibliographical review of the work of many researchers who contributed to this field. The representative equations and material models are explained throughout the second part of the thesis. Problematic element behavior is also discussed, including a study regarding element performance. The recommendation to obtain accurate and fast results in thermomechanical analyses is to use linear reduced integration hexahedrals, with a fine mesh density, and quadratic tetrahedrals in the zones that cannot be meshed with hexahedrals.

The models developed for the simulation of LTH and laser metal deposition are explained in detail in the middle chapters of the thesis. Results for several materials are presented as well, including studies of thermomechanical stressess and strains, phase transformations and the effect of several parameters in laser cladding.

The third part includes measurements using several experimental techniques in order to validate the model predictions and fine tune some of its parameters. Temperature measurements with thermocouples showed excellent agreement with simulations in several materials. Results from bending tests with steel sheets are similar to the calculated using the models.

Metallurgy and hardness measurements were used to validate the phase transformation model for steels, using samples from several laser surface melting tests. The results, both in the hardness profiles, heat affected zones and melted zones, are very good, showing differences in the melted depth in the samples where this depth is higher, due to the neglect of convection. Laser metal deposition tests of Ti6Al4V on Ti including single clad tracks as well as multiclad tracks, show similar melted zones, heat affected zones, and qualitatively the same microstructure.

Stress profiles on samples of Stellite 6b on AISI 304 steel were first estimated using nanoindentation techniques, obtaining maps with stresses similar to the calculated through the model. Although to fully characterize the stresses, X-Ray diffraction using synchrotron radiation was used on the previous samples, obtaining a similar stress profile with reasonably good agreement in the stress values.

List Of Contributions

Congresses

A. Suárez, M.A. Garrido, A. Rico, A. Yáñez, J. Rodríguez
Viability of the indentation technique for the determination of the residual stresses generated in Co-Cr coatings deposited by laser cladding. Ibertrib 2011. Madrid, Spain. 16-17/06/2011

A. Suárez, A. Yañez
Mechanical and metallurgical modelling of the laser cladding of steels. European Materials Reseach Society congress (EMRS). Niza, France. 9-13/05/2011

A. Suárez, M. J. Tobar, A. Yáñez, I. Pérez, J. Sampedro, V. Amigó, J. J. Candel
Modeling of phase transformations of Ti6Al4V during laser metal deposition Lasers In Manufacturing (LIM). Munich, Germany. 23-26/05/2009

A. Suárez, J. M. Amado, M. J. Tobar, A. Yáñez, E. Fraga, M. J. Peel
Estudio de las tensiones residuales generadas por la técnica del plaqueado láser mediante difracción de radiación sincrotrón. Photonics Valencia 2010. Valencia, Spain. 12-13/05/2010

A. Suárez, M. J. Tobar, A. Yáñez
Modelización mediante FEM del comportamiento termomecánico y metalúrgico del proceso de plaqueado por láser. Reunión Nacional de Óptica 2009 (RNO). Ourense, Spain. 14-17/09/2009

A. Suárez, J. M. Amado, M. J. Tobar, A. Yáñez, E. Fraga, M. J. Peel
Study of residual stresses generated in laser cladding by diffraction of synchrotron radiation. Lasers In Manufacturing (LIM). Munich, Germany.15-18/06/2009

A. Suárez, J. M. Amado, M. J. Tobar, A. Yáñez, E. Fraga, M. J. Peel
Study of residual stresses generation in laser cladding: synchrotron diffraction measurements and model based analysis. European Materials Reseach Society congress (EMRS). Estrasbourg, France. 8-12/06/2009

A. Suárez, M. J. Tobar, A. Yañez
Modeling of residual stress generation in laser cladding process with single, overlapping and multilayer laser scans. International Congress on Applications of Lasers Electro-Optics (ICALEO). Temecula, CA USA. 20-23/10/2008

A. Suárez, M. J. Tobar, A. Yañez
Modeling of residual stress generation in laser cladding process with single, overlapping and multilayer laser scans. European Materials Reseach Society congress (EMRS). Estrasbourg, France. 26-30/05/2008

A. Suárez, M. J. Tobar, A. Yañez
FEM simulations of laser cladding. 21th Meeting on Matematical Modeling of Materials Processing with Lasers (M4PL). Igls, Austria. 16-18/01/2008

A. Suárez, M. J. Tobar, A. Yañez
A FEM based approach to model stress generation in laser cladding processes. 20th Meeting on Matematical Modeling of Materials Processing with Lasers (M4PL). Igls, Austria. 17-19/01/2007

Articles

A. Suárez, J.M. Amado, M.J. Tobar, A. Yáñez, E. Fraga, M.J. Peel
Study of residual stresses generated inside laser cladded plates using FEM and diffraction of synchrotron radiation. Surface and Coatings Technology 204, pp. 1983-1988 (2010).

A. Suárez, M. J. Tobar, A. Yáñez, I. Pérez, J. Sampedro, V. Amigó, J. J. Candel
Modeling of phase transformations of Ti6Al4V during laser metal deposition. Physics Procedia 12, pp. 666-673 (2011).

Bibliography

[1] E. Kennedy, G.Byrne, and D.N. Collins. A review of the use of high power diode lasers in surface hardening. *Journal of Materials Processing Technology*, 155-156:1855–1860, 2004.

[2] A. Tizian, L.Giordano, and E. Ramous. Laser surface treatment by rapid solidification. In *Lasers in Materials Processing, ASM, Conference proceedings, Metals Park*, pages 108–115, 1983.

[3] S. Sjostrom. Interactions and constitutive models for calculating quench stresses in steel. *Materials Science and Technology*, 1:823–829, 1984.

[4] L. Giorleo, A. Liu, and B. Previtali. Apparent spot in circular laser hardening: effect of process parameters. *Int. J. Mater Forum*, 3:1119–1122, 2010.

[5] J. Mazumder. Laser heat treatment: The state of the art. *Journal of Metals*, 35:18–26, 1983.

[6] F. D Seaman. *Industrial Laser Handbook*. PennWell Books, 1986.

[7] T. Miokovic, V. Schulze, O. Vöhringer, and D. Löhe. Prediction of phase transformations during laser surface hardening of AISI 4140 including the effects of inhomogeneous austenite formation. *Materials Science and Engineering A*, 435-436:547–555, 2006.

[8] R. Patwa and Y.C. Shin. Predictive modeling of laser hardening of AISI 5150H steels. *International Journal of Machine Tools and Manufacture*, 47:307–320, 2007.

[9] W. Wu, N.G. Liang, C.H. Gan, and G. Yu. Numerical investigation on laser transformation hardening with different temporal pulse shapes. *Surface and Coatings Technology*, 200:2686–2694, 2006.

[10] R.S. Lakhar, Y.C. Shin, and M.J.M. Krane. Predictive modeling of multi-track laser hardening of AISI 4140 steel. *Materials Science and Engineering A*, 253:5017–5028, 2008.

[11] W.B. Li and K.E. Easterling. Residual stresses in laser transformation hardened steel. *Surface Engineering*, 2:43–48, 1986.

[12] N.S. Bailey, W. Tan, and Y.C. Shin. Predictive modeling and experimental results for residual stresses in laser hardening of AISI 4140 steel by a high power diode laser. *Surface and Coatings Technology*, 203:2003–2012, 2009.

[13] A. Otto and M. Schmidt. Towards a universal numerical simulation model for laser material processing. *Physics Procedia*, 5:35–46, 2010.

[14] J. Montalvo-Urquizo, Z. Akbay, and A. Schmidt. Adaptive finite element models applied to the laser welding problem. *Computational Materials Science*, 46:245–254, 2009.

[15] F. Kong and R. Kovacevic. 3D finite element modeling of the thermally induced residual stress in the hybrid laser/arc welding of lap joints. *Journal of Materials Processing Technology*, 210:941–950, 2010.

[16] E. Toyserkani, A. Khajepour, and S. Corbin. 3-D finite element modeling of laser cladding by powder injection: effects of laser pulse shaping on the process. *Optics and Lasers in Engineering*, 41:849–867, 2004.

[17] I. Tabernero, A. Lamikiz, E. Ukar, L.N. López de Lacalle, C. Angulo, and G. Urbikain. Numerical simulation and experimental validation of powder flux distribution in coaxial laser cladding. *Journal of Materials Processing Technology*, 210:2125–2134, 2010.

[18] G. Palumbo, S. Pinto, and L. Tricario. Numerical finite element investigation on laser cladding treatment of ring geometries. *Journal of Materials Processing Technology*, 155-156:1443–1450, 2004.

[19] M.J. Tobar, A.Suárez, J.C. Álvarez, J. M. Amado, and A. Yáñez. A 3D transient FEM analysis of residual stress generation during laser cladding. *Proceedings of the LANE 2007.*

[20] F. Brückner, D. Lepski, and E. Beyer. Calculation of stresses in two and three dimensional structures generated by induction asisted laser cladding. *Munich: Proceedings of the Fifth International WLT-Conference Lasers in Manufacturing, LiM 2009.*

[21] L. Costa, R. Vilar, T. Reti, and A.M. Deus. Rapid tooling by powder deposition: Process simulation using finite element analysis. *Acta Materialia*, 53:3987–3999, 2005.

[22] M.F. Ashby and K.E. Easterling. Transformation hardening of steel surfaces by laser beams-I Hypo-eutectoid steels. *Acta Metallurgica*, 32:1935–1948, 1984.

[23] C.H. Gür and J. Pan. *Handbook of Thermal Process Modeling of Steels.* Taylor & Francis, 2009.

[24] C. Leyens and M. Peters. *Titanium and Titanium Alloys: Fundamentals and Applications.* Wiley-VCH, 2003.

[25] P. J. Withers and H. K. D. H. Bhadeshia. Residual stress part 1 - measurement techniques. *Materials Science and Technology April Vol.*, 17:355–365, 2001.

[26] T. Maiman. *The laser odyssey.* Laser Press, 2001.

[27] A. Javan, W.R. Bennett, and D.R. Herriott. Population inversion and continuous optical maser oscillation in a gas discharge containing a He-Ne mixture. *Physical Review Letters*, 6:106–110, 1961.

[28] C.K.N. Patel. Continuous-wave laser action on vibrational-rotational transitions of CO2. *Physical Review*, 136:1187–1193, 1964.

[29] R. N. Hall, G. E. Fenner, J. D. Kingsley, T. J. Soltys, and R. O. Carlson. Coherent light emission from GaAs junctions. *Phys. Rev. Lett.*, 9:366–368, 1962.

[30] J.E. Geusic, H.M. Marcos, and L.G. van Uitert. Laser oscillations in Nd-doped yttrium aluminum, yttrium gallium and gadolinium garnets. *Applied Physics Letters*, 4:182–184, 1964.

[31] W.T Walter, M. Piltch, N. Solimene, and G. Gould. Pulsed-laser action in atomic copper vapor. *Bulletin of the American Physical Society*, 11:113, 1966.

[32] P.P Sorokin and J.R Lankard. Stimulated emission observed from an organic dye, chloro-aluminum phthalocyanine. *IBM Journal*, 10:162–163, 1966.

[33] F.J. McClung and R.W. Hellwarth. Giant optical pulsations from ruby. *Journal of Applied Physics*, 33:828–829, 1962.

[34] L.E. Hargrove, R.L Fork, and M.A Pollack. Locking of he-ne laser modes induced by

synchronous intracavity modulation. *Applied Physics Letters*, 5:4–5, 1964.

[35] W.N. Platte and J.F. Smith. Laser techniques for metals joining. *Welding Journal Research Supplement*, 42:481–489, 1963.

[36] J.E Anderson and J.E Jackson. Theory and application of pulsed laser welding. *Welding Journal*, 44:1018–1026, 1965.

[37] Anon. Laser "punches" holes in diamond wire-drawing dies. *Laser Focus*, 2:4–7, 1966.

[38] A.B.J. Sullivan and P.T. Houldcroft. Gas-jet laser cutting. *British Welding Journal*, 14:443–445, 1967.

[39] C. DeMichelis. Laser interaction with solids-a bibliographical review. *IEEE Journal of Quantum Electronics*, 6:630–641, 1970.

[40] F.E. Cunningham. The use of lasers for the production of surface alloys. Master's thesis, Massachusetts Institute of Technology, 1964.

[41] B.P. Fairand, B.A. Wilcox W.J. Gallagher, and D.N. Williams. Laser shock-induced microstructural and mechanical property changes in 7075 aluminum. *Journal of Applied Physics*, 43:3893–3896, 1972.

[42] Avco Everett Research Laboratory Inc. Cladding, 1976.

[43] Caterpillar Tractor Co. Method and apparatus for fusibly bonding a coating material to a metal article, 1977.

[44] Rolls-Royce. Application of metallic coatings to metallic substrates, 1981.

[45] C.R. Deckard. Method and apparatus for producing parts by selective sintering, 1987.

[46] M. Born and E. Wolf. *Principles of Optics*. Oxford, UK: Pergamon Press, 1986.

[47] A.M. Prokhorov, V.I.Konov, I. Ursu, and I.N. Milhailescu. *Laser Heating of Metals*. The Adam Hilger Series on Optics and Optoelectronics, 1990.

[48] D. Rosenthal. Mathematical theory of heat distribution during welding and cutting. *Welding Journal*, 20:230–234, 1941.

[49] M.von Allmen. *Laser-Beam interactions with materials-Physical principles and applications*. Berlin: Springer-Verlag, 1987.

[50] D. Bergström, J. Powell, and A.F.H. Kaplan. The absorptance of steels to Nd:YLF and Nd:YAG laser light at room temperature. *Applied Surface Science*, 253:5017–5028, 2007.

[51] D. Bergström. *The Absorption of Laser Light by Rough Metal Surfaces*. PhD thesis, Lulea University of Technology, 2008.

[52] J. Dowden. *The Theory of Laser Materials Processing*, chapter Laser Keyhole Welding: The Vapour Phase, pages 94–125. Bristol, UK: John Dowden (ed.), 2009.

[53] Y. Fu, A. Loredo, B. Martin, and A.B. Vannes. A theoretical model for laser and powder particles interaction during laser cladding. *Journal of Materials Processing Technology*, 128:106–112, 2002.

[54] J. Lin. Temperature analysis of the powder streams in coaxial laser cladding. *Optics & Laser Technology*, 31:565–570, 1999.

[55] W.M. Steen. *Laser Material Processing*. London: Springer, 1991.

[56] Jr. E. Kannatey-Asibu. *Principles of Laser Materials Processing*. Wiley, 2009.

[57] LaserInstitute of America. *Handbook of Laser Materials Processing*. Magnolia Publishing Inc, 2001.

[58] P. De la Cruz, M. Oden, and T. Ericsson. Effect of laser hardening on the fatigue strength and fracture of a B-Mn steel. *Int. J. Fatigue*, 20:389–398, 1998.

[59] D.I Pantelis, E.Bouyiouri, N. Kouloumbi, P. Vassiliou, and A. Koutsomichalis. Wear and corrosion resistance of laser surface hardened structural steel. *Surface and Coatings Technology*, 298:125–134, 2002.

[60] K.H. Lo, F.T.Cheng, C.T. Kwok, and H.C. Man. Effects of laser treatments on cavitation erosion and corrosión of AISI 440C martensitic stainless steel. *Materials Letters*, 58:88–93, 2003.

[61] C.T. Kwok, K.H. Lo, F.T. Cheng, and H.C. Man. Effect of processing conditions on the corrosion performance of laser surface melted AISI 440C martensitic stainless steel. *Surface and Coatings Technology*, 166:221–230, 2003.

[62] M.Y. Li, Y. Wang, B. Han, W.M. Zhao, and T. Han. Microstructure and properties of high chrome steel roller after laser surface melting. *Applied Surface Science*, 255:7574–7579, 2009.

[63] A. Conde, R.Colaco, R. Vilar, and J. De Damborenea. Corrosion behaviour of steels after laser surface melting. *Materials and Design*, 21:441–445, 2000.

[64] J. D. Majumdar, R. Galun, B.L. Mordike, and I. Manna. Effect of laser surface melting on corrosion and wear resistance of acommercial magnesium alloy. *Materials Science and Engineering A*, 361:119–129, 2003.

[65] H.S. Carslaw and J.C. Jaeger. *Conduction of Heat in Solids.* Oxford: Oxford Press, 1959.

[66] M. Lax. Temperature rise induced by a laser beam. *J. Appl. Phys*, 48:3919–3924, 1977.

[67] O.A. Sandven. Report of avco everett metalworking lasers. In *in 3rd Annual SPIE International Conference, San Diego, CA.*, 1979.

[68] V Gregson. *Laser Heat Treatment in Laser Materials Processing.* Amsterdam: North-Holland, 1983.

[69] I. Chen and S. Lee. Transient temperature profiles in solids heated with a scanning laser. *J. Appl. Phys.*, 54:1062–1066, 1983.

[70] C. Maier, P.Schaaf, and U. Gonser. Calculation of the temperature profile for laser treatment of metallic samples. *Materials Science and Engineering A*, 150:271–280, 1992.

[71] S.M. Zubair and M.A. Chaudhry. Heat conduction in a semi-infinite solid due to time-dependen laser source. *International Journal of Heat and Mass Transfer*, 39:3067–3074, 1996.

[72] J. Isenberg and S. Malkin. Effect of variable thermal properties on moving band source temperatures. *ASME Paper WA/Prod-5*, 74, 1974.

[73] S. Kou and D.K. Sun. Heat flow during the laser transformation hardening of cylindrical bodies. *Metallurgical Transactions A*, 14A:1859–1867, 1983.

[74] K. Koai, R. Damaschek, and H.W. Bergmann. Heat transfer laser hardening of rotating cylinders. *American Society of Mechanical Engineers*, 259:1–8, 1993.

[75] R. Festa, O.Manca, and V. Naso. A comparison between models of thermal fields in laser and electron beam surface processing. *International Journal of Heat and Mass Transfer*, 31:99–106, 1988.

[76] R. Festa, O. Manca, and V. Naso. Simplified thermal models in laser and electron beam surface hardening. *International Journal of Heat and Mass Transfer*, 33:2511–2518, 1990.

[77] H.E. Cline and T.R. Anthony. Heat treating and melting material with scanning laser or electron beam. *J. Appl. Phys.*, 48:3895–3900, 1977.

[78] D.J. Sanders. Temperature distributions produced by scanning gaussian laser beams. *Appl. Opt.*, 23:30–35, 1984.

[79] S. Kou, D.K. Sun, and Y.P. Lee. A fundamental study of laser transformation hardening. *Metall. Trans. A*, 14:643–653, 1983.

[80] X.F. Wang, X.D. Lu, G.N. Chen, Sh.G Hu, and Y.P. Su. Research on the temperature field in laser hardening. *Optics & Laser Technology*, 38:8–13, 2006.

[81] D. Sowdari and P. Majumdar. Finite element analysis of laser irradiated metal heating and melting processes. *Optics & Laser Technology*, 42:855–865, 2010.

[82] R. Komanduri and Z.B. Hou. Thermal analysis of the laser surface transformation hardening process. *International Journal of Heat and Mass Transfer*, 44:2845–2862, 2001.

[83] A. Yáñez, J.C. Álvarez, A. J. López, G. Nicolás, J. A. Pérez, A. Ramil, and E. Saavedra. Modelling of temperature evolution on metals during laser hardening process. *Applied Surface Science*, 186:611–616, 2002.

[84] B.S. Yilbas. Analytical solution for time unsteady laser pulse heating of semi-infinite solid. *Int. J. Mech. Sci.*, 39:671–682, 1997.

[85] W.B. Li, K.E. Easterling, and M.F. Ashby. Laser transformation hardening of steel- ii hyper-eutectoid steel. *Acta Metallurgica*, 34:1533–1543, 1986.

[86] M.F. Ashby and H.R. Sherliff. The prediction of case depth in laser transformation hardening. *Metallurgical Transactions A*, 22A:2459–2466, 1991.

[87] M. Davis, P. Kapadia, J. Dowden, W.M. Steen, and C.H.G. Courtney. Heat hardening of metal surfaces with a scanning laser beam. *Journal of Physics D: Applied Physics*, 19:1981–1997, 1986.

[88] T.L. Chen, Y.H.Guan, H.G. Wang, and J.T. Zhang. Study on austenite transformation during laser heating. *Journal of Materials Processing Technology*, 63:546–549, 1997.

[89] I. Felde, R. Kohlheb, G. Buza, B. Vero, and T. Reti. Microstructure and hardness prediction in laser heat treated steels using computer simulation. *IOM Communication*, pages 708–714, 1998.

[90] T. Reti, G. Bagyinszki, I. Felde, B. Vero, and T. Bell. Prediction of as-quenched hardness after rapid austenitization and cooling of surface hardened steels. *Computational Materials Science*, 15:101–112, 1999.

[91] G.N. Haidemenopoulos. Coupled thermodynamic/kinetic analysis of diffusional transformations during laser hardening and laser welding. *Journal of Alloys and Compounds*, 320:302–307, 2001.

[92] M.J. Tobar, C. Álvarez, J.M. Amado, A. Ramil, E. Saavedra, and A. Yáñez. Laser transformation hardening of a tool steel: simulation based parameter optimization and experimental results. *Surface and Coatings Technology*, 200:6362–6367, 2006.

[93] F. Lusquiños, J.C.Conde, S. Bonss, A. Riveiro, F. Quintero, R. Comesaña, and J. Pou. Theoretical and experimental analysis of high power diode laser (HPDL) hardening of AISI 1045 steel. *Appl. Surf. Sci.*, 4:948–95, 2007.

[94] S. Skavarenina and Y.C. Shin. Predictive modeling and experimental results for laser hardening of AISI 1536 steel with complex geometric features by a high power diode laser. *Surface and Coatings Technology*, 201:2256–2269, 2006.

[95] J.C. Rozzi, F.E. Pfefferkorn, F.P. Incropera, and Y.C. Shin. Transient thermal response of a rotating cylindrical silicon nitride workpiece subjected to a translating laser heat source: I-comparison of surface temperature measurements with theoretical results. *ASME Journal of Heat Transfer*, 120:899–906, 1998.

[96] J.C. Rozzi, F.E. Pfefferkorn, F.P. Incropera, and Y.C. Shin. Transient three-dimensional

heat transfer model for the laser assisted machining of silicon nitride: I-comparison of predictions with measured surface temperature histories. *International Journal of Heat and Mass Transfer*, 43:1409–1424, 2000.

[97] L. Orazi, A. Fortunato, G. Cuccolini, and G. Tani. An efficient model for laser surface hardening of hypo-eutectoid steels. *Applied Surface Science*, 256:1913–1919, 2010.

[98] R.K. Shiue and C. Cheg. Laser transformation hardening of tempered 4340 steel. *Metallurgical Transactions A*, 23A:163–170, 1992.

[99] L.M. Galantucci and L.Tricario. An experimental and numerical study on the influence of not uniform beam energy distribution in laser steel hardening. *Annals of the CIRP*, 48:155–158, 1999.

[100] M.K.H. Leung, H.C.Man, and J.K. Yu. Theoretical and experimental studies on laser transformation hardening of steel by customized beam. *International Journal of Heat and Mass Transfer*, 50:4600–4606, 2007.

[101] J. Grum and R. Sturm. Laser surface melt-hardening of gray and nodular irons. *Applied Surface Science*, 109-110:128–132, 1997.

[102] A. Roy and I. Manna. Mathematical modeling of localized melting around graphite nodules during laser surface hardening of austempered ductile iron. *Optics and Lasers in Engineering*, 34:369–383, 2000.

[103] Z. Zhang, D. Delagnes, and G. Bernhart. Microstructure evolution of hot-work tool steels during tempering and definition of a kinetic law based on hardness measurements. *Materials Science and Engineering A*, 380:222–230, 2004.

[104] G. Tani, L. Orazi, and A. Fortunato. Prediction of hypo eutectoid steel softening due to tempering phenomena in laser surface hardening. *CIRP Annals - Manufacturing Technology*, 57:209–212, 2008.

[105] American Society of Metals. *ASM Handbook 4: Heat Treating*. 1991.

[106] G. Tani, A. Fortunato, A. Ascari, and G. Campana. Laser surface hardening of martensitic stainless steel hollow parts. *CIRP Annals - Manufacturing Technolog*, 59:207–210, 2010.

[107] A. Bokota and S. Iskierta. Numerical prediction of the hardened zone in laser treatment of carbon steel. *Acta Metallurgica*, 44:445–450, 1996.

[108] A. Bokota and S. Iskierta. Numerical simulation of transient and residual stresses causes by laser hardening of slender elements. *Computational Materials Science*, 7:366–376, 1997.

[109] D. Grevey, L. Maiffredy, and A.B. Vannes. A simple way to estimate the level of the residual stresses after laser heating. *Journal of Mechanical Working Technology*, 16:65–78, 1988.

[110] Y.S. Yang and S.J. Na. A study on residual stresses in laser surface hardening of a medium carbon steel. *Surface and Coatings Technology*, 38:311–324, 1989.

[111] Y.S. Yang and S.J. Na. A study on the thermal and residual stress by welding and laser surface hardening using a new two-dimensional finite element model. *Proceedings of the Institution of Mechanical Engineers*, 204:167–173, 1990.

[112] F. Fattorini, F.M.M. Ricci, and A. Senin. Internal stress distribution induced by laser surface treatment. *Proceedings of the European Conference on Laser Treatment of Materials (ECLAT), Mordike*, pages 235–242, 1992.

[113] S. Denis, M. Boufoussi, J.Ch Chevrier, and A. Simon. Analysis of the development of residual stresses for surface hardening of steel by numerical simulation. *Proceedings of the International Conference on Residual Stresses (ICRS4), Baltimore*, pages 513–519, 1994.

[114] H-X. Zhan, Y. Wang, C-W. Li, T. Han, B. Han, and W-M. Zhao. Computational and experimental study of a melt hardened zone on a roller modified by wide-band laser treatment. *Optics & Laser Technology*, 41:251–257, 2009.

[115] J.C. Ion. *Laser processing of engineering materials.* Oxford: Butterworth-Heinemann, 2005.

[116] C. Bagger and F.O. Olsen. Review of laser hybrid welding. *J. Laser Appl.*, 17:2–14, 2005.

[117] D Rosenthal. The theory of moving sources of heat and its application to metal treatments. *Trans. Amer. Soc. Mech. Eng.*, 68:849–866, 1946.

[118] J. Goldak, J. Zhou, V. Breiguine, and F. Montoya. Thermal stress analysis of welds: from melting point to room temperature. *Trans. JWRI 25*, 25:185–189, 1996.

[119] B. Jones, A. Emery, and J. Marburger. An analytical and experimental study of the effects of previous termweldingnext term parameters in fusion welds. *Weld. J.*, 72:51–59, 1993.

[120] B. Jones, A. Emery, and J. Marburger. Design and analysis of test coupon for fusion welding. *ASME J. Press. Vess. Technol.*, 115:38–46, 1993.

[121] J.-B. Roelens, F.Maltrud, and J. Lu. Determination of residual stresses in submerged arc multi-pass welds by means of numerical simulation and comparison with experimental measurements. *Weld. World*, 33:152–159, 1994.

[122] J.-B. Roelens. Numerical simulation of multipass submerged arc weldingdetermination of residual stresses and comparison with experimental measurement. *Weld. World*, 35:110–117, 1995.

[123] L.-E. Lindgren, H.Runnemalm, and M.O. Nasstrom. Simulation of multipass previous termweldingnext term of a thick plate. *Int. J. Numer. Methods Engrg.*, 44:1301–1316, 1999.

[124] J. Goldak, A. Chakravarti, and M. Bibby. A new finite element model for welding heat sources. *Metall. Trans. B*, 15:299–305, 1984.

[125] L. E. Lindgren, H.-A. Häggblad, J. M. J. McDill, and A. S. Oddy. Automatic remeshing for three-dimensional finite element simulation of welding. *Computer Methods in Applied Mechanics and Engineering*, 147:401–409, 1997.

[126] J.M. McDill, J.A. Goldak, A.S. Oddy, and M.J. Bibby. Isoparametric quadrilaterals and hexahedrons for mesh grading algorithms. *Comm. Appl. Numer. Methods*, 3:155–163, 1987.

[127] J.M.J. McDill, A.S. Oddy, and J.A. Goldak. An adaptive mesh-management algorithm for three-dimensional automatic finite element analysis. *Trans. ASME*, 15:57–70, 1991.

[128] J.M.J. McDill and A.S. Oddy. Arbitrary coarsening for adaptive mesh management in automatic finite element analysis. *J. Math. Modelling Sci. Comput*, 2B:1072–1077, 1993.

[129] J.M.J. McDill, M.E. Klein, and A.S. Oddy. Data transfer for 3D h-adaptive thermal-elasto-plastic finite element analysis, simulations of materials processing: therory, methods and applications. *Proc. Numiform 95, Ithaca*, 95:463–468, 1995.

[130] H. Runnemalm and S.Hyun. Three-dimensional welding analysis using an adaptive mesh scheme. *Computer Methods in Applied Mechanics and Engineering*, 189:515–523, 2000.

[131] LarsFuglsang Andersen. *Residual stresses and deformations in steel structures.* Technical University of Denmark, 2000.

[132] D. Berglund and H. Alberg. Comparison of plastic, viscoplastic, and creep models when modelling welding and stress relief heat treatment. *Comput. Methods Appl. Mech. Engrg.*, 192:5189–5208, 2003.

[133] J. Devaux, D. Pont, and J. Leblond. Numerical simulation of the repair of a defect-

containing zone by a manual welding procedure. *ASME 10th Conference on Offshore and Arctic Engineering (OMAE)*, 1991.

[134] J. Mazumder and W.M. Steen. Heat transfer model for cw laser material processing. *J. Appl. Phys*, 51:941–948, 1980.

[135] B.S. Yilbas and A.Z. Sahin. Laser heating mechanism including evaporation process. *International Communications in Heat and Mass Transfer*, 21:509–518, 1994.

[136] B.S. Yilbas. Laser heating process and experimental validation. *International Journal of Heat and Mass Transfer*, 40:1131–1143, 1997.

[137] A. Matsunawa and V. Semak. The simulation of front keyhole wall dynamics during laser welding. *J. Phys. D: Appl. Phys.*, 30:798, 1997.

[138] V.A Khokhlov and S.I. Anisimov. *Instabilities in Laser-Matter Interaction.* Boca Raton, FL: CRC Press, 1995.

[139] V. Semak, W.D. Bragg, B. Damkroger, and S. Kempka. Transient model for the keyhole during laser welding. *J. Phys. D: Appl. Phys*, 15:61–64, 1999.

[140] P. Solana and J.L. Ocaña. A mathematical model for penetration laser welding as a free-boundary problem. *J. Phys. D: Appl. Phys.*, 30:1300, 1997.

[141] W. Sudnik, D. Radaj, and W. Erofeew. Computerized simulation of laser beam welding, modelling and verification. *J. Phys. D: Appl. Phys.*, 29:2811, 1996.

[142] W. Sudnik, D. Radaj, S. Breitschwerdt, and W. Erofeew. Numerical simulation of weld pool geometry in laser beam welding. *J. Phys. D: Appl. Phys.*, 33:662, 2000.

[143] G. Bruggemann, A. Mahrle, and T. Benziger. Comparison of experimental determined and numerical simulated temperature fields for quality assurance at laser beam welding of steels and aluminium alloys. *NDT and E International*, 33:453–463, 2000.

[144] A. Mahrle and J. Schmidt. The influence of fluid flow phenomena on the laser beam welding process. *International Journal of Heat and Fluid Flow*, 23:288–297, 2002.

[145] X. Chen and X.-H. Ye. Three-dimensional modelling of heat transfer and fluid flow in laser full-penetration welding. *J. Phys. D: Appl. Phys.*, 35:1049–1056, 2002.

[146] H. Du, L. Hu, J. Liu, and X. Hu. A study on the metal flow in full penetration laser beam welding for titanium alloy. *Computational Materials Science*, 29:419–427, 2004.

[147] H. Wang, Y. Shi, and S. Gong. Numerical simulation of lasereyhole welding processes based on control volume methods. *J. Phys. D: Appl. Phys.*, 39:4722–4730, 2006.

[148] K. Abderrazak, S. Bannour, H. Mhiri, G. Lepalec, and M. Autric. Numerical and experimental study of molten pool formation during continuous laser welding of AZ91 magnesium alloy. *Computational Materials Science*, 44:858–866, 2009.

[149] M.J. Tobar, I.M. Lamas, A. Yáñez, J.M. Sánchez-Amaya, Z. Bouka, and F.J. Botana. Experimental and simulation studies on laser conduction welding of AA5083 aluminium alloys. *Physics Procedia 5*, 5:299–308, 2010.

[150] R. Fabbro and K. Chouf. Dynamical description of the keyhole in deep penetration laser welding. *J. Laser Appl.*, 12:142–148, 2000.

[151] H. Ki, P.S. Mohanty, and J. Mazumder. Modeling of laser keyhole welding: Part i. mathematical modeling, numerical methodology, role of recoil pressure, multiple reflections, and free surface evolution. *Metallurgical and Material Transactions A*, 33:1817–1830, 2002.

[152] H. Ki, P.S. Mhohandy, and J. Mazumder. Modeling of laser keyhole welding: Part ii. simulation of keyhole evolution, velocity, temperature profile, and experimental verification. *Metallurgical and Material Transactions A*, 33:1831–1842, 2002.

[153] H. Koch, K-H. Leitz, A. Otto, and M. Schmidt. Laser deep penetration welding simulation based on a wavelength dependent absorption model. *Physics Procedia*, 5:309–315, 2010.

[154] A. Loredo, B. Martin, H. Andrzejewski, and D. Grevey. Numerical support for laser welding of zinc-coated sheets process development. *Applied Surface Science*, 195:297–303, 2002.

[155] M. Medale, C. Xhaard, and R. Fabbro. A thermo-hydraulic numerical model to study spot laser welding. *C. R. Mecanique*, 335:280–286, 2007.

[156] M. Gatzen and Z. Tang. CFD-based model for melt flow in laser beam welding of aluminium with coaxial magnetic field. *Physics Procedia*, 5:317–326, 2010.

[157] N. Chakraborty. The effects of turbulence on molten pool transport during melting and solidification processes in continuous conduction mode laser welding of copper-nickel dissimilar couple. *Applied Thermal Engineering*, 29:3618–3631, 2009.

[158] H. GuoMing, Z. Jian, and L. JianQang. Dynamic simulation of the temperature field of stainless steel laser welding. *Materials and Design*, 28:240–245, 2007.

[159] K.R. Balasubramanian, N.S. Shanmugam, G. Buvanashekaran, and K. Sankararayanasamy. Numerical and experimental investigation of laser beam welding of AISI 304 steel sheet. *Advances in Production Engineering & Management*, 3:93–105, 2008.

[160] A. Belhad, J.Bessrour, J.-E. Masse, M. Bouhafs, and L. Barrallier. Finite element simulation of magnesium alloys laser beam welding. *Journal of Materials Processing Technology*, 210:1131–1137, 2010.

[161] N.S. Shanmugam, G. Buvanashekaran, K. Sankaranarayanasamy, and S.R. Kumar. A transient finite element simulation of the temperature and bead profiles of T-joint laser welds. *Materials and Design*, 31:4528–4542, 2010.

[162] K. Salonitis, D.Drougas, and G. Chryssolouris. Finite element modeling of penetration laser welding of sandwich materials. *Physics procedia*, 5:327–335, 2010.

[163] C.S. Wu, H.L. Wang, and Y.M. Zhang. Numerical analysis of the temperature profiles and weld dimension in high power direct-diode laser welding. *Computational Materials Science*, 46:49–56, 2009.

[164] J. Sabbaghzadeh, M. Azizi, and M.J. Torkaman. Numerical and experimental investigation of seam welding with a pulsed laser. *Optics & Laser Technology*, 40:289–296, 2008.

[165] S. Bag, A. Trivedi, and A. De. Development of a finite element based heat transfer model for conduction mode laser spot welding process using an adaptive volumetric heat source. *International Journal of Thermal Sciences*, 48:1923–1931, 2009.

[166] C. Carmignani, R. Mares, and G. Toselli. Transient finite element analysis of deep penetration laser welding process in a singlepass butt-welded thick steel plate. *Computer Methods in Applied Mechanics and Engineering*, 179:197–214, 1999.

[167] G.A. Moraitis and G.N. Labeas. Residual stress and distortion calculation of laser beam welding for aluminium lap joints. *Journal of Materials Processing Technology*, 198:260–269, 2008.

[168] R. Spina, L. Tricarico, G. Basile, and T. Sibillano. Thermo-mechanical modeling of laser welding of AA5083 sheets. *Journal of Materials Processing Technology*, 191:215–219, 2007.

[169] M. Zain ul abdein, D. Nélias, J.-F. Jullien, and D. Deloison. Experimental investigation and finite element simulation of laser beam welding induced residual stresses and distortions in thin sheets of AA 6056-T4. *Materials Science and Engineering A*, 527:3025–3039, 2010.

[170] L. Chuan, Z.Jianxun, and N. Jing. Numerical and experimental analysis of residual stresses in full-penetration laser beam welding of Ti6Al4V alloy. *Rare Metal Materials*

and Engineering, 38:1317–1320, 2009.

[171] D. Deng and S. Kiyoshima. Numerical simulation of residual stresses induced by laser beam welding in a SUS316 stainless steel pipe with considering initial residual stress influences. *Nuclear Engineering and Design*, 240:688–696, 2010.

[172] C. Grignon, E. Petitpas, R. Perinet, and J. Condoure. Modélisation thermométallurgique appliquée au soudage laser des aciers. *Int. J. Therm. Sci.*, 40:669–680, 2001.

[173] S. A. Tsirkas, P. Papanikos, and Th. Kermanidis. Numerical simulation of the laser welding process in butt-joint specimens. *Journal of Materials Processing Technology*, 134:59–69, 2003.

[174] A. Capriccioli and P. Frosi. Multipurpose ANSYS FE procedure for welding processes simulation. *Fusion Engineering and Design*, 84:546–553, 2009.

[175] T. Zhang, C.S. Wu, G.L. Qin, X.Y. Wang, and S.Y. Lin. Thermomechanical analysis for laser + GMAW-P hybrid welding process,. *Computational Materials Science*, 47:848–856, 2010.

[176] D.-H. Kang, K.-J. Son, and Y.-S. Yang. Analysis of laser weldment distortion in the EDFA LD pump packaging. *Finite Elements in Analysis and Design*, 37:749–760, 2001.

[177] W.S. Chang and S.J.Na. A study on the prediction of the laser weld shape with varying heat source equations and the thermal distortion of a small structure in micro-joining. *Journal of Materials Processing Technology*, 120:208–214, 2002.

[178] M. Kemal Apalak, K. Aldas, and F. Sen. Thermal non-linear stresses in an adhesively bonded and laser-spot welded single-lap joint during laser-metal interaction. *Journal of Materials Processing Technology*, 142:1–19, 2003.

[179] P. Martinson, S. Daneshpour, M. Koçak, S. Riekehr, and P. Staron. Residual stress analysis of laser spot welding of steel sheets. *Materials and Design*, 30:3351–3359, 2009.

[180] A.S. Khanna, S. Kumari, S. Kanungo, and A. Gasser. Hard coatings based on thermal spray and laser cladding. *Int. J. Refract. Met. Hard Mater.*, 27:485–491, 2009.

[181] E. Toyserkani, S. Corbin, and A. Khajepour. *Laser cladding.* CRC Press, 2005.

[182] L. Lü, J.Y.H. Fuh, and Y.S. Wong. *Laser-induced materials and processes for rapid prototyping.* Kluwer Academic Publishers, 2001.

[183] V.M. Weerasinghe and W.M. Steen. Computer simulation model for laser cladding. *ASME HTD*, 29:15–23, 1983.

[184] A. Kar and J. Mazumder. One-dimensional diffusion model for extended solid solution in laser cladding. *Journal of Applied Physics*, 61:2645–2655, 1987.

[185] A. Kar and J. Mazumder. Extended solid solution and nonequilibrium phase diagram for Ni-Al alloy formed during laser cladding. *Metallurgical Transactions A*, 20:363–371, 1989.

[186] G. Agrawal, A. Kar, and J. Mazumder. Theoretical studies on extended solid solubility and nonequilibrium phase diagram for Nb-Al alloy formed during lase cladding. *Scripta Metalurgica et Materialia*, 28:1453–1458, 1993.

[187] A.F.A. Hoadley and M. Rappaz. A thermal model of laser cladding by powder injection. *Metall. Trans. B*, 23:631–642, 1992.

[188] N. Pirch, E.W. Kreutz, L. Möller, A. Gasser, and K. Wissenbach. Melt dynamics in surface processing with laser radiation. *ECLAT 90. Proceedings. Witzmannsberg: EMS Europ. Media Service*, page 56, 1991.

[189] M. Picasso and A.F.A. Hoadley. Finite element simulation of laser surface treatments including convection in the melt pool. *International Journal of Numerical Methods for*

Heat & Fluid Flow, 4:61–83, 1993.

[190] M. Picasso. An adaptive finite element algorithm for a two-dimensional stationary Stefan-like problem. *Comput. Methods Appl. Mech. Engrg.*, 124:213–230, 1995.

[191] M. Picasso, C.F. Marsden, J.D. Wagniere, A. Frenk, and M. Rappaz. A simple but realistic model for laser cladding. *Metallurgical and materials transactions B*, 25:281–291, 1994.

[192] L. Han, F.W. Liou, and K.M. Phatak. Modeling of laser cladding with powder injection. *Metallurgical and Materials Transactions B*, 35:1139–1150, 2004.

[193] J. Choi, L. Han, and Y. Hua. Modeling and experiments of laser cladding with droplet injection. *J. Heat Transfer*, 127:978–987, 2005.

[194] A. Kumar and S. Roy. Effect of three-dimensional melt pool convection on process characteristics during laser cladding. *Computational Materials Science*, 46:495–506, 2009.

[195] J.D. Kim and Y. Peng. Melt pool shape and dilution of laser cladding with wire feeding. *Journal of Materials Processing Technology*, 104:284–293, 2000.

[196] J.D. Kim and Y. Peng. Time-dependent FEM simulation of dilution control of laser cladding by adaptative mesh method. *ASME International Journal*, 14:177–187, 2000.

[197] G. Zhao, C. Cho, and J-D. Kim. Application of 3-d fem method using lagrangian formulation to dilution control in laser cladding process. *International Journal of Mechanical Sciences*, 45:777–796, 2003.

[198] C. Cho, G. Zhao, S-Y. Kwak, and C.B. Kim. Computational mechanics of laser cladding process. *Journal of Materials Processing Technology*, 153-154:494–500, 2004.

[199] S. Kumar and S. Roy. Development of theoretical process maps to study the role of powder preheating in laser cladding. *Computational Materials Science*, 37:425–433, 2006.

[200] Y. Lei, R. Sun, J. Lei, Y. Tang, and W. Niu. A new theoretical model for high power laser clad TiC/NiCrBSiC composite coatings on Ti6AlA4V alloys. *Optics and Lasers in Engineering*, 48:899–905, 2010.

[201] F. Wang, H. Mao, D. Zhang, X. Zhao, and Y. Shen. Online study of cracks during laser cladding process based on acoustic emission technique and finite element analysis. *Applied Surface Science*, 255:3267–3275, 2008.

[202] J.T. Hofman, F. de Lange, B. Pathiraj, and J. Meijer. FEM modeling and experimental verification for dilution control in laser cladding. *Journal of Materials Processing Technology*, 211:187–196, 2011.

[203] R. Jendrzejewski, I. Kreja, and G. Sliwinski. Temperature distribution in laser-clad multilayers. *Materials Science and Engineering A*, 379:313–320, 2004.

[204] W.-B. Li, H. Engström, J. Powell, Z. Tan, and C. Magnusson. Modelling of the laser cladding process - preheating of the blown powder material. *Lasers in Engineering*, 4:329–341, 1995.

[205] J. Lin. A simple model of powder catchment in coaxial laser cladding. *Optics & Laser Technology*, 31:233–238, 1999.

[206] J. Lin. Temperature analysis of the powder streams in coaxial laser cladding. *Optics & Laser Technology*, 31:565–570, 1999.

[207] J. Lin and B-C. Hwang. Coaxial laser cladding on an inclined substrate. *Optics & Laser Technology*, 31:571–578, 1999.

[208] J. Lin and B-C. Hwang. Clad profiles in edge welding using a coaxial powder filler nozzle. *Optics & Laser Technology*, 33:267–275, 2001.

[209] C-Y. Liu and J. Lin. Thermal processes of a powder particle in coaxial laser cladding.

Optics & Laser Technology, 35:81–86, 2003.

[210] G. Zhu, D. Li, A. Zhang, and Y. Tang. Numerical simulation of metallic powder flow in a coaxial nozzle in laser cladding direct metal deposition. *Optics & Laser Technology*, 43:106–113, 2011.

[211] A.H. Nickel, D.M. Barnett, and F.B. Prinz. Thermal stresses and deposition patterns in layered manufacturing. *Materials Science and Engineering*, 317:59–64, 2001.

[212] K. Dai and L. Shaw. Thermal and stress modeling of multi-material laser processing. *Acta Materialia*, 49:4171–4181, 2001.

[213] J.K. Kahlen and A. Kar. Residual stresses in laser-deposited metal parts. *Journal of Laser Applications*, 49:60–69, 2001.

[214] A. Vasinonta, J.L. Beuth, and M.L. Griffith. Process maps for laser deposition of thin-walled structures. *Proceedings 1999 Solid Freeform Fabrication Symposium, Austin, TX, USA*, pages 383–391, 1999.

[215] M. Labudovic, D. Hu, and R. Kovacevic. A three dimensional model for direct laser metal powder depositon and rapid prototyping. *Journal of Materials Science*, 38:35–49, 2003.

[216] A.M. Deus. *A thermal and mechanical model of laser cladding.* PhD thesis, Urbana, Illinois, 2004.

[217] J.W. Ringsberg, A. Skyttebol, and B. L. Josefson. Investigation of the rolling contact fatigue resistance of laser cladded twin-disc speciments: FE simulation of laser cladding, grinding and a twin disc test. *International Journal of Fatigue*, 27:702–714, 2005.

[218] R. Jendrzejewski and G. Sliwinski. Investigation of temperature and stress field in laser cladded coatings. *Applied Surface Science*, 254:921–925, 2007.

[219] R. Jendrzejewski, G. Sliwinski, M. Krawczuk, and W. Ostachowicz. Temperature and stress during laser cladding of double-layer coatings. *Surface and Coatings Technology*, 201:3328–3334, 2006.

[220] H-Y. Zhao, H-T. Zhang, C-H. Xu, and X-Q. Yang. Termperature and stress fields of multi-track laser cladding. *Trans. Nonferrous Met. Soc. China*, 19:495–501, 2009.

[221] A. Suárez, J.M. Amado, M.J. Tobar, A. Yáñez, E. Fraga, and M.J Peel. Study of residual stresses generated inside laser cladded plates using FEM and diffraction of synchrotron radiation. *Surface and Coatings Technology*, 204:1983–1988, 2010.

[222] S. Gosh and J. Choi. Three-dimensional transient finite element analysis for residual stresses in the laser aided direct metal/material deposition process. *Journal of Laser Applications*, 17:144–158, 2005.

[223] F. Brückner, D. Lepski, and E. Beyer. FEM calculations of thermally induced stresses in laser cladded coatings. *Munich: Proc. LIM, Lasers in Manufacturing 2007*, pages 97–103.

[224] F. Brückner, D. Lepski, and E. Beyer. Simulation of thermal stress in induction-assisted laser cladding. *Proc ICALEO 2007, Laser Institute of America, Orlando (USA)*, pages 647–656, 2007.

[225] F. Brückner, D. Lepski, and E. Beyer. Modeling the influence of process parameters and additional heat souces on residual stresses in laser cladding. *Journal of Thermal Spray Technology*, 16:355–373, 2006.

[226] A. Crespo, A. Deus, and R. Vilar. Finite element analysis of laser powder deposition of titanium. *ICALEO 2006 Congress Proceedings, Scottsdale, AZ*, 2005.

[227] L. Wang, S. Felicelli, Y. Gooroochurn, P. T. Wang, and M.F. Horstemeyer. Optimization of the LENS process for steady molten pool size. *Materials Science and Engineering A*,

474:148–156, 2008.

[228] L. Wang, S.D. Felicelli, and P. Pratt. Residual stresses in LENS-deposited AISI 410 stainless steel plate. *Materials Science and Engineering A*, 496:234–241, 2008.

[229] J. Mackerle. Finite element analysis and simulation of welding: a bibliography (1976-1996). *Model. Simul. Mater. Sci. Eng.*, 4:501–533, 1996.

[230] A.P. Mackwood and R.C.Crafer. Thermal modelling of laser welding and related processes: a literature review. *Optics & Laser Technology*, 37:99–115, 2005.

[231] L.-E. Lindgren. Finite element modelling and simulation of welding. part 1: Increased complexity. *J. Therm. Stresses*, 24:141–192, 2001.

[232] L.-E. Lindgren. Finite element modelling and simulation of welding. part 2: Improved material modelling. *J. Therm. Stresses*, 24:195–231, 2001.

[233] L.-E. Lindgren. Finite element modelling and simulation of welding. part 3: Efficiency and integration. *J. Therm. Stresses*, 24:305–334, 2001.

[234] C.A. Felippa, K.C. Park, and C. Farhat. Partitioned analysis of coupled mechanical systems. *Comput. Methods Appl. Mecha. Engrg.*, 190:3247–3270, 2001.

[235] O.C. Zienkiewicz and R.L.Taylor. *The finite element method.* Oxford, 2000.

[236] R. Lewis, K. Morgan, H. Thomas, and K. Seetharamu. *The Finite Element Method in Heat Transfer Analysis.* John Wiley & Sons, 1996.

[237] Ansys Inc. *ANSYS Theory reference manual.*

[238] Simulia Inc. *ABAQUS reference manual.*

[239] A. H. van de Boogaard, T. Meinders, and J. Huétink. Efficient implicit finite element analysis of sheet forming processes. *International Journal for Numerical Methods in Engineering*, 56:1083–1107, 2003.

[240] T. Belytschko. *Computational Methods for Transient Analysis*, chapter An overview of semidiscretization and time procedures, pages 3–65. North Holland, 1983.

[241] T.J.R. Huges. *Computational Methods for Transient Analysis*, chapter Analysis of transient algorithms with particular reference to stability behaviour, pages 67–155. North Holland, 1983.

[242] J. E. Moody and R.H. Hendel. Temperature profiles induced by a scanning CW laser beam. *J. Appl. Phys.*, 53:4364–4371, 1982.

[243] W.D. Rolph and K.J. Bathe. An efficient algorithm for analysis of non linear heat transfer with phase changes. *Int. J. Numer. Methods Engrg.*, 18:119–134, 1982.

[244] Y.V.L.N. Murthy, G.V. Rao, and P.K. Iyer. Numerical simulation of welding and quenching processes using transient thermal and thermo-elasto-plastic formulations. *Comput. Struct.*, 60:131–154, 1996.

[245] H.C. Huang and A. Usmani. *Finite Element Analysis for Heat Transfer.* Springer Verlag, 1994.

[246] K. Fujiwara, Y. Okamoto, A. Kameari, and A. Ahagon. The newton-raphson method accelerated by using a line search. comparison between energy functional minimization and residual minimization. *IEEE Transactions on Magnetics*, 41:1724–1727, 2005.

[247] P. Tarvydas and A. Noreika. Usability evaluation of finite element method equation solvers. *Electronics and electrical engineering*, 2:13–16, 2007.

[248] G. Dhondt. *The Finite Element for Three-dimensional Thermomechanical Applications.* John Wiley & Sons, 2004.

[249] A. Cifuentes and A. Kalbag. A performance study of tetrahedral and hexahedral elements in 3-D finite element structural analysis. *Finite Elem. Anal. Des*, 12:313–331, 1992.

[250] S. Benzley et al. A comparison of all hexagonal and all tetrahedral finite element meshes for elastic and elasto-plastic analysis. In *Proc. of 14th Ann.Int. Meshing Roundtable: Albuquerque, USA,*, 1995.

[251] S. M. Allen and E. L. Thomas. *The Structure of Materials.* John Wiley & Sons, 1999.

[252] M. Rappaz, M. Bellet, M. Deville, and R. Snyder. *Numerical Modelling in Materials Science and Engineering.* Springer, 2003.

[253] J.C. Simo and T.J.R. Huges. *Computational Inelasticity.* Springer, 1998.

[254] H.J.M. Geijselaers. *Numerical Simulation of Stresses due to Solid State Transformations: The Simulation of Laser Hardening.* PhD thesis, 2003.

[255] H. Mehrer. *Diffusion in Solids Fundamentals, Methods, Materials, Diffusion-Controlled Processes.* Springer, 2007.

[256] J. Crank. *The Mathematics Of Diffusion.* Oxford, 1970.

[257] F.M.B. Fernandes, S. Denis, and A. Simon. Mathematical model coupling phased transformation and temperature evolution during quenching of steel. *Materials Science and Technology*, 1:838–844, 1985.

[258] W.P. de Oliveira, M.A. Savi, P.M.C.L. Pacheco, and L. F. G. de Souza. Thermomechanical analysis of steel cylinders quenching using a constitutive model with diffusional and non-diffusional phase transformations. *Mechanics of Materials*, 42:31–43, 2010.

[259] Tian Dong. *Simulation and technology design of quenching of steel workpieces with complex shapes.* PhD thesis, Shangai Jiao Tong Universit, Shanghai, 1998.

[260] E.B. Hawbolt, B. Chau, and J.K. Brimacombe. Kinetics of austenite-ferrite and austenite-pearlite transformation in a 1025 carbon steel. *Metallurgical Transactions A*, 16:565–577, 1985.

[261] G. Roberts, G. Krauss, and R. Kennedy. *Tool Steels.* ASM International, 2000.

[262] G.R. Speich and W.C. Leslie. Tempering of steel. *Metall. Trans.*, 3:1043–1054, 1972.

[263] H. Tsuyao. Progress in martensitic transformations (I). *Shanghai Metals*, 25:1–8, 2003.

[264] J.S. Kirkaldy, D. Venugopalan, A.R. Marder, and J.I. Goldstein. Phase transformations in ferrous alloys. *The Metallurgical Society of AIME*, pages 125–148, 1984.

[265] G. Casalino, F. Curcio, F. Memola, and C. Minutolo. Investigation on Ti6Al4V laser welding using statistical and taguchi approaches. *J. Mater. Process. Technol.*, 167:422–428, 2005.

[266] M.S.F Lima. Laser beam welding of titanium nitride coated titanium using pulse-shaping. *Mater. Res.*, 8:323–328, 2005.

[267] V. N. Moiseyev. *Titanium Alloys in Russian Aircraft and Aerospace Applications.* Taylor & Francis, 2006.

[268] R. Balasubramaniam, A. Choubey, and B. Basu. Electrochemical behavior of Ti-based alloys in simulated human body fluid environment. *Trends Biomater. Artif. Organs*, 18:64–72, 2005.

[269] W. Sha and S. Malinov. *Titanium alloys: modelling of the microstructure, properties and applications.* CRC Press, 2009.

[270] Y.L. Kao, G.C. Tu, C.A. Huang, and T.T. Liu. A study on the hardness variation of alpha and beta pure titanium with different grain sizes. *Materials Science and Engineering A*, 398:93–98, 2005.

[271] F.X. Gil Mur, D. Rodríguez, and J.A. Planell. Influence of tempering temperature and time on the Ti-6A1-4V martensite. *Journal of Alloys and Compounds*, 234:287–289, 1996.

[272] Y. Fan, P. Cheng, Y.L. Yao, Z. Yang, and K. Egland. Effect of phase transformations on laser forming of Ti-6Al-4V alloy. *Journal of Applied Physics*, 98, 2005.

[273] G.S. Schajer. *Encyclopedia of Materials: Science and Technology*, chapter Residual Stresses: Measurement by Destructive Methods. Oxford, 2001.

[274] M. E. Fitzpatrick and A. Lodini. *Analysis of Residual Stress by Diffraction using Neutron and Synchrotron Radiation.* Taylor & Francis, 2003.

[275] Z. Hu, R. Kovacevic, and M. Labudovic. Experimental and numerical modeling of buckling instability of laser sheet forming. *International Journal of Machine Tools and Manufacture*, 42:1427–1439, 2002.

[276] K. C. Mills. *Recommended values of thermophysical properties for selected commertial alloys.* ASM international, 2002.

[277] T. Y. Tsui, W.C. Oliver, and G. M. Pharr. Influences of stress on the measurement of mechanical properties using nanoindentation: Part I. experimental studies in an aluminum alloy. *J. Mater. Res.*, 11:752–759, 1996.

[278] A. Bolshakov, W.C. Oliver, and G.M. Pharr. Influences of stress on the measurement of mechanical properties using nanoindentation-finite element simulations. *J. Mater. Res.*, 11:760–768, 1996.

[279] S. Suresh and A.E. Giannakopoulos. A new method for estimating residual stresses by instrumented sharp indentation. *Acta mater*, 46:5755–5767, 1998.

[280] B. Taljat and G.M.Pharr. Measurement of residual stresses by load and depth sensing spherical indentation. *Mater. Res. Soc. Symp. Proc.*, 594:519–524, 2000.

[281] J.G. Swadener, B. Taljat, and G.M. Pharr. Measurement of residual stress by load and depth sensing indentation with spherical indenters. *J. Mater. Res.*, 16:2091–2102, 2001.

[282] C.M. Lepienski, G.M. Pharr, Y.J. Park, T.R. Watkins, A. Misra, and X. Zhang. Factors limiting the measurement of residual stresses in thin films by nanoindentation. *Thin Solid Films*, 447-448:251–257, 2004.

[283] S. Carlsson and P.L. Larsson. On the determination of residual stress and strain fields by sharp indentation testing. part I: theoretical and numerical analysis. *Acta Materialia*, 49:2179–2191, 2001.

[284] S. Carlsson and P.L. Larsson. On the determination of residual stress and strain fields by sharp indentation testing. part II: experimental investigation. *Acta Materialia*, 49:2193–2203, 2001.

[285] Y-H. Lee and D. Kwon. Measurement of residual-stress effect by nanoindentation on elastically strained (1 0 0) W. *Scripta Materialia*, 49:1459–1465, 2003.

[286] Y-H. Lee and D. Kwon. Estimation of biaxial surface stress by instrumented indentation with sharp indenters. *Acta Materialia*, 52:1555–1563, 2004.

[287] J. Jang, D. Son, Y-H. Lee, Y. Choi, and D. Kwon. Assessing welding residual stress in A335 P12 steel welds before and after stress-relaxation annealing through instrumented indentation technique. *Scripta Materialia*, 48:743–748, 2003.

[288] www.matweb.com.

[289] A. Steuwer, M.J. Peel, and T. Buslaps. Aspects of residual stress determination using energy-dispersive synchrotron x-ray diffraction. *Materials Science Forum*, 267:524–525, 2006.

[290] U. de Oliveira, V. Ocelik, and J. Th. M. De Hosson. Residual stress analysis in co-based laser clad layers by laboratory X-rays and synchrotron diffraction techniques. *Surface & Coatings Technology*, 201:533–542, 2006.

[291] U. de Oliveira, V. Ocelik, and J. Th. M. De Hosson. Microstresses and microstructure in thick cobalt-based laser deposited coatings. *Surface & Coatings Technology*, 201:6363–6371, 2007.

[292] A. C. Larson and R. B. Dreele. *GSAS - General Structure Analysis System.* Los Alamos national Laboratory, 2004.

[293] M.R. Daymond, M.A.M. Bourke, R.B. VonDreele, B. Clausen, and T. Lorentzen. Use of rietveld refinement for elastic macrostrain determination and for evaluation of plastic strain history from diffraction spectra. *Journal of applied physics*, 82:1554 –1562, 1997.

[294] G.A. Webster and R.C. Wimpory. *Journal of Materials Processing Technology*, 117:395–399, 2001.

[295] H. Alberg and D. Berglund. Comparison of plastic, viscoplastic, and creep models when modelling welding and stress relief heat treatment. *Computer Methods in Applied Mechanics and Engineering*, 192:5189–5208, 2003.

[296] D.J. Bammann and A.R. Ortega. Modeling of casting, welding and advanced solidification processes. In *The Minerals, Metals & Materials Society,*, 1993.

"Seventy-five thousand generations ago, our ancestors set this program in motion," the second man said, and in all that time we will be the first to hear the computer speak."

"An awesome prospect, Phouchg," agreed the first man, and Arthur suddenly realized that he was watching a recording with subtitles.

"We are the ones who will hear", said Phouchg, "the answer to the great question of Life...!" "The Universe...!" "And Everything...!".

"Shhh," said Loonquawl with a slight gesture, "I think Deep Thought is preparing to speak!" There was a moment's expectant pause whilst panels slowly came to life on the front of the console. Lights flashed on and off experimentally and settled down into a businesslike pattern. A soft low hum came from the communication channel.

"Good morning", said Deep Thought at last.

"Er... Good morning, O Deep Thought," said Loonquawl nervously, "do you have... er, that is... "

"An answer for you?" interrupted Deep Thought majestically. "Yes. I have."

The two men shivered with expectancy. Their waiting had not been in vain.

"There really is one?" breathed Phouchg.

"There really is one," confirmed Deep Thought.

"To Everything? To the great Question of Life, the Universe and Everything?"

"Yes."

Both of the men had been trained for this moment, their lives had been a preparation for it, they had been selected at birth as those who would witness the answer, but even so they found themselves gasping and squirming like excited children.

"And you're ready to give it to us?" urged Loonquawl.

"I am", said Deep Thought. "Now?" inquired both men.

"Now," said Deep Thought."Though I don't think that you're going to like it."

"Doesn't matter!" said Phouchg. "We must know it! Now!"

"Alright", said the computer and settled into silence again. The two men fidgeted. The tension was unbearable.

"You're really not going to like it," observed Deep Thought.

"Tell us!"

"Alright," said Deep Thought. "The Answer to the Great Question... "

"Of Life, the Universe and Everything... " said Deep Thought.

"Yes...!"

"Is... " said Deep Thought, and paused.

"Yes... !!!... ?"

"Forty-two," said Deep Thought, with infinite majesty and calm.